

**COMPILATION AND CRITICAL ASSESSMENT OF OBSERVATIONS FROM A
SELECTION OF HISTORICAL TAILINGS DAM BREACH EVENTS FOR NUMERICAL
BREACH AND RUNOUT MODELLING**

by

Daniel Alexander Mackenzie Adria

B.A.Sc., University of British Columbia, 2018

A THESIS SUBMITTED IN PARTIAL FULFILLMENT OF
THE REQUIREMENTS FOR THE DEGREE OF

MASTER OF APPLIED SCIENCE

in

THE FACULTY OF GRADUATE AND POSTDOCTORAL STUDIES
(Geological Engineering)

THE UNIVERSITY OF BRITISH COLUMBIA
(Vancouver)

November 2022

© Daniel Alexander Mackenzie Adria, 2022

The following individuals certify that they have read, and recommend to the Faculty of Graduate and Postdoctoral Studies for acceptance, a thesis entitled:

Compilation and Critical Assessment of Observations from a Selection of Historical Tailings Dam Breach Events for Numerical Breach and Runout Modelling

submitted by Daniel Adria in partial fulfillment of the requirements for the degree of

Master of Applied Science in Geological Engineering

Examining Committee:

Dr. Scott McDougall, Assistant Professor, Geological Engineering, UBC
Supervisor

Dr. Erik Eberhardt, Professor and Director, Geological Engineering, UBC
Supervisory Committee Member

Dr. Ali Ameli, Assistant Professor, Earth, Ocean and Atmospheric Sciences, UBC
Supervisory Committee Member

Dr. Violeta Martin, Specialist Hydrotechnical Engineer, Knight Piésold Ltd., and Adjunct Professor, Civil Engineering, UBC
Supervisory Committee Member

Dr. Bernard Laval, Professor and Department Head, Civil Engineering, UBC
Additional Examiner

Abstract

Tailings Dam Breach Analyses and various modelling software are used to estimate consequences of a hypothetical failure at a Tailings Storage Facility. The results of such forward-analyses are used in risk assessments and emergency planning. Many model inputs and approaches are currently based on expert judgment or adapted from other fields. There is some existing research and guidance for modelling approaches applicable for Tailings Dam Breach Analyses, however, there are few resources available that assess the hydrotechnical and geotechnical characteristics for dam breach and runout modelling from multiple diverse events. This presents a challenge for the experts who must make specific judgements for forward-analysis with little available hindsight into previous events.

To address this knowledge gap, detailed investigations into 12 historical tailings dam breach events across a range of Tailings Storage Facility arrangements and taxonomies were completed. The investigations considered the outflow volumes, breach characteristics, and observations of downstream impacts. Some of these values or observations were previously reported by others for some events, but never previously compiled for the specific purpose of breach and runout modelling. These previous reports were critically assessed and included where relevant. Several original interpretations were made, and novel data were uncovered for many of the events evaluated in this thesis. Misconceptions regarding the events were frequently encountered, which likely contribute to the existing dearth of hindsight.

Using the compiled information, a back-analysis model was developed to simultaneously simulate the breach and the tailings runout for the 12 events using HEC-RAS. HEC-RAS is a publicly available software for water resources and geohazards modelling. The modelling used the parametric breach method and non-Newtonian flow capabilities within HEC-RAS. The non-Newtonian flow parameters were determined through a comprehensive calibration process. The quality of the terrain data and misconceptions were found to be the most influential on model fit to any observed impact.

The investigations and 12 models form the most comprehensive, diverse, and detailed tailings dam breach database to date. The insights from the investigations and modelling are applicable to forward-analysis Tailings Dam Breach Analyses, and the database serves as a springboard for multiple avenues of future research.

Lay Summary

Processing from mine projects creates a waste product known as tailings, which are commonly stored in perpetuity in large earthfill structures called tailings storage facilities. Computer models are used to predict the impacts from a failure of such tailings storage facilities as part of risk assessments and emergency planning. Limited information is known about past tailings storage facility failures, and the physical phenomena during the failure and runout are not well understood. This presents a challenge to the prediction models, as they may have unrealistic results and therefore little use for risk assessment and emergency planning. The focus of this research was on investigating and modelling past failure events. The findings can be used to guide computer modelling for predictive purposes, so mine owners, consultants, regulators, and civilian stakeholders can better understand and manage the risks associated with tailings storage facilities.

Preface

This thesis is original and independent work completed by the author. I was responsible for the investigations, numerical modelling, and writing of this thesis under the supervision of Dr. Scott McDougall. Dr. McDougall and I developed the proposal and scope of the thesis research. Under my supervision, Anda Cen assisted with initial modelling for this thesis and Amin Ahmed assisted with mapping and figure creation, as well as some modelling. I revised and finalized the modelling and figures created by Anda and Amin. Collaboration and feedback on the approach and deliverables were provided by Dr. McDougall, Dr. Violeta Martin, and various members of the CanBreach Research Program.

The inundation areas used in this thesis were initially compiled in Ghahramani et al. (2020). I edited and refined these areas for some events in this thesis. The database in this thesis was also initially based on the database in Rana et al. (2021b). Survey data for the Cadia events was provided by Newmont Mining Limited, which I subsequently processed and edited to use in a portion of the modelling.

A version of the investigation and modelling for the Harmony 4A event in South Africa, 1994 (colloquially known as the Merriespruit event) was presented as part of a presentation and article for the Tailings and Mine Waste conference in Banff, Canada [Adria, D., Ghahramani, N., Cen, A., McDougall, S., Rana, N., Evans, S. G., & Take, W. A. (2021). Advancements in the modelling of tailings dam breaches. In N. A. Beier, G. W. Wilson, & D. C. Sego (Eds.), *Proceedings of the Twenty-Fifth International Conference on Tailings and Mine Waste*, 7-10 November 2021, Banff, Alberta, Canada (pp. 324–332). Edmonton, Alberta; University of Alberta, Geotechnical Center]. I was the lead author, responsible for developing the methodology, modelling, and drafting the manuscript. Cen, A. assisted with the modelling. Ghahramani, N. and Rana, N. contributed data and manuscript edits. McDougall, S., contributed to the original concept and manuscript edits. Evans, S. G., and Take, W. A. assisted with editing the manuscript. The content from the conference article is adapted in Sections 4.3 and 4.4, and in Section B.3 in Appendix B.

A version of the investigation and modelling for the Mount Polley event in Canada, 2014, and Feijão event in Brasil, 2019, was presented in a technical article for Geoscience BC as part of a scholarship condition from the non-profit organization [Adria, D., McDougall, S., & Evans, S. G. (2022). *Geoscience BC Summary of Activities 2021*:

Minerals (Report 2022-01, pp. 81–91). Vancouver, BC: Geoscience BC]. I was the lead author, responsible for the original concept, analysis, modelling, and manuscript drafting. McDougall, S. and Evans, S. G. contributed manuscript reviews. W. Andy Take and Violeta Martin performed additional external review. The content from the technical article is included in Section 4.2 and Sections B.8 and B.12 in Appendix B.

Table of Contents

| | |
|---|--------------|
| Abstract | iii |
| Lay Summary | iv |
| Preface | v |
| Table of Contents..... | vii |
| List of Tables..... | ix |
| List of Figures | xi |
| List of Symbols | xvi |
| List of Acronyms..... | xviii |
| Acknowledgements | xix |
| Chapter 1: Introduction | 1 |
| 1.1 Background | 1 |
| 1.2 Problem Statement..... | 2 |
| 1.3 Research Objectives | 3 |
| 1.4 Research Hypotheses | 3 |
| 1.5 Research Approach and Thesis Structure..... | 3 |
| Chapter 2: A Review of Tailings Dam Breach and Runout..... | 5 |
| 2.1 Tailings Storage Facilities..... | 5 |
| 2.1.1 Tailings | 5 |
| 2.1.2 Tailings Dams..... | 6 |
| 2.2 Tailings Dam Breach | 8 |
| 2.2.1 Failure Modes..... | 8 |
| 2.2.2 Outflow Volumes..... | 11 |
| 2.2.3 Breach Characteristics..... | 11 |
| 2.3 Tailings Runout | 13 |
| 2.3.1 Impacts from Tailings Flows | 13 |
| 2.3.2 Downstream Environment | 15 |
| 2.4 Tailings Rheology..... | 16 |
| 2.5 Numerical Models..... | 22 |
| 2.5.1 Breach Modelling Considerations | 23 |
| 2.5.2 Runout Modelling Considerations | 24 |
| 2.5.3 Terrain datasets..... | 25 |
| 2.5.4 Model Calibration, Validation, and Verification | 26 |
| 2.6 Summary | 28 |
| Chapter 3: Development of a Tailings Dam Breach Database | 31 |
| 3.1 Investigated Events | 31 |
| 3.2 Data Sources..... | 32 |
| 3.3 Outflow Volume | 34 |
| 3.3.1 Supernatant Pond Volume..... | 34 |
| 3.3.2 Tailings Volume | 34 |
| 3.3.3 Tailings Solids and Interstitial Water..... | 35 |
| 3.4 Breach Processes and Formation Time | 36 |

| | | |
|-------------------|---|------------|
| 3.5 | Breach Geometry | 36 |
| 3.5.1 | Height Conventions | 37 |
| 3.5.2 | Trapezoidal Breach Shape | 40 |
| 3.6 | Runout Parameters | 42 |
| 3.6.1 | Quadratic Formula | 42 |
| 3.6.2 | Manning's Coefficient | 45 |
| 3.7 | Event Runout Observations..... | 46 |
| 3.8 | Local Runout Observations | 48 |
| 3.8.1 | Flow Depths..... | 48 |
| 3.8.2 | Arrival Times..... | 48 |
| 3.8.3 | Miscellaneous and Derived Observations..... | 49 |
| 3.9 | Discussion | 51 |
| 3.9.1 | Outflow Volumes..... | 51 |
| 3.9.2 | Breach Processes and Formation Time..... | 54 |
| 3.9.3 | Breach Geometry..... | 56 |
| 3.9.4 | Event and Local Observations | 58 |
| Chapter 4: | Numerical Modelling with HEC-RAS..... | 60 |
| 4.1 | Terrain Data and Modifications..... | 60 |
| 4.2 | Parametric Breach Modelling | 67 |
| 4.2.1 | Breach Weir Components..... | 67 |
| 4.2.2 | Stage-Storage Curves | 72 |
| 4.3 | Tailings Dam Breach Modelling with HEC-RAS | 76 |
| 4.3.1 | Overview of HEC-RAS and Modelling Approach | 76 |
| 4.3.2 | HEC-RAS Modelling Set-Up | 77 |
| 4.4 | Rheology and Model Calibration | 83 |
| 4.5 | Discussion | 88 |
| 4.5.1 | Terrain Data and Modifications | 88 |
| 4.5.2 | Parametric Breach and Runout Modelling in HEC-RAS | 91 |
| 4.5.3 | Rheology and Model Calibration..... | 94 |
| Chapter 5: | Concluding Remarks..... | 97 |
| 5.1 | Summary of Work and Main Findings | 97 |
| 5.2 | Recommendations for Future Research and Industry | 100 |
| 5.3 | Closure | 104 |
| | References..... | 106 |
| | Appendix A: Tailings Dam Breach and Runout Database..... | 122 |
| | Appendix B: Tailings Dam Breach and Runout Investigations and Modelling Summaries..... | 144 |

List of Tables

| | |
|--|-----|
| Table 2.1 Outflow Behaviour as a Function of Solids Concentration (CDA, 2021, Modified from O'Brien, 1986) | 19 |
| Table 3.1 Common Land Cover and Typical Manning's Coefficients for Two Dimensional Hydraulic Modelling (Arcement & Schneider, 1986; Janssen, 2016) | 46 |
| Table 5.1 Recommended for Distribution of Level of Effort for Forward-Analysis TDBAs | 103 |
| Table A.1 Investigated Tailings Storage Facilities and their Impoundment Characteristic | 123 |
| Table A.2 Investigated Tailings Dam Breach and Runout Events with their High-Level Classifications and Characteristics | 125 |
| Table A.3 Primary Data Sources and References listed by Event (Page 1 of 2) | 127 |
| Table A.4 Outflow Volumes | 129 |
| Table A.5 Breach Processes | 131 |
| Table A.6 Breach Heights and Trapezoid Breach Geometries | 133 |
| Table A.7 Runout Parameters | 135 |
| Table A.8 Local Runout Observations | 137 |
| Table A.9 Terrain Data used for the HEC-RAS Modelling in this Thesis | 140 |
| Table A.10 Recommendations for Improvements for Each Event | 142 |
| Table B.1 Prestavèl Outflow Volumes | 147 |
| Table B.2 Prestavèl Breach Geometry | 148 |
| Table B.3 Gillibrand Pond No. 6 Outflow Volumes | 155 |
| Table B.4 Gillibrand Pond No. 6 Breach Geometry | 156 |
| Table B.5 Gillibrand Pond No. 6 Rheological Parameters | 158 |
| Table B.6 Harmony 4A Outflow Volumes | 163 |
| Table B.7 Harmony 4A Breach Geometry | 163 |
| Table B.8 Aznalcóllar Outflow Volumes used in HEC-RAS Model | 172 |
| Table B.9 Aznalcóllar Breach Geometry | 173 |
| Table B.10 Tashan Breach Geometry | 180 |
| Table B.11 MAL Reservoir X Outflow Volumes | 187 |
| Table B.12 MAL Reservoir X Breach Geometry | 188 |
| Table B.13 MAL Reservoir X Observations and Modelled Results Comparison | 192 |

| | |
|--|-----|
| Table B.14 Kayakari Outflow Volumes | 198 |
| Table B.15 Kayakari Breach Geometry | 198 |
| Table B.16 Mount Polley Outflow Volumes | 204 |
| Table B.17 Mount Polley Breach Geometry | 205 |
| Table B.18 Mount Polley Observations and Modelled Results Comparison | 208 |
| Table B.19 Fundão Event I and Event II Deposited Volumes (Fundação Renova, 2016) | 214 |
| Table B.20 Fundão Event I Outflow Volumes..... | 215 |
| Table B.21 Fundão Event I Breach Geometry..... | 216 |
| Table B.22 Rheology for the Fundão Tailings Extrapolated from Measured Trends (Adopted from Machado, 2017)..... | 218 |
| Table B.23 Fundão Event I Observations and Modelled Results Comparison | 219 |
| Table B.24 Tonglüshan Outflow Volumes | 224 |
| Table B.25 Tonglüshan Breach Geometry | 224 |
| Table B.26 Measured Rheology for the Tonglüshan Tailings (Adopted from Zheng, 2018) | 227 |
| Table B.27 Cadia NTSF Outflow Volumes | 235 |
| Table B.28 Cadia NTSF Breach Geometry | 236 |
| Table B.29 Feijão Dam I Outflow Volumes..... | 244 |
| Table B.30 Feijão Dam I Breach Geometry..... | 244 |
| Table B.31 Feijão Dam I Land Cover and Selected Manning's Coefficients | 245 |
| Table B.32 Feijão Dam I Observations and Modelled Results Comparison | 247 |

List of Figures

| | | |
|-------------|--|----|
| Figure 2.1 | Schematic of TSF Cross Sections for Different Dam Construction Methods: A) Upstream, B) Centreline, and C) Downstream (CDA, 2021) .. | 7 |
| Figure 2.2 | Schematic of TSF Arrangements: a) Ring-Dyke, b) Side-Hill, and c) Cross Valley (Blight, 2010) | 7 |
| Figure 2.3 | Classification System for Tailings Dam Failures (CDA, 2021, Modified from Small et al., 2017) | 10 |
| Figure 2.4 | Outflow Volume Materials and Height for a hypothetical Case 1A dam breach with a Process II breach followed by Process I breach | 11 |
| Figure 2.5 | Comparison of Breach Width Definitions from Rana et al (2021a) and Froehlich (2008) | 12 |
| Figure 2.6 | Runout Zone Classification (Ghahramani et al., 2020)..... | 14 |
| Figure 2.7 | Shear Rate vs. Shear Stress Plot of Newtonian and Non-Newtonian Fluids | 17 |
| Figure 2.8 | Outflow Behaviour as a Function of Solids Concentration (CDA, 2021, Modified from Martin et al., 2019 and Julien & O'Brien, 1985) | 20 |
| Figure 2.9 | Measured Rheology Values for Tailings and Debris Flows (Modified from Martin et al., 2022) | 21 |
| Figure 2.10 | Distinction Between a DSM (Dotted Magenta), a DTM (Dashed Orange), and True Bare Earth Elevation (Solid Brown) | 26 |
| Figure 3.1 | Breach Hydraulic Control shown with A) Annotated Oblique photo of the Harmony 4A Breach, and B) Hypothetical Profile..... | 38 |
| Figure 3.2 | Height Conventions for A) Standard Breach Geometry, and B) Slab Breach Geometry | 39 |
| Figure 3.3 | Trapezoidal Breach Geometry at the Dam Crest | 41 |
| Figure 3.4 | Runout Distance Measurement Conventions | 47 |
| Figure 3.5 | Zone 1 Inundation Area versus Total Outflow Volume with Volumetric Solids Concentration for Unconfined Runout Events (Regression from Rana et al., 2021a)..... | 53 |
| Figure 3.6 | Process I Tailings Dam Breach Mean Erosion Rates Compared to Water Reservoir Dams (Data from Walder & O'Connor, 1997) | 55 |

| | | |
|-------------|--|----|
| Figure 3.7 | Observations of Breach Height versus Dam Height at the Breach Location | 57 |
| Figure 3.8 | Observed Breach Heights and Widths Compared to Water Reservoir Dams (Data from Wahl, 1998)..... | 58 |
| Figure 4.1 | Example Breach Channel Modifications A) Terrain Data before Breach Channel Modifications, B) Terrain Data after Breach Channel Modifications, and C) Satellite Imagery for Comparison | 62 |
| Figure 4.2 | Example River Channel Removal A) Terrain Data before River Channel Modifications, B) Terrain Data after River Channel Modifications, C) Satellite Imagery for Comparison, D) Cross Section through the Floodplain, and E) Profile along the Entire River Channel | 64 |
| Figure 4.3 | Example River Channel Removal A) Terrain Data before River Channel Modifications, B) Terrain Data after River Channel Modifications, C) Satellite Imagery for Comparison, D) Cross Section at the Canyon, and E) Profile along the River Channel at the Canyon | 65 |
| Figure 4.4 | Example Berm Addition A) Terrain Data before Berm Edits, B) Terrain Data after Berm Modifications, C) Satellite Imagery for Comparison, and D) Profile through Berm Modifications..... | 66 |
| Figure 4.5 | Example Artefact Removal A) Terrain Data before Artefact Removal, B) Terrain Data after Artefact Removal, and C) Aerial Imagery from March 10th, 2018, for Comparison..... | 67 |
| Figure 4.6 | Breach Width Progression Schematic in HEC-RAS | 70 |
| Figure 4.7 | A) Breach Head Profile Schematic, and B) Breach Head during Submerged Outflow | 72 |
| Figure 4.8 | Conventional Horizontal Slice and Inclined Slice Method for Stage-Storage Curves (Adapted from Schoeman, 2018)..... | 74 |
| Figure 4.9 | A) Six Idealized Shapes for the Outflow Volume During a Tailings Dam Breach B) Stage-Storage Curves for Idealized Shapes in Relative Values, and C) Stage-Storage Curves for the Idealized Shapes in Real Values (Adapted from Adria, McDougall et al., 2021). | 74 |
| Figure 4.10 | Example HEC-RAS Model Set-Up and Model Elements..... | 78 |
| Figure 4.11 | Example Computational Grid Design | 80 |
| Figure 4.12 | Rheology Calibration Process | 84 |

| | | |
|-------------|---|-----|
| Figure 4.13 | Example Modelled Areas for the ΩTm Metric..... | 86 |
| Figure 4.14 | Example Rheology Calibration Plot in Log-Log Scale | 87 |
| Figure 4.15 | 2D Connection and Flow Direction Schematic for a Curved Dam Crest in HEC-RAS | 92 |
| Figure B.1 | Terrain Modifications and Imagery for Prestavèl near the Romano Bridge. A) Terrain Before Channel Modification, B) Terrain After Channel Modification, C) Satellite Imagery for Comparison, D) Cross-section Along the Romano Bridge, E) Profile Along the Stava Creek Underneath the Romano Bridge | 149 |
| Figure B.2 | Prestavèl Rheology Calibration Plot in Log-Log Scale | 151 |
| Figure B.3 | Prestavèl Arrival Time Results | 151 |
| Figure B.4 | Prestavèl HEC-RAS Model Results A) Maximum Depth and B) Maximum Velocity | 152 |
| Figure B.5 | Terrain Edits and Imagery for Gillibrand Pond No. 6 A) Terrain Before Breach Channel Modification, B) Terrain After Breach Channel Modification, and C) USGS Aerial Imagery for Comparison..... | 157 |
| Figure B.6 | Gillibrand Pond No. 6 Rheology Calibration Plot in Log-Log Scale for A) The Viscous Scenario, and B) the Fluid Scenario. | 158 |
| Figure B.7 | Gillibrand Pond No. 6 HEC-RAS Model Results (Viscous Scenario) A) Maximum Depth and B) Maximum Velocity..... | 159 |
| Figure B.8 | Gillibrand Pond No. 6 HEC-RAS Model Results (Fluid Scenario) A) Maximum Depth and B) Maximum Velocity..... | 159 |
| Figure B.9 | Harmony 4A Gold Rheology Calibration Plot in Log-Log Scale..... | 165 |
| Figure B.10 | Harmony 4A HEC-RAS Model Results A) Maximum Depth and B) Maximum Velocity | 166 |
| Figure B.11 | Recorded Stage at the A39 El Guijo Gauge Operated by the Hydrographic Confederation of the Guadalquivir (IGME, 2001). | 170 |
| Figure B.12 | Terrain Modifications and Imagery for Aznalcóllar. A) Terrain Before Channel Modifications, B) Terrain After Channel Modifications, C) Satellite Imagery for Comparison, D) Cross-section Along the Turquoise Line, E) Profile Along the Entire Channel Within the Model Domain | 174 |
| Figure B.13 | Aznalcóllar Rheology Calibration Plot in Log-Log Scale | 176 |

| | | |
|-------------|---|-----|
| Figure B.14 | Recorded Stage at the A39 El Guijo Gauge (IGME, 2001) and HEC-RAS Model Results. | 176 |
| Figure B.15 | Aznalcóllar HEC-RAS Model Results A) Maximum Depth and B) Maximum Velocity | 177 |
| Figure B.16 | Tashan Rheology Calibration Plot in Log-Log Scale..... | 182 |
| Figure B.17 | Tashan HEC-RAS Model Results A) Maximum Depth and B) Maximum Velocity | 183 |
| Figure B.18 | Terrain Edits and Imagery for MAL Reservoir X at Devecser. A) Terrain Before Edits, B) Terrain After Edits, C) Satellite Imagery for Comparison, D) Cross-section Through the Devecser Forest, E) Profile along a Section of the Torna Creek by the Devecser Forest | 190 |
| Figure B.19 | MAL Reservoir X Rheology Calibration Plot in Log-Log Scale..... | 192 |
| Figure B.20 | MAL Reservoir X HEC-RAS Model Results A) Maximum Depth and B) Maximum Velocity | 193 |
| Figure B.21 | Overlap between Kayakari Zone 1 Inundation Extent (Ghahramani et al., 2020) and Tōhoku-Pacific Ocean Tsunami Impact (Matsuda et al., 2014; Suzuki et al., 2011) | 196 |
| Figure B.22 | Kayakari Rheology Calibration Plot in Log-Log Scale | 200 |
| Figure B.23 | Kayakari HEC-RAS Model Results A) Maximum Depth and B) Maximum Velocity | 201 |
| Figure B.24 | Terrain Edits and Imagery for Mount Polley. A) Terrain Before Channel Burning, B) Terrain After Channel Burning, C) Satellite Imagery for Comparison, D) Cross-section Along the Blue Line, E) Profile Along the Entire Channel Within the Model Domain | 206 |
| Figure B.25 | Mount Polley Rheology Calibration Plot in Log-Log Scale | 208 |
| Figure B.26 | Mount Polley HEC-RAS Model Results A) Maximum Depth and B) Maximum Velocity | 209 |
| Figure B.27 | Typical Terrain Edits and Imagery for Fundão Event I. A) Terrain Before Channel Burning, B) Terrain After Channel Burning, C) Satellite Imagery for Comparison, D) Cross-section Along the Blue Line, E) Profile Along a section of the Gualaxo do Norte River | 217 |
| Figure B.28 | Fundão Event I HEC-RAS Model Results up to 42 km for $C_v = 45\%$ A) Maximum Depth and B) Maximum Velocity..... | 220 |

| | | |
|-------------|---|-----|
| Figure B.29 | Terrain Edits and Imagery for Tonglüshan. A) Terrain Before Editing, B) Terrain After Editing, C) Pre-Failure Satellite Imagery for Comparison, D) Post-Failure Satellite Imagery for Comparison..... | 226 |
| Figure B.30 | Tonglüshan Rheology Calibration Plot in Log-Log Scale | 228 |
| Figure B.31 | Tonglüshan Runout Profile with Modelled Results | 228 |
| Figure B.32 | Tonglüshan HEC-RAS Model Results A) Maximum Depth and B) Maximum Velocity | 229 |
| Figure B.33 | Cadia NTSF Zone 1 Inundation Area A) Event I and B) Event II..... | 234 |
| Figure B.34 | Cadia NTSF Runout Profile (adapted from Jefferies et al. 2019) | 235 |
| Figure B.35 | Cadia NTSF Event II Rheology Calibration Plot in Log-Log Scale | 238 |
| Figure B.36 | Cadia NTSF Event II Runout Profile with Modelled Results | 238 |
| Figure B.37 | Cadia NTSF Event II HEC-RAS Model Results A) Maximum Depth and B) Maximum Velocity | 239 |
| Figure B.38 | Feijão Dam I Rheology Calibration Plot in Log-Log Scale..... | 246 |
| Figure B.39 | Feijão Dam I HEC-RAS Model Results A) Maximum Depth and B) Maximum Velocity | 248 |

List of Symbols

| | |
|-----------|--|
| A | Cross sectional area of flow |
| B_{Avg} | Average vertical breach width, as defined by Froehlich (2008) |
| B_B | Bottom breach width |
| B_T | Top breach width |
| B_W | Average planar breach width, as defined by Rana et al. (2021a) |
| B_* | Representative width for trapezoidal breach |
| b_{Bi} | Transient bottom breach width |
| b_{Ti} | Transient top breach width |
| C | Courant Number |
| C_D | Discharge coefficient for the weir equation |
| C_{Max} | Maximum volumetric solids concentration |
| C_v | Volumetric solids concentration |
| C_w | Gravimetric solids concentration |
| C_W | Weir coefficient for the weir equation |
| D | Depth of flow above channel bottom |
| d_i | Transient depth of flow |
| d_s | Representative particle size for the Quadratic formula (O'Brien, 1988) |
| d_{50} | Median particle size |
| e | <i>Void ratio</i> |
| FN | False Negative area, for Ω_{Tm} equation as defined by Barnhart et al. (2017) |
| FP | False Positive area, for Ω_{Tm} equation as defined by Barnhart et al. (2017) |
| g | Acceleration due to Earth's gravity |
| H | Total head |
| H_B | Breach height |
| h_{Bi} | Transient height of the breach |
| H_C | Crest height |
| H_D | Dam height |
| H_{DB} | Dam height at breach location |
| H_S | Slab height |
| H_W | Height of water above breach invert |
| K | Mean erosion rate, as defined in Walder & O'Connor (1997) |
| n | Gauckler-Manning's coefficient, or Manning's n |
| n_s | Shape factor for stage-storage curve |
| P | Pressure |
| Q | Magnitude of flow |
| R | Hydraulic radius of flow |
| S_f | Friction slope |
| t_i | Time in the model |
| T_f | Formation time |
| TP | True Positive area, for Ω_{Tm} equation as defined by Barnhart et al. (2017) |

| | |
|---------------|--|
| T_s | Slab thickness |
| V_I | Interstitial water volume |
| V_{Out} | Total outflow volume |
| V_P | Supernatant pond volume |
| V_S | Tailings solid volume |
| V_T | Tailings volume |
| v | Magnitude of fluid velocity |
| Z | Elevation of the channel bottom of flow |
| z_i | Transient elevation of the channel bottom of flow |
| Z_B | Breach invert elevation |
| Z_C | Dam crest elevation |
| Z_{CF} | Crest foundation elevation |
| Z_L | Left breach side slope |
| Z_R | Right breach side slope |
| Z_{TD} | Dam toe elevation |
| Z_{TB} | Breach toe elevation |
| α_i | Bagnold's empirical coefficient |
| β_H | Horizontal breach progression parameter |
| du/dy | Shear Rate |
| Δt | Computational time step |
| Δx | Computational grid resolution |
| ℓ | Fluid mixing length |
| ρ_m | Fluid mixture density |
| ρ_s | Solid particle density |
| ρ_w | Water density |
| μ | Dynamic Viscosity |
| τ | Shear Stress |
| τ_d | Dispersive stress component of the Quadratic formula (O'Brien, 1988) |
| τ_v | Viscous stress component of the Quadratic formula (O'Brien, 1988) |
| τ_T | Turbulent stress component of the Quadratic formula (O'Brien, 1988) |
| τ_y | Yield Stress |
| Ω_{Tm} | Metric for areal fit, as defined by Barnhart et al. (2021) |

List of Acronyms

| | |
|---------|---|
| ALOS | Advanced Land Observation Satellite |
| API | Application Programming Interface |
| ASTER | Advanced Spaceborne Thermal Emission and Reflection Radiometer |
| AW3D30 | Advanced Land Observation Satellite 3D – 30 m |
| BCMEM | British Columbia Ministry of Energy, Mines and Low Carbon Innovation |
| CDA | Canadian Dam Association |
| CPRM | Companhia de Pesquisa de Recursos Minerais [Mineral Resources Research Company] |
| DEM | Digital Elevation Model |
| DSM | Digital Surface Model |
| DTM | Digital Terrain Model |
| DWE | Diffusion Wave Equations |
| GIS | Geographical Information System |
| GISTM | Global Industry Standard on Tailings Management |
| HEC-RAS | Hydrologic Engineering Center River Analysis System |
| ICOLD | International Commission on Large Dams |
| InSAR | Interferometric Synthetic Aperture Radar |
| JAXA | Japan Aerospace Exploration Agency |
| LiDAR | Light Detection and Ranging |
| MAL | Magyar Alumínium Termelő és Kereskedelmi [Hungarian Aluminium Production and Trading Company] |
| SRTM | Shuttle Radar Topography Mission |
| SWE | Shallow Water Equations |
| TDBA | Tailings Dam Breach Analysis |
| TSF | Tailings Storage Facility |
| VBA | Visual Basic for Applications |

Acknowledgements

Funding for this research was provided by the CanBreach Research Program, comprising of Imperial Oil Resources Inc., Suncor Energy Inc., BGC Engineering Inc., Klohn Crippen Berger, Golder Associates Ltd. [now a member of WSP Global], and the Natural Sciences and Engineering Research Council of Canada. Financial support was also provided by Geoscience BC and various awards from the Department of Earth, Ocean and Atmospheric Sciences.

My sincere thanks to my supervisor, Scott McDougall, for his suggestions and constant nudging to go outside my technical comfort zone. These were instrumental in the thesis research and to make me a better engineer. I would also like to thank thesis committee members Erik Eberhardt and Ali Ameli. Their suggestions on the proposed concepts and statistics were helpful in the early stages of my research. Andy Take (Queen's University), Stephen Evans (University of Waterloo) and the wider CanBreach group also brought valuable viewpoints.

I am fortunate to have support and mentorship from the team at Knight Piésold Ltd., both prior to and during my research. I have too many teachers and friends there to name them all, but they know who they are. Violeta Martin has been a technical and personal role model for the past 4 years in particular, and I am lucky to have her as a supervisor at KP and a thesis committee member at UBC.

The coronavirus pandemic made for an interesting graduate degree. To my past and present colleagues in the UBC Geohazards Research Team: Alex, Sahar, Jovian, Andrew, Bea, Eimile, and Bing, thanks for sharing your technical expertise and the laughs that helped make two years of remote or hybrid work manageable. The two undergraduate research assistants, Anda Cen and Amin Ahmed, also did a fantastic job with modelling and other thesis support, despite my scattered thoughts and many revisions. I am also indebted to Negar Ghahramani and Nahyan Rana, who were invaluable to the investigations and modelling. They were brilliant sounding boards during my research (whether my ideas were good or bad) and provided a useful perspective on many topics related to tailings dam breaches.

Special thanks are owed to my past roommates during my degree: my brother Michael, my cousin Jen and her husband Kevin, and little Beatrix and Margaux. It was never a dull moment in the house, in the best of ways. The love and support from Emilie

are greatly appreciated, and I am so glad that she is at my side (just as I am at hers). Finally, I am immensely grateful to my parents, Kim and Robert; their love, patience, sacrifice, and guidance were and are fundamental to the position I am in and the person I am today.

“On two occasions I have been asked, ‘Pray, Mr. Babbage, if you put into the machine wrong figures, will the right answers come out?’ I am not able rightly to apprehend the kind of confusion of ideas that could provoke such a question.”

Charles Babbage, 1864

Chapter 1: Introduction

In this chapter, the overall context for the thesis is established by introducing the background, research problem, research objectives and hypotheses, and describing the overall research approach.

1.1 Background

Open-pit mines produce a large volume of tailings that are stored in massive impoundments behind earthfill dams, which are referred to as Tailings Storage Facilities (TSFs). Conditions and requirements for the design, construction, and operation of TSFs can be highly variable, and unfavourable geotechnical, meteorological, or structural circumstances can cause a breach or failure of the dam (Rana et al., 2021a). As these tailings dams are among the largest structures constructed in the world (Vick, 1990; ICOLD, 2001), their failure results in catastrophic consequences to downstream communities, devastates the environment, and erodes public trust in the mining industry (Santamarina et al., 2019, and the references therein).

The Global Industry Standard on Tailings Management (GISTM) strives to achieve a goal of zero harm to people and the environment from TSFs (GISTM, 2020). To support this goal, the Standard requires that mine owners and operators analyse the potential societal, economic, and environmental consequences of a hypothetical but credible tailings dam breach event for their TSFs. Similarly, all dams following the Canadian Dam Association (CDA) Dam Safety Guidelines are recommended to complete a dam breach study, including tailings dams (CDA, 2013). These Tailings Dam Breach Analyses (TDBAs) are becoming a critical aspect of a risk assessments for TSFs and can also be used to improve emergency planning, response, and mitigation measures (Martin et al., 2022). The CDA Technical Bulletin on Tailings Dam Breach Analysis (2021) is the most comprehensive description of the process and technical considerations for a TDBA to date. A TDBA can be a simple desktop study, where conservative application of empirical relations or qualitative analysis are used to meet the scope and objective. Alternatively, detailed studies, complete with site-specific characterization and numerical modelling, can be used for more detailed quantification of consequences (CDA, 2021). This thesis focuses on the detailed study and numerical modelling approach.

1.2 Problem Statement

Much has been said about limitations and uncertainties of TDBAs (Pirulli et al., 2017; CDA, 2021; Ghahramani et al., 2022; Martin et al., 2022;). Carefully investigating each assumption, input variable, and modelling approach for every dam breach study is not feasible due to limitations with budgets and schedules. Expert judgment is commonly invoked to address these concerns (Adria et al., 2021; Martin et al., 2022). Without the contextual background for past tailings dam breach events, misconceptions about important field processes may arise (Rana et al., 2021a).

Misconceptions also inevitably impact the calibration, validation, and application of numerical models. Ghahramani et al. (2022) noted such difficulties when modelling two of the best documented cases (i.e., Prestavèl, Italy, 1985, and Harmony 4A, South Africa, 1994, also known as the Stava and Merriespruit events). Ghahramani et al. recognized that more model calibration of tailings flows is needed. However, even the most comprehensive tailings dam breach database currently available (Rana et al., 2021b) primarily focuses on failure conditions, failure triggers, and broad statistical approaches, rather than the subsequent breach processes and localized runout characteristics relevant for numerical modelling of such events. A review of the literature for specific cases shows a dearth of reliable and nuanced observations from past tailings dam breach events to compile such a database. Basic reporting regarding tailings dam breach characteristics is often described as lacking in detail and reliability (Rana et al., 2021a; Rico et al., 2008). For example, Sanz-Ramos et al. (2022) noted substantial uncertainties and inconsistencies regarding the breach and runout characteristics for the Aznalcóllar event in Spain, 1998, despite over 400 scientific publications on the event.

The validity (or invalidity) of a model is equally dependent on the input parameters as the conceptual or theoretical basis of the model itself (Oreskes et al., 1994; Rykiel, 1996). As Ghahramani et al. (2022) and Rana et al., 2021a noted, there are often misconceptions or insufficient information for model inputs and model benchmarking for TDBAs. There must be a continued effort to bolster knowledge on both fronts to support expert judgement for assessing such hazards (Ghahramani et al., 2022; Gibson et al., 2022; Zubrycky, 2020). This thesis aims to provide model inputs and continue model benchmarking to address these knowledge gaps through investigating and then modelling of a dozen tailings dam failure events.

1.3 Research Objectives

To address the challenges in Section 1.2, the main objectives for this research are:

- Investigate historical tailings dam breach events to compile standardized observations, including:
 - Refined outflow volumes,
 - Breach characteristics and geometries,
 - Runout observations,
- Set up and calibrate a numerical model for each tailings dam breach event with publicly available model software, and
- Make the observations and numerical model set-ups available to support future research.

1.4 Research Hypotheses

Along with the research objectives, the following hypotheses were tested:

- The variation in breach characteristics and geometries can be explained by classifying the breach processes for each event,
- Lower volumetric solids concentration in the breach outflow is a strong contributory factor to larger inundation area and runout distance (within the Zone 1 area, defined by Ghahramani et al., 2020), and
- Some of the misconceptions in observations or model inputs can be attributed to inconsistent or unstandardized reporting of tailings dam breach events.

1.5 Research Approach and Thesis Structure

A literature review of tailings dam breach and runout events is provided in Chapter 2. Existing frameworks and the state of practice are also summarized in this chapter to give context for the subsequent investigations. Key challenges and knowledge gaps are identified in order to be addressed within this thesis or in future research.

The investigation process for the tailings dam breach events is presented in Chapter 3. This process consisted of two lines of effort: (1) a literature review of academic and technical articles for each event was completed and previously reported variables that meet standardized definitions were compiled, and (2) novel observations were made based on an ensemble of additional sources, including anecdotal accounts, news articles, photographs, and further interpretation of the academic and technical literature. The focus

of the investigation was placed on the outflow volumes, the breach process, breach geometry, and localized runout observations.

The numerical modelling methodology is described in Chapter 4. The numerical modelling was completed with Hydrologic Engineering Center's River Analysis System (HEC-RAS versions 6.1 and 6.2) using the parametric breach approach and non-Newtonian flow capabilities of the software. The compiled database informed many of the model inputs and used a mix of publicly accessible and commercial terrain data. The non-Newtonian flow inputs were determined with a systematic calibration approach. An additional trial-and-error calibration approach was undertaken if additional runout observations or tailings characterization existed. Commonly required adjustments to the terrain data are also described.

The research and findings are summarized in Chapter 5. The recommendations for future research and implications for industry and forward analysis TDBAs are listed, informed by the both the investigations and modelling process. The summary tables from the tailings dam breach event investigations are presented in Appendix A. A detailed failure narrative, parameter investigation results, modelling process and results, and recommendations for further work for each event are included in Appendix B.

Chapter 2: A Review of Tailings Dam Breach and Runout

This literature review provides an overview of tailings dams and failures. A background on tailings dams is provided in Section 2.1. Existing frameworks for breach and runout scenarios and numerical models are described in Sections 2.2 and 2.3. Overviews of rheology formulas and numerical models are presented in Sections 2.4 and 2.5 respectively. Finally, the main challenges and knowledge gaps to be addressed in this thesis and future work are outlined in Section 2.6.

2.1 Tailings Storage Facilities

2.1.1 Tailings

A large volume of low-grade ore is produced in a conventional open-pit mine operation. The desired resource is extracted from the ore using mechanical and chemical processes. The remaining slurry contains ground rock and process effluents from the processing plant, referred to as tailings (Blight, 2010). This thesis considers tailings to include both the tailings solids and interstitial (pore) water, following the definition from Rana et al. (2021a). Tailings solids are fine-grained (clay to sand-sized particles), and can vary in mineralogy, grain size distribution, and specific gravity for different mining projects. The interstitial water can include additional chemical or environmental hazards such as cyanide or arsenic from the mineral processing. Tailings can behave as a semi-solid or a weak soil; however, they are prone to high pore pressures and can be susceptible to liquefaction. These characteristics depend on the local geology and mine operation (Blight, 2010).

Tailings production is accelerating globally to meet mineral demands (Franks et al., 2021). The vast quantities of tailings produced combined with environmental concerns require their management and storage within large dam structures, typically in perpetuity (Blight, 2010; Vick, 1990). This thesis follows the terminology from Rana et al. (2022), where a tailings dam is a constructed embankment designed to impound the tailings. A tailings dam is a single element within a tailings storage facility (TSF), which in turn is defined as the impounded tailings, tailings dam or dams, supernatant pond, spillway, and any appurtenant structures or physical systems related to the management of the TSF.

2.1.2 Tailings Dams

Tailings dams differ from earthfill dams for water reservoirs in several critical aspects (CDA, 2021). A tailings dam is raised according to the production of tailings, resulting in a facility evolving over years to decades, as opposed to water reservoir dams, which are built in a few construction seasons at most. Tailings are not the only material within tailings dams; a supernatant pond is a common feature of tailings facilities. The supernatant pond may store contaminated process water, be used for dust control, be used to reduce acid rock drainage, or be a simple result of the water content used in the slurry from the pipeline transportation (CDA, 2021). Water reservoirs contain only water. Due to their soil-like characteristics, tailings can be relied upon to provide structural support to the tailings dam in some cases.

Tailings dams can be categorized according to the direction the dam is raised (CDA, 2021), as shown in Figure 2.1. Earthfill dams for water reservoirs are all built with the downstream construction method (Vick, 1990). Blight (2010) summarized the general geometric arrangements that tailings dams may take, as shown in Figure 2.2. Multiple tailings compartments are occasionally constructed, potentially resulting in permutations of the basic arrangements of a single TSF, termed “stepped” or “composite” TSFs within this thesis. Stepped TSFs are where one compartment is downstream of the other (e.g., the Prestavèl mine, Luino & de Graff, 2012; the Cadia mine, Jefferies et al., 2019). Composite TSFs are where sections of the impounded tailings volumes are divided by internal embankments and potentially used for different types of tailings solids or supernatant pond volumes (e.g., the Harmony mine, Wagener, 1997; the Aznalcóllar mine, McDermott & Sibley, 2000; MAL Red Mud Reservoir, Turi et al., 2013).

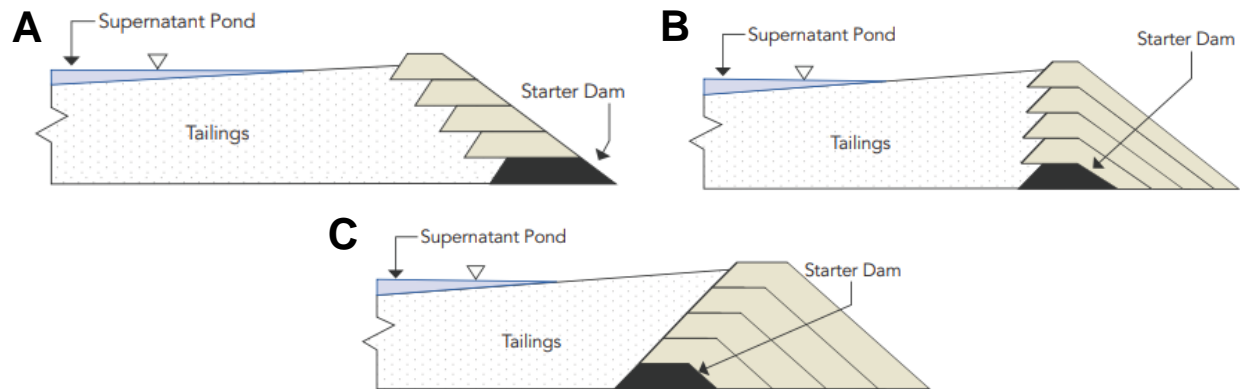


Figure 2.1 Schematic of TSF Cross Sections for Different Dam Construction Methods: A) Upstream, B) Centreline, and C) Downstream (CDA, 2021)

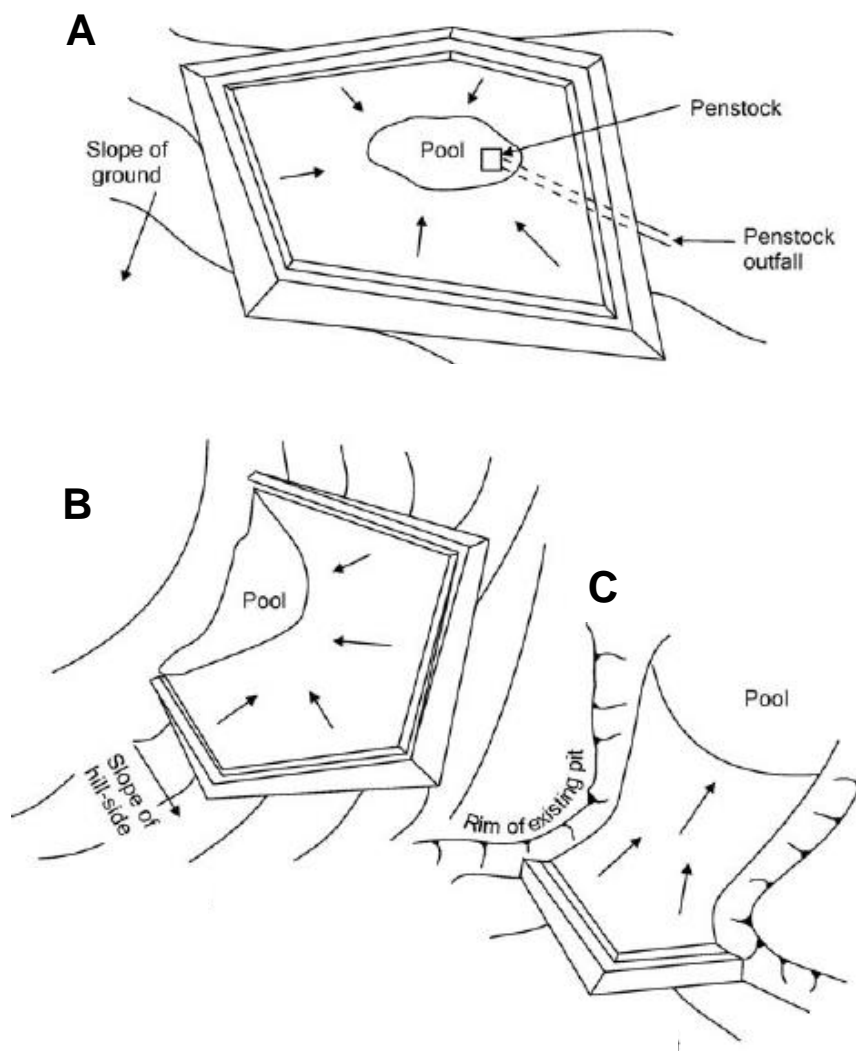


Figure 2.2 Schematic of TSF Arrangements: a) Ring-Dyke, b) Side-Hill, and c) Cross Valley (Blight, 2010)

The failure of a tailings dam can be catastrophic, with high fatalities, destruction of critical infrastructure, regional geomorphology impacts, and environmental contamination commonly associated with such failures (Rana et al., 2021a; Santamarina et al., 2019; and the references therein). The various arrangements discussed previously may also create distinct breach scenarios, such as a cascading breach or a breach containing several different tailings types with different flow behaviours. A Tailings Dam Breach Analysis (TDBA) estimates the consequences of a failure for a given TSF to inform risk assessments and emergency preparedness plans (CDA, 2019a and 2019b; Martin et al., 2022). In some jurisdictions these TDBAs are a legal requirement, such as in British Columbia (BCMEM, 2017). Regardless of any legal requirement, several guidelines highlight the importance of them (e.g., CDA, 2013; GISTM, 2020; CDA, 2021). There is limited literature on the hydrotechnical and geotechnical considerations associated with TDBAs, with the CDA Technical Bulletin on Tailings Dam Breach Analysis (2021) being one of the first documents specific to tailings dam breaches from a professional society.

2.2 Tailings Dam Breach

2.2.1 Failure Modes

Within the CDA Dam Safety Guidelines (2013, 2019a), failure mode analysis is used to define the breach scenarios to be considered for engineering purposes and emergency planning, including in dam breach analysis. A failure mode is defined as the combination of failure cause or causes, a failure mechanism, and an ultimate breach of the dam. The failure cause or causes are conditions that promote the onset of a failure mechanism. These causes can be long-term preconditioning phenomena or short-term triggering events proximal to the breach event, and internal or external to the TSF (Rana et al., 2022). Examples of tailings dam failure causes are described in Rana et al., (2021a). The failure mechanism is an event that could, but does not necessarily, lead to a breach of the dam. Common examples of failure mechanisms are overtopping, structural instability and deformation, and internal erosion (CDA, 2021). A breach is defined as an occurrence where tailings and water uncontrollably flow from a TSF during a sudden physical failure of the tailings dam (CDA, 2021; Rana et al., 2022) following the failure cause or causes and failure mechanism.

During a TDBA, it is assumed that a failure cause and mechanism have progressed to a breach event without necessarily explicitly defining the cause and the

mechanism (CDA, 2013, 2019a and 2021). Following the CDA, this thesis focuses on the investigation and modelling of the tailings dam breach, rather than a possible failure of any TSF elements that do not lead to a physical breach. CDA (2013, 2019a) describes two hydrologic conditions to be considered for TDBA, sunny day and flood conditions (which were later renamed to fair weather and flood-induced conditions respectively in CDA, 2021). These hydrologic conditions are used to bound the scenarios for risk assessments. For the investigations of past tailings dam breaches, the hydrologic conditions are known, therefore the framing hydrologic conditions are not needed.

CDA (2021) discuss two main breach processes. Process I includes erosional processes where the velocity or shear stress of flowing water carries away the dam materials and tailings. Process I breaches commonly follow overtopping and internal erosion failure mechanisms. Such failures evidently involve relatively high supernatant pond volumes and are characterized by long durations of outflow (i.e. many minutes to hours). The Aznalcóllar event in Spain, 1998, is an example of a primarily Process I breach, where the outflow volume was predominantly from the supernatant pond and eroded tailings and took 7 hours to discharge (Alonso & Gens, 2006a; McDermott & Sibley, 2000). Process II breaches are initiated by a mechanism other than erosion and include, but are not limited to, slope instability or foundation failure. Such failures are often described as brittle or near-instantaneous and involve the outflow and discharge of liquefied or non-liquefied tailings. A notable Process II breach example is the Feijão event in Brazil, 2019. A monitoring camera captured the breach and demonstrated the peak outflow of liquefied tailings with no supernatant pond occurred within seconds, and the outflow terminated within 5 minutes (Robertson et al., 2019).

CDA (2021) includes a framework classification system from Small et al., (2017) to aid selecting failure modes and breach processes. The key factors to consider include a presence of a supernatant pond that could be released during a breach, and the potential of the tailings to liquefy and flow. The classes are summarized in Figure 2.3.

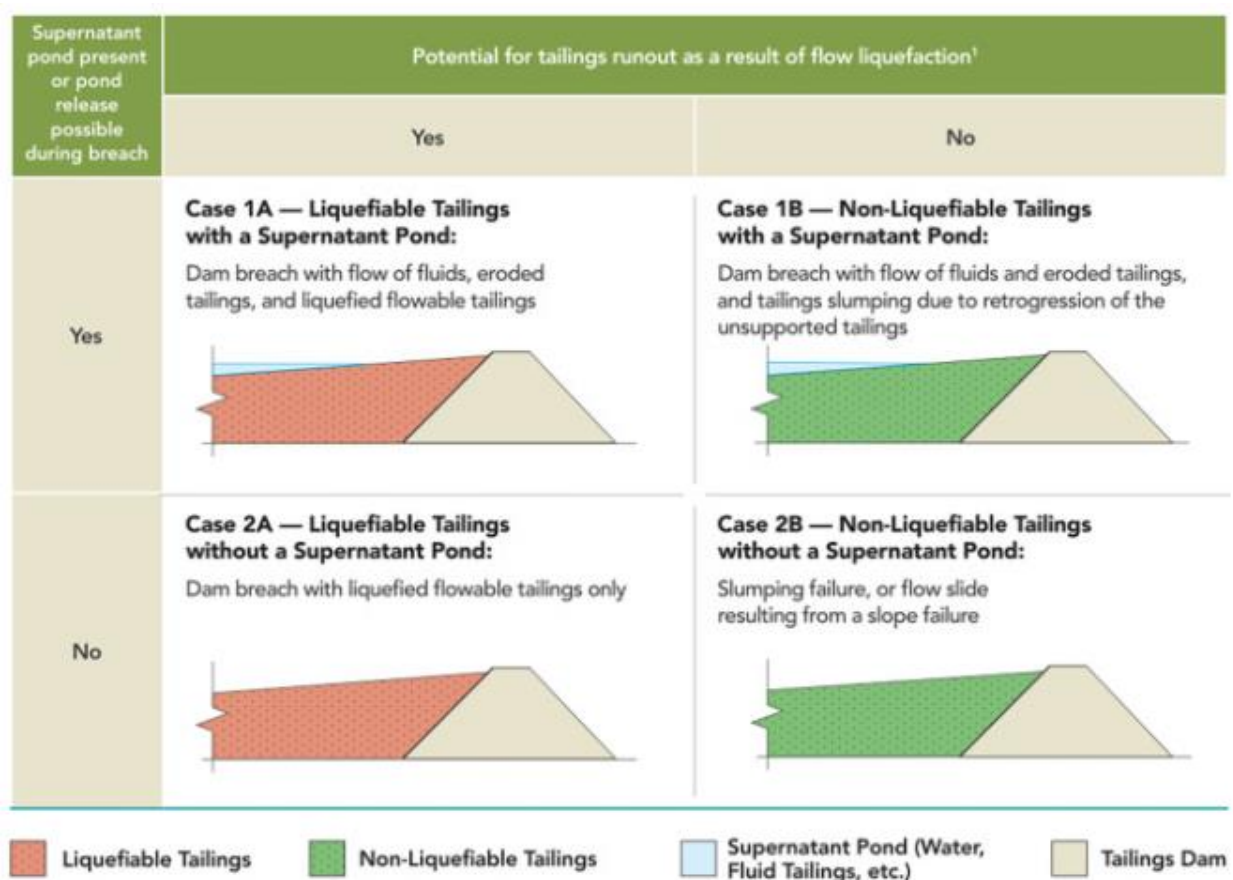


Figure 2.3 Classification System for Tailings Dam Failures (CDA, 2021, Modified from Small et al., 2017)

Specifics of a failure cause and a failure mechanism are not direct inputs to various numerical models, nor can they be known with certainty for forward-analysis. Consideration of failure causes and mechanisms is still implicitly useful for selecting breach processes and overall modelling approaches for such forward analysis. Process I breaches can occur for 1A and 1B cases, while Process II could occur for all CDA cases (CDA, 2021). Furthermore, breaches may demonstrate both processes; either process may occur first, and the timing between each process may be long or short (CDA, 2021; Fontaine & Martin, 2015). Rana et al. (2021a, 2021b) compiled the failure causes and estimated CDA classes for tailings dam breach case studies, but to date no breach processes are included in databases (i.e., Rico et al., 2008; Concha Larrauri & Lall, 2018; Rana et al., 2021b). A database of observed breach processes that followed the failure causes and mechanisms of tailings dam breach cases can be used by professionals in selecting failure modes for forward analysis and risk assessments.

2.2.2 Outflow Volumes

The outflow volume from a water reservoir dam breach can be reliably estimated before and after a breach, as all the stored volume above the breach invert can be expected to discharge (Froehlich, 2016). During a tailings dam breach, the tailings may stabilize and discharge only a portion of the total impounded tailings volume, leaving a depression behind in the TSF. Previous tailings dam breach events have outflow volume ratios from 10% to 100% (Rana et al., 2021a).

CDA (2021) recommends the following outflow volume components be considered: supernatant pond, eroded tailings, liquefied or non-liquefied tailings, as appropriate for the TSF conditions and failure mode, and dam materials. The supernatant pond can include the operating pond volume and the inflow storm volume. The tailings volume can be further separated into interstitial water and tailings solids. These volumes are visualized in Figure 2.4.

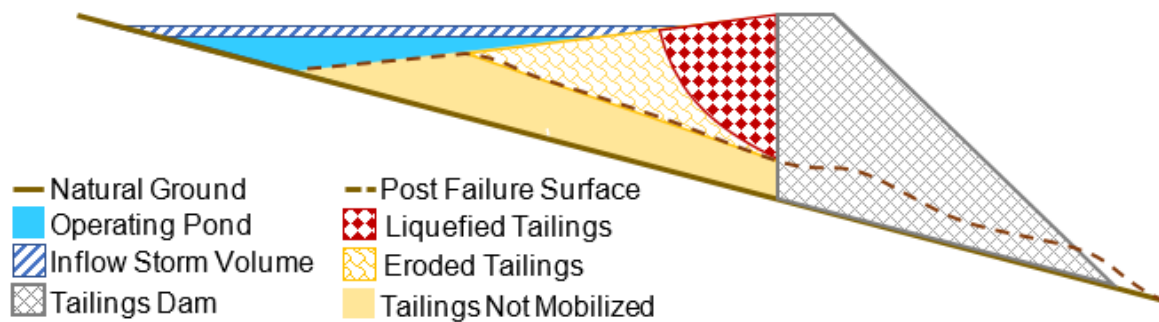


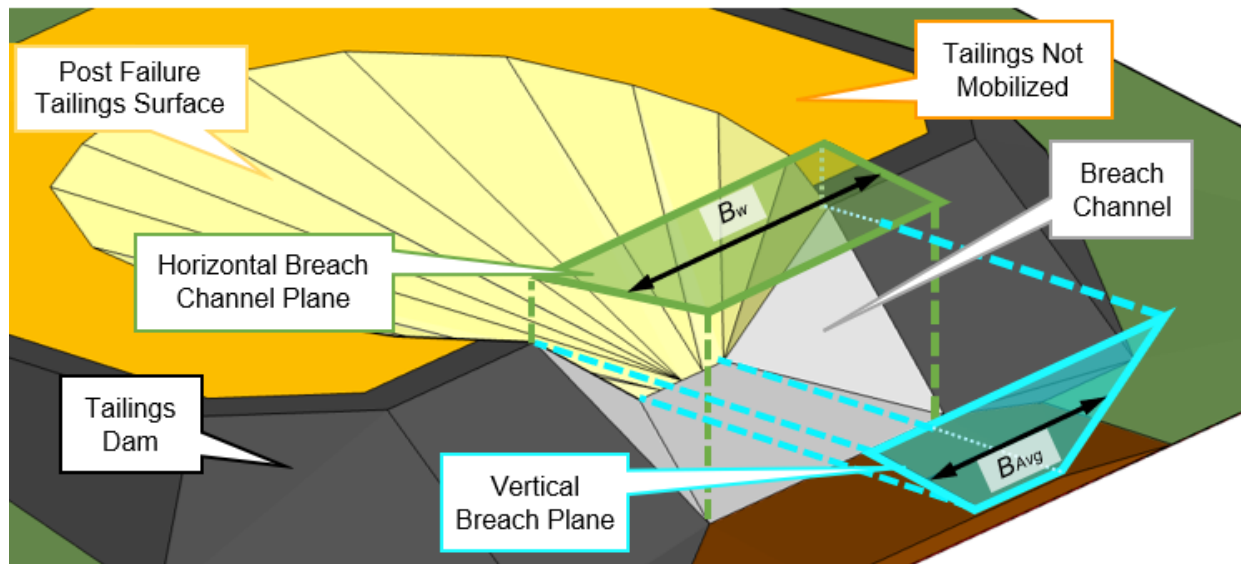
Figure 2.4 Outflow Volume Materials and Height for a hypothetical Case 1A dam breach with a Process II breach followed by Process I breach

Databases of tailings dam breaches usually only report the total outflow volume without separating the solids and water volumes (e.g., Rico et al., 2008; Concha Larrauri and Lall, 2018; Piciullo et al., 2022). The volumetric solids concentration plays an important role in outflow volumes and runout behaviour (Rana et al., 2021a; Martin et al., 2022). At best, the supernatant pond volumes are compiled for a limited number of cases in Rana et al. (2021b), such as the Mt Polley event (Morgenstern et al., 2015).

2.2.3 Breach Characteristics

Geometric characteristics of past tailings breaches of interest for breach modelling (e.g., breach depth and breach width) are often not available or of limited reporting. For example, the dam height of tailings dam breaches has been included in previous databases (e.g., Rico et al., 2008, Concha Larrauri & Lall, 2018, Rana et al., 2021b). Dam

height is not synonymous with breach height, however, and in fact it has been found to be a poor predictor for breach characteristics for erosional failures of water reservoir dams (Wahl, 2004, Wahl, 2014). The mean breach width, as reported in Rana et al. (2021b), corresponds to the average planar width of the breach channel. The vertical average width at the hydraulic control (i.e., the narrowest section of the breach) is more relevant for breach flow of water reservoir dams (Froehlich, 2008; Wahl, 2014). The difference between these width definitions is illustrated in Figure 2.5. Limited estimates of breach heights or widths for tailings dam breaches exist and to date they have not been compiled or meaningfully assessed. In comparison, Wahl (2014) and Locat (2022) summarized over 65 and 49 geometries for water-reservoir dam breaches and sensitive clay landslides, respectively. Evidently basic geometric observations for tailings dam breaches are comparatively lacking.



Notation:

B_w Average Planar Breach Width, as defined by Rana et al. (2021a)

B_{Avg} Average Vertical Breach Width, as defined by Froehlich (2008)

Figure 2.5 Comparison of Breach Width Definitions from Rana et al. (2021a) and Froehlich (2008)

In addition to the geometric characteristics of the breach, the time component of a breach is an important aspect for warning time, peak breach outflow, and flood wave arrival time for water reservoir dams (Froehlich, 2008). Wahl (1998) defined two distinct time periods for water reservoir breaches: the initiation time and the formation time. The initiation time begins with the first awareness of potential for dam failure and lasts until the formation time starts. The formation begins when the breach channel first develops

until the ultimate breach dimensions are reached. The formation time does not include the total duration of the breach outflow. These two periods align with the CDA (2013) failure mode framework, as the failure mechanism occurs at the start of the initiation time while the breach process occurs at the start of the formation time. The formation time has a large influence on the breach outflow (Froehlich, 2008; CDA, 2019b). No compilation of any time component of any definition currently exists for tailings dam breach events.

Physical experimental work on tailings dam breach geometries and formation times has recently been completed at Queen's University. Walsh et al. (2021) found the breach arc length on the upstream face of a dam during erosional breaches conducted in flume scale experiments was a better predictor of the headcut growth and overall outflow than the vertical hydraulic control width. They commented that the breach arc length approach is well-positioned for forward analysis of shallow upstream slopes commonly seen on tailings beaches. Walder & O'Connor (1997) compared the mean erosion rate (defined as the breach height divided by the formation time) for water reservoir dams and landslide dams and found they generally varied between 10 m/hr to 100 m/hr. Walsh (2019) found that the presence of a tailings beaches resulted in a lower peak flow during flume scale experiments. This may indicate that Process I breaches of tailings dams may demonstrate similar or lower mean erosion rates (and therefore similar or lower formation times) as the range found in Walder & O'Connor. Unfortunately, limited to none information on breach arc lengths for water reservoir dams or tailings dam failures and formation times for tailings dams exists to compare to these laboratory findings.

2.3 Tailings Runout

2.3.1 Impacts from Tailings Flows

Tailings runout may result in physical consequences through physical damage to constructed or natural environment. Additional impacts from tailings can occur within waterbodies downstream of the physical damage, but are often transient, difficult to quantify, and far reaching (Ghahramani et al., 2020). The impacts can be quantified as features or observations specific to a location and time, or observations relating to the whole event. Observations can also be qualitative, but such observations are more difficult to use as model validation or calibration and are subjective (Heiser et al., 2017). Within this thesis, runout characteristics are used to refer to local and event features collectively.

Quantitative event observations include but are not limited to inundation area, runout distance, fatalities, or financial cost. Inundation area and runout distance have been compiled for tailings dam breaches (e.g., Rico et al., 2008; Concha Larrauri & Lall, 2018). Ghahramani et al. (2020) refined such observations for past failures by classifying the impacts into Zone 1 and Zone 2. Zone 1 is defined as the extent of the main solid tailings deposit, which is characterized by remotely visible or field-confirmed sedimentation, above typical bankfull elevations if extending into downstream river channels. Zone 2 is the area downstream of Zone 1 further impacted by the tailings flow in some form (e.g., geochemical or environmental impacts). These definitions are visualized in Figure 2.6. The Zone 1 and Zone 2 extents for past tailings dam breach and runout events were estimated based on aerial and satellite imagery in Ghahramani et al. and Rana et al. (2021b). Both studies reported uncertainty based on the mapped area and the resolution of the available imagery. Moreover, CDA (2021) notes that TDBAs should extend to the point where tailings runout is within the river channel, an extent like Zone 1.

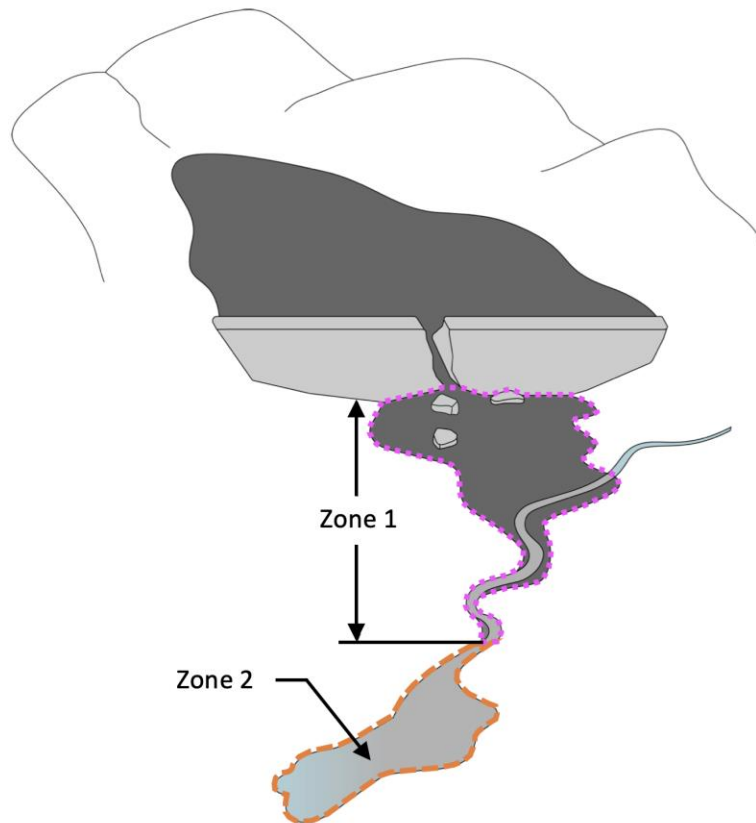


Figure 2.6 Runout Zone Classification (Ghahramani et al., 2020)

Local runout observations include but are not limited to the flow depth, velocity, and arrival time at a specific time or location. Annis & Nardi (2018) and Rollason et al. (2018) use the term Volunteered Geographic Information for local observations of flood impacts when such information comes from citizenry using platforms unconventional to academia (e.g., Twitter, YouTube, Instagram). The general term 'local runout observations' is used in this thesis, however the goal of compiling data for improving models used in hazards is shared between this thesis and the referenced authors. Local observations are commonly included within academic and technical characterization of geophysical mass flows and are useful for validating numerical models (Heiser et al., 2017). Some local runout observations have also been reported for tailings dam breaches (e.g., max depth in Wagener, 1997; arrival times in Takahashi, 2014), but in general, relevant observations are rare for tailings dam breach events. There has not been an effort to compile these types of observations to date.

In addition to their utility for model calibration, local runout characteristics such as depth or velocity have been shown to be better indices than inundation area alone for determining fatality rates for landslides and floods (Jakob et al., 2012, Bureau of Reclamation, 2015). A database of standardized local characteristics could support both numerical model benchmarking and improving vulnerability estimating methods specific for tailings runout.

2.3.2 Downstream Environment

The runout characteristics are affected by the terrain, which includes the channel slope, flow path shape, obstructions, watercourses, and land cover type of the downstream environment. The terrain is widely noted to exert substantial control on the runout characteristics of debris flows, floods, mudflows, rock avalanches and debris flows (e.g., Corominas, 1996; Brunner, 2014; Aaron, 2017; Meadows & Wilson, 2021; Mitchell, 2021).

Downstream environments have been qualitatively classified as channelized or unconfined travel paths for tailings runout for statistical analysis (Small et al., 2017; Ghahramani et al., 2020; Rana et al. 2021a). Channelized travel paths are constrained by relatively steep side slopes of a valley or gully, while unconfined travel paths are relatively flat and allow the spreading of the tailings from an early stage. Channelized travel paths usually involve steeper channel gradients, and the concentrated flows result in greater velocities and runout distances compared to unconfined flows (Rana et al. 2021a). This simple qualitative classification is useful for comparing case studies or

regression analysis but cannot address site specific features (Rana et al., 2021a). Because of this issue, numerical models are recommended for detailed TDBAs (Martin et al., 2022, Rana et al. 2021a). Within numerical models, terrain features for the site are explicitly used to estimating runout impacts, therefore the qualitative classification from Small et al. (2017) is not strictly considered within this thesis.

In addition to the terrain, the surface or texture of the environment can present an external resistance to flow. The most common quantitative measures of resistance to flow for open channel flows are empirical roughness coefficients such as the friction factor, Chezy coefficient, Gauckler-Manning coefficient, and roughness height (Akan & Iyer, 2021). There has been extensive literature and semi-systematic methods developed for determining roughness values (e.g., Chow, 1959; Barnes, 1967; Arcement & Schneider, 1989). Arcement & Schneider (1989) provide guidance for assigning a base roughness associated with a surface (e.g., smooth concrete has a lower roughness compared to coarse gravel) and adjustments to the base value for various roughness elements (i.e., flow obstructions, variations in channel size and shape, or vegetation) to determine a total roughness for a river channel. Similar guidance for floodplains is also provided in Arcement & Schneider. Regardless of the selected coefficient or specific values, CDA (2021) recommends the roughness be carefully considered and the sensitivity of assumed values be addressed.

2.4 Tailings Rheology

Rheology is the study of the deformation and flow of matter, including fluids and “soft solids” that can plastically flow under applied forces (CDA, 2021). Water follows Newton’s law of viscosity, where shear stresses are linearly proportional to shear strain rates, and the line depicting this relationship passes through the origin, as shown in Figure 2.7. Fluids that do not obey this relationship are termed non-Newtonian. The slope of shear stress to strain rate for non-Newtonian fluids is non-linear and can increase or decrease with shear rate (termed dilatant or pseudo-plastic, respectively). The shear stress to shear rate relationship may begin above the origin. Some non-Newtonian fluids demonstrate time-dependency, where either the rheological properties increase or decrease without shear (aging), increase with shear (rheopexy), or decrease with shear (thixotropy). In general, more flowable fluids have higher shear rates at a given shear stress compared to less flowable fluids. There is no theoretical equation to fully define non-Newtonian

fluids, therefore many equations are empirically based (O'Brien & Julien, 1988). Some rheological formulas are shown graphically in Figure 2.7.

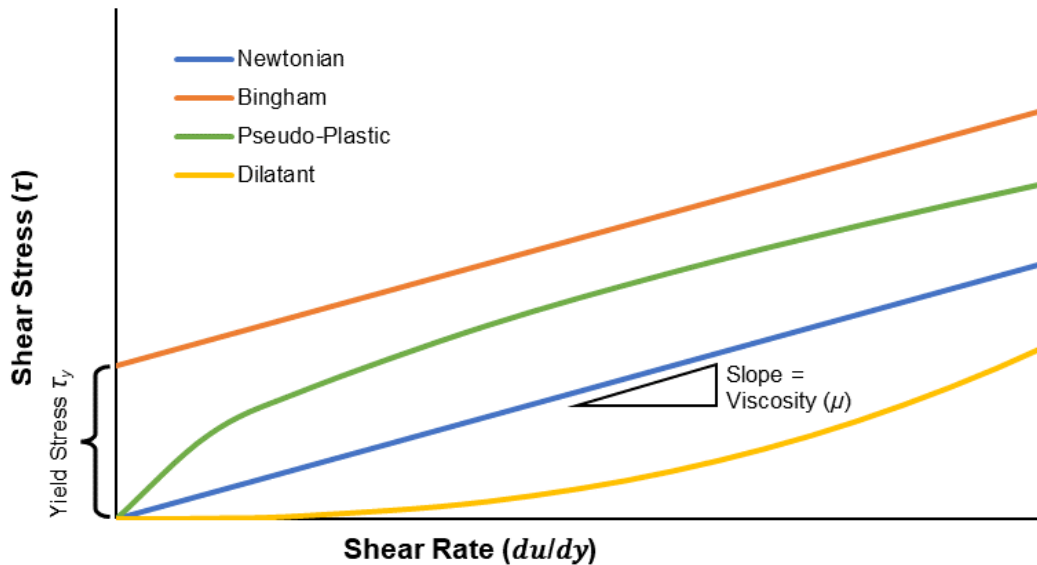


Figure 2.7 Shear Rate vs. Shear Stress Plot of Newtonian and Non-Newtonian Fluids

Other rheological formulas include the Herschel-Bulkley, Casson, Quadratic, and Voellmy formulas. Each formula has its own definitions, considerations, and limitations. The commonality between these formulas is that multiple parameters are needed to define the fluid rheology, as opposed to the singular parameter of viscosity needed for Newtonian fluids. The fluid's initial resistance to flow, or the minimum shear stress for evidence of flow, is represented by a non-zero y-intercept on the shear rate vs. shear stress plot. The initial resistance to flow is commonly called the yield stress (Nguyen & Boger, 1983). The names and definitions of a fluid's resistance to flow, once mobilized, are more varied across the formulas. Generally, they correspond to the slope of the relationship at a given shear rate and are occasionally termed viscosity as well (O'Brien, 1986, CDA, 2021). Within this thesis, yield stress and viscosity are used as terms to describe the internal initial resistance to flow and internal resistance to flow once mobilized, respectively. Likewise, rheological flow properties refer collectively to yield stress, viscosity, or other associated parameters for various rheology formulas within this thesis.

The hyperconcentrated water-tailings mixture observed in tailings can resist applied stress without motion due to the cohesion, collision, or friction between the tailings

particles, and therefore display rheological flow properties when considering the fluid behavior as a bulk unit (O'Brien & Julien, 1988; CDA, 2021). Depending on the proportion of the solids in the flow, tailings can exhibit characteristics close to water (Newtonian) or to thick pastes (fully non-Newtonian). The rheological flow properties for a given tailings sample may vary temporally and spatially and affect both breach and runout processes for tailings breach and runout flow. The variations commonly occur through changes in solids concentration, such as the transition from Process I to Process II (or vice versa) during the breach, erosion of additional sediment during runout, or dilution of the flow from large watercourses during runout (CDA, 2021). O'Brien (1986) proposed a classification system for the continuum between water and landslides, which was adopted and modified by the CDA for tailings dam breach and runout (Table 2.1 and Figure 2.8). The solids proportion can be defined either by volume or by mass, however within this thesis the solids concentration is defined exclusively by volume.

Table 2.1 Outflow Behaviour as a Function of Solids Concentration (CDA, 2021, Modified from O'Brien, 1986)

| CDA Class | Flow Type | Solids Concentration by Volume (C_v in %) | Flow Characteristics |
|------------------|------------------|---|---|
| Cases 1A or 1B | Water Flood | < 20 | Water flood with conventional suspended load and bedload |
| | Mud Flood | 20 – 30 | Distinct wave action; fluid surface; all particles resting on bed in quiescent fluid condition |
| | | 30 – 35 | Separation of water on surface; waves travel easily; most sand and gravel size particles settled out and move as bedload |
| | | 35 – 40 | Marked settling of gravels and cobble sized particles; spreading nearly complete on horizontal surface; liquid surface with two fluid phases appears; waves travel on surface |
| | | 40 – 45 | Flow mixes easily; shows fluid properties in deformation; spreads on horizontal surfaces but maintains an inclined fluid surface; waves appear but dissipate rapidly |
| Case 2A | Mud Flow | 45 - 48 | Flow of saturated, liquefied tailings at or above liquid limit forming a slurry; may show fluid like properties |
| | | 48 – 55 | Flow of saturated liquefied tailings; may show fluid like properties |
| Case 2B | Flow Slide | 55 – 65 | Various forms of outflow movement of non-liquefied, partly saturated tailings, does not show fluid properties |
| | | 65 – 80 | Various forms of outflow movement of non-liquefied, moist, or partly saturated tailings, does not show fluid properties |

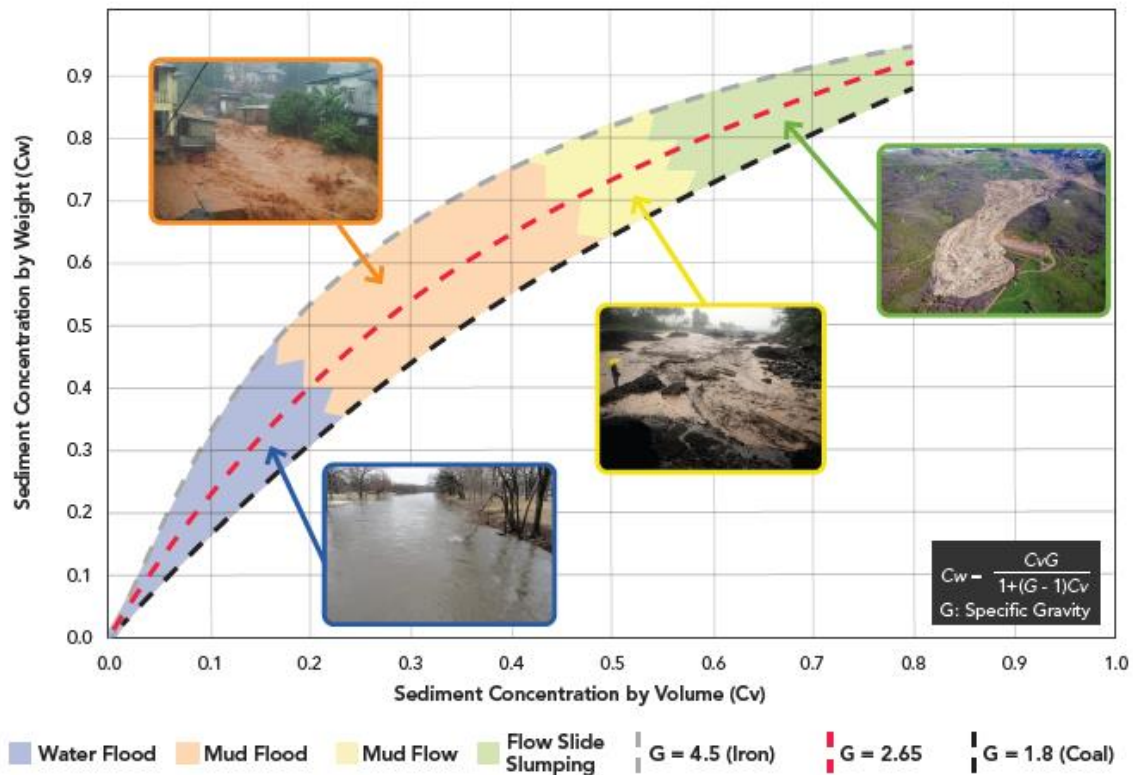


Figure 2.8 Outflow Behaviour as a Function of Solids Concentration (CDA, 2021, Modified from Martin et al., 2019 and Julien & O'Brien, 1985)

Beyond qualitative classification, quantifying rheological values is no simple task and requires substantial laboratory effort and expertise. Applying measurement methods or conditions inappropriately to a given tailings sample can produce results an order of magnitude off from the proper value for the desired purpose (O'Brien, 1986; Boger, 2009). Aside from volumetric solids content, the rheology of tailings can be affected by the specific gravity, tailings particle size and distribution, tailings particle shape, acidity, mineralogy, and chemical additives. Boger (2009) and Martin et al. (2022) demonstrate variability in measured rheology for tailings and comparable debris flows across a single sample with varying solids concentration (typically two orders of magnitude across the mud flood range) and variability between multiple samples at a given solids concentration (up to three orders of magnitude). This diversity in rheology is visualized in Figure 2.9 in a semi-log plot. The data for a single sample typically only covers a solids concentration range of 10% to 20%, which reflects the difficulties in measuring a wide range of solids concentrations with a single measurement device or method (Martin et al. 2022). Extrapolation of rheology trends carries uncertainties (Martin et al., 2022).

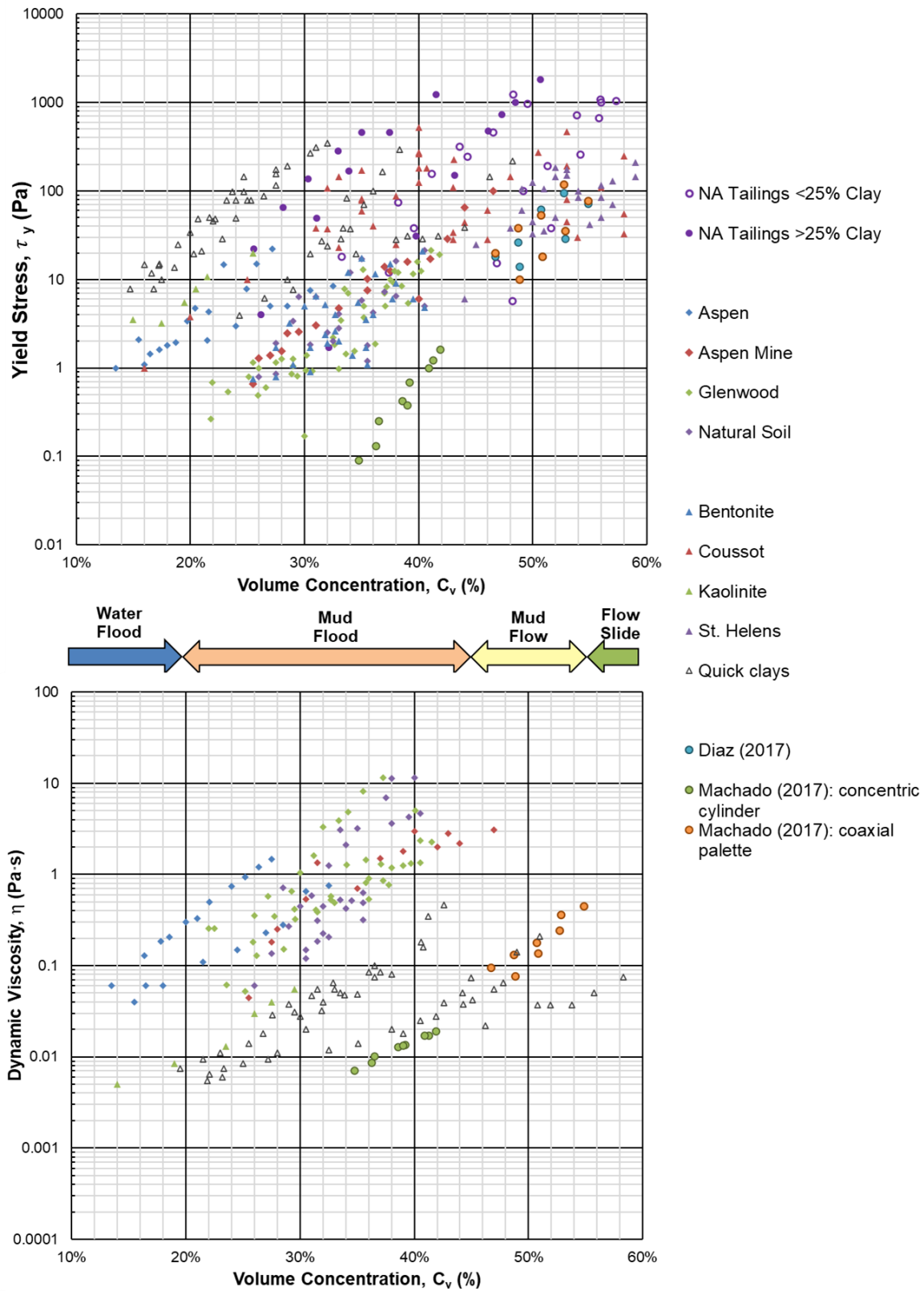


Figure 2.9 Measured Rheology Values for Tailings and Debris Flows (Modified from Martin et al., 2022)

Alternatively, rheological values can be determined through back-analysis and calibration of case studies (e.g., Pirulli et al., 2017; Lumbroso et al., 2019; Ghahramani et al., 2022). The variability and relative scarcity of measured rheology for tailings (Martin et al., 2022) makes this approach attractive, as it may allow insights on rheology from past events where tailings samples may no longer be available. The downsides of calibrated rheology from back-analysis are the equifinality problem (Gibson et al., 2022) and that calibrated rheology does not necessarily match a fluid's true rheology (Liu & Henderson, 2020; Gibson et al., 2020). Iverson (2003) goes as far as stating rheological formulas as a concept are insufficient to characterize the complexity of interparticle behaviour of debris flows.

2.5 Numerical Models

Early predictive work for tailings dam breach and runout characteristics used regression equations (e.g., Rico et al. 2008). The relations are between simple observed characteristics (i.e., impounded volume, outflow volume, dam height, runout distance, and runout area). These regression equations do not provide the detailed runout characteristics needed for risk assessments and emergency planning. Furthermore, there is persistent concern that these regression equations do not address site-specific conditions for a given tailings dam, and may lead to flawed judgement (Martin et al., 2015; Small et al., 2017; CDA, 2021; Rana et al., 2021a).

Numerical modelling is a common tool used to address these considerations and meet relevant standards, regulations, and best practices. Numerical models involve many simplifications of real-world phenomena, and includes assumed conditions, parametrizations, and limitations. Nonetheless, numerical models can prove useful to answer specific questions for engineering purposes (e.g., Box, 1976; Rykiel, 1996; Aaron et al., 2018; Brunner et al., 2020). Various numerical model software have been used to simulate the breach process or runout of a tailings dam breach. These software were commonly originally developed for hydraulic modelling or landslide runout analysis (e.g., Pirulli et al., 2017, Ghahramani et al., 2022, Gibson et al., 2022). Within this thesis, model is used to refer to any software with numerical modelling capability, modelling is the action of choosing the model set-up and inputs, and modeller is the professional doing the modelling.

The experience and knowledge of the modeller are commonly the most critical elements to the quality of a model, rather than the selected model itself (Brunner et al., 2020, Ghahramani et al., 2022, Martin et al., 2022). Furthermore, computation power increases and software updates occur frequently, rendering specific comments and comparisons between models obsolete relatively frequently (Martin et al., 2022). General considerations for modelling for TDBAs are highlighted below to provide context for modelling choices and model results within this thesis. CDA (2021) provides an overview of individual software for tailings breach and runout modelling that is available commercially or within academic organizations. McDougall (2017) and Brunner et al. (2020) give further detail on models for landslide and hydraulic modelling respectively.

2.5.1 Breach Modelling Considerations

The initial conditions of the breach and how the outflow is calculated varies depending on the software used. A common option within hydraulic model software is to compute breach flow within the model based on the weir equation, or to input externally developed breach hydrographs at predefined locations (Goodell et al., 2018, CDA, 2021, Ghahramani et al., 2022). Some hydraulic model can explicitly simulate the dynamic erosional process as the breach develops (e.g., HEC-RAS, XBeach, EMBREA-MUD), but such an approach is ill-adapted for Process II breaches. Landslide models commonly use a block start initial condition, where the flowing mass is fully fluid and located within the model domain at the initial time in the model (e.g., Hungr, 1995, Moretti et al., 2015, Aaron et al., 2017), which are inappropriate for a slower Process I breach.

Breach modelling set-ups within all models are evolving, with greater options becoming available to the modeller over time (e.g., Mitchell, 2021), although to date no commercial model has included the breach arc length method from Walder et al. (2015) and Walsh et al. (2021). Aside from the erosionally-based breach models, all methods are subject to uncertainty with estimating breach characteristics (i.e., ultimate size and shape of the weir and breach formation time) for forward analysis (Froehlich, 2008; Wahl, 2004). Empirical equations or guidance exists for water reservoir dam breaches, and have been summarized by Brunner (2014), but these equation involve some uncertainty (Wahl, 2014). This uncertainty is compounded by the questionable applicability of empirical equations based on water reservoir dam failures for tailings dam breach modelling (Martin et al. 2015).

The weir equation method for modelling the breach hydrograph, also known as the parametric beach method, is founded on Torricelli's natural law of fluids, and is independent of the fluid characteristics (Francis, 1855). The breach characteristics must be defined by the modeller. It has been shown to be flexible for modelling both erosional breaches (e.g., for earthfill dams, Wahl, 2004, Froehlich, 2008, Goodell et al., 2018) or instantaneous release (e.g., brittle failure of concrete arch dams, USBR, 1988, Froehlich, 2016, Brunner et al., 2018) for water reservoirs. Beyond the uncertainty of breach characteristics, the parametric breach method has not been verified against tailings breaches.

2.5.2 Runout Modelling Considerations

A simple differentiator between models is the dimensionality, where decreasing dimensionality averages flow along the vertical or bed-normal direction (i.e., 2D modelling) or vertical and lateral directions (i.e., 1D modelling). As discussed by Brunner et al. (2020), higher dimensions require successively increasing computation power and input requirements, and do not necessarily guarantee improved results. Two-dimensional models are preferable to one-dimensional models for complex flow directions common in dam breach scenarios, and current computation power allows 2D tailings dam breach and runout models to run in a reasonable timeframe (Martin et al., 2022). Most models have two-dimensional capabilities (CDA, 2021).

Non-Newtonian flow is now a common feature in many models (CDA, 2021); however, the available rheology formulas and specific capabilities vary by software. A common limitation is the solids concentration of the fluid is limited temporally or spatially (e.g., Gibson et al., 2022, Martin et al., 2022). If the model is limited to a single fluid or the Process I and Process II breach types are estimated to occur simultaneously, a single-phase approach with an average solids concentration may be used (CDA, 2021). Ghahramani et al. (2022) found that different model software with different inputs result in different back-calculated non-Newtonian properties.

Erosion may not be limited to the breach process itself and may influence the downstream runout impacts and tailings deposition. For example, Cuervo et al. (2017) noted that channel incision up to 7 m deep occurred during the Mount Polley event in Canada, 2014. Models that assume the erosion is negligible are referred to as a fixed-bed or fixed-boundary models (Chanson, 2004). Entrainment models can simulate the erosion or deposition and do not rely on the fixed-bed assumption remaining valid during

runout modelling. Entrained volumes have been noted to influence the flow characteristics and runout mobility for debris flows (McDougall and Hungr, 2005; Pudasaini & Krautblatter, 2021; Zubrycky, 2020). Entrainment models typically require a greater number of input parameters and modelling effort than fixed-bed models (Gibson et al., 2022; Pudasaini & Krautblatter).

2.5.3 Terrain datasets

The terrain data are the one of the most important inputs to modelling landslides or floods (Zhao & Kowalski, 2020; Meadows & Wilson, 2021). Martin et al. (2022) showed a forward analysis TDBA where better definition of the terrain affected the modelled inundation area far greater than the outflow volume or peak breach outflow. Meadows & Wilson (2021) commented that substantial errors were common in global satellite sources, which negatively affect the reliability of flood risk assessments. In particular, Meadows & Wilson noted the impacts of vegetation in digital surface models (DSMs). Similarly, Turner et al. (2022) demonstrated substantial differences between model results with a global satellite source versus a high-quality DEM generated by satellite photographs and geophysical processing. An uncertain input with strong sensitivity is of great concern to a modeller (Ghahramani et al., 2022), and terrain is a universal input to all models. Therefore, an understanding of DEMs and potential issues is warranted for proper modelling of tailings runout, regardless of selected model.

Remote sensing technologies, such as photogrammetry using structure-from-motion, interferometric synthetic aperture radar (InSAR), or light detection and ranging (LiDAR), can be used to generate a DEM. Global or near global DEM coverage is publicly available from various agencies (e.g., the Shuttle Radar Topography Mission or SRTM, Advanced Land Observation Satellite or ALOS, and Advanced Spaceborne Thermal Emission and Reflection Radiometer or ASTER) and is commonly considered in flood modelling (Meadows and Wilson, 2021). Alternatively, site-specific data can be collected for a TDBA, typically at greater expense (Martin et al. 2022). Depending on the remote sensing technology, interference from vegetation, cloud cover, and water bodies may exist to varying degrees in the elevation model. DEMs may also include random errors or “noise” (Meadows and Wilson, 2021). The inclusion or exclusion of the previous elements have led to various definitions of a DEM. Meadows and Wilson (2021) defines a DSM to be a dataset that includes the top surface of vegetation and structures, a digital terrain model (DTM) to be the ground elevation underlying the vegetation and structures, and a

DEM to be a general term for both DSMs and DTMs. Within this thesis, the terminology from Meadows and Wilson (2021) is followed, as visualized in Figure 2.10. The DEM used in a hydraulic model is ideally a DTM with channel bathymetry included (Brunner et al., 2014, 2020, Meadows and Wilson, 2021, Martin et al. 2022).

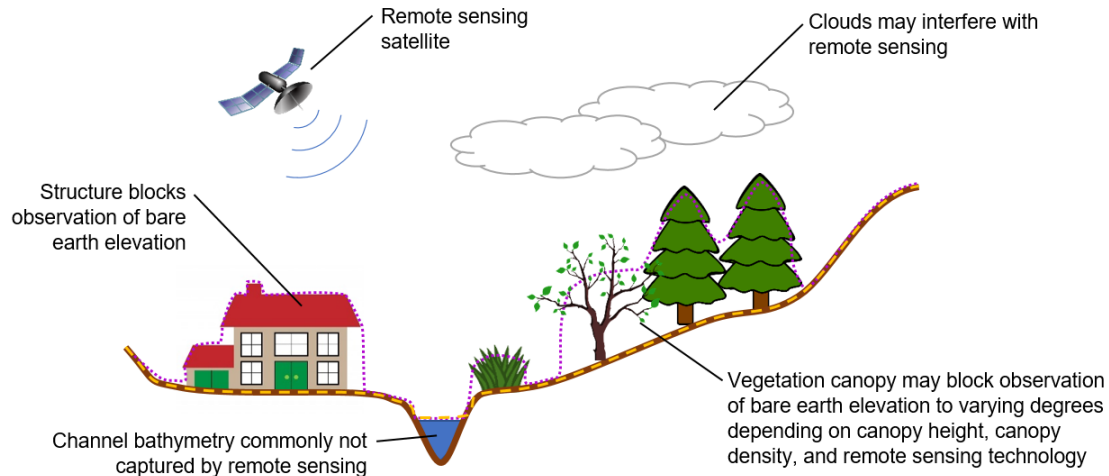


Figure 2.10 Distinction Between a DSM (Dotted Magenta), a DTM (Dashed Orange), and True Bare Earth Elevation (Solid Brown)

Within many hydraulic models (e.g., HEC-RAS, FLO-2D, RiverFlow-2D, FLOW-3D), the input DEM is in the form of gridded elevation, like pixels from a digital photograph. Two key measures of quality are the horizontal resolution of the grid and the vertical accuracy of the elevation values (Turner et al., 2022). Horizontal resolutions can range from 0.5 m for local uncrewed aerial vehicle surveys or specialized commercial satellites to 30 m to 90 m for global public datasets (e.g., SRTM, ASTER, ALOS). Finer horizontal resolution can represent smaller features within the area of interest, which may be relevant to hydraulic controls of inundation in flat terrain (Martin et al., 2022). Various standards exist for reporting vertical accuracy (e.g., ASPRS, 2015), and it is self-evident that low accuracy terrain is less desirable for input to any analysis. The costs associated with fine horizontal resolution and high vertical accuracy tends to limit DEMs of such quality to small areas. This tradeoff between cost and desired high quality of large terrain extents poses a challenge for professionals conducting TDBAs.

2.5.4 Model Calibration, Validation, and Verification

Any modelling exercise should include some mention or discussion of model calibration and validation. The topic is fraught with opposing philosophies and controversies (e.g.,

Oreskes et al., 1994; Rykiel, 1996). To give context to the discussions within Chapters 3 and 4 and avoid potential polemics, several terms are defined here.

Model calibration is the manipulation of input variables to obtain a match between observed and modelled results. Ideally, calibration is quantitative, as the adjustments and observed errors can be explicitly quantified, although calibration is occasionally qualitative (e.g., the modelled areal fit to the observed impact area can be assessed visually). Calibration can range from simple trial-and-error (e.g., Ghahramani et al., 2022) or very sophisticated like the parameter estimation PEST (e.g., Aaron et al., 2019).

Model validation is the assessment if a model is useful for a scientific or engineering purpose. Broadly speaking, three questions are applicable to model validation:

1. Are the estimated or calibrated inputs within reason or realistic?
2. Are the differences between observations and the calibrated model results within acceptable tolerances?
3. Do the model simplifications impact the engineering decision or policy that initiated the modelling?

The first two questions relate to the calibration process. A model that produces results that matches observations but is based on inputs that differ from the prototype conditions or accepted practice should not be considered highly valid. More validity is assigned to models that rely on fewer calibrated inputs and instead use observed or universally accepted inputs. More observations that can be used for comparison to the model results increase the assessed model validity. Subjectivity in answering this question arises when multiple observations compete during calibration. In other words, does one aim for a good model match for a single observation at the expense of other observations, or use model inputs that can result in moderate but equal errors across multiple observations? These two questions may become quite subjective when inputs and calibration constraints are uncertain. Correlation between inputs may or may not be known and may be difficult to account for during modelling (El-Ramly et al., 2002).

The last question is regarding the purpose and scope of the model, and therefore substantially varies between models and events. For example, a 1D model involves more simplifications than a 2D or 3D model for runout modelling, even if the input data are the same between all models. If the downstream environment is highly channelized however, then a 1D model may suffice for risk assessments, despite the greater simplification

(Martin et al., 2022). Determining when simplifications are still “good enough” appears to be the most enduring and popular form controversy with model validation (e.g., Iverson, 2003 and 2017).

Each question has overlap with the other questions, is sensitive to uncertainty, and is subjective. A model, including the input data, needs to be re-validated under any change in context (Rykiel, 1996). For example, Ghahramani et al. (2022) benchmarked several models with two tailings dam breach events, however the successes or weaknesses of those models and input data are not necessarily relevant to another tailings dam breach event with different input data and conditions. Using the three questions can help determine whether a specific input or model approach is “more valid” than another modelling choice.

Lastly, verification or “truth” is a common discussion point regarding modelling. Occasionally this discussion surfaces as “mechanical” verification, relating to logical errors in model software code (colloquially, “bugs” in the code). Mechanical verification is commonly addressed by the software developer prior to publishing or selling a software or for major version updates (e.g., Brunner, 2018). Andrews et al. (2019) notes engineers are still legally and ethically responsible for code errors within software they use in most Canadian provinces however (e.g., Newfoundland and Labrador, Alberta, and Ontario), regardless of who originally developed the software. Another discussion is regarding true knowledge or “conceptually” verified models that represent all physical phenomena (Box, 1976; Oreskes et al., 1994, Rykiel, 1996). A conceptually verified model is regarded by some as necessary for scientific purposes (Iverson, 2003) while others consider it an impossibility (Oreskes et al., 1994). The demands of society cannot afford such a luxury as a verified model; therefore, engineers and others often do not require strict conceptual verification (Box, 1976; Burland, 1987; Rykiel, 1996; Aaron et al., 2018). Instead, a model may simply be “operationally” verified, where model inputs are realistic and informed by professional judgement and model results are useful for a defined purpose and interpreted by experts. The term “operationally verified” is in effect synonymous with validated (Rykiel, 1996). This thesis follows the latter convention and philosophy.

2.6 Summary

Conventional mine operations and mineral processing produce a mixture of water and fine-grained particles called tailings, which may include additional chemical and

environmental hazards. Tailings are stored behind dam structures; however, these tailings dams differ in several ways from earthfill water retaining dams. Some of the key differences from water reservoir dams include the construction method (i.e., upstream, centreline, or downstream), facility arrangement, and impounded material characteristics.

The comparative diversity in tailings dams leads to correspondingly diverse breach scenarios. Substantial judgement is required to select credible failure modes and scenarios for TDBAs. Past tailings dam breach events have demonstrated slow erosional breaches that take hours, while non-erosional breaches can take as little as several seconds to minutes. No compilation of breach processes exists. Observed outflow volumes and breach characteristics from past tailings breach events have been reported to some extent but would need to be improved in detail and nuance to better inform forward analysis. Breach characteristics are likewise not well reported for either breach process.

Tailings runout results in many consequences in the downstream environment. Recent work has standardized the reporting regarding the impact area for tailings runout. Similar standardization and compilation of other characteristics have not been completed to date. Previous classification of the terrain shape and substrate provide qualitative comparisons between tailings dam breach characteristics but are limited by their inherent simplicity for risk estimates and emergency planning. Numerical models are recommended to address the site-specific needs of a given tailings dam.

The hyperconcentrated mixture of tailings solids and water behaves in a non-Newtonian manner. Non-Newtonian flow is complex, and the flow characteristics of a hyperconcentrated fluid can change under different conditions. There are multiple formulations for non-Newtonian flow, however, measurement of flow properties for a given formula is difficult in laboratory conditions. Back analysis offers some advantages for estimating non-Newtonian flow properties but comes with its own downsides as well.

Models are evolving and capabilities for tailings dam breaches are being added. Breach modelling methods either are specific to a single breach process or have not been verified for tailings dam breach flows. The lack of observed tailings dam breach characteristics represents a challenge for breach modelling methods that require these parameters as inputs. The approach for modelling the tailings runout varies on the software assumptions. Knowledge of the site-specific conditions and the limitations of the selected software, as well as experience, are key requirements of a modeller.

Publicly accessible and global terrain datasets from satellite sources are commonly required to fully model the large extent possible for large tailings dams. These terrain datasets have been noted to be lacking in quality for the purpose of TDBAs, limiting the confidence in modelled results.

Model calibration is a different process than validation. Calibration implicitly involves some form of validation, through the assessment of the range of inputs used and the results produced therein. A model and its inputs need to be validated for each tailings dam breach event.

Chapter 3: Development of a Tailings Dam Breach Database

The tailings dam breach events investigated, along with the data sources that were relied upon for this database, are described in Sections 3.1 and 3.2. The variables in Sections 3.3 to 3.5 are observations of tailings dam breach characteristics. The list of characteristics selected is similar to databases for water reservoir dam breaches (e.g., Wahl, 2014) with some additions relevant to tailings dam breaches, specifically relating to the outflow volume variables. The variables in Section 3.6 contain characteristics related to the flow or runout behaviour and include a mix of measured inputs and calibrated runout parameters. The list of breach characteristics and runout parameters are commonly required as inputs for modelling, but the list is not comprehensive for every model software. Non-physical model inputs (e.g., computational cell resolution) are not included as they are specific to individual model software. The characteristics defined and discussed in Sections 3.7 and 3.8 are not inputs to numerical models, rather they are measures used in calibration and validation. Finally, a discussion of the findings from all the investigations is included in Section 3.9. The values of all characteristics for each event are included in the tables in Appendix A. Specific details and commentary on the investigations for each event are presented and discussed in Appendix B.

3.1 Investigated Events

The events investigated in this thesis were selected from the database in Rana et al. (2021b). They were chosen based on their TSF characteristics and the availability of information to compile the database and support the numerical modelling (discussed in Chapter 4). TSFs vary in their impounded material properties, construction method, arrangement, and potential travel path of tailings runout. The new database covers a diverse set of tailings dam breach events to reflect the heterogeneity observed with TSFs and be of wider applicability in forward analysis. Sufficient information is required to estimate inputs, develop a numerical model, and calibrate the results. The availability and quality of publicly accessible terrain data is also a key consideration in selecting the events (as previously discussed in Section 2.5.3).

The selected events and some of their impoundment characteristics are presented in Table A.1, with the associated dam breach and runout events in Table A.2 in Appendix A. The name of the mine company or official TSF was used for each event, with the colloquial name or names (commonly the name of a nearby town or geographical

region) presented in parentheses. When the breach occurred at multiple compartments of a TSF, the individual compartments were included as sub-items in italics. The compilation included various CDA classes, except for 2B events. This is explained by the relative under-reporting of 2B events (Rana et al., 2021a). All dam raising methods are accounted for, but upstream tailings dams were the most common in this database. Between the historical popularity of upstream dams (Franks et al., 2021) and the additional design and monitoring needed to mitigate the risks of upstream dams (Morgenstern, 2018), it is not surprising that upstream dams formed the majority herein. The tailings type were mostly hard rock tailings, which is also aligned with the database from Rana et al. (2021). The arrangements of the TSF and travel paths of the runout are relatively diverse in this database as well.

Previous tailings dam breach databases (i.e., Rico et al., 2008; Concha Larrauri & Lall, 2018; Rana et al., 2021) include several dozen events, depending on the specific database and variable. A dozen events were considered in this thesis, primarily due to the comparatively more detailed investigation of each event and practical time constraints. Further information relevant to the breach and runout characteristics of each event can be found in Appendix B, and general information about them can be found in Rana et al. (2021a and 2021b).

3.2 Data Sources

The investigations considered three data source types: technical reports, civilian news reports, and peer-reviewed journal articles. In this thesis, technical reports were considered to be the documents issued by governments or companies after the event that investigated some element of the failure. They typically focused on the conditions leading to and during the tailings dam breach, but sometimes addressed runout characteristics as well. Civilian news was limited to online articles found on various websites. These types of news typically focused on the tailings runout and the subsequent impacts. Academic journal articles covered any or all stages and may reference either technical reports or civilian news articles. Publicly available translation software was occasionally required for non-English sources, which may result in a loss of nuance for the technical discussion in such sources.

The data sources and references are presented in Table A.3 in Appendix A. The evidence generally fell into four categories in these sources: simple observations,

measured data, anecdotes, and photographs. Simple measurements are dimensions (e.g., height or width) or timing of characteristics that do not require sophisticated instruments to determine (e.g., “the tailings stain on the building was 2 m tall”, or “the tailings arrived at 12:00 PM”). Simple measurements were found in all source types. Measured data includes topographic surveys and mapping or scientific instruments like seismographs, flow gauges, or laboratory tests (e.g., a post-failure DEM from a LiDAR survey, or cone penetration test results from the tailings prior to failure). These data were exclusive to academic literature or technical reports. Qualitative descriptions or simple observations too broad to be considered quantitative (e.g., “the tailings wave was very high” or “the breach occurred some time after lunch”) are considered anecdotes in this thesis. These are most common in civilian news articles but can occasionally be repeated in academic literature. Anecdotes were often not specific enough or did not include useful details, and as such, were not included in the database or used for model calibration in this thesis. Photographs were found in all source types. They cannot be relied upon for detailed or accurate assessments alone, but often can help cross-check other evidence, provide a sense of scale, or are helpful visuals to technical reporting where inputs or calibration measures for numerical modelling may not be explicitly stated.

Scaled and detailed topographic surveys presented visually in academic or technical reports were considered reliable in this thesis. Written reporting from firsthand forensic work and field investigations carried out by experts were also considered credible. When multiple anecdotal reports of similar observations at a specific location exist, the anecdotes were treated as reliable. Photographs were only considered if they included some form of approximate scale or were accompanied by additional verifiable information, such as the elements above. Individual eyewitness accounts and anecdotes were not considered verifiable without further evidence to support them. Eyewitness accounts rarely came with sufficient quantitative elements or detail to be of use for developing, calibrating, or validating a model (e.g., no specific time or location was reported) regardless of their veracity. Sources that included unverifiable, contradictory, or incorrect information were still included in Table A.3, with further justification and detail on the assessment and exclusion of their details in Appendix B. When a range of values were reported, the average was taken if other supporting information or context was not available to confirm any of the reported values.

3.3 Outflow Volume

The outflow volumes are compiled in Table A.4 in Appendix A. The supernatant pond, tailings solids, and interstitial water were individually compiled or estimated for each event, following the framework from CDA (2021). The following subsections describe the approach and effort to confirm previously reported volumes and quantify them where none existed.

High-level comments are included for each event to categorize the confidence (i.e., high, moderate, and low) for each material volume and the dominant transport mechanism for the tailings (i.e., liquefaction, erosion, or slumping). Given the range of data sources, the confidence level is primarily a subjective assessment, as it is not possible to quantify the uncertainty in any consistent manner for all events.

3.3.1 Supernatant Pond Volume

The supernatant pond volume (V_P) is typically the easiest volume to estimate for tailings dam breach events. In many cases, it is readily apparent from eyewitnesses, aerial imagery, or mine documentation that there was no supernatant pond at the TSF at the time or that it did not discharge during the breach (e.g. for Cadia in Jefferies et al. 2019, or for Feijão in Robertson et al., 2019). For TSFs with supernatant ponds, mine operators may undertake regular bathymetric surveys for operational requirements, allowing for relatively confident supernatant pond volume estimates at the time of the breach (e.g., for MAL Reservoir X in Turi et al., 2013 and Mecsi, 2013; and for Mount Polley in Morgenstern et al., 2015).

For breach events with a supernatant pond but without bathymetric surveys, the uncertainty and the subjectiveness of volume estimates increased. Any reported observations of the maximum or average supernatant pond depth, combined with the surface area of the pond from satellite imagery or scaled figures, helped determine a likely supernatant pond volume or a reasonable range. This range was adjusted based on any additional information, such as photographs and qualitative descriptions of the three-dimensional pond shape.

3.3.2 Tailings Volume

Where possible, the tailings volume (V_T) that outflowed during the breach for each event was estimated as discharging due to erosion, slumping, or liquefaction, primarily based on the descriptions in the data sources. Like supernatant pond volumes based on

bathymetric surveys, the discharged tailings volumes estimated from topographic surveys in literature are relatively trustworthy (e.g., Muramoto et al., 1986; Jefferies et al., 2019; Robertson et al., 2019). When survey data was not mentioned or did not exist, alternate methods were considered to cross-check reported tailings volumes, based on the framework from CDA (2021).

When imagery or photographs allowed, a simplified cone of depression was generated, and its volume was compared to the reported volume. Each cone used a combination of the average residual slope in the TSF (taken from reporting or estimated from aerial imagery and the dam height), photographs of the event, and any additional information available to refine the shape. Natural flood events rarely experience volumetric solids concentrations higher than 30% (O'Brien, 1986; and Garcia et al., 2008). This volume-based rule of thumb was adopted in this thesis as a guide for cross-checking eroded tailings volume estimates, similar to Fontaine and Martin (2015) and Small et al., (2017).

3.3.3 Tailings Solids and Interstitial Water

Once the tailings volume was confirmed for an event, the tailings were proportioned into tailings solids and interstitial water if not previously done so in existing sources. This was done by assuming saturated conditions and using the void ratio reported in Rana et al. (2021b) to determine the proportion of interstitial water and tailings solids according to Equations 3.1 and 3.2:

$$V_T = V_S + V_I \quad (3.1)$$

$$V_I = V_T * \left(\frac{e}{e+1} \right) \quad (3.2)$$

where V_T is the tailings volume, V_S is the tailings solids volume, V_I is the interstitial water volume, and e is the pre-failure void ratio.

When no void ratio for the tailings prior to failure was reported, it was assumed to be 1. This implies half of the released tailings volume is tailings solids and half is interstitial water. This assumption was based on the range of void ratios in Vick (1990) for conventional hydraulically placed tailings and in Rana et al. (2021b) for tailings dam breach events. Rana et al. (2021a) also indicate there is a strong prevalence for the TSFs in these events to have poor drainage, suggesting the simplification of saturated conditions appears reasonable for the estimates herein.

3.4 Breach Processes and Formation Time

Breach processes were estimated from the descriptions of failure conditions and mechanisms and any observations of the runout, particularly the duration of outflow. The classification was straightforward in most cases. Breaches without a release of a supernatant pond are considered Process II breaches, as there is no free water to initiate erosion. Breaches with outflow described in terms of hours are considered Process I breaches, as all Process II are characterized by near-instantaneous collapses. Several events exhibited multiple breach mechanisms. In such cases, further interpretation was required to assign a dominant breach process. The breach process for each event partially informed the modelling approach as well, which is discussed in Chapter 4. The compiled failure causes, breach processes, and formation times are presented in Table A.5 in Appendix A.

The formation time (T_f) was estimated for each event and the breach initiation time and outflow duration were compiled when available. No variation from Wahl's definition (1998) for formation time for water reservoir dam breaches was used. Estimating a formation time for water reservoir dam breaches is non-trivial even for experts and carries some uncertainty (Wahl, 2004). The formation time was estimated for Process I breaches using eyewitness accounts and narratives, which involves some level of uncertainty and subjectiveness. No quantitative estimate of uncertainty has been made for this thesis, but any uncertainty would be comparable to that discussed by Wahl.

The formation time of all Process II breaches was considered instantaneous, or 0 seconds. While any breach is not truly instantaneous, the events with direct evidence or reliable eyewitness accounts suggest formation times equivalent to 10 seconds or less for Process II breach events (e.g., for Prestavèl in Takahashi, 2014; Fundão in Morgenstern et al., 2016; and Feijão in Robertson et al., 2019). Reducing the time for loss of strength and breach progression from near-instantaneous to instantaneous is a well-known and commonly used simplification in landslide modelling and breach analysis of concrete arch dams (e.g., Aaron et al., 2018; USBR, 1988).

3.5 Breach Geometry

The breach geometry was defined in this thesis generally following the conventions in water reservoir dam breach modelling (e.g., Wahl, 1997, 2004; Froehlich, 2008). Spatially, the breach geometry is measured at the hydraulic control (i.e., typically the

narrowest section of the breach). Temporally, it is the geometry at the termination of the formation time, or the point in time when the breach no longer increases in depth or width during outflow.

Chanson (2004) defines hydraulic control as the location where flow conditions are based solely on the geometry of the control section and are independent of the upstream and downstream conditions. Morgenstern et al. (2015) provided a commentary on the progression of the breach geometry and hydraulic control for the Mount Polley tailings dam breach. Walsh (2019) investigated hydraulic controls for tailings dam geometries in flume scale experiments (albeit following a different geometry convention, as discussed in Chapter 2). It is therefore concluded that an assessment of the hydraulic control is still relevant for tailings outflow, despite the definition originating from water flow mechanics. For some events, the hydraulic control is explicitly described (e.g., Morgenstern et al.) or is otherwise easily apparent. For other events, the variation in dam construction methods, facility arrangements, and breach processes specific to tailings dam breaches made identifying the hydraulic control difficult and subjective. Additional labelling and conventions were developed for this thesis to reduce the subjectivity in determining the hydraulic control. These conventions required a balance between standardization among all events while conforming to the specific considerations for the hydraulic control of individual events. The breach geometries are presented in Table A.6 in Appendix A. Each geometric dimension is defined and described in the following subsections.

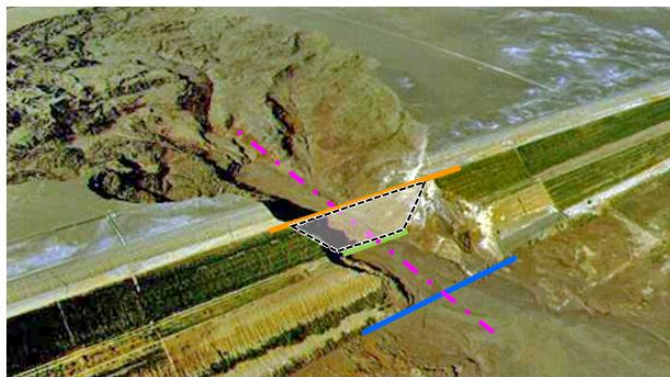
3.5.1 Height Conventions

The International Commission on Large Dams (ICOLD, 2011) defines dam height (H_D) to be the difference between the dam crest elevation (Z_C) and the dam toe elevation (Z_{TD}) of the lowest point of the dam (i.e., the deepest section of the dam). For each event, the pre-failure dam crest alignment was set at the change in angle between the tailings beach and the dam slope, as determined graphically from profiles of the tailings dams from literature or visually in Google Earth imagery. The dam height is often used for regulatory or classification purposes (e.g., World Register of Dams). It has also been included in past tailings dam breach databases as a measure of the potential energy of a breach and a predictor of other runout characteristics (e.g., Concha Larrauri & Lall, 2018). The breach is not always located at the deepest section of the dam for all events, however, and the foundation elevation along the crest can vary greatly for ring-dyke or side-hill TSF configurations. For tailings dams built on steeper slopes, the natural ground below the

crest may be noticeably higher than the lowest foundation elevation for the dam. To address these concerns for tailings dams, additional height variables were defined in this thesis for more relevant comparisons than the dam height alone.

The concept of a “setting-out-line” for referencing the dimensions of a breach was used by Morgenstern et al. (2015) and was adopted here as well. It is noted that the setting-out-line is a two-dimensional plane, not a one-dimensional line as implied by its name. The setting out line was considered to project directly downwards from the dam crest alignment. The breach invert elevation (Z_B) was set at the intersection of the setting out line and the post-failure surface, which may or may not be the original ground elevation or crest foundation (Z_{CF}). These locations are shown in Figure 3.1, with an annotated sketch of the Harmony 4A breach hydraulic control and a hypothetical schematic profile for clarity.

A



Legend:

- Dam Crest Alignment
- Invert Alignment
- Toe Alignment
- - - Setting out Line / Plane
- - - Post-Failure Alignment

B

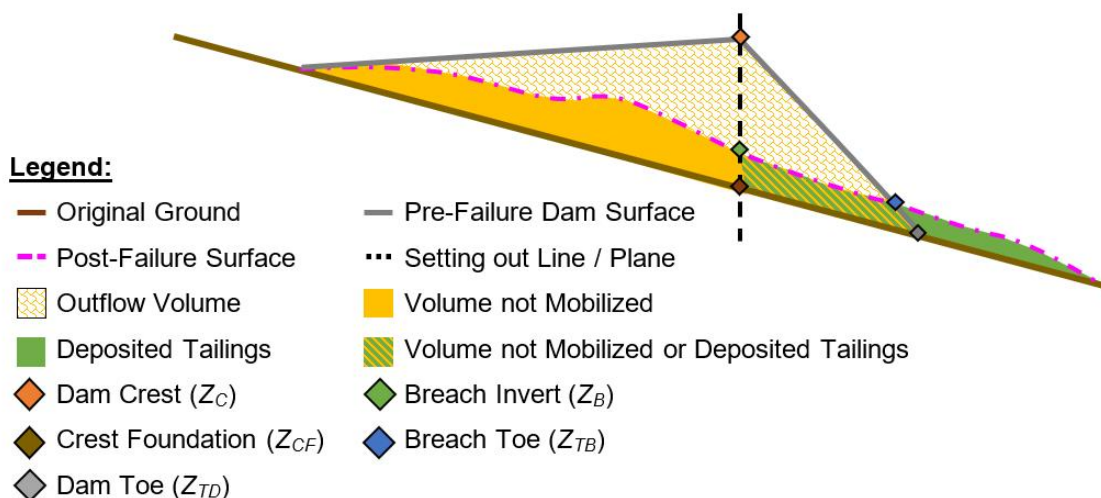


Figure 3.1 Breach Hydraulic Control shown with A) Annotated Oblique photo of the Harmony 4A Breach, and B) Hypothetical Profile

The breach height (H_B) was measured as the difference between the dam crest elevation and the breach invert. The breach height was not measured between the elevation of the dam crest and the breach toe (Z_{TB}). This was done as the hydraulic control for the breach outflow was visually assessed to be better defined at the crest for most of the events. The dam height at the breach location (H_{DB}) was defined following the same convention as ICOLD (2011), however Z_{TD} at the breach location was used rather than the lowest Z_{TD} of the entire TSF. If the breach occurred at the deepest section of the dam, H_{DB} would be the same as H_D . The crest height at the breach location (H_C) is the difference between Z_C and Z_{CF} . The crest height at the location of failure would represent the maximum potential breach height at the breach location. These height definitions are shown visually in Figure 3.2A with a hypothetical schematic profile. For a limited number of events, the water surface elevation of the supernatant pond was reported, so the height of the water above the breach bottom (H_w) could be determined. The H_w is a common variation of the breach height definition in water dam breach databases (e.g., Wahl, 1998). The H_w is referenced in Appendix B as relevant to the limited number of events with such information.

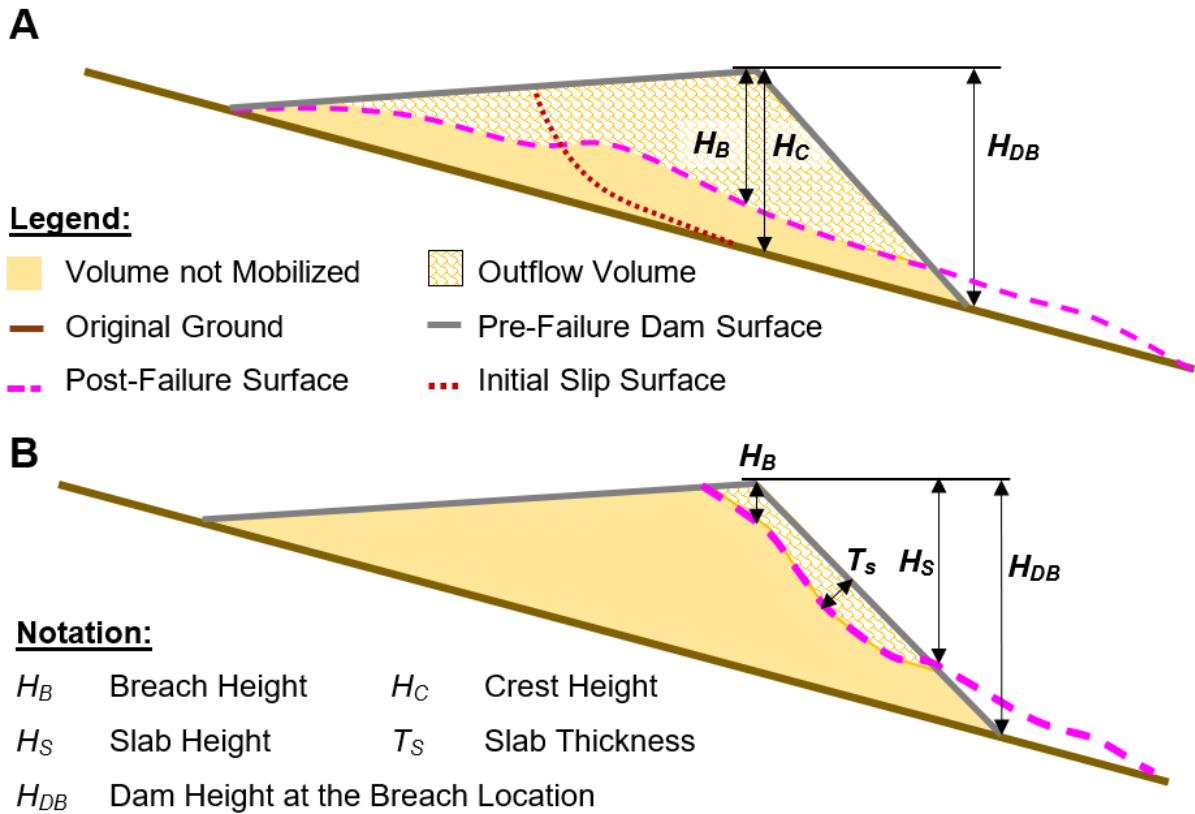


Figure 3.2 Height Conventions for A) Standard Breach Geometry, and B) Slab Breach Geometry

For a few cases, an alternate convention was used. When the maximum thickness of the tailings outflow volume measured normal to the average post-failure surface slope (T_s) was larger than the breach height, the event in question was considered using a different convention. This scenario is shown schematically in Figure 3.2B. This distinction was made as the hydraulic control was assessed to be at the breach toe in these failure events (e.g., for Kayakari in Ishihara et al., 2015). The source area for this scenario is visually similar to slab avalanche source areas as defined by the United Nations Educational, Scientific and Cultural Organization (UNESCO, 1981). Consequently, the tailings dam breach events that meet the T_s criterion are termed slab events in this thesis.

The initial slip surface during the breach may be below the post-failure invert elevation, but some measure of tailings self-damming may occur such that the post-failure invert is above the initial slip surface (e.g., Harmony 4A in Blight & Fourie, 2005). Determining the initial slip surface is more difficult than the post-failure surface (Blight & Fourie, 2005). The slip surface is also more relevant to the potential outflow volume rather than the actual outflow volume, which may be less than the potential outflow volume due to backwatering from the terrain or self-damming (Martin et al., 2022). In this thesis, the breach height was always measured using the post-failure invert, but the estimated deposited tailings depth below the post-failure invert was mentioned as relevant. A hypothetical initial slip surface is shown in Figure 3.2A for visual reference.

The various heights were determined using any elevation data from academic or technical reporting, including figures or maps. In roughly half of the events, detailed and reliable elevation data was available for the heights, particularly the breach height. In the remaining cases, inferences regarding the breach height were necessary. The most common of these inferences was a comparison of the reported regulatory dam height to images or descriptions of the breach height (e.g., the dam breached to roughly half its height, based on photographs). Evidently, such approximations are more uncertain but have some precedence in water reservoir dam breach assessments (Froehlich, 2008; Wahl, 2014).

3.5.2 Trapezoidal Breach Shape

In this thesis, a trapezoid was used to approximate the breach shape, as shown in Figure 3.3. The trapezoid is defined using the breach height (H_B), top breach width (B_T), and bottom breach width (B_B). The orientation of the breach cross-section is taken looking in the downstream direction. The trapezoid alternatively can be defined with the average

breach width (B_{Avg}), and left and right breach side slopes (Z_L and Z_R). The breach side slopes do not necessarily need to be the same between the left and right side slopes.

The trapezoid approximation can be collapsed to a rectangular breach shape (through vertical breach side slopes) to a V-shaped breach (using 0 m for B_B). The trapezoidal approximation is often applied in forward-analysis for water-reservoir dam breaches for its simplicity and flexibility (Froehlich, 2008). Observations of past water-reservoir breaches and large-scale embankment failures also showed that a trapezoid approximated the breach shape rather well (Froehlich, 2008; Morris et al., 2007). The downside of a trapezoid breach shape is that it may not represent highly irregular, composite, or curvilinear breach shapes.

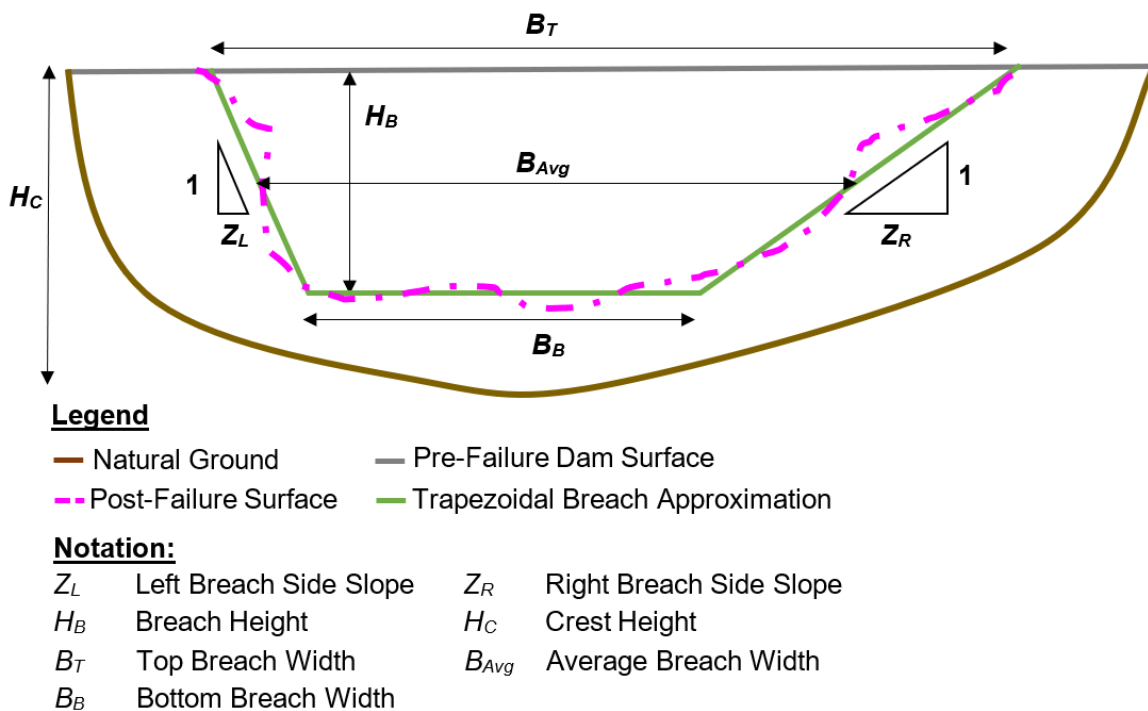


Figure 3.3 Trapezoidal Breach Geometry at the Dam Crest

For a few events, the dam crest alignment included a bend at the same location as the breach. For example, the Feijão event included two slight bends near each abutment while the Fundão involved two large setbacks with multiple bends. A subjective assessment was made for each event whether the bend was large enough that an alternate alignment was warranted. This alternate alignment was a straight line between the right and left side of the breach, with the breach geometry taken at the alternate alignment. Part of this subjective assessment was informed by the modelling approach, discussed in Chapter 4.

The breach geometry is relatively simple to observe and report after a breach event, as the ultimate depth and widths can be safely surveyed even without detailed surveying equipment (Froehlich, 2008). Consequently, average breach width and breach depth are the most widely reported characteristics for water reservoir dam breaches (Wahl, 2014). Confident estimates of breach depth and widths can be acquired for some events from presented survey information (e.g., 2014 Mt. Polley; Morgenstern et al., 2015), but surveys of tailings dam breaches appear less common than water reservoir dam breaches.

The breach width (top, bottom or average) is sometimes compared to the dam height (Wahl, 1998; USACE, 2007) to give a normalized comparison between events or for forward analysis. Photographs of the breach were used to get an approximation of the breach widths using the ratio of the dam height to the breach width for the events without survey information. This method is not exact, as photographs may be oblique and lack a reported scale (other than the visual of the dam height). Froehlich (2008) noted such approximate measurements were also necessary for water reservoir dam breaches in some cases.

3.6 Runout Parameters

Runout parameters consist of non-Newtonian parameters for the fluid and a roughness parameter for the downstream environment. The backgrounds for these parameters were discussed in Chapter 2 (Sections 2.3.2 and 2.4). Runout parameters are infrequently available in the literature for these events, as they require extensive laboratory testing, back-calibration with a numerical model, or expert judgement.

The runout parameters used in this thesis are presented in Table A.7 in Appendix A, however they should be viewed together with the commentary on the runout calibrations in Sections 4.4 and 4.5.3. Substantial caution should be exercised when considering these parameters in this thesis, as some of them are calibrated and not independently measured. The calibrated values may not be transferable to a different numerical model software simulation of the same event (as concluded by Ghahramani et al., 2022), or a different event with the same model software.

3.6.1 Quadratic Formula

This thesis uses the Quadratic formula (O'Brien, 1991) for the non-Newtonian tailings runout. The Quadratic formula is defined with Equation 3.3:

$$\tau = \tau_y + \tau_v + \tau_T + \tau_d \quad (3.3)$$

where τ is the shear stress, τ_y is the fluid yield stress, τ_v is the viscous stress, τ_T is the turbulent stress, and τ_d is the dispersive stress. The individual components may be written as Equations 3.4, 3.5, and 3.6:

$$\tau_v = \mu \frac{du}{dy} \quad (3.4)$$

$$\tau_T = \rho_m \ell^2 \left(\frac{du}{dy} \right)^2 \quad (3.5)$$

$$\tau_d = \alpha_i \rho_s \left[\left(\frac{C_{Max}}{C_v} \right)^{1/3} - 1 \right]^{-2} d_s^2 \left(\frac{du}{dy} \right)^2 \quad (3.6)$$

Where μ is the fluid viscosity, du/dy is the shear rate, ρ_m is the fluid mixture density, ℓ is the fluid mixing length, α_i is Bagnold's empirical coefficient, ρ_s is the solid particle density, C_{Max} is the maximum volumetric solids concentration for the fluid, C_v is the volumetric solids concentration of the fluid, and d_s is the representative particle size. The turbulent stress is alternatively defined using the Manning's coefficient in HEC-RAS, therefore the mixing length is not considered in this thesis. The turbulent stress includes the fluid mixture and is discussed in the following subsection.

Julien and Lan (1991) found that the Quadratic formula performed well across a range of particle sizes, volumetric solids concentrations, and shear rates for laboratory testing of hyperconcentrated water-solid mixtures. They also demonstrated that the majority of the contribution to shear stress comes from the yield stress and viscosity stress terms in the Quadratic formula. With low concentrations of small particles at shear rates commonly observed in mud floods and mudflows, the Quadratic formula essentially collapses into the simpler Bingham formula (Julien and Lan, 1991). Gibson et al. (2020) confirmed the corollary, where high concentrations of large particles at high shear rates had large turbulent-dispersive terms in physical and numerical modelling flume scale experiments. Gibson et al. noted that the partially theoretical and physical basis (discussed below) to the turbulent-dispersive parameter offers some advantages over the fully empirical Herschel-Bulkley parameters. Gibson et al. also noted the Bingham formula under-predicted internal losses when paired with the measured yield stress and viscosity of the materials in the HEC-RAS model, while the Quadratic formula results paired well with the measured rheology parameters. Given the diversity of tailings materials, breach characteristics, and runout environments, the additional complexity of the Quadratic

formula (e.g., compared to the Bingham formula) is warranted for its flexibility for the diverse events herein.

The specific gravity of the tailings particles is commonly reported in academic or technical reports, which can be easily converted to density. Not all cases had reported densities or specific gravity for the tailings particles. Gibson et al. used the median particle size (d_{50}) as the representative particle size in their comparison between numerical model results in HEC-RAS and laboratory observations. The same approach was adopted for this thesis. When a particle size distribution was not available for the tailings from each event, a representative particle size was assumed using any qualitative descriptions of the tailings particle size and the Wentworth (1922) particle size classification (e.g., tailings described as fine sands were assigned a representative grain size of 250 microns, according to the upper limit for fine sands from Wentworth, 1922).

The remaining inputs (i.e., Bagnold's empirical coefficient, density of water, and maximum volumetric solids concentration) are empirical, measured, or theoretical parameters that have been determined by previous assessments of non-Newtonian flows. They have been repeatedly found to be well constrained as constants. Bagnold's constant is unitless and commonly accepted as 0.01 (Bagnold, 1954; Takahashi, 1980; Julien & Lan, 1991, O'Brien et al., 1993). The density of water is typically assumed as 1,000 kg/m³ for hydraulic modelling software (e.g., HEC-RAS, Brunner, 2020). The maximum volumetric solids concentration for the quadratic formula is often quoted as 61.5%, based on the packing theory of uniform spheres (Gibson et al., 2020, Julien & Lan, 1991). The uniform sphere packing theory actually indicates a maximum volumetric solids concentration of approximately 74% (Bagnold, 1954) and the maximum volumetric solids concentration of well graded natural materials (i.e., non-uniformly sized particles) in debris flows is around 84% (Rickenmann, 1999; Rickenmann, 2001; Ancey, 2007). No information was found regarding the maximum theoretical volumetric solids concentration for any individual tailings dam failure. This value was assumed in this thesis to be a constant equal to 84% to be in line with Gibson et al.

There are only two unknown rheological parameters, yield stress and viscosity, that are "tuned" in the calibration process for each event in this thesis (discussed in Chapter 4). This is aligned with the number of parameters requiring calibration of other rheology formulas or runout models. Even a model such as D-Claw, which is constrained by independent measurements of intrinsic material properties (Iverson & George, 2014),

requires calibration of sensitive model parameters (Iverson & George, 2016). The range of measured rheology data from Martin et al. (2022) can be used as limits to any calibrated yield stresses and viscosities from this thesis. Furthermore, specific practical experience with tailings characteristics and measured rheology as in Boger (2011) or Adams et al. (2017) can be used to refine this range for a given tailings dam breach event if information is available.

3.6.2 Manning's Coefficient

Out of the roughness parameters listed in Section 2.3.2, the Gauckler-Manning's coefficient was used in this thesis for the downstream environment. The coefficient is colloquially known as Manning's Coefficient or Manning's n . The unit of Manning's coefficient is $\text{s/m}^{1/3}$; however, it is often omitted (Chanson, 2004). This roughness parameter was selected due to the extensive literature on Manning's Coefficient, and it is the preferred roughness parameter in HEC-RAS (Brunner, 2020). The implementation of the turbulent stress using Manning's Coefficient is shown in Equation 3.7:

$$\tau_T = \rho_m \frac{gn^2}{R^{1/3}} |v|^2 \quad (3.7)$$

Where ρ_m is the fluid mixture density, g is the acceleration due to Earth's gravity, n is the Manning's Coefficient, R is the hydraulic radius, and v is magnitude of the flow velocity. The fluid mixture density is defined with Equation 3.8:

$$\rho_m = \rho_w + (\rho_s - \rho_w) C_v \quad (3.8)$$

Where ρ_w is the density of water, ρ_s is the solid particle density, and C_v is the volumetric solids concentration.

The Manning's Coefficients selected for each event were based on the procedure outlined in Arcement and Schneider (1986). Table 3.1 shows typical land cover and Manning's Coefficients considered for the events and modelling in this thesis; however, individual values were informed by the site-specific conditions for each event. These conditions were determined through photographs, descriptions, and Google Earth Imagery available for each event prior to the tailings dam breach. The Manning's Coefficients calculated herein were compared to other guidance such as Janssen (2016) as well.

Table 3.1 Common Land Cover and Typical Manning’s Coefficients for Two Dimensional Hydraulic Modelling (Arcement & Schneider, 1986; Janssen, 2016)

| Land Cover Types | Manning’s Coefficient |
|----------------------------------|-----------------------|
| Bare earth, natural rock | 0.02 to 0.03 |
| Grassland, open fields, pastures | 0.03 to 0.06 |
| Rivers or small waterbodies | 0.03 to 0.08 |
| Moderate brush and vegetation | 0.05 to 0.08 |
| Forested or densely vegetated | 0.08 to 0.12 |
| Urban or dense suburban | 0.12 |

3.7 Event Runout Observations

The Zone 1 inundation areas and runout distances for the events in this thesis have been previously estimated or compiled by Ghahramani et al. (2020) and re-confirmed by Rana et al. (2021b). The estimated Zone 1 runout distances and inundation areas from Ghahramani et al. are included in Table A.1 in Appendix A. Other event observations (e.g., fatalities or financial costs) are more related to the population or value placed on the area affected by the tailings runout than the runout characteristics themselves.

The convention for measuring distance has not been defined in previous databases (e.g., Rico et al., 2008, Concha Larrauri & Lall, 2018, Ghahramani et al. 2020). It appears that runout distances have included a mix of distances measured along the river centreline or thalweg, along the centreline of the tailings flow (but not necessarily the river centreline), or the shortest straight line distance. These conventions are shown conceptually in Figure 3.4. Inundation areas provide more spatial information than the runout distance (i.e., two-dimensional information versus one-dimensional) and are less subjective than distances. For such reasons, only the Zone 1 inundation areas are directly incorporated into the model calibration, as discussed in Chapter 4.

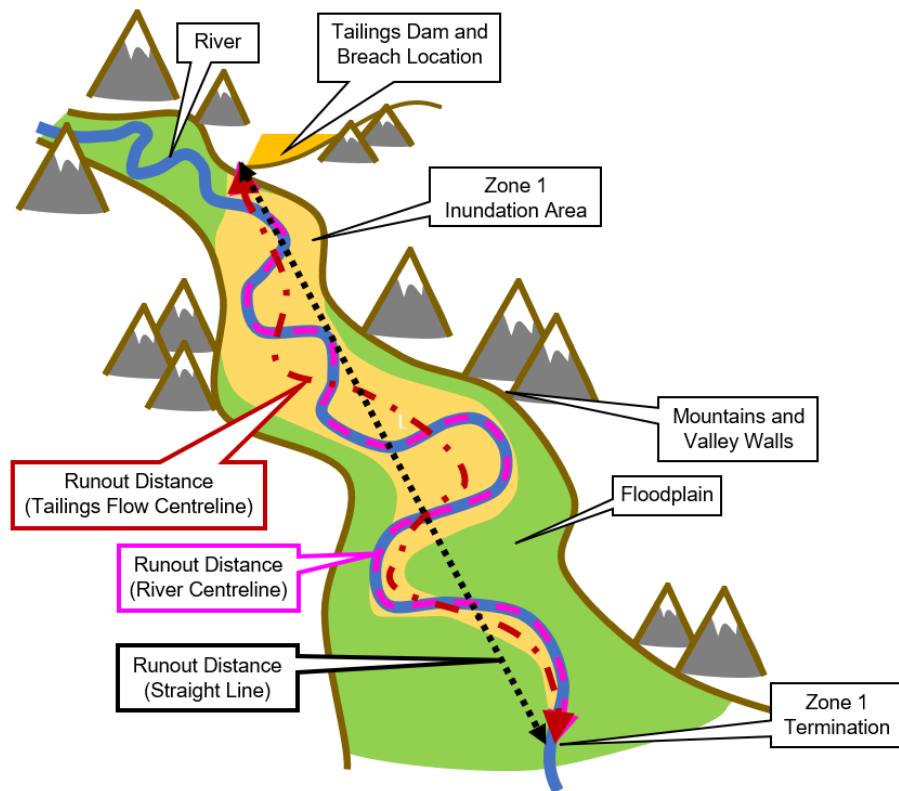


Figure 3.4 Runout Distance Measurement Conventions

The convention for the Zone 1 inundation area is well defined in Ghahramani et al. (2020), and the same convention and mapped inundation areas are adopted in this thesis, except as noted below. The investigations in this thesis were more in-depth than those described in Ghahramani et al. (2020) or Rana et al., (2021b), as befitting the lesser number of events investigated and the increased detail needed for hydraulic numerical modelling compared to statistical relationships. The scope of this thesis did not initially include revising the Zone 1 inundation areas, however, during the investigations for this thesis, additional evidence was identified for several events that suggested they needed to be updated. For consistency, adjustments to the Ghahramani et al. Zone 1 inundation areas were avoided when possible. Adjustments were made if they were small, clearly and strongly evidenced, and simple to implement. The events with larger recommended adjustments were noted for future work, but no adjustments to these inundation areas were made in this thesis. Specific details for any adjustments or recommended updates are described in Appendix B.

3.8 Local Runout Observations

The local observations are broadly categorized as flow depths, arrival times, and miscellaneous or derived observations. The type and uncertainty of local observations compiled vary according to the method of observation, the knowledge of the observer (e.g., an untrained civilian versus a subject matter expert in tailings flows), and the timing of the observation. The number of observations compiled for each event were limited by practical time constraints and the desktop-level nature of the investigations. For some events, only one or two local observations with limited confidence were found, while a few events had none. The local runout observations for each event are summarized in Table A.8 in Appendix A.

3.8.1 Flow Depths

The flow depth is one of the basic elements for hazard mapping and may be for the peak depth of the tailings runout or for the final deposition depth after flow has ceased (CDA, 2019, 2021). Tailings runout can leave indicators of the maximum flow depth through mud high-water marks on buildings, trees, and infrastructure. These indicators can be safely observed and photographed after the event without sophisticated survey equipment and are the most common measures of depth available (e.g., for Harmony 4A in Wagener, 1997, and for Aznalcóllar in Eptisa, 1998). For some events, eyewitnesses recounted their observation of flow depth at a time likely around the maximum flow velocity or depth (e.g., for Prestavèl in Takahashi, 2014).

The final depths of the tailings deposit may be reported from field visits for forensic engineering and impact studies (e.g., for Aznalcóllar in Gallart et al., 1999). Final depths also can be surveyed throughout the inundation area (e.g., for Cadia in Jefferies et al., 2019), but some survey information prior to failure is necessary for proper change detection analysis. These full surveys are rarer, as they are generally limited to more recent events with shorter runout distances where detailed topographic surveys are feasible. A complete set of pre- and post-failure surveys for an event would be a rich data source for model calibration and validation.

3.8.2 Arrival Times

The arrival time is the time that takes for the tailings to reach a location and may be defined for the arrival of the tailings runout front, the peak depth of the tailings, or peak flow of the tailings (CDA, 2019a, 2021). Unfortunately, the arrival time cannot be observed

after an event unless timestamped video or scientific instruments register the event (see Section 3.8.3). This limits observations primarily to eyewitness accounts, which are often difficult to determine a location or are only qualitative.

In forward analysis, the dam failure sequence is hypothetical and not associated with a specific time or date, therefore the arrival time must include a reference time (e.g., the time since the formation time or the start of the flood event). While the tailings dam failures in the current database are obviously not hypothetical, two or more observations at two or more different locations are still needed to use arrival time as a back-analysis model calibration and validation tool. This is required as the relative arrival time of the tailings flow is used in model calibration and validation rather than an absolute arrival time. In simpler terms, the breach could be set to begin in a back-analysis numerical model at an incorrect time to arrive at a downstream location at the correct time. With multiple arrival time locations, the confidence in the timing of the flood wave increases. The time of the onset of failure at the tailings dam is often one of the time and locations pairs that can be used to determine the relative timing further downstream for the back-analysis models in this thesis.

3.8.3 Miscellaneous and Derived Observations

Beyond the simple measurements of depth and arrival time, some events had secondary observations reported where their values come from additional interpretation or are derived from a combination of other observations. In rare cases, scientific instruments installed in the vicinity of the tailings runout for other purposes unintentionally (but fortunately) captured some feature of the runout. The data from these sources may require additional expert interpretation, but generally can provide multi-faceted information invaluable to support model calibration and validation. These more complex observations were found to be rarer than the simple measurements of depth and arrival time but were still useful in the model calibration and validation process and thus warranted discussion.

The average velocity of the tailings runout is occasionally reported (e.g., for Fundão in Morgenstern et al., 2016; for Prestavèl in Takahashi, 2014). These estimates are usually based on arrival time (i.e., the distance between two locations divided by the difference in arrival time between them) rather than a direct measurement of velocity. Therefore, the original arrival times for each location were considered a more appropriate model calibration and validation tool than the average velocity between them.

For some tailings dam breach events, pre- and post-failure surveys (as mentioned in Section 3.8.1) were completed by other parties; however, due to uncertainties or other considerations, the actual survey data is not reported or shown by the other parties. Instead, the total tailings volume deposited in an area, or the total tailings volume that passed a location are reported, as calculated from the change in topography from the pre- and post-failure surveys. These values were assumed to be reliable, like outflow volumes calculated using survey information (Section 3.3).

Hydrometric gauges can provide a time-series of the tailings runout depth if they were located in the Zone 1 inundation area. This time-series can give information about the arrival time of the flood wave front, peak tailings depth, arrival time of the peak tailings depth, final (deposited) tailings depth, and the general trend in depth and timing between all these elements. Hydrometric gauges are also useful outside of Zone 1, as they can constrain the arrival time or other runout characteristics (e.g., for Feijão in CPRM, 2019). Such quantitative and straightforward information is useful in model calibration and validation, but caution and judgement should be exercised under some conditions. Depth time-series are preferred to flow time-series for model calibration and validation. Most stage-discharge rating curves at hydrometric gauges are invalid for events like extreme floods or tailings runout therefore the calculated flow may not be reliable (Ayala-Carcedo, 2004; BGC, 2022; Lang et al., 2010). Furthermore, as these instruments are directly in the tailings flow path, they are vulnerable to damage, which may limit the confidence in their recorded data (IGME, 2001). Lastly, hydrometric gauge data can be affected by other phenomena in addition to tailings runout. Identifying these other phenomena and differentiating the data can be difficult, particularly when the hydrometric gauge is outside of the Zone 1 extent (i.e., in the Zone 2 extent). Hydrometric gauge data was considered when available for the events, including gauges outside the Zone 1 extent. The data was interpreted and assessed for relevance to model validation and for the described concerns as part of the event investigations.

Seismograph data require expert interpretation to invert the frequency into a force-time function. These force-time functions have provided insight into the timing, duration, and dynamics of landslide events (Mitchell, 2021, and the references therein) and for a limited number of tailings dam breach events (e.g., Takahashi, 2014). No seismic inversion analysis was completed in this thesis, but interpretation by others was occasionally relied upon for model calibration and validation when available.

3.9 Discussion

Rico et al. (2008) and Rana et al. (2021a) commented that reporting on tailings dam failures are usually incomplete, with poor data availability or quality. This was found to be the case for many of the events investigated herein as well. Many of the approaches to estimate or confirm some of the characteristics or observations are based on rules of thumb or simple geometric comparisons. Consequently, these approaches cannot provide insight beyond a rough sense of proportion for the characteristics. The rules of thumbs rarely were able to invalidate reported values without additional primary sources. The following discussion includes the limitations and common uncertainties across multiple events.

Despite the high-level concerns above, it is believed that this database provides an improvement in understanding of the tailings dam breach events considered and enhances the numerical modelling of similar events. General insights regarding the results of the investigations for each characteristic, possible use of cases for forward analysis, and suggested future research are outlined. The discussion on runout parameters is included in Chapter 4, as it is more relevant to the rheology calibration method used in the numerical modelling, detailed therein.

3.9.1 Outflow Volumes

It was rare that a comprehensive breakdown of the volume (e.g., for Mount Polley in Cuervo et al., 2017) was available, despite the impact of the total outflow volume and the volume concentration on breach and runout characteristics. In general, the outflow volumes were the characteristics most difficult to assess and were affected by uncertainty in reporting. For example, the most reliable estimate of the tailings that discharged in the Aznalcóllar event (Spain, 1998) was initially assessed to be 1.3 M m^3 of tailings (tailings solids and interstitial water) and 5.5 M m^3 of supernatant pond for both compartments combined, as reported by McDermott & Sibley (2000). The rough volume of discharged tailings for the North Pyroclastic Pond was estimated using an eighth of a cone. An estimated radius of 800 m and a height of 25 m (the remaining 3 m to meet the 28 m dam height being the supernatant pond) gave a volume of 2.1 M m^3 , nearly double the reported tailings volume. McDermott & Sibley's involvement with the legal proceedings that followed the event gave their estimate credibility and the geometric estimate is acknowledged as unsophisticated, therefore the reported tailings volume was included in

the database and subsequent modelling. After the investigation and numerical modelling for Aznalcóllar was completed for this thesis, Sanz-Ramos et al. (2022) published additional and novel evidence on the event. Sanz-Ramos et al. estimate the total outflow volume ranged from 11.5 M m³ to 15.4 M m³, with a tailings solid volume between 2.3 M m³ to 4.6 M m³. Not all events have uncertainty in the outflow volume as high as Aznalcóllar, however, the idea that multiple authors for previous databases (e.g., Rico et al., 2008; Lurrari and Lall, 2018; Rana et al., 2021b) and this thesis can critically assess the outflow volume for Aznalcóllar and yet be possibly underestimating by a factor of 2 is evidently concerning.

Regardless of the uncertainty discussed above, numerous advances in characterization for each outflow volume were made during this thesis. The volumetric solids concentration for the tailings runout was estimated with relative confidence for nine of the twelve tailings dam breach events, which is an increase to the few events noted by Rana et al. (2021a). The tailings transport mechanism (i.e., erosion, liquefied flow, slumping) was estimated for each of the events, which is a key consideration for runout modelling (CDA, 2021). Such details are useful for assessing the variation in mobility and can be used to continue work initiated by Ghahramani et al. (2020) and Rana et al. (2021a).

The unconfined events in this thesis are shown in Figure 3.5 and compared to the regression line from Rana et al. (2021), with labels for the volumetric solids concentration. Additional arbitrary lines at one half order of magnitude above and below the regression line are shown for clarity. The impact of solids concentration is apparent in the high relative mobility for the Aznalcóllar and MAL Reservoir X events (IDs 4 and 6). Events 4 and 6 included comparatively shallower slopes in the Zone 1 extent, yet they still exhibit the greatest residual above the regression from Rana et al. The outflow volume, solids concentration, and inundation area reported by Sanz-Ramos et al. (2022) for the Aznalcóllar is shown with ID 4*; however, the conclusion is the same regarding the mobility of the event. The unconfined events in this thesis with volumetric solids concentration above the mudflow characteristics boundary (i.e., $C_v > 45\%$, following O'Brien, 1988) all exhibited lower relative mobility, being closer to or lower than the “average” relative mobility represented by the regression line. The tailings runout for the Tashan event (ID 5) was on a 10% slope (i.e., steeper than for most other unconfined events in this thesis) and the tailings runout for the Harmony 4A event (ID 3) was primarily

on a hard wet surface (Blight & Fourie, 2005). These features may explain their slightly higher relative mobility compared to other events with high volumetric solids concentration. Further work regarding contributory factors for runout is needed to better understand trends or develop statistical relation, but this effort is hampered in this thesis by the limited number of events included. This guidance could be used for high-level engineering planning or regional risk analysis (e.g., Innis & Kunz, 2020), once the sample size is increased.

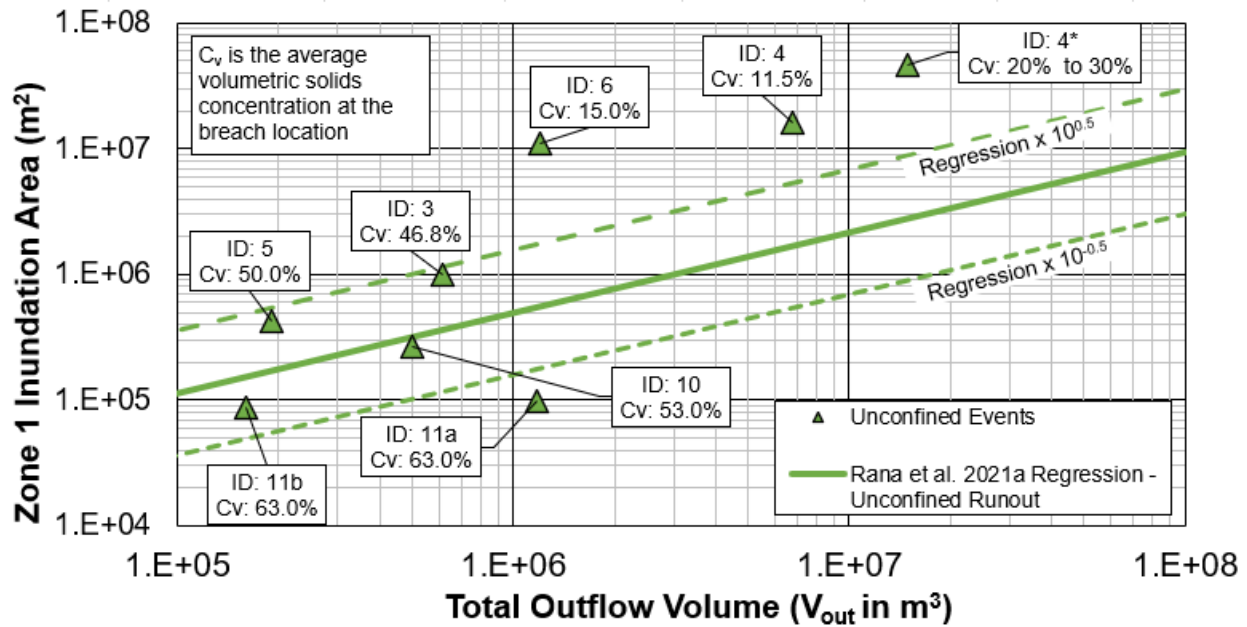


Figure 3.5 Zone 1 Inundation Area versus Total Outflow Volume with Volumetric Solids Concentration for Unconfined Runout Events (Regression from Rana et al., 2021a).

Geometric or temporal details were explicitly discussed and included in the database as relevant. For example, the Prestavèl event in Italy, 1985, has been widely described to be a cascading failure of a stepped facility (Luino and De Graff, 2012; Takahashi, 2014). This arrangement for Prestavèl is commonly ignored in databases that include this event (e.g., Rico et al., 2008; Larrauri and Lall, 2018; Piciullo et al., 2022) or numerical modelling of the event (e.g., Takahashi, 2014; Pirulli et al., 2017). The Cadia NTSF event in Australia, 2018, has previously been simplified to a single event in databases (e.g., Rana et al., 2021b) despite two different flow characteristics (a slump and liquefied flow) occurred with 48 hours passing between each event. Similarly, the Fundão event in Brazil, 2015, discharged 32.2 M m³ of tailings on the day of the primary failure, and then discharged a further 11.5 M m³ of tailings over the next several months

during multiple separate rainfall events (Fundação Renova, 2016). The cumulative discharged tailings volume of 43.7 M m³ is then reported in databases (e.g., Piciullo et al., 2022) without the nuance or context regarding the timing of the discharges. These simplifications may be necessary for the scope and purpose of the previous work, but they obscure the phenomena or considerations that would be useful for forward-analysis of facilities having similar arrangements or conditions.

3.9.2 Breach Processes and Formation Time

Rana et al. (2021b) previously identified the failure conditions and mechanisms for the events in this thesis. Based on that work and the references therein, there was sufficient evidence to determine the breach process and complete the failure mode for each event with comparatively little uncertainty. Similarly, the narratives available in the literature were sufficient to estimate formation times for all events. Initiation times or outflow durations were harder to determine but are included as available.

Conventional fault tree or event tree analyses are often used in failure modes and effects analysis (FMEA) or Probable Failure Mode Analysis (PFMA) for dam safety, including tailings dams (DeNeale et al., 2019). Fault tree analysis starts with the breach of the dam and works backwards through potential events leading to the breach, while event tree analysis works forward through time and the events needed to initiate a breach. In other words, most dam safety risk analysis considers the first two steps of a failure mode, the failure cause(s) and the failure mechanism(s) but does not include the breach process. In this thesis, the breach process was not found to be only dependent on failure mechanisms for all cases. For example, the Mount Polley and Aznalcóllar TSFs experienced a failure trigger typically associated with Process II breaches (foundation failure), but primarily breached through an overtopping and erosion failure mechanism associated with Process I breaches. On the other hand, Harmony 4A experienced a trigger associated with a Process I breach (overtopping), but primarily experienced a Process II breach. These findings suggest that risk analysis may need to include the breach process in their assessment, as the probability and consequences (and therefore the risk) would differ between each breach processes even if they were initiated by the same failure mode.

The three non-upstream dams in this database experienced some form of Process I breaches, where the dominant tailings transport mechanism was erosional. The two events that were fully Process I breaches (Aznalcóllar and Mount Polley) had

formation times quite slow for their height (less than 15 m/hr) compared to the mean erosion rates for dam failures in Walder & O'Connor (1997), as shown in Figure 3.6. This could be explained by tailings beaches representing an additional resistance to erosion and slowing the breach formation. Walsh (2019) also obtained slower dam breaches in flume scale experiments with a tailings beach compared to scale dams without tailings beaches. The other Process I breach was at the MAL Reservoir X in Hungary, 2010, where the downstream constructed dam experienced some form of structure failure described with brittle behaviour. Even with this “partial” Process II breach process, the mean erosion rate of Mal Reservoir X embankment was 88 m/hr, which is still within the range of mean erosion rates observed in Walder & O'Connor (1997). This suggests that water reservoir dam breaches or landslide dam breaches may be useful analogues for Process I breaches at tailings dams. More research is warranted to confirm this finding.

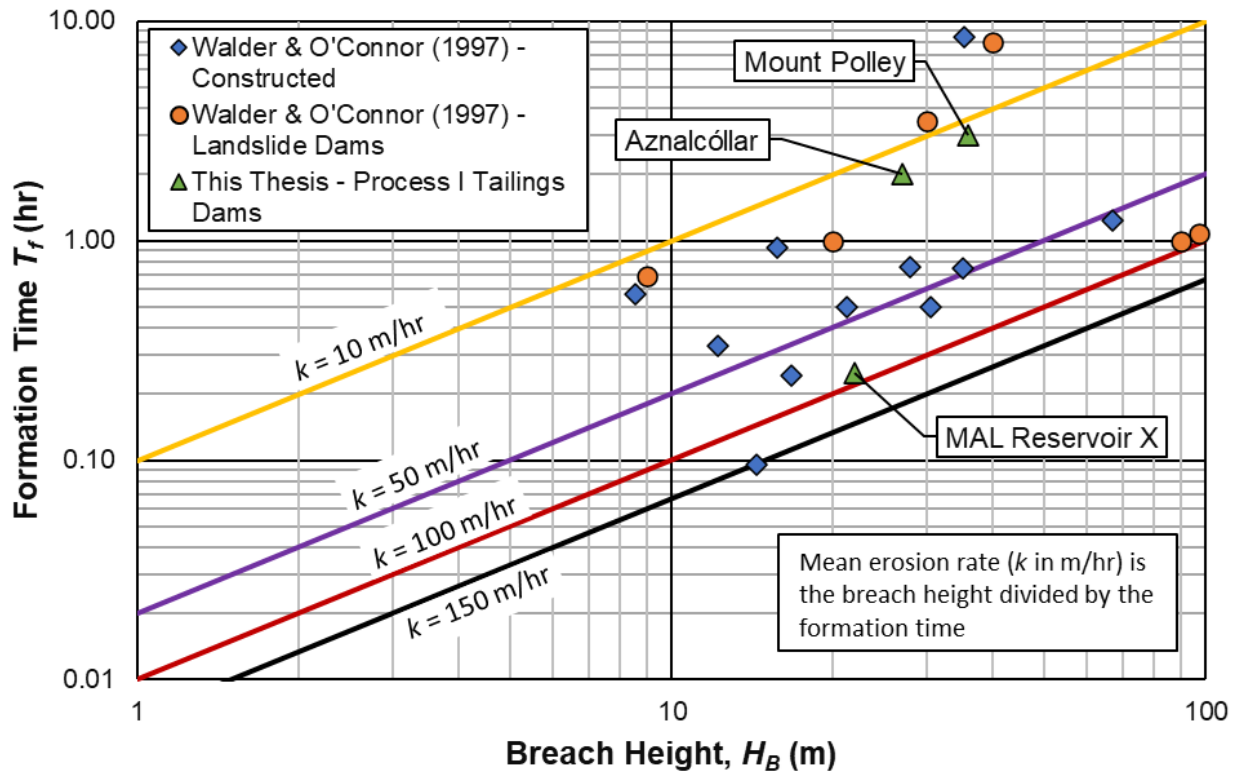


Figure 3.6 Process I Tailings Dam Breach Mean Erosion Rates Compared to Water Reservoir Dams (Data from Walder & O'Connor, 1997)

All upstream dams in this thesis experienced Process II breaches. The events were selected based on the availability of data, which is typically higher for destructive and notable events, and appears to occur more often with Process II breaches. Consequently, this observation may be a result of selection bias, rather than any physical

basis. It is not recommended to assume that upstream dams only experience Process II breaches at this time because of the limited number of tailings dam breach events in this database. More upstream tailings dam failure events should be assessed to further explore the frequency of Process II breaches for upstream tailings dams. Furthermore, the corollary that centreline or downstream dams cannot experience Process II breaches is equally not tenable, as downstream water reservoir dams may also undergo a Process II breach (e.g., for Edenville Dam in France et al., 2022).

3.9.3 Breach Geometry

The confidence regarding the breach geometry for all the evaluated events varied. The uncertainty primarily came from a simple lack of information or reporting on the geometry. When reporting was available, it was generally found to be reliable given the relative simplicity of these characteristics (i.e., compared to three dimensional volumes, discussed in Section 3.9.1).

The assumption that the dam crest represents the hydraulic control came from conventions in water reservoir dams, however, it was not found to be suitable for all events. Unsurprisingly, the assumption appeared to work the best for Process I events, which appeared to be most similar to water reservoir dam breaches. These events had clear hydraulic controls and were estimated herein in the same location as previous authors (e.g., for Mount Polley in Morgenstern et al., 2015; for Aznalcóllar in Sanz-Ramos et al., 2022). The confidence on the hydraulic control was more varied for Process II events. The lower confidence Process II events were events with limited information to fully constraint the hydraulic control and geometry (e.g., for Fundão in Machado, 2017) or smaller facilities with geometric features (e.g., a corner of the dam crest alignment) that intersected with the breach geometry (e.g., for Prestavèl in Muramoto et al., 1986; for Gillibrand No. 6 in Harder & Stewart, 1996; for Fundão in Morgenstern et al., 2016). A novel convention for the “slab” events in this thesis was developed and therefore should be further explored or refined. In general, the hydraulic control for the slab events was low, however, the numerical modelling for the Cadia NTSF Event II showed that the slab convention may have some merit (see Chapter 4 and Appendix B for further details).

The breach height (as a ratio of the crest height) is plotted against the crest height at the breach location in Figure 3.7. The breach height is commonly assumed to be the crest height (i.e., the breach invert is at ground level) for forward analysis (CDA, 2021). Such an approximation appears reasonable for the Process I events (i.e., the breach

height to crest height ratio is nearly 100% in all cases). The Process II events demonstrate more variation in the ratio but are generally at least 50% when excluding slab events. The breach height often is required to be equal to the dam crest to meet existing regulatory requirements or industry guidance (e.g., FERC, 2015) for dam hazard classification. Risk assessments or emergency planning for various scenarios (including partial breaches) can be informed by the range of height ratios in Figure 3.7.

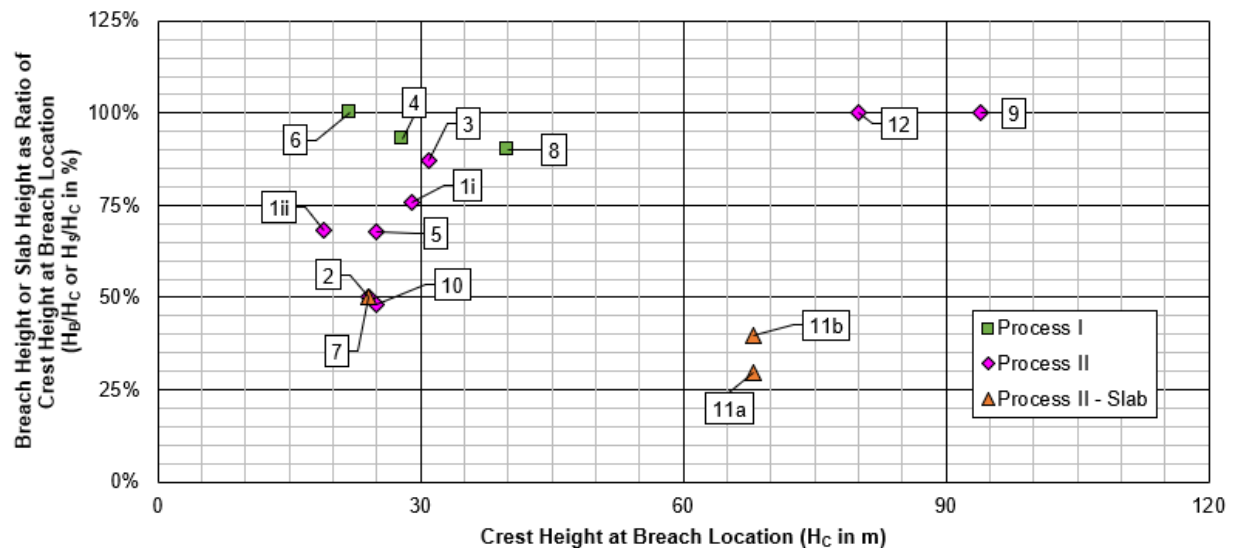


Figure 3.7 Observations of Breach Height versus Dam Height at the Breach Location

The breach height is plotted against the average breach width, following the comparison shown in Wahl (1998), in Figure 3.8, along with the water reservoir dam breaches in Wahl. The breach width to breach height ratio is a useful normalization for facilities with different dam heights, and various ratios are shown with the coloured lines on the same figure. The tailings dam breach events tend to have higher breach heights than the water reservoir breaches but are comparable in terms of the width to height ratio. The Process II events appear to have wider breaches on average compared to the Process I breaches and water reservoir dam breaches, and show greater scatter in the width to height ratio. More events need to be assessed to confirm these trends.

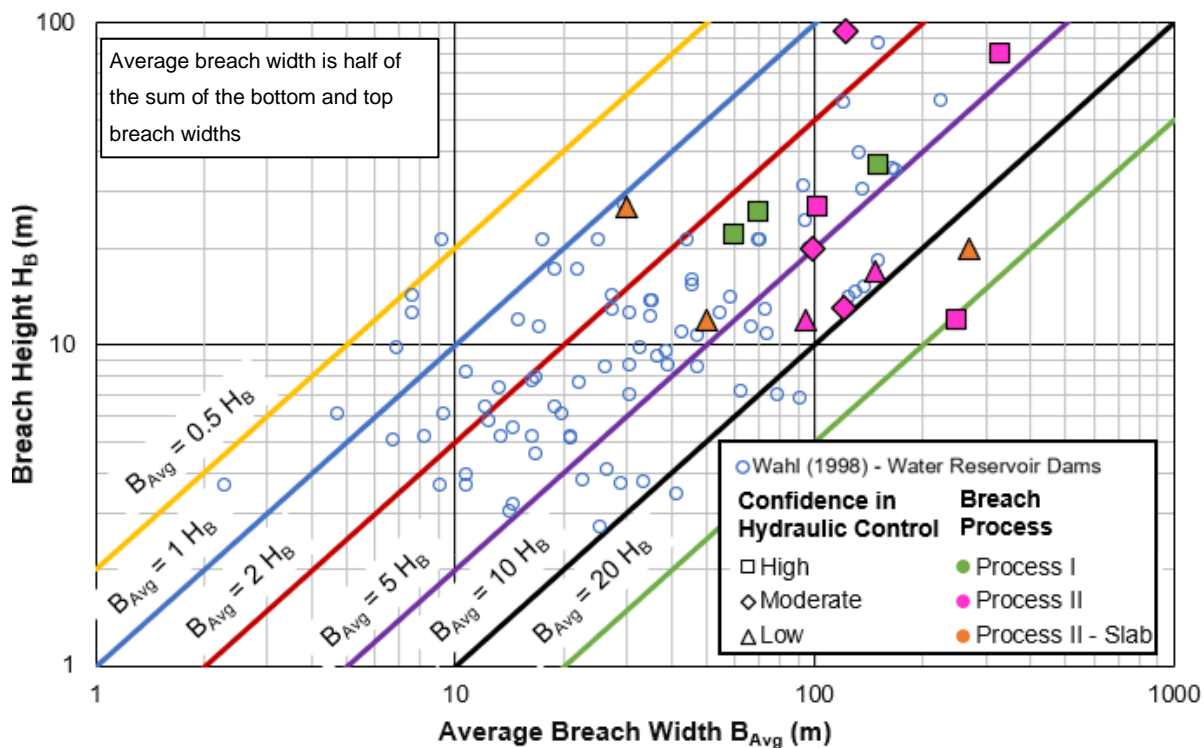


Figure 3.8 Observed Breach Heights and Widths Compared to Water Reservoir Dams (Data from Wahl, 1998)

In terms of a breach shape, approximating the breach geometry as a vertical trapezoid appears sufficient for most events. It is an approximation however, and is not ideal for all events (e.g., a U-shaped or compound shape breach). Pre- and post-failure survey information from site-specific surveys or using InSAR methodologies is useful for addressing these concerns, as they would eliminate the need for this approximation.

3.9.4 Event and Local Observations

Local observations came in many different forms and from different sources, therefore general comments are not fully applicable to all of them. Many of the reported local observations came from untrained observers, which limited their usefulness in model validation. Another major obstacle was that no location or time was associated with the observations for many cases, therefore they could not be used for model validation, regardless of their reliability. Overall, the uncertainty for the local observations is subjectively assessed to be as high as the uncertainty with outflow volumes, discussed in Section 3.9.1

Flow depth observations were the most common observations found and tended to contain enough evidence to be considered reliable. For example, a description of the

location and rough estimate of the peak flow depth accompanied by a photograph of the tailings stain height with some sense of scale at a given location was sufficient to be considered reliable. Arrival times were found to be one of the most valuable calibration constraints along with the Zone 1 inundation area (discussed in Chapter 4), so effort was made to compile as many arrival times as possible. Unfortunately, they were found to be far less reliable than depths.

The inundation areas directly impact the model calibration process, any uncertainty or error affects the modelled results. The following examples show the dual importance of using local observations for model calibration or validation, as noted by Ghahramani et al. (2022). Event and local observations used in model calibration require just as much effort to validate as any other model input.

The Kayakari event in Japan, 2011, was triggered by an earthquake of magnitude 9.0 (Ishihara et al., 2015) and had a Zone 1 inundation area of 150,000 m². A tsunami resulting from the earthquake then impacted the coast of Japan roughly 30 mins to an hour later, which was mapped by Matsuda et al. (2014). The tsunami was not considered by Ghahramani et al. (2020), which includes 86,000 m² of overlap of the tsunami impacted area with the tailings inundation area. Based on the available aerial imagery and terrain data, it was determined herein that 70,000 m² of the tailings inundation area should be removed and attributed primarily to the tsunami. Such a change would not materially affect the fitted trend lines in Ghahramani et al., but this difference did materially affect the modelling calibration process.

After the Feijão event in Brasil, 2019, the Brazilian Geological Survey reported a frontal arrival time at the Paraopeba River, some 9 km downstream of the Feijão TSF, of 30 mins. This was based on a hydrometric gauge that measured the filling of a “reservoir” behind the subsequent landslide dam in the Paraopeba River created by the tailings (CPRM, 2019). However, Lumbroso et al. (2021) instead relied on anecdotal reporting from a newspaper from China to support their numerical modelling in MIKE 21. The anecdotal reporting was not specific nor was any evidence included, but it was used to conclude the arrival time at the Paraopeba was between 1.5 hrs to 2 hrs. Their modelled arrival times were then labelled as “observed arrival times” in Gibson et al. (2022). Both had excellent areal match within what Ghahramani et al. (2020) mapped as the Zone 1 extent. Without the true arrival time to the Paraopeba River, their models have unintentionally deceptive good performance.

Chapter 4: Numerical Modelling with HEC-RAS

This chapter describes the approach taken for modelling the tailings dam breach and runout events in this thesis. The terrain data considerations are presented in Section 4.1. The general numerical modelling methodology is presented in Section 4.2. The rheology calibration process is discussed in Section 4.3. Finally, a discussion on the general findings is included in 4.4. Specific details and commentary on the modelling for each event are presented and discussed in Appendix B.

4.1 Terrain Data and Modifications

The terrain data used in this thesis consisted of a mix of publicly available and commercial data, in raster format. The public data were typically lower resolution (i.e., larger terrain cells) and were poorer quality, but can be obtained for no cost. The public data were either sourced from the relevant national geological survey agency or the ALOS World 3D – 30 m (AW3D30) from the Japan Aerospace Exploration Agency (JAXA) when no such national data were available. Other publicly available global terrain data (e.g., the Shuttle Radar Topography Mission, SRTM) were ultimately considered less appropriate for the runout modelling than the AW3D30 product. Both the AW3D30 and SRTM datasets are DSMs, and therefore introduce an error through inclusion of vegetation or other structures.

The commercial data was the Airbus Defense and Space WorldDEM DTM, purchased from third party providers for some events when the benefit of higher resolution and quality was deemed worth the monetary cost. The WorldDEM (12 m horizontal resolution) is stated to be a bare-earth dataset, which should be ideal for flood modelling (Meadows and Wilson, 2021). Newcrest Mining Limited provided digitized contours from the site-specific surveys for the Cadia Event. Terrain rasters were interpolated from the contour data for the modelling in this thesis.

The various terrain data sources and some of their characteristics are presented in Table A.9 in Appendix A. Most of the terrain datasets required some form of adjustment, and about half of them required substantial adjustments in the downstream environment. Meadows and Wilson (2021) note vertical errors are usually positive biased (i.e., the terrain data is above the true bare-earth elevation). This phenomenon was observed herein as well, with most of the modifications being removal of features within the terrain data to approximate bare-earth conditions. All terrain modifications were made with the

tools in HEC-RAS. The following subsections detail common types of modifications used, with specific dimensions and reasoning for each event included in Appendix B.

The modified terrain data have higher resolutions than the original data in the following figures for the example modifications. The modified regions typically used a finer resolution than the original or raw terrain data, as they often involved important features smaller in scale than the original resolution could physically represent. The upscaling occurred during the export of the modified terrain from HEC-RAS for mapping in external GIS software, as any exported data from HEC-RAS needs a consistent resolution. In the runout modelling, the original resolution is used for unmodified terrain data, while the finer resolution is used for the modified terrain. This variable terrain resolution is possible through the HEC-RAS sub-grid hydraulic calculation approach, discussed further in Section 4.3.

Breach Channels

The terrain data was surveyed prior to the breach or after remedial work for all events. Consequently, the breach channel was removed from the TSF to ensure the breach flow was realistically constrained proximal to the breach. Without starting the tailings runout in the HEC-RAS model at the dam crest with a breach channel, the tailings flow either would have to start at the dam toe or on top of the dam crest. These other options have little physical sense and result in the tailings flow spreading more than the observed inundation area, and therefore were not pursued.

The ‘Channel Modification’ tool in HEC-RAS was used for all breach channel modifications. The geometry for the breach channel (i.e., bottom width, side slopes, and height) was based on the breach geometry as discussed in Chapter 3, and then smoothly connected to the ground at the toe of the dam. Photographs and aerial imagery also qualitatively informed the breach channel modifications. The tailings dam had to be ‘built up’, to reach the elevation of the dam crest at the time of failure for some events. This was done with the ‘High Ground Modification’ tool, with the geometry (i.e., crest elevation and dam side slope) informed by any available academic literature or technical reporting. Evidently, the uncertainty and possible error in breach geometry would carry through to the breach channel modifications. Compared to the following terrain modification types, however, these modifications are considered more certain given how much effort was expended on investigating the breach geometry, as described in Chapter 3.

An example of a breach channel removal is shown in Figure 4.1, from the Feijão HEC-RAS model with the Airbus Defense and Space WorldDEM DTM. The contours from the modified terrain data are overlaid on the satellite imagery for comparison. The breach geometry was estimated from Robertson et al. (2019) and February 2019 satellite imagery from Google Earth (i.e., a week after the failure). Overall, this edit was considered to be relatively representative of the actual terrain surface post-failure and to have low uncertainty.

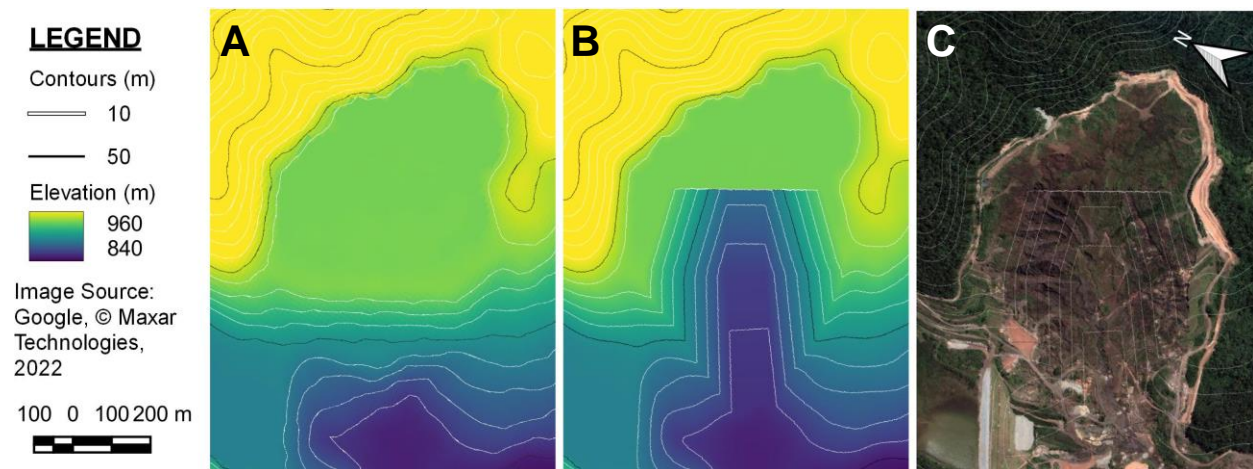


Figure 4.1 Example Breach Channel Modifications A) Terrain Data before Breach Channel Modifications, B) Terrain Data after Breach Channel Modifications, and C) Satellite Imagery for Comparison

River Channels

Many of the events ran out along river channels. These riparian areas may contain several features that require terrain data modification prior to runout modelling. The technologies used in global terrain datasets often cannot penetrate water, instead returning the elevation of the water surface (Meadows and Wilson, 2021). Depending on the flow capacity of the river relative to the flow of the tailings runout, this error may or may not be of consequence (Martin et al., 2022). River channels are often accompanied by vegetation of varying density. If the terrain data is a DSM rather than a DTM (i.e., bare-earth), the river thalweg may appear as a ridge rather than a low point as it should. When the river passes through a canyon section that is narrower than the resolution of the terrain data, the river may be artificially elevated to around the crest of the canyon, or even higher if vegetation overhangs the canyon. Bridges over rivers also appear as solid obstructions to flow in terrain data in raster format. The flow capacity is reduced or

obstructed, and the flow paths are erroneous in the terrain data compared to the real-world environment for these conditions.

A channel was cut into the terrain to remove all these different flow obstructions using the 'Channel Modification' tool in HEC-RAS. The alignment and linear extent (i.e., the distance along the centreline of the modification) of the channel removal was primarily informed by the terrain data itself. The river channel modifications followed the path of minimum elevation (i.e., the steepest path up and down the ridges or interference) within the terrain data until a local minimum was reached. The channel slope of the modifications was linear between the elevation of each local minimum. The geometry of the channel (i.e., width, depth, and side slopes) was estimated based on any available information, such as reported characteristics in literature, or visually estimated from satellite imagery.

Two examples of river channel removal are shown in Figures 4.2 and 4.3, from the Aznalcóllar and Fundão HEC-RAS models, respectively. The Aznalcóllar example shows riparian vegetation "speckles" all along the channel in the DTM05 terrain data from the National Geographic Institute of Spain. The DTM05 data was surveyed in 2019 and currently assessed as one of the higher quality public terrain data found. These speckles were removed, otherwise they slowed down the tailings flood wave front. The geometry of the channel was informed by commentary from Gallart et al. (1999) and 2003 satellite imagery from Google Earth (i.e., 5 years after the failure). The terrain data path, Gallart et al. and satellite imagery were in good agreement. The river channel modifications spanned the entire 40 km length of the HEC-RAS model domain for the Aznalcóllar event.

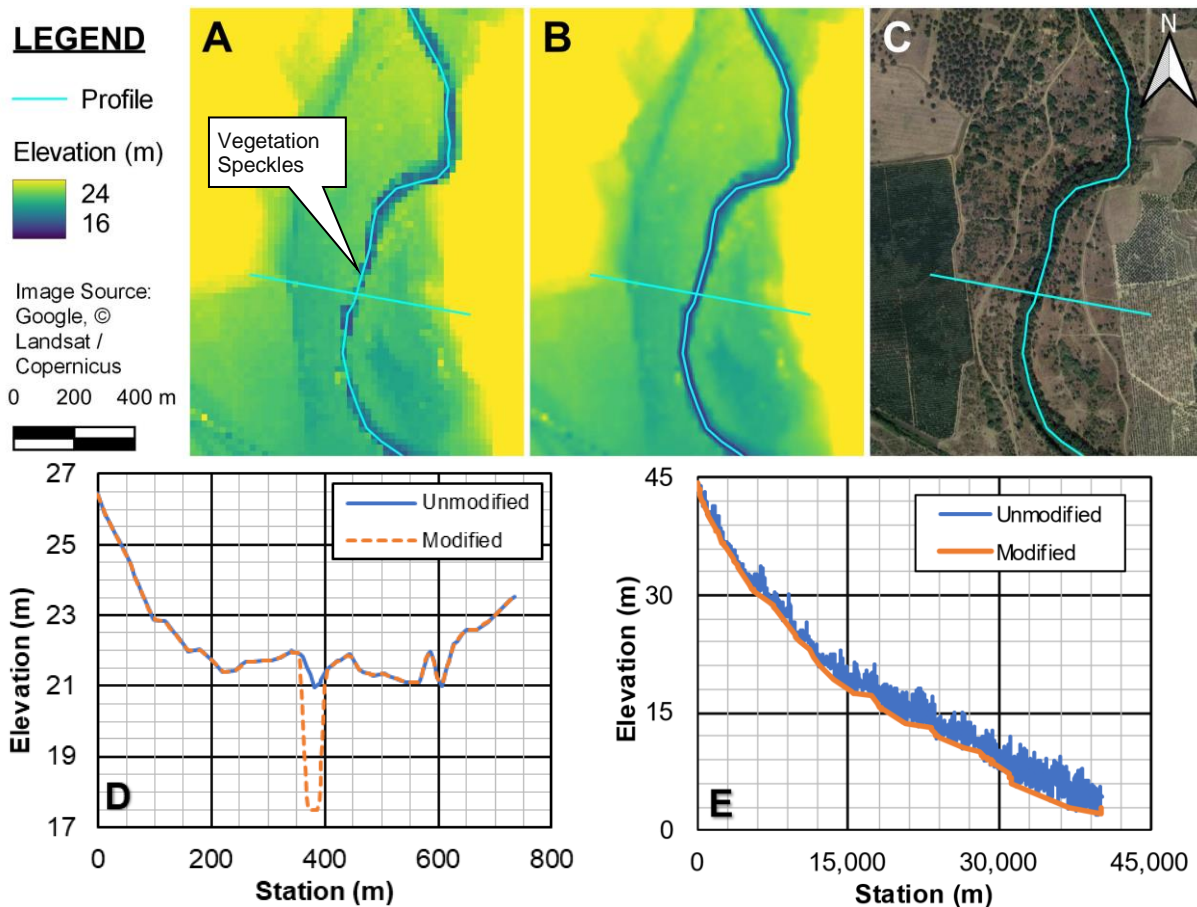


Figure 4.2 Example River Channel Removal A) Terrain Data before River Channel Modifications, B) Terrain Data after River Channel Modifications, C) Satellite Imagery for Comparison, D) Cross Section through the Floodplain, and E) Profile along the Entire River Channel

The Fundão example includes a narrow canyon section (approximately 6 m wide at the bottom based on satellite imagery) that was not captured by the AW3D30 terrain data (30 m horizontal resolution). In fact, the elevation at the canyon section is more than 30 m above the river upstream of the canyon, creating a saddle shape. Immediately downstream of this saddle, a foot bridge on the Estrada Real crosses the river as well, creating another ridge or saddle in the AW3D30 data 15 m above the channel. Satellite imagery does not align with the minimum elevation path in the terrain data; the satellite imagery was considered more reliable for this case. The geometry was assumed based solely on imagery, as no further information was found. The crudeness of these modifications was warranted to provide hydraulic connectivity, as these interferences prevented the simulated tailings runout from inundating some 330,000 m² observed to be impacted by the actual tailings runout upstream of the foot bridge and canyon.

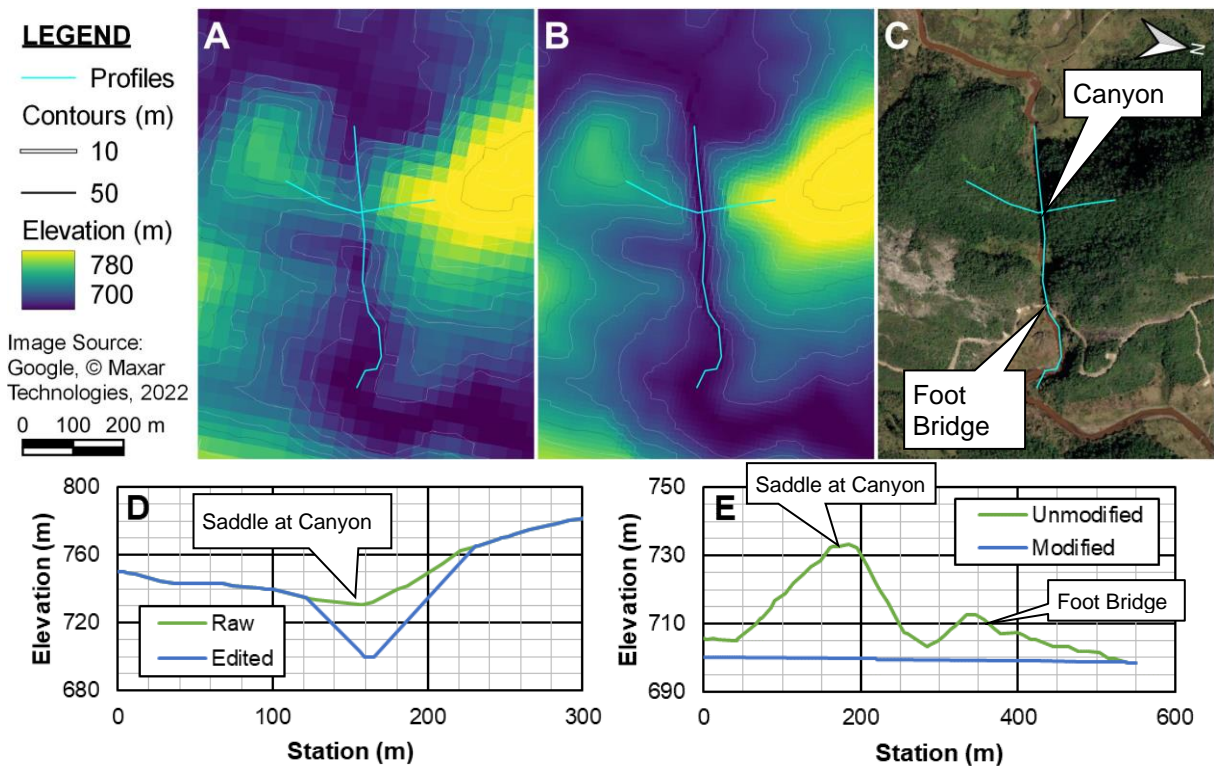


Figure 4.3 Example River Channel Removal A) Terrain Data before River Channel Modifications, B) Terrain Data after River Channel Modifications, C) Satellite Imagery for Comparison, D) Cross Section at the Canyon, and E) Profile along the River Channel at the Canyon

Berms

Occasionally berms, roadways, or other constructed ridges in the terrain were observed in satellite imagery, but not within the terrain data. Like the rivers in canyon sections, these linear features are smaller in scale (i.e., narrower) than the resolution of the terrain data, but can still affect the flow path or flow capacity. The approach to the terrain modifications to add roadways or berms was identical to the river channel modifications, however, the geometry modifications were made with the 'High Ground Modification' tool in HEC-RAS.

An example of a berm addition is shown in Figure 4.4, from the Tonglūshan HEC-RAS model with the Airbus Defense and Space WorldDEM DTM. The contours from the modified terrain data are overlayed on the satellite imagery for comparison. The berm geometry was assumed based solely on imagery, as no further information was found. The crudeness of these modifications was warranted, as the berms partially confined the tailings runout (Ghahramani et al. 2020; Rana et al., 2021b) and were found to be important in the HEC-RAS model herein as well.

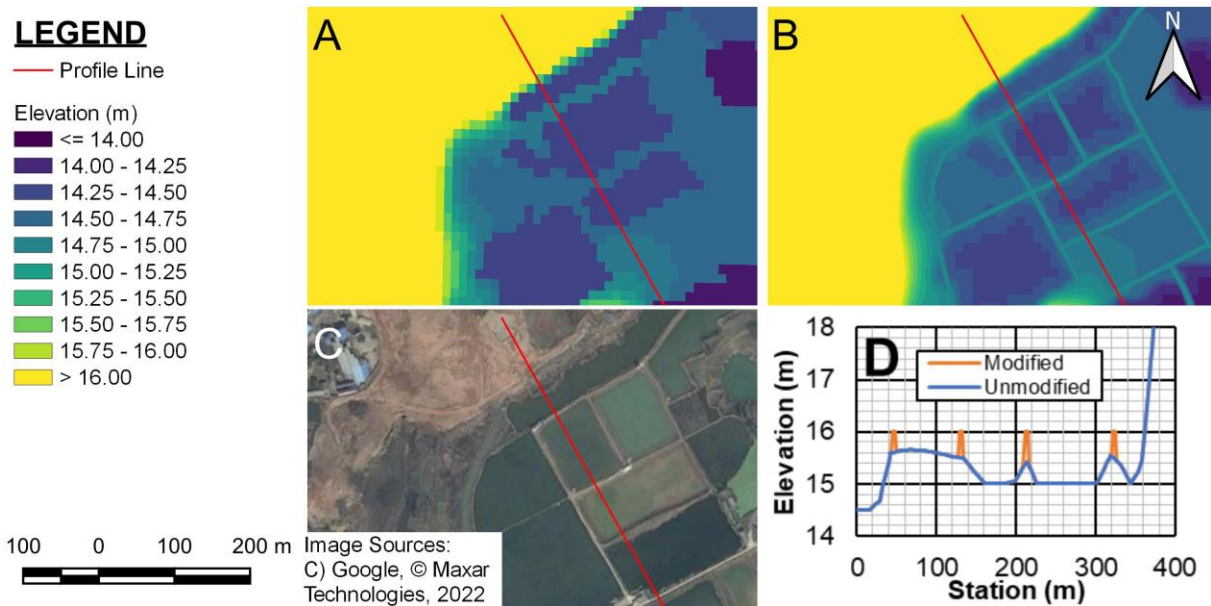


Figure 4.4 Example Berm Addition A) Terrain Data before Berm Edits, B) Terrain Data after Berm Modifications, C) Satellite Imagery for Comparison, and D) Profile through Berm Modifications

Artefacts

Large regions of terrain data estimated to be affected by artefacts (i.e., errors or irregularities) or vegetation (i.e., with a DSM) in amorphous areas affected the tailings flows but required a different approach than the linear modifications previously described. The 'Polygon Modification' tool in HEC-RAS was sufficient to remove the artefacts from the terrain by interpolating a surface inside a polygon surrounding the artefacts. When the surface underlying the artefact was believed to be non-monotonic (i.e., it could not be represented by linear interpolation), contours were manually drawn and a raster produced from the altered contours for the area requiring modification.

An example of an artefact removal is shown in Figure 4.5, from the Cadia North TSF Event II HEC-RAS model with the terrain data derived from the aerial surveys provided by Newcrest Mining Ltd. A polygon was used to smooth the irregularities in the Cadia South TSF supernatant pond and achieve a level surface. The contours from the modified terrain are shown on the satellite imagery in Figure 4.5C for comparison. The modified terrain, while not representative of the actual surface under the Cadia South TSF supernatant pond, did not interrupt the tailings runout like the original terrain data.

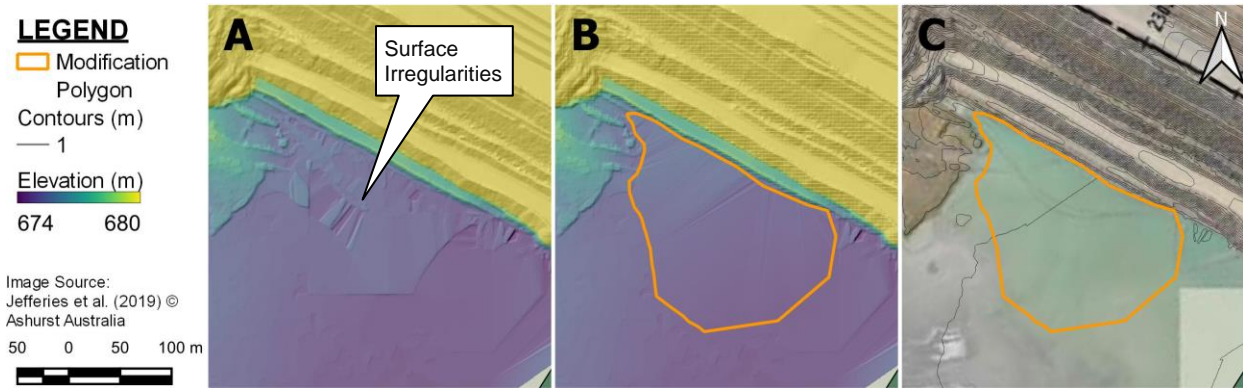


Figure 4.5 Example Artefact Removal A) Terrain Data before Artefact Removal, B) Terrain Data after Artefact Removal, and C) Aerial Imagery from March 10th, 2018, for Comparison

4.2 Parametric Breach Modelling

The parametric breach method was selected for the modelling of all events. The parametric breach method is well-utilized in water dam breach studies to develop the breach hydrograph (Wahl, 1998; Wahl, 2004; Froehlich, 2008; Goodell et al., 2018). As preliminary work for this thesis, Adria et al. (2021) applied the parametric approach to the Harmony 4A event. The authors concluded that the parametric breach approach was flexible for the different breaches in Rana et al. (2021b). Furthermore, the comparatively low input requirements for the parametric approach is suitable for the limited reporting available for most events.

Adria et al. (2022) continued the assessment of the parametric breach method, using for the 2014 Mount Polley event in Canada and the 2019 Feijão event in Brasil as case studies. They compared the modelled hydrograph to timing of flow characteristics observed at those events. The Mount Polley event was a Process I breach with a large supernatant pond that eroded the tailings. The Feijão event was a Process II breach with liquefied tailings and no supernatant pond. These events were selected for their relatively high degree of reporting and to assess the parametric breach method against varied and dissimilar scenarios. The following subsection includes portions of Adria et al. (2022).

4.2.1 Breach Weir Components

The parametric breach method dynamically computes the breach discharge using the common weir equation, where the weir is increasing in size in time. Walder et al. (2015) define the general weir equation as shown in Equation 4.1:

$$Q = C_w B H^{3/2} \quad (4.1)$$

where Q is the flow, C_W is the weir coefficient, B is the weir width, and H is the total head. Each variable is discussed in the following subsections. As variables are changing in time as the breach forms and the outflow volume discharges, the subscript i is used to denote the transient value for each variable at time t_i . Process II breaches are treated as instantly fully formed breaches in this thesis. In such events, the breach width and breach height are fully formed and do not have a transient value.

Weir Coefficient

The weir coefficient, C_W accounts for roughness, turbulence losses, and non-hydrostatic effects (Chanson, 2004). It is dependent on flow conditions and the shape of the weir (Chanson, 2004). A broad crested weir is commonly used for breach modelling (Brunner, 2014) and the weir coefficient is defined using Equation 4.2 for broad crested weirs (Chanson, 2004):

$$C_W = \frac{2}{3} C_D \sqrt{\frac{2}{3} g} \quad (4.2)$$

where C_D is the discharge coefficient (unitless), and g is the acceleration due to Earth's gravity.

The C_D is typically taken as 1 for a steady state, well defined smooth weir, resulting in a C_W of $1.70 \text{ m}^{1/2}/\text{s}$ (Chanson, 2004; Brunner, 2020). As a breach is not steady, turbulent, and hydraulically inefficient, the C_D is commonly assumed to be lower than for a steady state, smooth weir (Brunner, 2014). The C_W for a breach conceptually can slightly vary over time as flow conditions change, however a prediction of the magnitude and timing of this variation in the value of C_W is difficult to predict (Brunner, 2014). Khahledi et al. (2015) assessed weir coefficients for non-Newtonian fluids, specifically including kaolin and bentonite mining slurries. They found the non-Newtonian fluids to have coefficients similar to that of water. The experiments were performed under steady-state flow conditions, using flume set-ups similar to constructed weirs and fluids with low yield stresses and viscosities, unlike those of typical tailings deposits in TSFs. Consequently, it is not clear if the conclusions are applicable to tailings dam breaches with higher yield stresses and viscosities.

A C_D between 0.65 and 0.97 has been found to be appropriate for erosional breaches of water reservoir dams (Goodell & Brunner, 2012; Brunner, 2014) using the parametric breach approach. Walsh (2019) conducted laboratory scale overtopping breaches of downstream dams with a shallow sloping beach to represent a TSF breach.

Walsh found a C_D of 0.96 to 0.98 performed well for the elliptical breach weir geometry they considered. While the findings from Walsh are in the same range as the guidance from Goodell & Brunner and Brunner, the elliptical weir is upstream of the vertical weir considered here and would not include some of the losses mentioned by Brunner (2014).

Process II breaches occur on a much shorter scale than the Process I and are therefore more chaotic and hydraulically inefficient. Ritter (1892) derived an analytical set of equations for a perfectly instantaneous breach, ignoring frictional and turbulence losses in the downstream environment. The Ritter equations can be reduced to the same form as the weir equation, with a C_D of 0.54 (i.e., a C_W of $0.928 \text{ m}^{1/2}/\text{s}$). Despite valid criticism that ignoring the losses in the analytic solution overpredicts the leading edge of the outflow in the downstream environment, the Ritter equations match experimental results closely at the location of the instantaneous breach (Schoklitsch, 1917; Arbutnot and Strange, 1960, Froehlich, 2016).

Adria et al. (2022) found that values of $1.44 \text{ m}^{1/2}/\text{s}$ and $0.928 \text{ m}^{1/2}/\text{s}$ for the C_W performed satisfactory for the Mount Polley and Feijão events respectively (corresponding to a C_D of 0.84 and 0.54, respectively). The C_W is also currently limited to a constant value in HEC-RAS. Consequently, the modelling for the Process I events used a constant C_W of $1.44 \text{ m}^{1/2}/\text{s}$ and the modelling for the Process II events used a constant C_W of $0.928 \text{ m}^{1/2}/\text{s}$ to be in line with the findings in Adria et al. and the current limitations in HEC-RAS.

Weir Width

To adapt a uniform width to the variable width for the trapezoid in the parametric breach method, a representative width B_* can be analytically determined through integrating Bernoulli's equation across a trapezoidal width section (Froehlich, 2016), represented in Equation 4.3:

$$B_* = \frac{3}{5} b_{Bi} + \frac{2}{5} b_{Ti} \quad (4.3)$$

where b_{Bi} is the transient bottom breach width and b_{Ti} is the transient top breach width. The b_{Bi} depends on the breach progression, as defined in Equations 4.4 and 4.5:

$$\beta_H = \begin{cases} t_i/T_f & t_i \leq T_f \\ 1 & t_i > T_f \end{cases} \quad (4.4)$$

$$b_{Bi} = \beta_H B_B \quad (4.5)$$

where β_H is the horizontal breach progression parameter (unitless) and T_f is the formation time. The form for the breach progression shown in Equation 4.4 is linear. Brunner (2014) also proposed a sine-curve for the progression, which is included in HEC-RAS, and Froehlich (2008) noted other breach progressions can be hypothesized. Walsh (2019) observed linear breach width growth in laboratory-scale erosional breaches of tailings dams. Consequently, a linear progression was adopted for Process I breaches. Process II breaches are instantaneous, and therefore do not consider any progression curve. The breach width progression is shown in a cross section schematic in Figure 4.6. The transient top breach width is calculated according to Equation 4.6:

$$b_{Ti} = b_{Bi} + (Z_R + Z_L) d_i \quad (4.6)$$

where Z_R and Z_L are the left and right breach side slopes and d_i is the breach flow depth. The flow depth is calculated in the HEC-RAS model and is addressed in the following subsection.

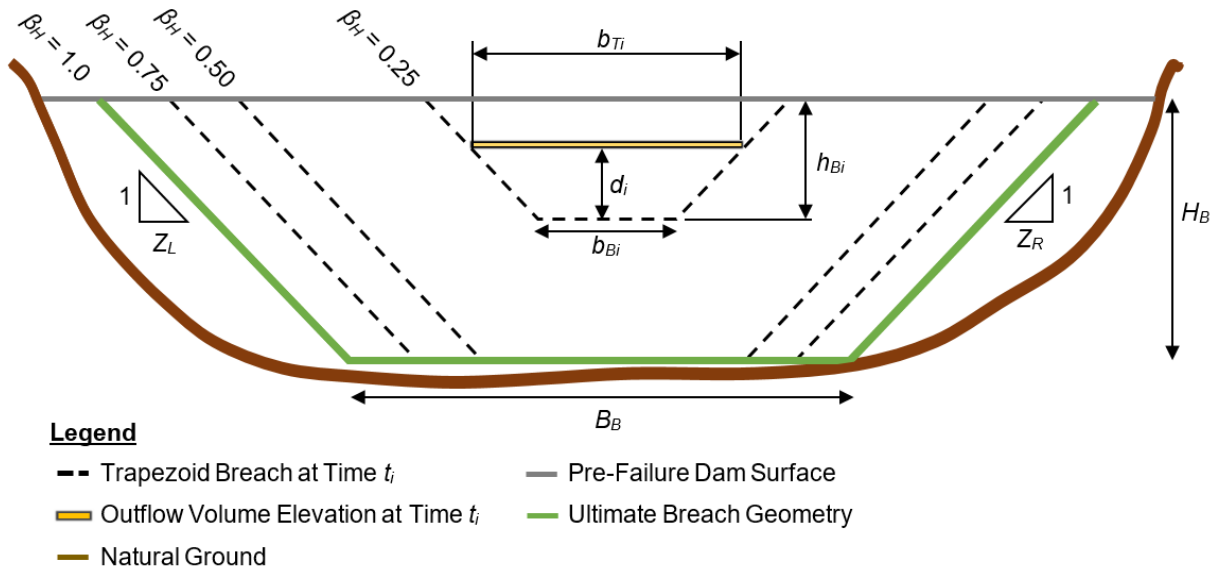


Figure 4.6 Breach Width Progression Schematic in HEC-RAS

Total Head

The total head H is derived from the Navier-Stokes equations for fluid flow. Chanson (2004) defines the total head with Equation 4.7:

$$H = \frac{v^2}{2g} + Z + D + \frac{P}{\rho_m g} \quad (4.7)$$

where v is the flow velocity, g is the acceleration due to gravity, Z is the elevation of the channel bottom of the flow compared to a specified datum, D is the depth of flow above the invert, P is the pressure at the free surface of the fluid, and ρ_m is the density of the

fluid. The specified datum in this case is the breach invert. The pressure is often ignored, as the atmospheric pressure is constant between upstream and downstream of a weir (Chanson, 2004).

The velocity can be approximated by assuming or estimating a Froude number, as in Walsh et al. (2021). Alternatively, the velocity can be ignored by considering the elevation of the fluid upstream of the breach and within the facility as wholly representative of the total head (Chanson, 2004). Total head in a hydraulic system is constant, except for head losses. Head losses are assumed to be low upstream of a hydraulic control, therefore the total head at the breach weir can be approximated with the maximum elevation in the reservoir or facility, when the velocity is near zero (Chanson, 2004). Downstream of the breach weir, head losses are larger and need to be accounted for. These head losses and the total head are calculated by the two-dimensional hydraulic modelling in HEC-RAS, discussed in Section 4.3.

The flow depth and breach invert elevation are both changing over time during a breach and tracked within the HEC-RAS model; it is more convenient to redefine the datum to be transient and located at the breach channel invert elevation. In that case, the total head is expressed only in terms of transient flow depth d_i over the breach invert at time t_i . The transient breach height is determined using Equation 4.8:

$$h_{Bi} = \beta_V \beta_H \frac{H_B}{B_B} \quad (4.8)$$

where β_V is the vertical breach progression parameter (unitless), with the remaining variables previously defined. Froehlich (2008) notes that scale experiments and observations of real water reservoir dam breach events indicate the horizontal and vertical growth of the breach are the same, therefore the β_V was set as 1. The h_{Bi} and the d_i are shown in Figure 4.6, as well as in a profile schematic in Figure 4.7. As the B_B is twice the H_B in the example in Figure 4.6, when the β_V is 1, the h_{Bi} reaches the H_B when the b_{Bi} is half of the B_B . By the same reasoning, a breach that is four times as wide as it is tall will reach the ultimate breach height as the transient breach bottom width is a quarter of the ultimate bottom reach width if the β_V is 1.

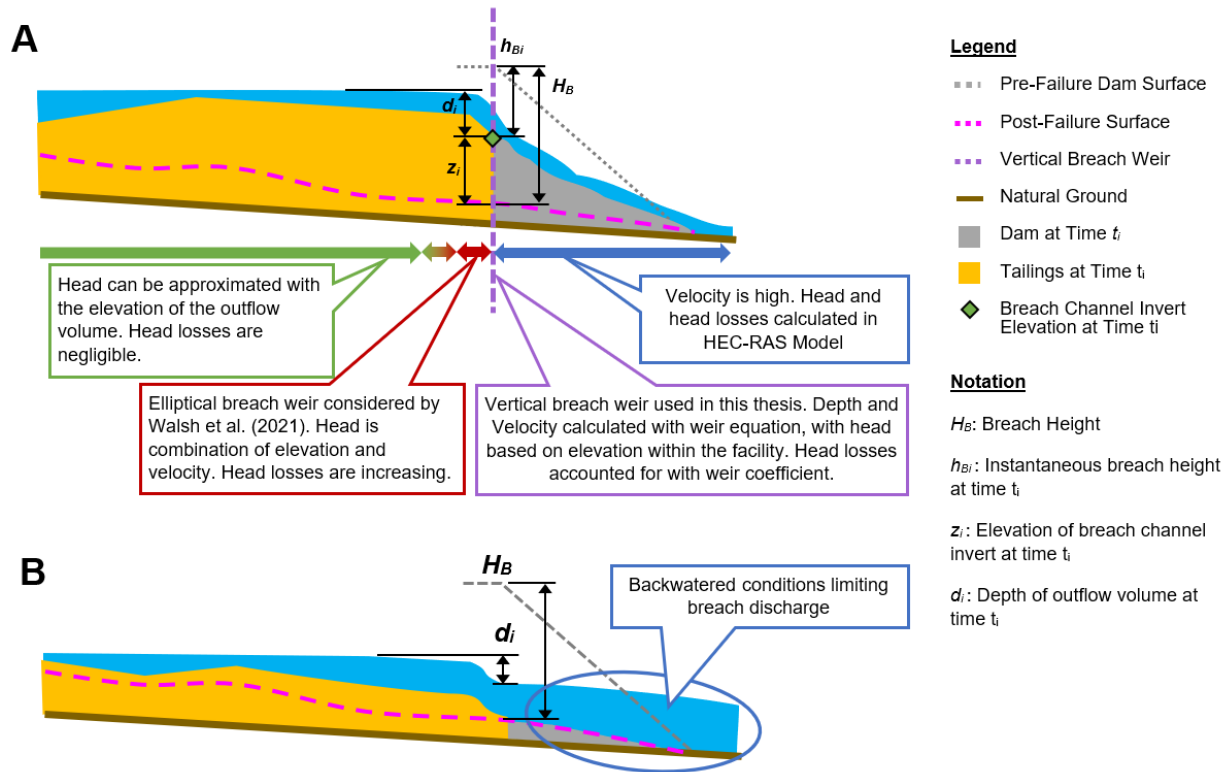


Figure 4.7 A) Breach Head Profile Schematic, and B) Breach Head during Submerged Outflow

If the tailwater is submerged for any reason (e.g., as noted by Walsh et al. (2021) or Martin et al., 2022), the discharge decreases. HEC-RAS accounts for this effect by using the higher of the transient breach invert elevation or the downstream flow elevation as the datum to determine the total head. This is shown visually in Figure 4.7B.

4.2.2 Stage-Storage Curves

The outflow volume upstream of the breach can be included in a one-dimensional or two-dimensional numerical model, bypassing some of the assumed conditions described in Section 4.2.1. The flow depth and velocity are iteratively calculated throughout the TSF as it discharges through the parametric breach weir. This is known as dynamic routing (Goodell & Wahlin, 2009). Alternatively, the outflow volume can be abstracted as a single curve where the relationship between the cumulative outflow volume and elevation is used to determine the elevation used in the breach weir calculation. This relationship is known as a stage-storage or elevation-volume curve (Goodell & Wahlin, 2009; Schoeman, 2018; Adria et al., 2022).

The dynamic routing approach is held to be more accurate, but the stage-storage curve simplification is attractive for several reasons (Goodell & Wahlin, 2009). The

abstraction of the three-dimensional shape of the initial condition of the outflow into a two-dimensional curve removes the need for conservation equations of momentum and mass, greatly decreasing the computational requirement. With a stage-storage curve, the parametric breach method could be used thousands of times in Monte Carlo analysis within a short time frame (Goodell, 2013) or even be implemented in a spreadsheet software without any model software. The dynamic routing approach also requires terrain data with the post-failure surface, while the stage-storage curve can be generated with idealized geometry. To date, no post-failure survey data for tailings dam breach events are publicly available. Ghahramani et al. (2022) approximated the post-failure surface for the Prestavèl and Harmony 4A events. This approximation is not trivial nor possible for other events with limited reporting. Considering the effort required to develop an idealized and approximate surface in the terrain for twelve events and the uncertainty of using such idealized geometry in dynamic routing, the stage-storage curve approach was adopted in this thesis.

To generate a stage-storage curve, the outflow volume is sliced horizontally at discrete elevations, the volume between each slice is determined as the product of the elevation interval and the slice area, and then the inter-slice volume is cumulatively summed. It can be derived from an idealized shape approximating the outflow reservoir (e.g., Walder & O'Connor, 1997) or a bespoke curve can be calculated from real, irregular post-failure terrain data, if such data exists. The process is shown schematically in Figure 4.8 for an outflow volume idealized as a semi cone, a common assumption in TDBAs (CDA, 2021). A semi cone and other three dimensional shapes are shown in Figure 4.9A. All shapes share a height of 5 m and are limited to be within an arbitrary boundary of 20 m by 10 m. The general form of the stage-storage curve for each idealized shape is shown in Figure 4.9B, where the curves are expressed in relative terms. The semi-cone, tetrahedron and funnel have the same mathematical form and are represented with a single curve shape in Figure 4.9B. Each shape has a different total volume within the same boundary. Figure 4.9C shows the actual stage-storage curve for each shape, demonstrating the difference in shape and volume for all the shapes. The red faces in Figure 4.9A would be against the breached section and the coloured faces serve to identify the shapes with the corresponding coloured curves in Figure 4.9C.

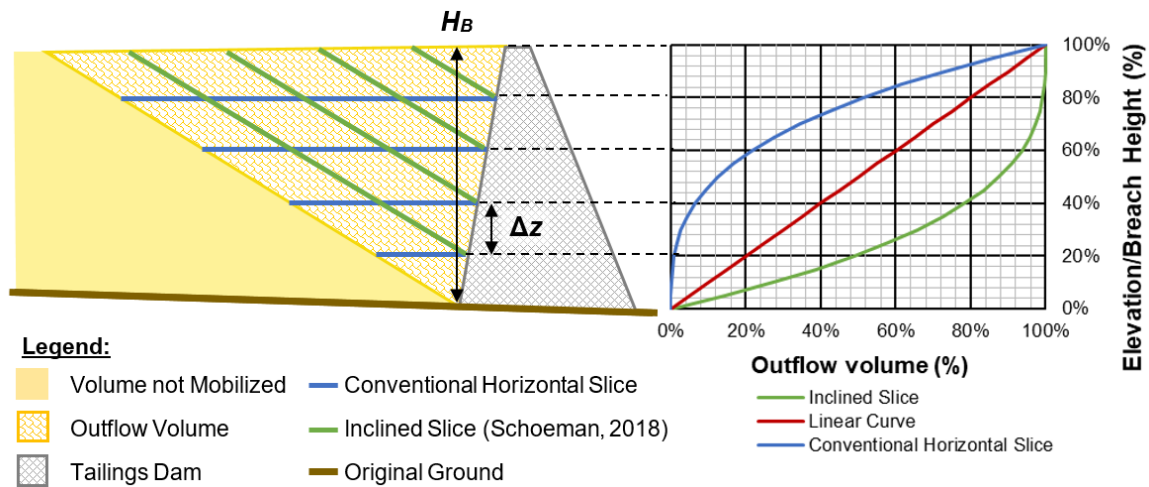


Figure 4.8 Conventional Horizontal Slice and Inclined Slice Method for Stage-Storage Curves (Adapted from Schoeman, 2018)

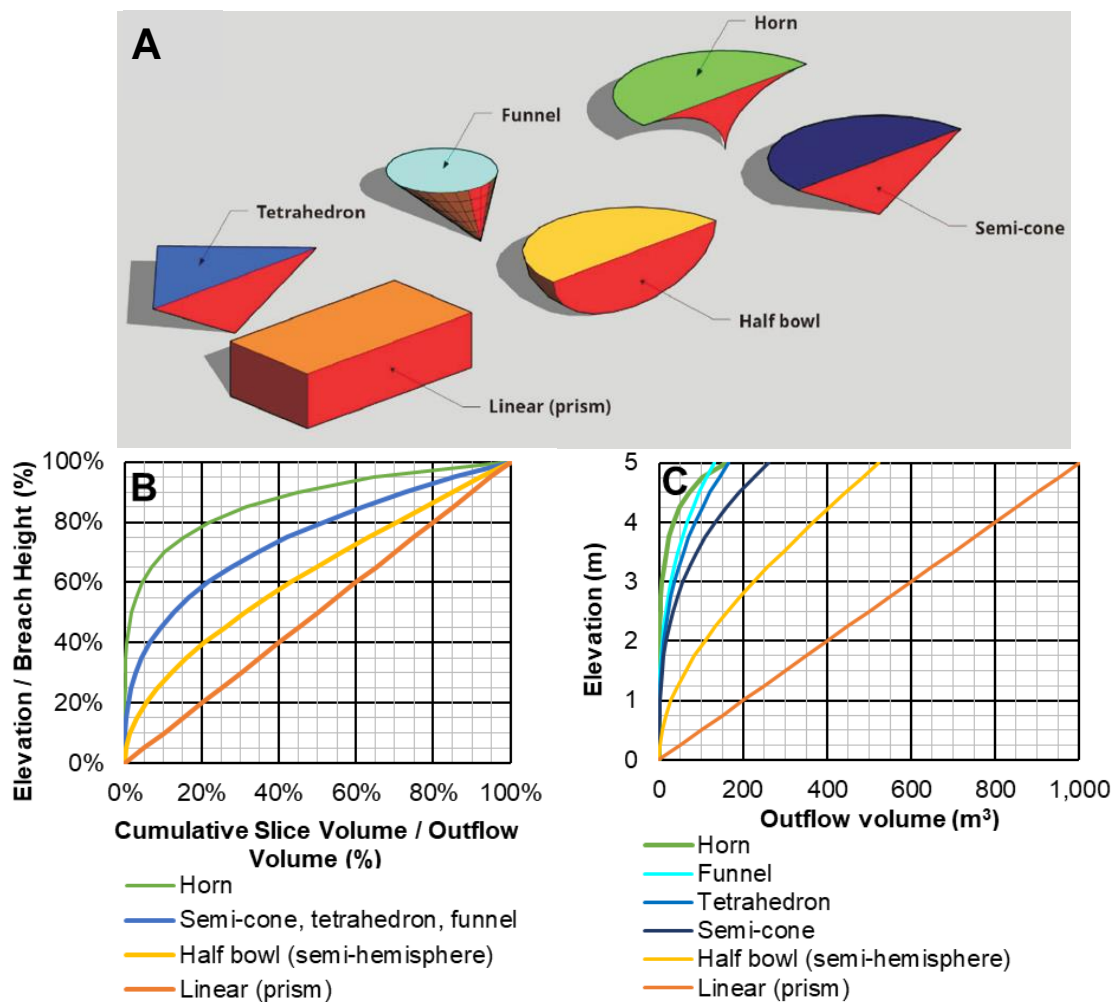


Figure 4.9 A) Six Idealized Shapes for the Outflow Volume During a Tailings Dam Breach B) Stage-Storage Curves for Idealized Shapes in Relative Values, and C) Stage-Storage Curves for the Idealized Shapes in Real Values (Adapted from Adria et al., 2022).

A downside to the stage-storage curve is the implication that the volume upstream of the breach has a level surface during the entirety of the breach (i.e., level-pool routing). As evident by non-level post-failure residual slopes in TSFs, such an assumption is difficult to justify for tailings dam breach modelling. Schoeman (2018) presented an alternative stage-storage method specifically for tailings-dam breaches, termed the 'inclined slice method'. With any continuous and idealized shape, the volume is sliced at equal intervals at an angle equal to the residual slope of the tailings; the difference in volume between any two elevation intervals represents the volume for that elevation slice. The cumulative volume for all slices is summed just as with the conventional method. The inclined slice process is shown in Figure 4.8 for the same semi cone. A linear stage-storage relationship is also shown, as it is the simplest form to represent the outflow volume across the vertical extent of the breach height.

The inclined slice principle applies to other shapes, where the slices are taken as a smaller but congruent version of the final failure surface (Schoeman, 2018). A hybrid approach can also be used where the tailings portion of the outflow volume is represented with an inclined slice stage-storage curve, while the supernatant pond portion is represented by a conventional horizontal stage-storage curve (Schoeman, 2018; CDA 2019b). According to Schoeman, the inclined nature intuitively represents a more realistic representation of the flow of tailings mobilized due to erosion or slumping during a tailings-dam breach.

Adria et al (2022) found that the inclined slice method proposed by Schoeman (2018) had some merit for the Mount Polley event. The conventional curve fully discharged the entire outflow volume almost 12 hours before the observed flow cessation. The alternative stage-storage curves considered, including the inclined slice, a hybrid curve, and a linear relationship, all matched the timeline of the breach much better. On the other hand, Adria et al. found that the conventional horizontal slice stage-storage curve used in the Feijão breach hydrograph matched the timeline for that event better than the inclined slice or linear relationships.

The modelling for the Process I events used a linear stage-storage relationship and the modelling for the Process II events used an horizontal slice stage-storage curve with an idealized semi-cone shape based on the findings in Adria et al. (2022). The generalized form of the cumulative volume (v_i) at a given elevation above the breach invert elevation is shown in Equation 4.9:

$$v_i = (V_S + V_I + V_P) * \left(\frac{z_i}{H_B}\right)^{n_s} \quad (4.9)$$

where V_S is the tailings solids volume, V_I is the interstitial water volume, V_P is the supernatant pond volume, H_B is the breach height, z_i is the breach elevation, and n_s is the shape factor. The shape factor is 1 for a linear relationship and 3 for a semi-cone relationship (Walder & O'Connor, 1997). A linear form was used for the Process I breaches rather than a hybrid or inclined slice approach as the level of reporting was insufficient for other Process I events to support the development of a stage-storage curve more complex than a linear relationship.

4.3 Tailings Dam Breach Modelling with HEC-RAS

The following subsections primarily detail the general HEC-RAS model set-up choices and procedures used in this thesis. The theoretical basis and model components of HEC-RAS are mentioned as relevant herein, but a full discussion of such matters is left to the HEC-RAS User Manuals and Tutorials. Specific details on each HEC-RAS model for individual events are included in Appendix B. Recommendations for future model improvements are summarized in Table A.10 in Appendix A, with further elaboration in Appendix B for each modelled event.

4.3.1 Overview of HEC-RAS and Modelling Approach

The Hydrologic Engineering Center's River Analysis System (HEC-RAS) is a software suite widely used across global jurisdictions for water resource engineering and open-channel hydraulic analysis (Gibson et al., 2021; Adria et al., 2021; Gibson et al., 2022). As a product of the US Army Corps of Engineers (USACE), it is maintained and updated with new features and publicly available without restriction. HEC-RAS has a range of features, including: 1D, 2D (depth averaged flow), or 1D-2D hybrid flow; dam breach modelling; sediment transport and water quality analyses; and mapping, plotting, and animation tools (Brunner, 2020). HEC-RAS is downloaded 100,000 times per year over 200 countries and is recognized in the emergency management landscape, particularly for flood risk management (Gibson et al. 2022). HEC-RAS was previously limited to Newtonian flow (i.e., water below 20% to 30% volumetric solids concentration), which would not be appropriate for flow containing substantial solid volumes, commonly observed in tailings dam breaches. In June 2021, HEC-RAS 6.0 was released, which

included common rheological formulations for single fluid flow (Gibson et al., 2021) and terrain modification options (see Section 4.1).

The intent of this thesis is to provide a database of tailings dam breach characteristics and numerical modelling advice for TDBAs agnostic of any numerical model software. A single software was used, however, for practical reasons, and therefore the database is not strictly agnostic of numerical model software. HEC-RAS (ver. 6.1) was selected as the numerical model in this thesis for several reasons: the high existing use in flood risk management, public availability, and the diversity of features in the software.

All runout modelling for this thesis was completed in two-dimensions (i.e., depth-averaged) with the shallow water equations (SWEs) and fixed-bed terrain. HEC-RAS employs an Eulerian-Lagrangian method and a finite-volume approximation for the volume and momentum continuity equations in the SWEs. HEC-RAS also offers a simpler set of equations, the Diffusion Wave Equations (DWEs), which are much faster and less prone to numerical instability at the expense of ignoring some temporal and spatial acceleration (Gibson et al., 2021). The results based on the DWEs were shown by Gibson et al. (2022) to not differ substantially from the results using the SWEs for a back-analysis of the Feijão event. Regardless, the more numerically accurate SWEs were used for all events in this thesis.

4.3.2 HEC-RAS Modelling Set-Up

The HEC-RAS model set-up for each of the events was relatively standard between each event once the breach characteristics were identified (see Chapter 3) and terrain modifications were completed (See Section 4.1). The modelling methodology is described in a linear sequence herein, however, the numerical modelling involved troubleshooting and iterations throughout the process. The iterations were generally minor refinements of the model components. Major and unique changes are discussed in Section 4.5. Some model troubleshooting also resulted in a revisit of the investigations (see Chapter 3) or terrain modifications (see Section 4.1). An example of the HEC-RAS model elements from the Feijão model is shown in Figure 4.10. The model elements shown are common to the majority of the models for each event in this thesis.

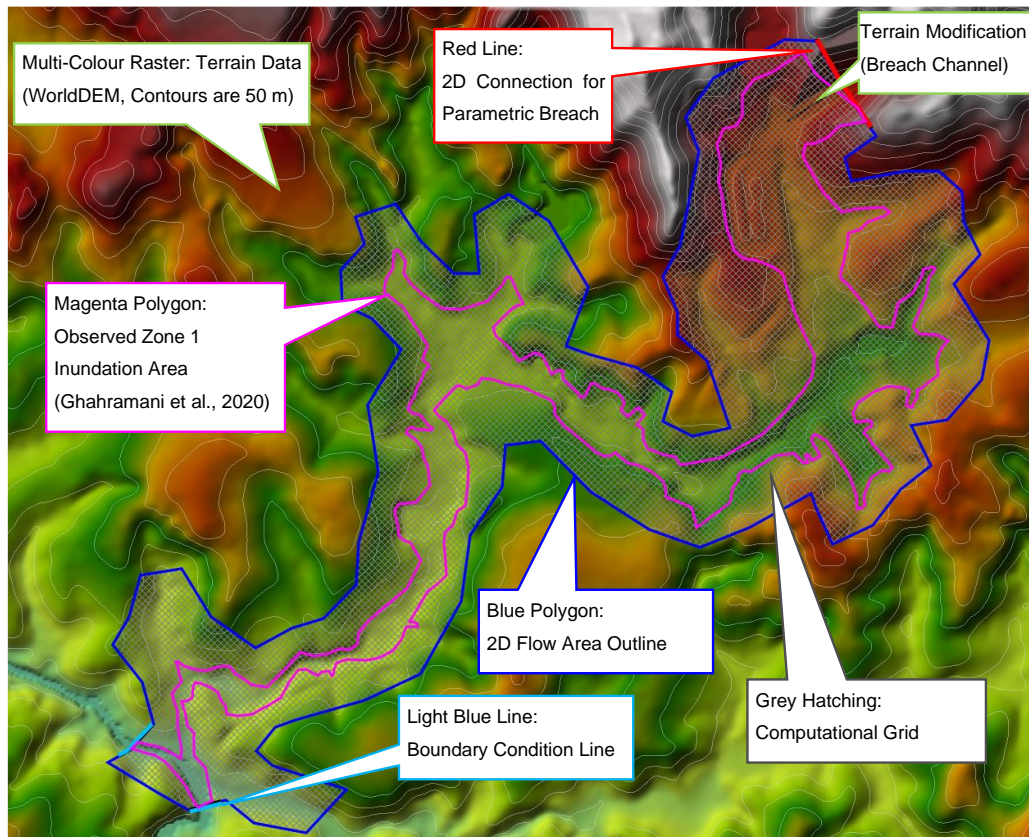


Figure 4.10 Example HEC-RAS Model Set-Up and Model Elements

HEC-RAS Geometry Data

The HEC-RAS Geometry establishes the spatial locations of various elements and is not related to the breach geometry. First, the parametric breach elements are added. The stage-storage curve (discussed in Section 4.2.2) is input in the HEC-RAS model as a “Storage Area” component at the TSF upstream of the dam crest. A “2D Connection” is drawn in line with the dam crest, which represents the dam prior to the breach. The 2D Connection situates the hydraulic control, and therefore the 2D Connection must be accurately aligned to the estimated hydraulic control for the actual event. The Storage Area for the stage-storage curve does not have to be reflective of where the actual outflow volume originated, as it is coupled to the 2D Connection in HEC-RAS.

A single ‘2D Flow Area’ was drawn around the Zone 1 inundation area shapefile (as mapped by Ghahramani et al. 2020). The 2D Flow Area is where the tailings runoff is modelled with the SWEs by HEC-RAS. The boundary of the 2D Flow Area acts as a slip boundary, (i.e., an infinitely tall frictionless wall), therefore the boundary is placed far enough from the flow paths under all model troubleshooting and rheology calibration

scenarios. For events where all tailings runout ceased and deposited within the Zone 1 impact area (i.e., an event without a Zone 2 impact area, as defined by Ghahramani et al., 2020), no further elements are needed in the HEC-RAS Geometry. A “Boundary Condition Line” is added to the extent of the 2D Flow Area for events where the tailings runout transitioned to bankfull flow within a river (i.e., an event with a Zone 2 impact area). The Boundary Condition Line acts as a sink, as it allows flow to exit the 2D Flow Area under predefined conditions (see the Unsteady Flow Data subsection).

Within the 2D Flow Area, HEC-RAS performs the hydraulic calculations at regular intervals, which is known as the computational grid. HEC-RAS has two grid features that warrant discussion: sub-grids and unstructured grids. A sub-grid represents the terrain in a cell with a miniature stage-storage curve and the terrain at cell faces is represented with a rating curve. The computational grid can be simultaneously structured or unstructured in HEC-RAS. A structured grid consists of a constant interval and shape (e.g., a square or triangle). An unstructured grid can have varying intervals, shapes, and number of vertices for each cell. Structured grids are desirable for computational simplicity (i.e., to reduce computation time), while unstructured grids can be used to better represent certain terrain features (e.g., a meandering river). The computational grid in HEC-RAS is structured by default, but “Breaklines” can be used to create sections of unstructured grids. Breaklines enforce cell boundaries that occur at important terrain features that may be smaller than the computational grid. “Refinement Regions” can be used to create a grid-within-a-grid of a different computational grid resolution. Refinement Regions also act as polygonal Breaklines. These model elements and the sub-grid approach allows for coarser cell resolutions to be used (and therefore reducing computation time) while maintaining the detail of the underlying terrain data.

A few rules of thumb were considered to inform the baseline resolution of the computational grid. Informal guidance typically recommends around 6 cells per flow width (Brunner, 2020; Forest & Brunner, 2020), which was followed here at a minimum. The flow width occasionally varied quite a bit, so the narrowest section of the Zone 1 inundation was used as the governing flow width. Alternatively, Refinement Regions were employed with a finer resolution to prevent excessively fine resolutions for other locations. Breaklines were defined at any ridges or terrain features smaller than the computational grid resolution in any horizontal direction. The computational grid resolution was limited to the terrain data resolution or higher, as any decrease in computational grid resolution

is not realized beyond the resolution of the terrain data in most cases. The general exception to this rule occurs when the slope of the terrain is steep and the terrain resolution is coarse; in this case, a finer resolution is used to have enough computational points to describe the rapidly changing water surface (Brunner, 2020). An example of a computational grid design from the Tonglūshan model is shown in Figure 4.11, where Breaklines are used for the berms added to the terrain (see Section 4.1). The berms were 8 m at their widest, while the computational grid resolution was 12 m, necessitating the use of the Breaklines. The computational grid resolution was also varied as part of routine troubleshooting to confirm no model convergence issues were present.

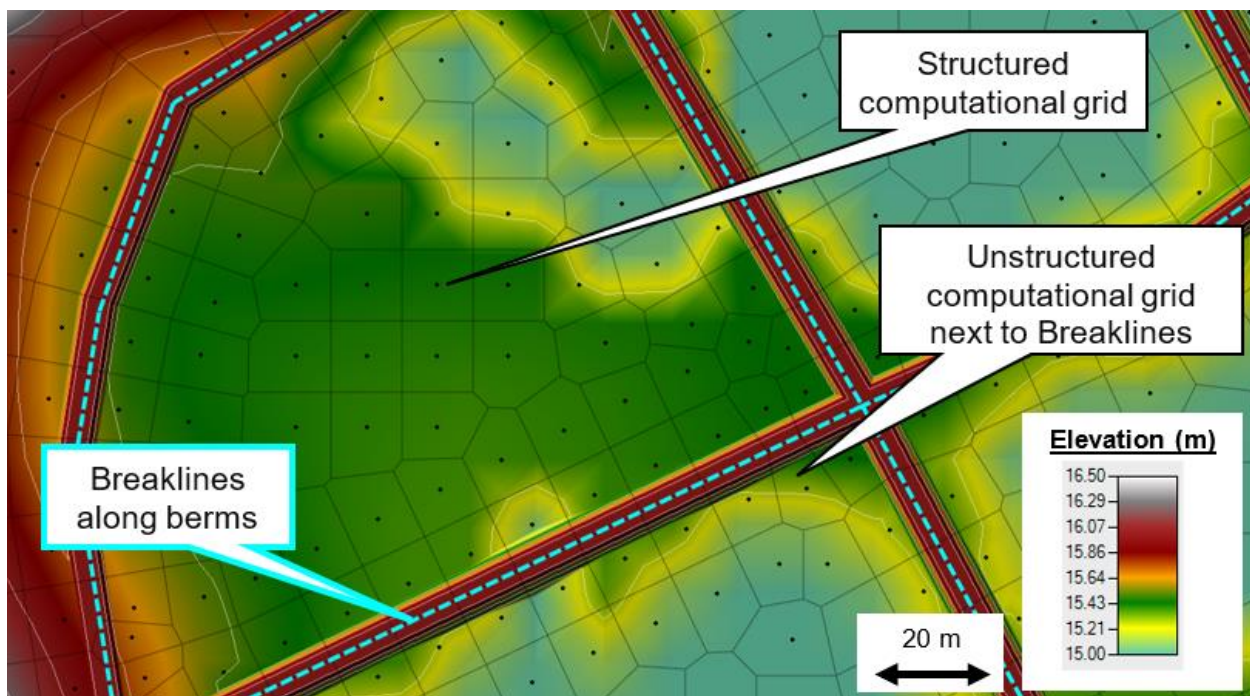


Figure 4.11 Example Computational Grid Design

The Manning's coefficients are input to the HEC-RAS Geometry as manually delineated polygons, or "Mann n Regions". Alternatively, a raster representing the land cover types and a conversion table between land cover types and the selected Manning's Coefficients can be assigned to the HEC-RAS Geometry. Land cover rasters can allow for more detailed delineation of land cover (and therefore Manning's Coefficient) without manual effort. Publicly available land cover rasters were not used for most events because they often did not have adequate resolution to describe variation in land cover visible within the Zone 1 extents. They also commonly showed land cover types that differed from the descriptions of the event or what is visible in Google Earth. Most HEC-RAS models used manual delineation for the events in this thesis for these reasons.

HEC-RAS Unsteady Flow Data

The initial elevation of fluid in the Storage Area is assigned in the Initial Conditions in the Unsteady Flow Data. The elevation is set at the dam crest elevation for all events.

Boundary Conditions Lines are defined spatially in the Geometry Data, however, the flow characteristics are defined in the Unsteady Flow Data in HEC-RAS. The Boundary Conditions Lines are assigned “Normal Depths” boundary conditions. This exclusively removes fluid from the HEC-RAS model. The Normal Depth calculates the volume to remove from the adjacent grid elements at each time step. The volume is calculated using Manning’s Equation, which is defined with Equation 4.11:

$$Q = \frac{1}{n} A R^{2/3} S_f^{1/2} \quad (4.11)$$

where Q is the flow, n is the Manning’s Coefficient, A is the flow cross sectional area, R is the hydraulic radius, and S_f is the friction slope. The flow area and hydraulic radius are calculated at each time step in the model based on the fluid elevations at each cell adjacent to the Boundary Condition Line and the terrain shape at the Boundary Condition Line. The flow is multiplied by the model time step to determine the volume. The friction slope is selected by the modeller and input in the Unsteady Flow Data. The friction slope is commonly approximated as the land slope in the vicinity of the Boundary Condition Line (Brunner, 2020). This convention was used in this thesis.

The rheology parameters, including the volumetric solids concentration, maximum volumetric solids concentration, representative particle size, yield stress, and viscosity, are input in the Unsteady Flow Data. The volumetric solids concentrations were based on the tailings solids and total outflow volumes in Table A.4 in Appendix A. The representative particle size is shown in Table A.7. The yield stress and viscosity were varied as part of the rheology calibration process, described in Section 4.4. The maximum volumetric solids concentration used was 84% following Gibson et al. (2021), as no information was available for tailings to suggest otherwise.

The particle density in Table A.7 is not used, as the particle density is a constant 2,650 kg/m³ in HEC-RAS and cannot be adjusted. The particle densities for all the tailings in the events considered in this thesis are higher than the default constant value in HEC-RAS, therefore the dispersive and turbulent stress components are underestimated in the models. The difference between the measured tailings particle densities and the default HEC-RAS value are minor; they are typically around 7% larger than the default for most

events in this thesis. The two events in Brasil (Feijão and Fundão) in this thesis are the exception to this, as the iron tailings are 20% to 40% denser than the HEC-RAS default. The dispersive and turbulent components are the smallest components unless either the solid particles are large, the solids content is close to the maximum volumetric solids concentration, or the roughness is very high (Julien & Lan, 1991; Gibson et al. 2021). In general, the events in this thesis do not meet these criteria. Between these two considerations, the underestimate from using the default particle density is currently assessed to be either minor or negligible. If the capability to vary the particle density is added to HEC-RAS, the Brazilian events can be re-run to better quantify this underestimate.

HEC-RAS Unsteady Plan Data

The Unsteady Plan Data includes many of the computational choices and temporal parameters, and couples the HEC-RAS Geometry and Unsteady Flow Data for a single model simulation run. The model was set to start from the beginning of the breach formation time. The model end time (i.e., the model duration) was determined through manual model iteration until the tailings flow ceased within the 2D Flow Area. Flow cessation was arbitrarily considered when the tailings runout velocity was less than 1 mm/s. These iterations considered both very low and very high rheological inputs (i.e., yield stress and viscosity). In channelized events, the high rheological inputs produced longer durations, as tailings crept down the valleys without ceasing, while the low rheological inputs rapidly reached the Zone 1 termination. In unconfined events with shallow slopes, low rheological inputs resulted in a longer model duration as the tailings also did not cease, while higher rheological inputs caused the modelled tailings to cease rapidly on the shallow slopes.

The time step was constant throughout the model duration. A long time step leads to numerical instability, as HEC-RAS becomes unable to resolve the rapidly changing depths and velocities. An overly short time step unnecessarily increases the computation time and may lead to numerical diffusion errors (Brunner, 2020). The time step for each modelled event was based on the Courant condition, as shown in Equation 4.12:

$$C = \frac{v \Delta t}{\Delta x} \quad (4.12)$$

where C is the Courant Number, v is the computed flow velocity, Δt is the computational time step, and Δx is the computation grid resolution. An estimated flow velocity is used

for the first model simulation, then the time step is iteratively refined during model troubleshooting, if necessary. Ideally, C is maintained around 1, with a suggested maximum C of 3, otherwise numerical instabilities are likely to occur (Brunner, 2020). A C close to 0 indicates overly fine time steps are used. With variable computational grid resolutions and temporally and spatially varying velocities within the model, there is some unavoidable variation in C . The modelled tailings runout downstream of the breach tended to have the greatest velocities, particularly for the Process II events. The time step was selected and adjusted until the modelled C was around 2 or less downstream of the breach.

The breach characteristics are input in the Unsteady Plan Data as a “Storage Area Connection Breach”. These characteristics include the breach process, the breach geometry, and the parametric breach weir coefficients. These characteristics are discussed in Sections 3.4, 3.5, and 4.2 respectively. The ultimate breach geometry downstream of the 2D Connection (i.e., in the 2D Flow Area) was previously added to the model as a terrain modification (Section 4.1).

4.4 Rheology and Model Calibration

The Quadratic formula was used in all models in this thesis, as discussed in Section 3.6.1. Unlike all the other variables in the database, the yield stress and viscosity were determined through calibration with HEC-RAS, rather than direct observation.

The methodology for the yield stress and viscosity calibration was developed to partially explore and address the non-uniqueness of rheology inputs in calibrated tailings dams breach models noted by Ghahramani et al. (2022). The overall workflow is shown in Figure 4.12. The coloured dashed boxes represent conceptual stages of the calibration that are discussed in further detail in the following subsections.

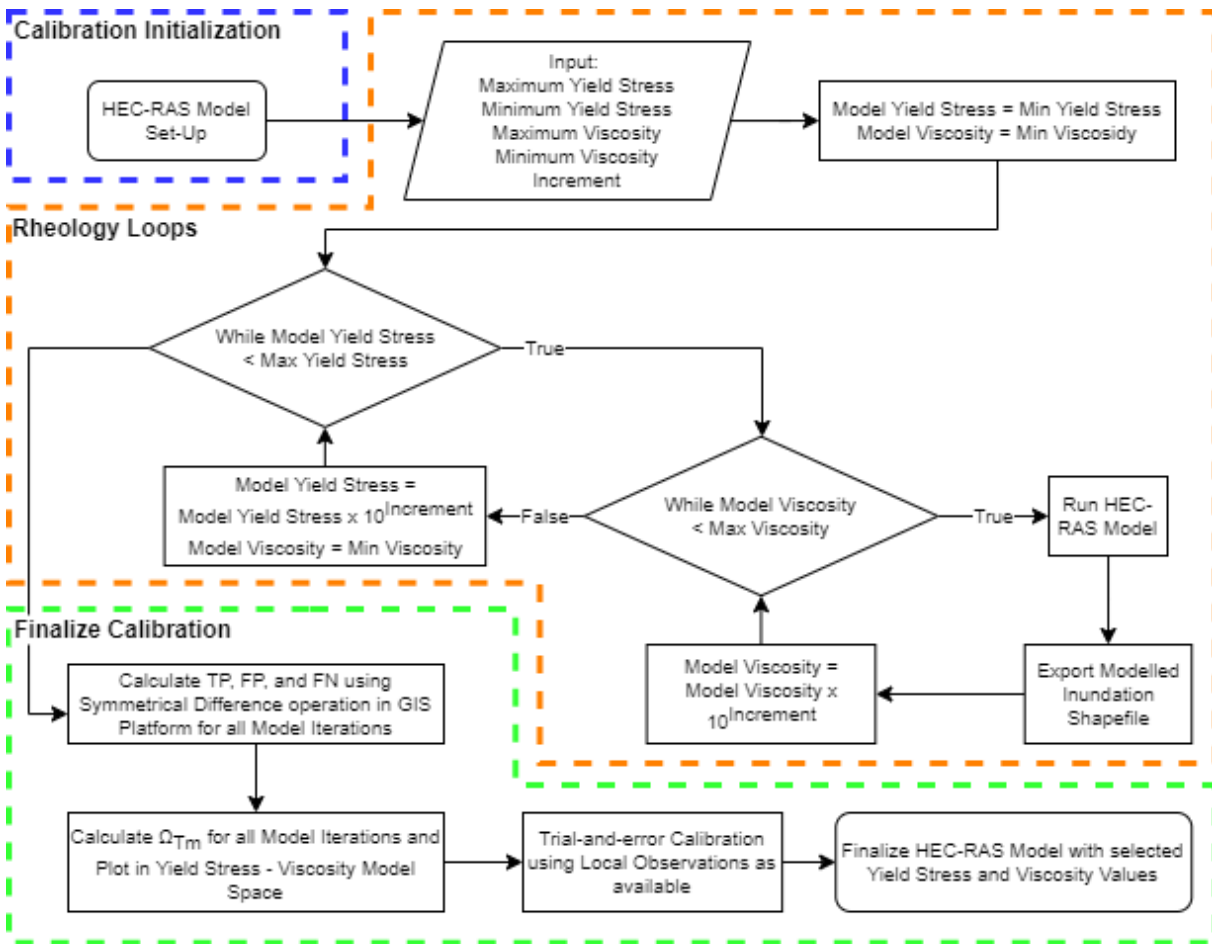


Figure 4.12 Rheology Calibration Process

Calibration Initialization

The HEC-RAS model is set up as described in Section 4.3.1. The rheology values are set at an initial estimate for model troubleshooting and to confirm the HEC-RAS model set-up is appropriate. The initial rheology values are based on the range from Martin et al. (2022) and further informed by any description of the runout characteristics from the event. For comparison, this calibration initialization is akin to the manual trial-and-error approach described in Ghahramani et al. (2022). Furthermore, multiple rheology inputs were manually tested during this stage to confirm the set-up is robust for the range of rheology values to be used in the second stage of the calibration. The selection of the initial rheology values had no bearing on the final calibrated values. Models that took a long time to compute (e.g., due to a long model duration or very short time step) used a truncated model duration.

Rheology Loops

HEC-RAS has a built in Application Programming Interface (API), where it can be controlled through Virtual Basic for Applications (VBA) commands. A program was written to run hundreds of model iterations systematically and automatically with different rheology inputs. The program is a nested loop that starts with a model with low yield stress and viscosity, then incrementally increases the viscosity and then yield stress for each model iteration. The maximum inundation area is exported by HEC-RAS as a shapefile after each model iteration.

To constrain the loops, a range of yield stress and viscosity values must be selected. Different tailings samples have measured yield stress and viscosity spanning nearly three orders of magnitude for a given volumetric solids concentration, based on the data in Martin et al. (2022). Not all events in this thesis have confirmed volumetric solids concentration, further increasing the possible range of rheology values for a given event. Furthermore, the rheology database in Martin et al. may not be representative of the full range of rheology for all tailings. The range used in the calibration typically used a range around 4 to 5 orders of magnitude to reflect these uncertainties in rheology.

The increase in the rheology was exponential, to suit the scale and range of measured rheology values. The increment exponent ranged from 0.1 to 0.25 depending on the event. (i.e., the rheology increased by a factor of approximately 1.25x to approximately 3.16x). A smaller increment exponent gives a finer resolution for the calibration, but increases the number of iterations and, correspondingly, the amount of time for the computer to complete the loops. Typically, a full completion of the calibration loops took around 8 hours for each event, and it took 12 hours for the longest calibration loops. A second calibration was run with a smaller range of rheology and smaller increment for a more precise calibration for some events, within practical time restraints.

Final Calibration

A quantitative measure of model performance is desirable to remove the subjective element involved with the modeller choosing which values are best. Heiser et al. (2017) presented a metric to assess the areal performance of the model, which considers the degree of over- and under-estimation. Barnhart et al.'s (2021) scaled version of Heiser et al.'s metric was used, which is defined using Equation 4.13:

$$\Omega_{Tm} = \left(1 - \frac{TP-FP-FN}{TP+FP+FN}\right)/2 \quad (4.13)$$

where Ω_{Tm} is the scaled metric, TP is the true positive model area, FP is the false positive model area, and FN is the false negative model area. Ω_{Tm} varies between 0 (perfect model performance) and 1 (worst model performance). The modelled areas are shown visually in Figure 4.13, using a model iteration result from the Tonglüshan model as the example. A symmetrical difference operation returns non-overlapping features between two shapes, which was used to calculate the TP, FP, and FN areas for each model iteration. This was done in a Geographical Information System (GIS) platform (i.e., QGIS ver. 3.22), and the Ω_{Tm} values for individual model iterations were calculated in a separate spreadsheet.

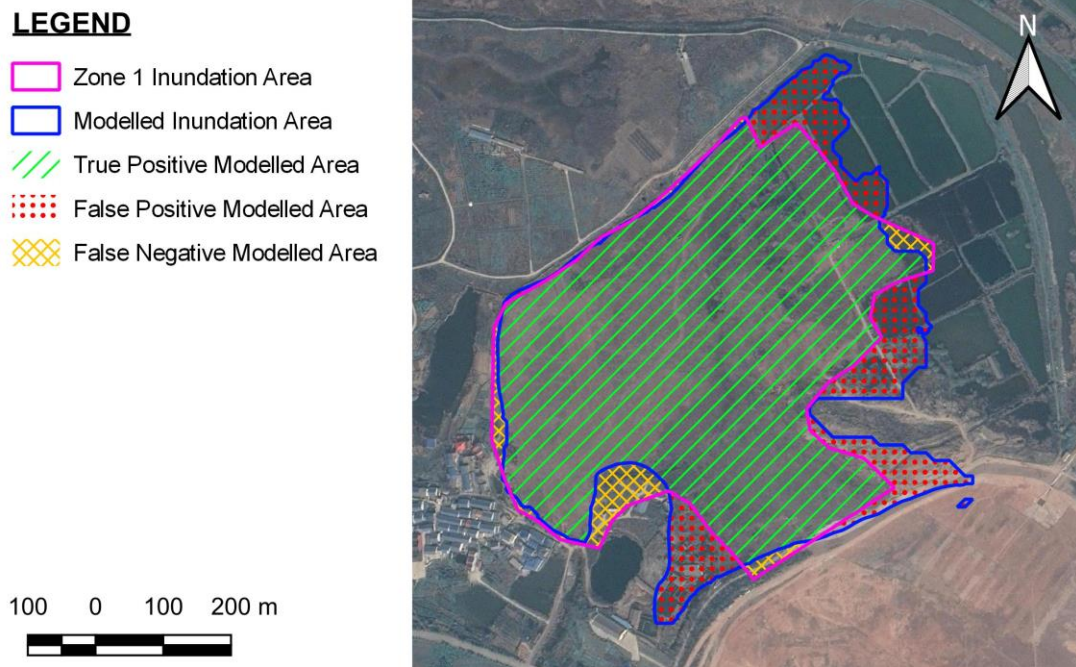


Figure 4.13 Example Modelled Areas for the Ω_{Tm} Metric

The Ω_{Tm} for each model iteration (i.e., with different rheology inputs) is plotted together in a contour map. The contour map and its data allow for a more insightful view on the combinations of yield stress and viscosity that still meet the same relative areal fit to the observed Zone 1 inundation area. Each modelled event has its own Ω_{Tm} contour map. An example of a contour plot is shown in Figure 4.14, using the calibration results from the Harmony 4A model. The tick marks on the y and x axis roughly represents a 1.58x increase in the rheology inputs for this calibration plot (i.e., ten to the power of the increment used, which was 0.2 for Harmony 4A). The orange “X” signifies the minimum value of Ω_{Tm} (i.e., best areal performance) for the calibration results in the example plot. The minimum Ω_{Tm} was 0.167 with a yield stress and viscosity of 160 Pa and 160 Pa·s,

respectively, for the Harmony 4A model. A black rectangle is also included in Figure 4.14 that denotes the range of measured yield stresses and viscosities from all the samples contained in Martin et al. (2022) for the estimated solids concentration of 50% for the Harmony 4A model. As discussed in the Rheology Loops subsection, the calibration for each event considered a wider range of rheology than shown in Martin et al.

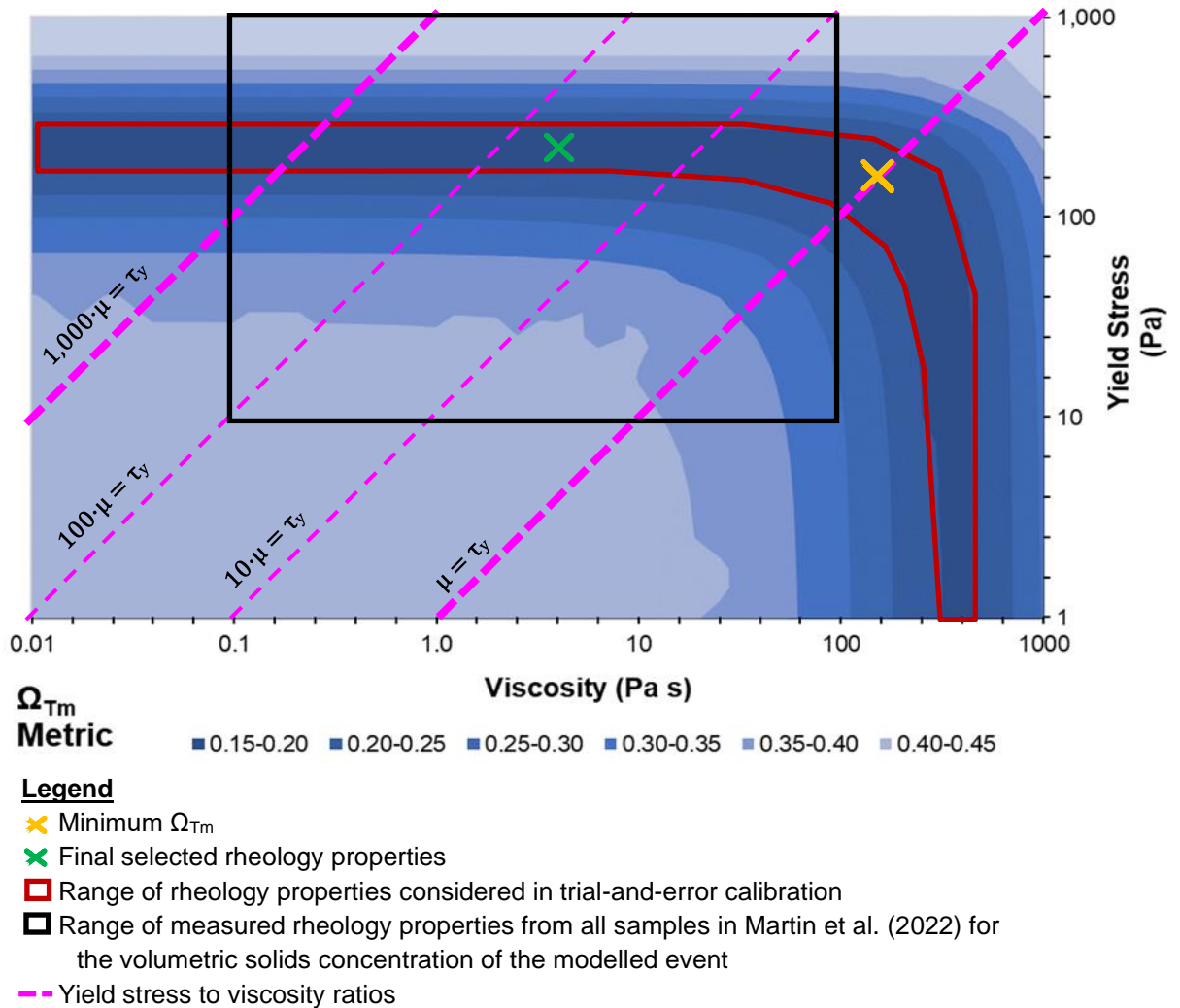


Figure 4.14 Example Rheology Calibration Plot in Log-Log Scale

When available, additional local runout observations were used to refine or further constrain the yield stress and viscosity values. Additional trial-and-error calibration was performed in the yield stress and viscosity model space that resulted in Ω_{Tm} values close to the minimum Ω_{Tm} for each particular event. A red polygon has been added to Figure 4.14 to signify the model space considered for the Harmony 4A model. The green “X” signifies the final selected yield stress and viscosity values. For example, a slightly higher yield stress with a much lower viscosity resulted in marginally worse areal performance

($\Omega_{Tm} = 0.169$), but a much closer match to observed peak depths for the Harmony 4A event. The rheology calibration plots for each modelled event shown in Appendix B have axes with tick marks that represent varying levels of increase in the rheology inputs, depending on the increment used in the calibration loops.

A novel heuristic was used to help assess the yield stresses and viscosities, which is the yield stress to viscosity ratio. The ratio is in units of Pa/Pa·s but does not have any physical meaning, hence the label as a heuristic. Within the values in Martin et al. (2022), the ratio varies for a specific sample at different solids concentrations, and between different samples at the same solids concentration. In general, the yield stress to viscosity ratios in Martin et al. range between 1 Pa/Pa·s and 1,000 Pa/Pa·s. Dashed magenta lines are included in Figure 4.14 to indicate various yield stress to viscosity ratios. This heuristic cannot be used to determine which set of calibrated rheology inputs represents the true rheology of the tailings material for a given event, but rheology inputs with yield stress to viscosity ratios that are above the range seen in Martin et al. (i.e., 1 Pa/Pa·s to 1,000 Pa/Pa·s) are not likely to be valid or realistic values.

4.5 Discussion

4.5.1 Terrain Data and Modifications

Some of the terrain modifications were limited to assumptions or simplifications, as satellite imagery was the only basis for estimating their geometry. Natural river channels display variable widths and depths but manually implementing such complex edits would be very time intensive and difficult to justify without extensive field surveys, particularly as some of the modifications had linear extents tens of kilometres long. In some instances, the satellite imagery and terrain data suggested differences in alignment, which required a subjective assessment on which source was more reliable. This uncertainty is exacerbated when the terrain data was surveyed years before or after the event and satellite imagery is not available proximate to the date of the failure. The errors introduced by the poorly constrained modifications were considered to have a lesser impact on the results compared to using terrain data without modifications. In the context of model calibration, validation, and verification, these modifications were not calibrated in any meaningful sense (i.e., modifications were not minutely adjusted until model results improved) nor are they verified to the unknown, true terrain features. The terrain data with

modifications are justified and assessed to be “more valid” than the terrain without modifications.

Roughly half of these errors were noticed prior to running any HEC-RAS models. The remaining half of the terrain errors were only noticed after initial troubleshooting models were compared to the observed Zone 1 inundation area from Ghahramani et al. (2020) or other local runout observations. For example, the troubleshooting Fundão models used Newtonian flow to test the extent of the 2D Flow Area. The first model set-up had a volume conservation issue leading to a total outflow volume of 35 M m³ of fluid (approximately 10% more volume than the observed 32.2 M m³ outflow volume) being input into the 2D Flow Area. This model overestimated the areal impact nearly everywhere in the model as one might expect when using Newtonian flow characteristics for a high solids concentration flow (the volumetric solids concentration was estimated as 60% at the breach) and higher-than-correct volume. The tailings flow could not reach the Mirandinha Stream however, due to the canyon saddle mentioned in Section 4.1. This discrepancy prompted the canyon saddle modification for future model iterations. Forward analysis TDBAs do not have the benefit of hindsight through observed inundation areas to locate or confirm terrain errors.

Outflow volumes and lower rheological flow characteristics are associated with faster runout and greater inundation extent, and often named as the highest-influence inputs in runout models (e.g., Gibson et al., 2022; Ghahramani et al., 2022). Based on the experience in this thesis, the terrain has a far greater impact than either volume or rheology. For example, the observed runout distance 8 hrs after the Fundão breach event was at least 42 km and possibly further (Robson, 2017). The final modelled results for Fundão reached 42 km within 8 hrs. This model included rheology measured directly from the Fundão tailings material (i.e., a yield stress of 170 Pa and viscosity 1.2 Pa·s for a solids concentration of 60%, extrapolated from the rheological trends reported by Machado, 2017). The terrain data, ALOS World 3D-30 m, required extensive modifications for the heavily vegetated narrow valley throughout the Zone 1 extent, which manifested as numerous ridges and constrictions. An alternative HEC-RAS model was run, inspired by the initial troubleshooting and volume conservation experience described above. This alternative model was identical to the final model except with Newtonian flow characteristics (i.e., no yield stress and viscosity of 0.001 Pa·s), an outflow volume intentionally set to 50% above the observed outflow volume, and no terrain modifications.

After a model duration of 8 hrs, this alternative Fundão model only reached 24 km downstream of the breach, severely underestimating the observed velocity of the flood wave.

The example above is somewhat facetious; however, it demonstrates more implications for forward analysis and risk analysis. Turner et al. (2022) also found that a DSM resulted in severely underestimated arrival times compared to a high-quality DTM for a hypothetical TDBA. They did not adjust the other model parameters between their comparisons. The volume and rheology adjustments for the alternative Fundão model are unrealistic, but ultimately would be considered “conservative” in a risk analysis context. However, the consequence of failure for the Fundão event with these “conservative” adjustments would still be substantially underestimated if the terrain was not assessed and modified. Within many academic publications regarding TDBAs (e.g., Novell Morell, 2022; Mahdi et al., 2020; Pirulli et al., 2017; Gibson et al., 2022; Daneshvar and Zsaki, 2018), the terrain assessments appear cursory. If this same low amount of effort is prevalent in forward analysis TDBAs, the underestimated risk globally may be concerningly high.

This thesis used a mix of publicly available terrain data and commercial terrain data. It is estimated that an equal amount of time was spent assessing and modifying the terrain as the investigation for all the breach characteristics and local runout observations combined. This effort was not limited to the publicly available data commonly criticized as inappropriate for runout modelling (i.e., DSMs, such as ALOS World 3D-30 m). Substantial modifications were also required for the purchased data or publicly available data claiming to be “flood modelling appropriate” or “bare-earth” by their providers or others. Bridges, heavy vegetation, and speckle errors present in these data prevented any “off-the-shelf” use in runout modelling for the events in this thesis. Lumbroso et al. (2019) labelled the accuracy of the Airbus WorldDEM DTM (12 m horizontal resolution) as “surpassing that of any global satellite-based elevation model available”. In this thesis, more than half of the events that used the same WorldDEM DTM data required relatively major modifications. The publicly available DEMs used in this thesis required even further modifications than the WorldDEM DTM.

A positive counterpoint to the above concerns involves the modelling for the Cadia NTSF Event. Site-specific high resolution and quality terrain data was surveyed by Newcrest Mining Ltd. and was provided for use in this thesis. The LiDAR required minor

modifications, but the site-specific terrain data, along with the commentary in the Expert Panel Report by Jefferies et al. (2019), allowed for a more detailed model and close fit between modelled results and observed runout. In effect, the quality of the model is highly correlated with the quality of the terrain. This conclusion, along with commentary in Turner et al. (2022) and the CDA TDBA Guidelines (2021), strongly suggest terrain with higher quality than what is publicly available should be considered as the minimum for TDBAs.

4.5.2 Parametric Breach and Runout Modelling in HEC-RAS

Two concerns are related to the parametric breach modelling. The first is the uncertainty in the definition of the hydraulic control and the second is the stage-storage curve approximation.

The uncertainty in hydraulic control, along with the breach geometry, was previously discussed in Section 3.9.3; the novel challenge associated with the hydraulic control was numerical instabilities or issues in HEC-RAS introduced by unusually shaped hydraulic controls. The vector of the modelled velocity immediately downstream of a 2D Connection in HEC-RAS is strictly perpendicular to the 2D Connection, which is suitable for breaches of straight dam crests. The events with non-straight dam crests often had flow directions that were not strictly perpendicular to the dam crest. This resulted in incorrect flow directions near the boundary of the 2D Flow Area in HEC-RAS and in some cases, numerical instabilities and volume conservation errors.

An example of this issue with a curving dam crest is shown in Figure 4.15, from the Fundão event. Morgenstern et al. (2016) concluded that the Fundão failure initiated at the setback by the left abutment, and an eyewitness said the dam flowed like a wave straight down the valley. With a 2D Connection in HEC-RAS along the dam crest, the flow is forced in an incorrect direction. The volume conservation errors arise when multiple flow directions intersect (e.g., at interior corners in Figure 4.15). The finite-volume SWEs cannot be solved (i.e., within computational tolerances) as HEC-RAS attempts to iteratively balance the volume and head in the Storage Area, the modelled flow at the 2D Connection, and the volume and head in the computation cells at the interior corners. This issue was the reason for the volume conservation error in the Fundão model described in Section 4.5.1.

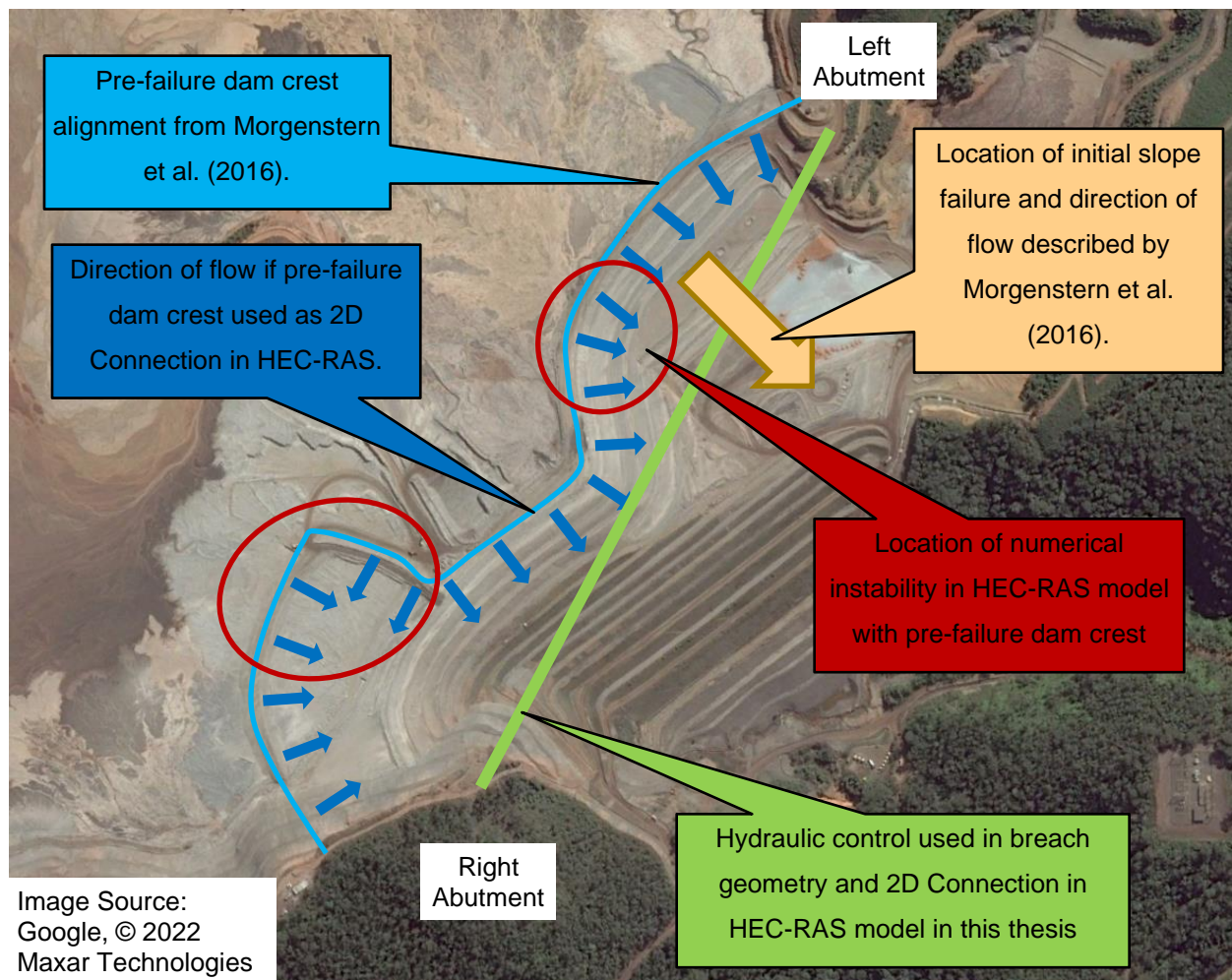


Figure 4.15 2D Connection and Flow Direction Schematic for a Curved Dam Crest in HEC-RAS

Runout models are most sensitive to the breach characteristics or modelling approach immediately downstream of the dam, before runout parameters (i.e., Manning's n or rheological parameters) can substantially affect the modelled runout (Brunner, 2014; Iverson & George, 2019). The stage-storage curve would be included in the modelling approach in this regard. The main concern about the assumed stage-storage curves is primarily related to the level of abstraction associated with the approach, rather than any identified deficiencies. Adria et al., (2022) noted the method performed well for the two events considered in that work, however two successful tests was likely insufficient to validate a method. After using the stage-storage curve for twelve events in this thesis, no major concerns relating to the stage-storage were identified for any event. Furthermore, Adria et al. only assessed the breach outflow hydrographs; modelling the full runout simultaneously with the breach allows for model comparison with any local runout

observations immediately downstream of the dam. The Feijão event had video camera evidence of the breach, which was used to estimate the frontal velocity at two locations within 1 km of the dam toe (de Lima et al., 2020). The modelled velocities were quite close to the observed values in most calibration simulations, partially validating the breach characteristics and stage-storage approach. The observed duration of the breach outflow stated by Turi et al. (2013) was correctly predicted using the stage-storage and parametric approach in the MAL Reservoir X event in Hungary. Likewise, the modelled arrival time matched observations from Turi et al. at the village of Kolontár, 1 km downstream of MAL Reservoir X. Events with a timeline or narrative of the breach or local runout observations immediately downstream of the breach are unfortunately limited, however. Continued research is warranted to further validate or identify limitations with the stage-storage and parametric approach, but it appears promising based on the work in this thesis.

HEC-RAS is limited to a single-phase fluid. Some of the events in this thesis demonstrated variable solids concentration, such as temporally (e.g., the Mount Polley outflow transitioning from solely the supernatant pond to the tailings and supernatant pond to tailings only) or spatially (e.g., the Fundão tailings runout mixing with the downstream rivers over 100 km). The average solids concentration was used in this thesis, and any calibrated yield stress and viscosity inputs would correspond to the average solids concentration. These average condition inputs may be insufficient to describe either the upper or lower range of the solids concentration for a given event. The developers of HEC-RAS are implementing variable solids concentrations (and therefore variable yield stress and viscosity) in future releases of HEC-RAS. This new capability should address this issue, but the existing single-phase fluid approach in HEC-RAS was a limitation in this thesis.

Existing guidance for modelling with HEC-RAS and prior experience with dam breach analysis (e.g., in the work described in Martin et al., 2022) was useful for the modelling in this thesis. Other than the concerns listed above, the modelling was relatively straight-forward. Compared to the efforts required to investigate each tailings dam breach event (as discussed in Chapter 3) and the modifications required for the terrain (Section 4.1), the model set-up and troubleshooting was a relatively small portion of the total research effort. This reinforces the notion that the modelling or the specific software used is of secondary importance to the experience of the modeller and quality of the input data.

4.5.3 Rheology and Model Calibration

Iverson (2003) and Iverson & George (2014) suggest that runout models should be based on measurable characteristics and avoid “tuning” model inputs to achieve a good fit. Calibration is still a necessary component when faced with uncertainties, and calibrated inputs can have discriminatory power when analyzing case histories (Aaron et al., 2018). As discussed in Section 2.5.4, calibration is not synonymous with validation, which is the assessment of the model inputs (calibrated or otherwise), the model results, and the model itself. Section 4.4 described the calibration, while this section discusses the validation effort.

Firstly, the calibration is a function of more than just the two rheology inputs of yield stress and viscosity. Any deficiencies in the input data (i.e., breach characteristics, runout characteristics, and terrain data), Zone 1 inundation area, or local runout observations directly reduce the validity of the model. This is applicable to any model software and not just HEC-RAS. As discussed in Sections 3.9 and 4.5.1, there are frequently uncertainties or misconceptions regarding input data, inundation area, or local runout observations. Consequently, the poor validity of a model is more likely attributable to issues other than calibration; notably, the Aznalcóllar model in this thesis and runout modelling for the Feijão event in other parties’ work suffers from inadequate inputs or runout observations (i.e., both local and event observations). Regarding models, Box (1976) states “it is inappropriate to be concerned about mice when there are tigers abroad”; it appears that calibration is the mice in the context of back-analysis TDBAs.

At face value, the calibration procedure in this thesis appears to be brute-force tuning. The range of values used for the Rheology Loops in the calibration were based on the measured yield stress and viscosity, however, the final calibration also included a further assessment of the values. Boger (2009) and Adams et al. (2017) include measured yield stresses, viscosities, and other tailings characteristics (e.g., particle size distribution, clay content, and mineralogy). Those discussions could be used to infer general trends for tailings without measured rheology, however, basic characteristics are often not available for the events in this thesis. For example, the density of the tailings particles is only known for two thirds of the events (discussed in Section 3.6.1 and shown in Table A.7). The estimate of rheology based purely on tailing characteristics could be speculative due to the limited geotechnical information available, depending on the data

sparsity for a given event. This necessitates the back-analysis “tuning” and comparison to a database of measured yield stress, as performed in this thesis.

Conceptually, the yield stress and viscosity for the tailings from a given event, if they were measured, should be within the range of observed values from Martin et al. (2022), have a yield stress to viscosity ratio between 1 to 1,000, and result in a modelled inundation area close to the observed inundation area. Even with measured rheology, a numerical model would not perfectly replicate the inundation, (i.e., due to minor errors in other inputs, errors in the terrain, or other model simplifications such as depth-average flow and single fluid rheology), and therefore would have a non-zero Ω_{Tm} . These bounds are represented on Figure 4.14 by the black rectangle, the thicker dashed magenta lines, and the red polygon, respectively. The region where all the bounds overlap is substantially smaller than the initial range of rheology considered in the calibration; only 30 simulations (i.e., roughly 8% of the simulations) in the Harmony 4A calibration simulation had Ω_{Tm} values within the overlap region. This overlap region commonly would be at least one order of magnitude in viscosity values and a quarter order of magnitude in yield stress. The secondary trial-and-error calibration for local runout observations does re-introduce some subjectivity to the process; overall, it is a net benefit to the calibration. When the modelled results were compared to the local runout observations, a smaller subset of the calibration simulations from the overlap were able to meet these additional constraints. The uncertainty in volumetric solids concentration and lack of local runout observations proximal to the breach for some events limit the amount of refinement possible with this validation process; hence the caution given regarding the calibrated values in general.

Two events considered in this thesis, Fundão and Tonglūshan, had the yield stress and viscosity of the tailings measured by other parties. The Tonglūshan modelling in this thesis included the full calibration process to compare the calibrated yield stress and viscosity to the measured values. The calibrated values were between half to one order of magnitude greater than the measured values, lending some credence to commentary in Iverson (2003) regarding calibration as purely a parameter tuning exercise. There were several possible explanations for the difference in rheology (discussed in Appendix B), indicating the calibration process in this thesis may not be the cause of the difference. The Fundão model took 2 hrs for a single model simulation to compute, therefore the calibration process was omitted and instead only the measured rheological properties were used in the model due to practical time constraints. The modelled results aligned

with multiple local runout observations for the Fundão event, in contrast to the Tonglüshan model. Evidently, more research is warranted on measuring rheological parameters for the purpose of tailings dam breaches.

Chapter 5: Concluding Remarks

This chapter summarizes the work completed and underscores the main findings. Detailed summaries are provided at the end of Chapters 3 and 4, with specific comments for each event included in Appendix B. Suggestions for future research and implications for industry are discussed and the research objectives and hypotheses are revisited.

5.1 Summary of Work and Main Findings

The completed work and main findings are summarized below. The findings are associated with each summarized component of work using parentheses at the end of each listed finding.

Completed Work

1. The tailings solids volume, interstitial water volume, and supernatant pond volumes in the outflow were compiled from previous reports or newly estimated for the 12 dam breach events. A thorough review of discrepancies between reported volumes was completed. The volumetric solids concentrations in the outflow volumes were explicitly estimated for the first time for multiple events. The arrangement of the TSFs involved in the breach events were qualitatively classified. Overall, investigating the outflow volumes took roughly 15% of the total effort in this thesis.
2. Breach characteristics were compiled from previous reports or newly estimated for the 12 dam breach events. The breach characteristics included the breach process classification, formation time, and breach geometry. The breach process was based on the definition from CDA (2021), and the conventions for formation time and geometry were adapted from water reservoir dam breach work (e.g., Wahl, 1998; Froehlich, 2008). Additional height conventions (i.e., crest height and the slab breach height) were introduced specifically for tailings dam breach scenarios. Overall, investigating the breach characteristics took roughly 10% of the total effort in this thesis.
3. Local runout observations were compiled from previous reports or newly estimated for the 12 dam breach events. The Zone 1 inundation areas from Ghahramani et al. (2020) were reviewed. The local runout observations most frequently were tailings depths and arrival times for various temporal definitions (e.g., the flood wave front, peak of the flood wave, or final deposition). Other observations were also compiled, as available. Overall, investigating the runout observations took roughly 15% of the

total effort in this thesis, but this effort varied a lot depending on the data sparsity for each event.

4. Publicly available terrain data were used or commercial data were obtained. Modifications were made to the terrain data to add the breach channel, remove ridges and vegetation near rivers, remove artefacts or irregularities, and add terrain features not captured in the original survey. Overall, finding, assessing, and modifying the terrain took roughly 40% of the total effort in this thesis.
5. A HEC-RAS model with a parametric breach and depth-averaged, single-phase, fixed-bed flow was developed for the 12 events to simultaneously model the tailings dam breach and tailings runout. A calibration approach was used to select yield stress and viscosity values for each event. The modelled results were quantitatively compared to the observed Zone 1 inundation areas and any local runout observations. Overall, the modelling and calibration took 20% of the total effort in this thesis.

Main Findings

- A. Total outflow volumes have previously been compiled but are often noted by others as uncertain. Estimating subsets within the outflow volume (i.e., tailings solids, interstitial water, or supernatant pond) was equally or more uncertain. (Completed Work 1).
- B. Frequently, academic literature or news reports contained erroneous outflow volumes or volumes that lack important and relevant nuance in the context of TDBAs. These misconceptions contribute to the uncertainty associated with tailings dam breach events. (Completed Work 1).
- C. The average volumetric solids concentration ranged between 15% and 48% for Process I events and up to 63% for Process II events. (Completed Works 1 and 2).
- D. The breach process is not strictly dependent on failure conditions and triggers. Some events experienced triggers associated with erosional failures (Process I), but had breach processes comparable to slope failures (Process II) or vice versa. No distinct contributory variables for this exchange of triggers and processes were found for these events, but conclusions are limited by the small sample size. (Completed Work 2).
- E. The formation times for the Process I breaches were comparable to past observations of earthfill dam breaches for water reservoirs, and possibly on the slower side. This observation aligns with guidance elsewhere but is only based on three events in this

thesis. The formation times for Process II events were assumed to be instantaneous. Nothing in the investigations (i.e., existing literature or novel interpretations) indicated that this was an inappropriate simplification. (Completed Work 2).

- F. The breach height was nearly the same height as the crest height for all Process I events in this thesis. The breach height ranged between 50% and 100% of the crest height for Process II events, demonstrating greater variability than the Process I events. High scatter and data sparsity prevents definitive conclusions regarding any contributory variables to the varying breach heights for Process II events. (Completed Work 2).
- G. The breach widths for Process II events were wider than those of Process I events, on average for a given breach height, but demonstrated greater variability. High scatter and data sparsity prevents definitive conclusions regarding any contributory variables to the larger breach widths for Process II events. (Completed Work 2).
- H. The frequency of academic literature and civilian news repeating unverified or erroneous local runout observations was similar to the frequency of erroneous outflow volumes. There is a clear need to cross-examine reported observations to the same level as outflow volumes or breach characteristics. (Completed Work 3).
- I. Publicly available DSM terrain datasets (e.g., ALOS World 3D-30 m or SRTM v3.0) with near global coverage were found to be highly affected by vegetation or other errors and are therefore not recommended for use in TDBAs. Commercial terrain datasets were found to be better than the publicly available datasets but did not meet the criteria for a bare-earth DTM appropriate for flood modelling either, despite claims to the contrary. Many terrain modifications were required to better approximate bare-earth conditions. (Completed Work 4).
- J. The parametric breach approach and stage-storage approach was promising for breach modelling, but further work is required to corroborate its appropriateness or find limitations in use for tailings dam breaches. Modelled results with instantaneous formation times for the Process II breaches were found to align with observations immediately downstream of the TSF. (Completed Work 5).
- K. The runout modelling set-ups were generally the most straight-forward processes, compared to the investigations on the breach characteristics and runout observations and any terrain modifications. Standard flood modelling guidance for HEC-RAS was applicable to the tailings dam breach and runout modelling. (Completed Work 5).

- L. The calibrated yield stresses and viscosities were within the range of previously measured values for tailings, which spans orders of magnitude between different samples. The lack of information regarding geotechnical or rheological characteristics for the 12 events does not prevent model validation but is a hindrance for validation efforts. (Completed Work 5).
- M. Poor terrain quality was qualitatively found to have the largest impact on runout modelling, more so than inputs conventionally described as the most influential (i.e., outflow volume). Arrival times were more heavily affected by terrain errors for highly channelized terrain, while inundation areas were more affected by terrain errors in unconfined events. (Completed Works 4 and 5).
- N. Observed arrival times were found to be useful calibration or model validation constraints for channelized breach events. Observed peak depths or final deposition depths were useful constraints for unconfined events. (Completed Works 3 and 5).

5.2 Recommendations for Future Research and Industry

The opportunities to improve and extend the advancements presented in this thesis are summarized below. The recommendations are split between long-term academic research ideas and practices that the mining industry and TDBA professionals can implement immediately. The industry recommendations are associated with each research recommendation using parentheses at the end of each listed industry recommendation.

Recommendations for Future Research

1. Investigate and model more tailings dam breach events.
 - a. As described in Section 5.1, many of the findings for the outflow volumes and breach characteristics are tempered by limited data. Confirming or corroborating trends between TSF characteristics/conditions and outflow volumes and breach characteristics with more events can reduce uncertainty in model inputs for forward-analysis TDBAs.
 - b. More comparisons between modelled results using the parametric breach approach with a stage-storage curve and laboratory scale experiments for tailings dam breaches would help identify refinements or limitations in the approach. Alternatively, a full three-dimensional model of the entire breach process using

post-failure topography could be compared to the parametric breach approach to possibly gain insights for a scale larger than possible in laboratory settings.

2. Revisit the events in this thesis in greater detail.
 - a. Some events can be refined with additional time, effort, or cost (e.g., modelling the entirety of the Zone 1 inundation area for the Fundão event: purchasing better terrain for many events in this thesis). New information published by others (e.g., Sanz-Ramos et al. 2022, for the Aznalcóllar event) and uncovered in this thesis also suggests some model inputs and models should eventually be revised (e.g., the Aznalcóllar model).
 - b. The parametric breach approach is a simplification of the erosional process for Process I breaches, and the fixed bed modelling in this thesis neglects erosion in the downstream environment. Collecting geotechnical characteristics and local runout observations related to erosion and erosion modelling would be a valuable avenue of improvement for some of the events in this thesis (e.g., Mount Polley).
 - c. The focus of TDBAs and this thesis is on the Zone 1 extent, however, the transition between Zone 1 and Zone 2 is not necessarily discrete (e.g., Feijão, MAL Reservoir X). Local runout observations relating to sediment transport and water quality and the modelling of the Zone 1 to Zone 2 transition are relatively unexplored fields.
3. Perform field-visits for past tailings dams breach events.
 - a. All the investigations and modelling in this thesis were completed at a desktop level. Field visits and on-site investigations may reduce uncertainty in the outflow volumes and breach characteristics and uncover additional local runout observations, if the downstream conditions have been preserved.
 - b. This work can be done alongside investigations and modelling of other tailings dam breach events or refinements of events considered in this thesis (Recommendations 1 and 2).
4. Perform a global assessment of sensitivity in numerical models for TDBAs.
 - a. Ghahramani et al. (2022) initiated work on the uncertainty and model sensitivity using the First Order, Second Moment method on two events modelled in four different models. The addition of the HEC-RAS models of the events in the thesis can strengthen conclusions from Ghahramani et al.

- b. Ultimately, the modelled depths and velocities are inputs to further assessments of human fatalities, infrastructure damage, and environmental impacts from a tailings dam breach. Previous vulnerability estimates relate depth and velocity to structural damage and fatality rates for landslides or water dam breach floods (e.g., Jakob et al. 2011; USBR, 2014), but no such estimates or guidance exist for tailings runout. This information would be of particular use in loss-of-life calculations following a forward-analysis TDBA.
 - c. This work can be done alongside investigations and modelling of other tailings dam breach events or refinements of events considered in this thesis (Recommendations 1 and 2) and would be facilitated by the field visits and eyewitness interviews (Recommendation 3).
5. Develop a database for pre- and post-failure terrain data for breached TSFs and the downstream environment.
- a. Outflow volumes are three-dimensional by definition, therefore reporting only the value of total volume introduces a loss of spatial information. Detailed pre- and post-failure surveys would be publicly available to reconstruct the three-dimensional distribution of the tailings volume and supernatant pond volumes.
 - b. A database such as this can be applied to reduce uncertainty in outflow volumes, some breach characteristics, and the definition of hydraulic control. It would also support validation of the parametric breach approach and mobile-bed models that estimate erosion at the dam breach location or in the downstream environment.

Recommendations for Industry

- A. Use similar proportions of effort for each stage or model input for forward-analysis TDBAs as in this thesis. Some tasks are not strictly transferable between back-analysis (i.e., as in this thesis) to forward-analysis, therefore Table 5.1 is provided as a starting guideline. Depending on the complexity of a TSF and its failure modes or the available information or resources, the distribution can be adjusted as needed for each study. The level of effort could be either the time allocated for each task or financial costs (e.g., purchasing better terrain data). The tailings dam breach events and modelling in this thesis showed that more accurate modelling was the result of good quality inputs rather model sophistication. Consequently, 80% of the total effort is recommended for tasks relating to model inputs, prior to any breach and runout modelling is completed.

**Table 5.1 Recommended for Distribution of Level of Effort for Forward-Analysis
TDBAs**

| This Thesis | | Recommendation for Forward Analysis | |
|--------------------------------------|-----------------|-------------------------------------|-----------------|
| Component | Level of Effort | Component | Level of Effort |
| Outflow Volume Investigation | 15% | Outflow Volume Estimation | 25% |
| Breach Characteristics Investigation | 10% | Breach Characteristics Estimation | 15% |
| Runout Observation Investigation | 15% | N/A | - |
| Terrain Modifications | 40% | Terrain Modifications | 40% |
| Breach and Runout Modelling | 10% | Breach and Runout Modelling | 10% |
| Rheology Calibration | 10% | Sensitivity Analysis | 10% |

- B. Estimate separate probabilities and consequences of a breach for a Process I and Process II breach for each failure mode in a FMEA or PFMA. Depending on the specific TSF conditions and downstream environment, these processes may result in a substantially different risk profile.
- C. Specify which breach process is considered in TDBA scenarios. When Process II breaches are considered appropriate, use observations or methods relevant to Process II breaches, rather than adapting from experience with earthfill dams for water reservoirs. These observations can be based on this thesis or from experience more analogous to a Process II breach than from strictly hydraulic modelling practice (e.g., landslide modelling).
- D. Obtain higher accuracy and resolution terrain data for TDBAs, preferably as a bare-earth DTM. The professionals conducting TDBAs should review the terrain for vegetation, above ground features or other errors, and make modifications as necessary. The financial cost of obtaining good quality terrain is likely offset by a reduction in consulting fees for a TDBA professional to review and modify bad quality terrain. Furthermore, better quality terrain results in less uncertainty in consequence estimation and therefore less uncertainty in risk assessments.
- E. Include an expert with experience in TDBAs in any Expert Panel convened to investigate the failure, in the unfortunate event of a tailings dam breach in the future. This recommendation is essentially the Future Research recommendations 1 and 3

but performed immediately after a breach. An investigation aimed at the breach process and runout observations in parallel to the investigation on the conditions and cause of the failure would give more detail on the breach and runout than any desktop investigation years after the event (e.g., like in this thesis) with less uncertainty and effort.

- F. Publish pre- and post-failure terrain data for any TSF that experienced a breach. The recent events in this thesis appear to have such survey data (e.g., for Feijão in Robertson et al., 2019; for Fundão in Fundação Renova, 2016; for Mount Polley in Morgenstern et al., 2015), but they are not publicly available in digital form. If the organizations that hold such data publish them or otherwise put the data in the public domain, it would support the tailings dam breach topography database (Future Research 5).

5.3 Closure

This work was undertaken to fill the need for more back-analysis modelling of tailings dam breach events noted by Rana et al. (2021) and Ghahramani et al. (2022). The research objectives (Section 1.3) were met, although for a smaller number of events than initially planned. The first two research hypotheses (Section 1.4) were partially tested; the limited number of events hampered clear insights.

The last research hypothesis was resolutely confirmed. Early on, it became apparent that the existing reporting was scattered, lacking nuance, and erroneous in many cases. It was for this reason that the number of events considered was low, compared to previous studies (e.g., Wahl, 1998; Froehlich, 2008; Rana et al., 2021; Ghahramani et al., 2022), as each investigation and modelling required more cross-examination or interpretation than initially estimated. Despite this, the largest single database of detailed observations and modelling specific to the geotechnical and hydrotechnical considerations for tailings dam breach events was developed as part of this thesis.

The spirit of the research was intended to encourage continuous improvement and challenge faulty observations of the 12 events considered in this thesis. Many avenues of research and aspects requiring further investigation or refinement were identified during the investigations and modelling. It is recognized that the conventions used or developed in this thesis and the breach and runout modelling may still be imperfect, or

even introduce or promote a few misconceptions, given the quantity and desktop nature of the investigations and modelling. As recommended in Section 5.2, any future improvements to the work presented in this thesis are welcomed, towards the goals of improving expert judgement in Tailings Dam Breach Analyses and zero harm to people and the environment from Tailings Storage Facilities.

References

- Aaron, J. B. (2017). *Advancement and Calibration of a 3D Numerical Model for Landslide Runout Analysis*. University of British Columbia.
- Aaron, J. B., Stark, T. D., & Baghdady, A. K. (2018). Closure to “Oso, Washington, Landslide of March 22, 2014: Dynamic Analysis” by Jordan Aaron, Oldrich Hungr, Timothy D. Stark, and Ahmed K. Baghdady. *Journal of Geotechnical and Geoenvironmental Engineering*, 144(9), 2014–2017. [https://doi.org/10.1061/\(ASCE\)GT.1943-5606.0001934](https://doi.org/10.1061/(ASCE)GT.1943-5606.0001934)
- Aaron, J., Hungr, O., Stark, T. D., & Baghdady, A. K. (2017). Oso, Washington, Landslide of March 22, 2014: Dynamic Analysis. *Journal of Geotechnical and Geoenvironmental Engineering*, 143(9), 05017005. [https://doi.org/10.1061/\(asce\)gt.1943-5606.0001748](https://doi.org/10.1061/(asce)gt.1943-5606.0001748)
- Adria, D., Ghahramani, N., Cen, A., McDougall, S., Rana, N., & Evans, S. G. (2021). Advancements in the modelling of tailings dam breaches. In N. A. Beier, G. W. Wilson, & D. C. Sego (Eds.), *Proceeding of the Twenty-Fifth International Conference on Tailings and Mine Waste, 7-10 November 2021, Banff, Alberta, Canada* (pp. 324–332).
- Adria, D., McDougall, S., & Evans, S. G. (2022). Parametric Method for Tailings-Dam Breaches and its Application to the Breach Event at the Mount Polley Mine, South-Central British Columbia (NTS 093A). *Geoscience BC Summary of Activities 2021: Minerals*, 81–92.
- Airbus Defense and Space. (2015). *WorldDEM 12 m DTM Elevation Data*.
- Akan, A., Osman, & Iyer, S. S. (2021). Chapter 3: Normal Flow. In *Open Channel Hydraulics* (2nd ed.). Elsevier. <https://doi.org/10.1016/B978-0-12-821770-2.00007-5>
- Alonso, E. E., & Gens, A. (2006a). Aznalcóllar dam failure. Part 1: Field observations and material properties. *Géotechnique*, 56(3), 165–183.
- Alonso, E. E., & Gens, A. (2006b). Aznalcóllar dam failure Part 3: Dynamics of the motion. *Géotechnique*, 56(3), 203–210.
- ANA (n.d.). *Hydrologic Data for Station 40740000*. National Water and Sanitation Agency of Brasil
- Ancey, C. (2007). Plasticity and geophysical flows: A review. *Journal of Non-Newtonian Fluid Mechanics*, 142, 4–35. <https://doi.org/10.1016/j.jnnfm.2006.05.005>
- Andrews, G. C., Shaw, P., & McPhee, J. (2014). Chapter 7: Computers, Software, and Intellectual Property. In *Canadian Professional Engineering and Geoscience: Practice and Ethics* (6th ed.). Nelson Education Limited.

- Annis, A., & Nardi, F. (2019). Geo-spatial Information Science Integrating VGI and 2D hydraulic models into a data assimilation framework for real time flood forecasting and mapping. *Geo-Spatial Information Science*, 22(4), 223–236. <https://doi.org/10.1080/10095020.2019.1626135>
- AP Archive. (1994). *South Africa Mudslide Video Footage*. <http://www.aparchive.com/metadata/youtube/d756d9ba1a1279072e75fbf0c7edcf8d>
- Arbuthnot, G. L. J., & Strange, J. N. (1960). *Floods resulting from suddenly breached dams: Conditions of minimum resistance and Hydraulic model investigation*.
- Arcement, G. J. J., & Schneider, V. R. (1989). *Guide for Selecting Manning's Roughness Coefficients for Natural Channels and Flood Plains*.
- Arcuri, M., Laia Otávio, P., & Suñer, R. (2015). Territories and heritage in the mud of negotiation: challenges for community museology at the Fundão. *Archives of the Federal University of Minas Gerais Natural History Museum*, 24(1), 209–244.
- Ayala-Carcedo, F. J. (2004). The Rupture of the mining waste pond in Aznalcóllar (Spain) in 1998 and the ecological disaster consequence of the Guadiamar River: Causes, effects and lessons. *Geological and Mining Bulletin of the Geological Mining Institute of Spain*, 115(4), 711–738.
- Bagnold, R. A. (1954). Experiments on a Gravity-Free Dispersion of Large Solid Spheres in a Newtonian Fluid under Shear. *Proceedings of the Royal Society of London. Series A, Mathematical and Physical Sciences*, 225(1160), 49–63.
- Bánvölgyi, G. G. (2018). The Failure of the Embankment of the Red Mud Reservoir at Ajka (Hungary). *Proceedings of the 36th International ICSOBA Conference, Belem, Brazil, 29 October - 1 November 2018*, 387–400.
- Barnes, H. H. J. (1967). *Roughness characteristics of natural channels*. U.S. Geological Survey, Paper 1849, 213 p.
- Barnhart, K. R., Jones, R. P., George, D. L., McArdell, B. W., Staley, D. M., & Kean, J. W. (2021). Multi-model comparison of computed debris flow runout for the 9 January 2018 Montecito, California post-wildfire event. *Journal of Geophysical Research: Earth Surface*, 126, 1–43. <https://doi.org/10.1029/2021JF006245>
- Berti, G., Villa, F., Dovera, D., Genevois, R., & Brauns, J. (1988). Disaster of Stava, Northern Italy. *Proceedings of the American Society of Civil Engineers, Geotechnical Engineering Division, Specialty Conference*.
- BGC Engineering Incorporated. (2022). *Frequency-Magnitude Relationship for the Coldwater River (Draft)*. Project No.: 0511009.05.04

- Blight, G. E., & Fourie, A. B. (2005). Catastrophe revisited – disastrous flow failures of mine and municipal solid waste. *Geotechnical and Geological Engineering*, 23, 219–248. <https://doi.org/10.1007/s10706-004-7067-y>
- Blight, G. E. (2010). *Geotechnical Engineering for Mine Waste Storage Facilities*. CRC Press/Balkema.
- Boger, D. V. (2009). Rheology and the resource industries. *Chemical Engineering Science*, 64(22), 4525–4536. <https://doi.org/10.1016/j.ces.2009.03.007>
- Box, G. E. P. (1976). Science and Statistics. *Journal of the American Statistical Association*, 71(356), 791–799. <https://doi.org/https://doi.org/10.2307/2286841>
- Health, Safety and Reclamation Code for Mines in British Columbia Health, Safety and Reclamation Code for Mines in British Columbia*, (2017). British Columbia Ministry of Energy and Mines, Victoria, British Columbia, Canada.
- British Columbia Ministry of Energy and Mines. (2015). *Mount Polley Mine Tailings Storage Facility Breach, August 4, 2014: Investigation Report of the Chief Inspector of Mines*.
- Brunner, G. (2014). *Using HEC-RAS for Dam Break Studies*. Training Document 39.
- Brunner, G. (2020). *HEC-RAS User's Manual Version 6.3*.
- Brunner, G., Sanchez, A., Molls, T., & Parr, D. A. (2018). *HEC-RAS Verification and Validation Tests*. Research Document 59.
- Brunner, G., Savant, G., & Heath, R. E. (2020). *Modeler Application Guidance for Steady versus Unsteady, and 1D versus 2D versus 3D Hydraulic Modeling*. Training Document 41
- Burland, J. B. (1987). The teaching of soil mechanics: a personal view. In E. T. Hanrahan, T. L. L. Orr, & T. F. Widdis (Eds.), *Proceedings of the Ninth European Conference on Soil Mechanics and Foundation Engineering Dublin, 31 August-3 September 1987* (Issue 3, pp. 1427–1447).
- Canadian Dam Association. (2013). *Dam Safety Guidelines 2007 (2013 Edition)*.
- Canadian Dam Association. (2019a). *Technical Bulletin: Application of Dam Safety Guidelines to Mining Dams*.
- Canadian Dam Association. (2019b). *Workshop on CDA Bulletin on Tailings Dam Breach Analysis*.
- Canadian Dam Association. (2021). *Technical Bulletin: Tailings Dam Breach Analysis*.
- Cariboo Regional District. (2014). *Aerial Video Footage of the Mount Polley Tailings Dam Breach around 8:00 AM*.

https://www.mountpolleyreviewpanel.ca/sites/default/files/report/2014-08-04_08_46_34.mp4

- Chandler, R. J., & Tosatti, G. (1995). The Stava tailings dams failure, Italy, July 1985. *Proceedings of the Institution of Civil Engineers, Geotechnical Engineering*, 67–79.
- Chanson, H. (2004). *Hydraulics of Open Channel Flow* (2nd ed.). Elsevier Butterworth-Heinemann. Oxford, United Kingdom.
- Chow, V. Te. (1959). *Open Channel Hydraulics*. McGraw-Hill Book Co. New York, New York, U.S.A.
- Concha Larrauri, P., & Lall, U. (2018). Tailings dams failures: Updated statistical model for discharge volume and runout. *Environments - MDPI*, 5(2), 1–10. <https://doi.org/10.3390/environments5020028>
- Colombo, P. &. (2003). The collapse of the Stava tailings basins – Analysis of the event and observations. 19th July 1985. In G. Tosatti (ed.), *A review of scientific contributions on the Stava valley disaster (eastern Italian Alps)*, pp. 335-358.
- Corominas, J. (1996). The angle of reach as a mobility index of small and large landslides. *Canadian Geotechnical Journal*, 33, 260–271.
- CPRM. (2015). *Special Report on the Doce River Basin*. Mineral Resources Research Company Geological Survey of Brasil.
- CPRM. (2019). *Special Monitoring from the Paraopeba River Basin: Report I Hydrological and Sediment Metric Monitoring*. Mineral Resources Research Company Geological Survey of Brasil.
- Cuervo, V., Burge, L., Beaugrand, H., Hendershot, M., & Evans, S. G. (2017). Downstream Geomorphic Response of the 2014 Mount Polley Tailings Dam Failure, British Columbia. In M. Mikoš, Y. Yin, & K. Sassa (Eds.), *Proceedings of the Fourth World Landslide Forum, Ljubljana, Slovenia* (pp. 281–289).
- Daneshvar, P., & Zsaki, A. M. (2018). Simulation of Tailings Flow Resulting from a Dam Breach Using Smoothed Particle Hydrodynamics. *Environmental & Engineering Geoscience*, XXIV (3), 263–279.
- de Lima, R. E., de Lima Picanço, J., Freitas da Silva, A., & Aline Acordes, F. (2020). An anthropogenic flow type gravitational mass movement: the Córrego do Feijão tailings dam disaster, Brumadinho, Brazil. *Landslides*, 17, 2895–2906. <https://doi.org/10.1007/s10346-020-01450-2>
- DeNeale, S. T., Baecher, G. B., Stewart, K. M., Smith, E. D., & Watson, D. B. (2019). *Current State-of-Practice in Dam Safety Risk Assessment*. Report No. ORNL/TM-2019/1069

- Duvenhage, T. J. (1998). *An Environmental Management Plan for the Merriespruit Slimes Dam Disaster Area*. Rand Afrikaans University.
- El-Ramly, H., Morgenstern, N. R., & Cruden, D. M. (2002). Probabilistic slope stability analysis for practice. *Canadian Geotechnical Journal*, 39(3), 665–683.
- Engels, J. (2006). *Los Frailes, Aznalcóllar, Spain*.
<https://tailings.info/casestudies/losfrailes.htm>
- Eptisa. (1998). *Investigation of the Failure of the Aznalcóllar Tailings Dam*.
- European Environment Agency. (n.d.). *EU-DEM Elevation Data (ver 1.1)*.
- Fontaine, D., & Martin, V. (2015). Tailings mobilization estimates for dam breach studies. *Proceedings of the Tailings and Mine Waste 2015, Vancouver, BC, October 26 to 28, 2015*, 342–356.
- Forest, M., & Brunner, G. (2020). *RAS Solution Blog Post: HEC-RAS Subgrid Bathymetry Theory and Application*. <https://www.kleinschmidtgroup.com/ras-post/hec-ras-subgrid-bathymetry-theory-and-application/>
- Fourie, A. B., Blight, G. E., & Papageorgiou, G. (2001). Static liquefaction as a possible explanation for the Merriespruit tailings dam failure. *Canadian Geotechnical Journal*, 38, 707–719. <https://doi.org/10.1139/cgj-38-4-707>
- France, J. W., Alvi, I. A., Miller, A. C., Williams, J. L., & Higinbotham, S. (2022). *Investigation of Failures of Edenville and Sanford Dams*.
- Francis, J. B. (1855). Part II. Experiments on the Flow of Water over Weirs, and in Short Rectangular Canals. In *Lowell Hydraulic Experiments* (pp. 71–143). Little, Brown and Company. Boston, Massachusetts, U.S.A.
- Franks, D. M., Stringer, M., Torres-Cruz, L. A., Baker, E., Valenta, R., Thygesen, K., Matthews, A., Howchin, J., & Barrie, S. (2021). Tailings facility disclosures reveal stability risks. *Scientific Reports*, 11(1), 1–7. <https://doi.org/10.1038/s41598-021-84897-0>
- Froehlich, D. C. (2008). Embankment Dam Breach Parameters and Their Uncertainties. *Journal of Hydraulic Engineering*, 134(12), 1708–1721.
[https://doi.org/10.1061/\(ASCE\)0733-9429\(2008\)134](https://doi.org/10.1061/(ASCE)0733-9429(2008)134)
- Froehlich, D. C. (2016). Predicting Peak Discharge from Gradually Breached Embankment Dam. *Journal of Hydraulic Engineering*, 21(11).
[https://doi.org/10.1061/\(ASCE\)HE.1943-5584.0001424](https://doi.org/10.1061/(ASCE)HE.1943-5584.0001424)
- Fundação Renova. (2016). *Updated Integrated Environmental Recovery Plan*.
- Gallart, F., Benito, G., Martin-Vide, J. P., Benito, A., Prio, J. M., & Regues, D. (1999). Fluvial geomorphology and hydrology in the dispersal and fate of pyrite mud

- particles released by the Aznalcóllar mine tailings spill. *Science of the Total Environment*, 242, 13–26.
- García, M. H., Macarthur, R. C., French, R., Miller, J., Bradley, J., Grindeland, T., & Hadley, H. (2008). Sedimentation Hazards. In M. H. Garcia (Ed.), *Sedimentation Engineering - Process; Measurements; Modelling; and Practice* (pp. 885–908). American Society of Civil Engineers.
- Genevois, R., & Tecca, P. R. (1993). The tailings dams of Stava (northern Italy); an analysis of the disaster. In R. N. Chowdhury & M. Sivakumar (Eds.), *Proceedings of the international conference on Environmental management, geo-water and engineering aspects* (pp. 23–36).
- Gens, A., & Alonso, E. E. (2006). Aznalcóllar dam failure Part 2: Stability conditions and failure mechanism. *Géotechnique*, 56(3), 185–201.
- Geospatial Information Authority of Japan. (2016). *DEM5A Elevation Data*.
- Ghahramani, N., Chen, H. J., Clohan, D., Liu, S., Llano-Serna, M., Rana, N. M., McDougall, S., Evans, S. G., & Take, W. A. (2022). A benchmarking study of four numerical runout models for the simulation of tailings flows. *Science of the Total Environment*, 827, 154244. <https://doi.org/10.1016/j.scitotenv.2022.154245>
- Ghahramani, N., Mitchell, A., Rana, N. M., McDougall, S., Evans, S. G., & Take, W. A. (2020). Tailings-flow runout analysis: examining the applicability of a semi-physical area – volume relationship using a novel database. *Natural Hazards and Earth System Sciences*, 20, 3425–3438.
- Gibson, S., Floyd, I., Sánchez, A., & Heath, R. (2021). Comparing single-phase, non-Newtonian approaches with experimental results: Validating flume-scale mud and debris flow in HEC-RAS. *Earth Surface Processes and Landforms*, 46(3), 540–553. <https://doi.org/10.1002/esp.5044>
- Gibson, S., Moura, L. Z., Ackerman, C., Ortman, N., Amorim, R., Floyd, I., Eom, M., Creech, C., & Alejandro, S. (2022). Prototype Scale Evaluation of Non-Newtonian Algorithms in HEC-RAS: Mud and Debris Flow Case Studies of Santa Barbara and Brumadinho. *Geosciences*, 12(3), 134. <https://doi.org/10.3390/geosciences12030134>
- Globo. (2019). Vale dam breaks in Brumadinho, MG. <https://g1.globo.com/mg/minas-gerais/noticia/2019/01/25/bombeiros-e-defesa-civil-sao-mobilizados-para-chamada-de-rompimento-de-barragem-em-brumadinho-na-grande-bh.ghtml>
- Golder Associates. (2016). *Update Report: Post-Event Environmental Impact Assessment Report*. Report No.: 1411734-124-R-Rev0-10000

- Goodell, C., & Brunner, G. (2012). *RAS Solution Blog Post and Comments: Flow spike after peak of dam breach floodwave*. <https://www.kleinschmidtgroup.com/ras-post/flow-spike-after-peak-of-dam-breach-floodwave/>
- Goodell, C., Johnson, D., Raeburn, R., Monk, S., Karki, A., & Lee, A. (2018). Probabilistic dam breach modelling using HEC-RAS and McBreach. *Proceedings of the 38th United States Society on Dams Annual Conference and Exhibition, Miami, Florida*.
- Goodell, C., & Wahlin, B. (2009). Dynamic and Level Pool Reservoir Drawdown-A Practical Comparison for Dam Breach Modeling. *Proceedings of the 33rd IAHR World Congress "Water Engineering for a Sustainable Environment"*.
- Google LLC. (2022). *Google Earth Pro* (7.3.4).
- Harder Jr, L. F., & Stewart, J. P. (1996). Failure of Tapo Canyon Tailings Dam. *Journal of Performance of Constructed Facilities*, 10(3), 109–114.
- Heiser, M., Scheidl, C., & Kaitna, R. (2017). Evaluation concepts to compare observed and simulated deposition areas of mass movements. *Computational Geosciences*, 21, 335–343. <https://doi.org/10.1007/s10596-016-9609-9>
- Hungr, O. (1995). A model for the runout analysis of rapid flow slides, debris flows, and avalanches. *Canadian Geotechnical Journal*, 32(4), 610–623. <https://doi.org/10.1139/t95-063>
- IGME. (2001). Regional geographical, geological, and hydrogeological framework of the Guadiamar river basin [in Spanish]. *Geological and Mining Bulletin of the Geological Mining Institute of Spain*, 13–34.
- Index. (2010, October 5). Sludge spill in Veszprém county. https://index-hu.translate.google/belfold/2010/10/04/izzapomles_vezsprem_megyeben/?p=4&x_tr_sl=hu&x_tr_tl=en&x_tr_hl=de
- Indra Sistemas S.A. (2015). *EU-DEM Upgrade Documentation EEA User Manual EU-DEM Upgrade*.
- Innis, S., Lynd, J., Kunz, N., & Reemeyer, L. (2021). Regional perspectives and trends of land at risk from tailings storage facility failures. In N. A. Beier, G. W. Wilson, & D. C. Sego (Eds.), *Proceeding of the Twenty-Fifth International Conference on Tailings and Mine Waste, 7-10 November 2021, Banff, Alberta, Canada*.
- International Commission on Large Dams. (2011). *Constitution of the International Commission on Large Dams*.
- International Commission on Large Dams. (2001). *Bulletin 121: Tailings Dams Risk of Dangerous Occurrences*.

- International Council on Mining & Metals. (2020). *Global Industry Standard on Tailings Management*.
- Ishihara, K., Ueno, K., Yamada, S., Yasuda, S., & Yoneoka, T. (2015). Breach of a tailings dam in the 2011 earthquake in Japan. *Soil Dynamics and Earthquake Engineering*, 68, 3–22. <https://doi.org/10.1016/j.soildyn.2014.10.010>
- Iverson, R. M. (2003). The debris-flow rheology myth. In R. & Chen (Ed.), *Debris-Flow Hazards Mitigation: Mechanics, Prediction, and Assessment* (pp. 303–314).
- Iverson, R. M. (2018). Discussion of “Oso, Washington, Landslide of March 22, 2014: Dynamic Analysis” by Jordan Aaron, Oldrich Hungr, Timothy D. Stark, and Ahmed K Baghdady. *Journal of Geotechnical and Geoenvironmental Engineering*, 144(9), 2015–2017. [https://doi.org/10.1061/\(ASCE\)GT.1943-5606.0001933](https://doi.org/10.1061/(ASCE)GT.1943-5606.0001933)
- Iverson, R. M., & George, D. L. (2019). Valid debris-flow models must avoid hot starts. *Proceedings of the 7th International Conference on Debris-Flow Hazards Mitigation*, 25–32.
- Iverson, R. M., & George, D. L. (2014). A depth-averaged debris-flow model that includes the effects of evolving dilatancy I. Physical basis. *Proceedings of the Royal Society of London. Series A, Mathematical and Physical Sciences*, 470(2170).
- Iverson, R. M., & George, D. L. (2016). Modelling landslide liquefaction, mobility bifurcation and the dynamics of the 2014 Oso disaster. *Géotechnique*, 66(3), 175–187.
- Jakob, M., Stein, D., & Ulmi, M. (2012). Vulnerability of buildings to debris flow impact. *Natural Hazards*, 60, 241–261. <https://doi.org/10.1007/s11069-011-0007-2>
- Janssen, C. (2016). *Manning's n Values for Various Land Covers to Use for Dam Breach Analyses by NRCS in Kansas*.
- Japan Aerospace Exploration Agency. (2021). *ALOS Global Digital Surface Model Version 3.2 Elevation Data*.
- Jefferies, M., Morgenstern, N. R., & Wates, J. (2019). *Report on NTSF Embankment Failure*. Report No. H356804-00000-22A-230-0001, Final
- Julien, P. Y., & Lan, Y. (1991). Rheology of Hyperconcentrations. *Journal of Hydraulic Engineering*, 117(3), 346–353.
- Lang, M., Pobanz, K., Renard, B., Renouf, E., & Sauquet, E. (2010). Extrapolation of rating curves by hydraulic modelling, with application to flood frequency analysis. *Hydrological Sciences Journal*, 55(6). <https://doi.org/10.1080/02626667.2010.504186>

- Liu, S., & Henderson, M. (2020). An Overview on Methodologies for Tailings Dam Breach Study. *Proceeding of the Twenty-Fourth International Conference on Tailings and Mine Waste*.
- Locat, P. (2022). Coulées dans les argiles sensibles de l'Est du Canada [Flows in the sensitive clays of Eastern Canada]. *8e Conférence Canadienne Sur La Géotechnique et Les Risques Naturels [8th Canadian Conference on Geotechnique and Natural Hazards]*, 12-15 June 2022, Québec City, Canada.
- Luino, F., & Graff, J. V. De. (2012). The Stava mudflow of 19 July 1985 (Northern Italy): a disaster that effective regulation might have prevented. *Natural Hazards and Earth System Sciences*, 12, 1029–1044. <https://doi.org/10.5194/nhess-12-1029-2012>
- Lumbroso, D., Davison, M., Body, R., Petkovšek, G., Wallingford, H. R., Park, H., & Ox, O. (2021). Modelling the Brumadinho tailings dam failure, the subsequent loss of life and how it could have been reduced. *Natural Hazards and Earth System Sciences*, 21, 21–37.
- Machado, N. C. (2017). *Back Analysis of the Floodwave Propagation from the Fundão Dam Rupture with Different Numerical Models and Simulation Hypotheses*. UNIVERSIDADE FEDERAL DE MINAS GERAIS.
- Mahdi, A., Shakibaeinia, A., & Dibike, Y. B. (2020). Numerical modelling of oil-sands tailings dam breach runout and overland flow. *Science of the Total Environment*, 703. <https://doi.org/10.1016/j.scitotenv.2019.134568>
- Martin, V., Adria, D., & Wong, H. (2022). Inundation Modelling of Non-Newtonian Tailings Dam Breach Outflows. *Proceedings of the 27th World Congress of the International Commission on Large Dams: Question 105*, 501.
- MapBiomass. (2018). *MapBiomass Collection 5.0 Landcover Data*. <https://mapbiomas.org/en/products>
- Martin, V., Fontaine, D., & Cathcart, J. (2015). Challenges with conducting tailings dam breach studies. *Proceedings of Tailings and Mine Waste 2015 Conference*, 314–328.
- Matsuda, N., Sugito, N., Ishiguro, S., Sano, S., Uchida, C., & Suzuki, Y. (2014). *Distribution map of tsunami run-up heights from the 2011 off the Pacific coast of Tohoku Earthquake - 1/25,000 compilation map*.
- McDermott, R. K., & Sibley, J. M. (2000). The Aznalcóllar Tailings Dam Accident - A Case Study. *Mineral Resources Engineering*, 9(1), 101–118.

- McDougall, S. (2017). 2014 Canadian Geotechnical Colloquium: Landslide runout analysis — current practice and challenges. *Canadian Geotechnical Journal*, 54, 605–620.
- McDougall, S., & Hungr, O. (2005). Dynamic modelling of entrainment in rapid landslides. *Canadian Geotechnical Journal*, 42(5), 1437–1448.
- Meadows, M., & Wilson, M. (2021). A Comparison of Machine Learning Approaches to Improve Free Topography Data for Flood Modelling. *Remote Sensing*, 13(2).
- Mecsi, J. (2013). Technical Analyses and Lessons of The Embankment Failure at the Ajka Red Mud Reservoir. *Proceedings of the Seventh International Conference on Case Histories in Geotechnical Engineering*, May, 66-77.
- Mitchell, A. D. (2021). *Modelling Variability in Mobility for Rapid Landslide Runout*. University of British Columbia.
- Moretti, L., Allstadt, K., Mangeney, A., Capdeville, Y., Stutzmann, E., & Bouchut, F. (2015). Numerical modeling of the Mount Meager landslide constrained by its force history derived. *Journal of Geophysical Research: Solid Earth*, 2579–2599. <https://doi.org/10.1002/2014JB011426>. Received
- Morgenstern, N. R., Vick, S. G., & Van Zyl, D. (2015). *Report on Mount Polley Tailings Storage Facility Breach*.
- Morgenstern, N. R., Vick, S. G., Viotti, C. B., & Watts, B. D. (2016). *Fundão Tailings Dam Review Panel Report on the Immediate Causes of the Failure of the Fundão Dam*.
- Morris, M. W., Hassan, M. A. A. M., & Vaskinn, K. A. (2007). Breach formation: Field test and laboratory experiments Breach formation: Field test and laboratory experiments. *Journal of Hydraulic Research*, 45, 9–1. <https://doi.org/10.1080/00221686.2007.9521828>
- Muramoto, Y., Uno, T., & Takahashi, T. (1986). Investigation of the Collapse of the tailings dam at Stava in the northern Italy [in Japanese]. *Annals of the DPRI*, 29A, 19–52.
- National Aeronautics and Space Administration. (2015). *Shuttle Radar Topography Mission*.
- National Assembly of Hungary (2011). *The environment caused by the rupture of the red mud reservoir near Kolontár, and the disclosure of responsibility related to a disaster and similar disasters in the future parliamentary investigation committee aimed at preventing about the result of this investigation*
- National Geographic Institute of Spain. (2019). *DTM05 Elevation Data*.

- National Oceanic and Atmospheric Administration. (1993). *Climatological Data for Camarillo Area, CA December 1993 and January 1994* (Issue December, p. 1993).
- Novell Morell, M. (2022). *Modelling of dam breach flows; past and future mine tailings dam cases*. Delft University of Technology.
- Nguyen, Q. D., & Boger, D. V. (1983). Yield Stress Measurement for Concentrated Suspensions. *Journal of Rheology*, 27(4), 321–349.
<https://doi.org/10.1122/1.549709>
- Van Niekerk, H. J., & Viljoen, M. J. (2005). Cause and Consequences of the Merriespruit and Other Tailings-Dam Failures. *Land Degradation & Development*, 201–212. <https://doi.org/10.1002/ldr.681>
- O'Brien, J. S., & Julien, P. Y. (1988). Laboratory Analysis of Mudflow Properties. *Journal of Hydraulic Engineering*, 114(8), 877–887.
- O'Brien, J. S. (1986). *Physical Processes, Rheology and Modelling of Mud Flows*. Colorado State University.
- O'Brien, J. S., Julien, P. Y., & Fullerton, W. T. (1993). Two-Dimensional Water Flood and Mudflow Simulation. *Journal of Hydraulic Engineering*, 119(2), 244–261.
- Oreskes, N., Shrader-Frechette, K., & Belitz, K. (1994). Verification, Validation, and Confirmation of Numerical Models in the Earth Sciences. *Science*, 263(5147), 641–646.
- Palu, M. C., & Julien, P. Y. (2019). Modeling the Sediment Load of the Doce River after the Fundão Tailings Dam Collapse, Brazil. *Journal of Hydraulic Engineering*, 145(5). [https://doi.org/10.1061/\(ASCE\)HY.1943-7900.0001582](https://doi.org/10.1061/(ASCE)HY.1943-7900.0001582)
- Palu, M. C. (2019). *Floodwave and Sediment Transport Assessment Along the Doce River After the Fundão Tailings Dam Collapse (Brazil)*. Colorado State University.
- Petley, D. (2019). *The speed of the Brumadinho tailings dam landslide*. The Landslide Blog. <https://blogs.agu.org/landslideblog/2019/02/04/brumadinho-tailings-dam-landslide/>
- Piciullo, L., Storrøsten, E. B., Liu, Z., Nadim, F., & Lacasse, S. (2022). A new look at the statistics of tailings dam failures. *Engineering Geology*, 303.
<https://doi.org/10.1016/j.enggeo.2022.106657>
- Pirulli, M., Barbero, M., Marchelli, M., & Scavia, C. (2017). The failure of the Stava Valley tailings dams (Northern Italy): numerical analysis of the flow dynamics and rheological properties. *Geoenvironmental Disasters*, 4.
<https://doi.org/10.1186/s40677-016-0066-5>
- Pudasaini, S. P., & Krautblatter, M. (2021). The mechanics of landslide mobility with erosion. *Nature Communications*, 12. <https://doi.org/10.1038/s41467-021-26959-5>

QGIS. (2021). *QGIS Białowieża* (3.22).

Ramalhoso, W., & Rebello, A. (2019). Dam breaks in Brumadinho and hits house; victims taken to BH. UOL. <https://noticias.uol.com.br/cotidiano/ultimas-noticias/2019/01/25/barragem-da-mineradora-vale-rompe-na-regiao-metropolitana-de-belo-horizonte.htm>

Rana, N. M., Ghahramani, N., Evans, S. G., McDougall, S., Small, A., & Take, W. A. (2021). Catastrophic mass flows resulting from tailings impoundment failures. *Engineering Geology*, 292(October 2020), 106262. <https://doi.org/10.1016/j.enggeo.2021.106262>

Rana, N. M., Ghahramani, N., Evans, S. G., McDougall, S., Small, A., & Take, W. A. (2021b). *A Comprehensive Global Database of Tailings Flows. Borealis, the Canadian Dataverse Repository*.

Rana, N. M., Ghahramani, N., Evans, S. G., Small, A., Skermer, N., McDougall, S., & Take, W. A. (2022). Earth-Science Reviews Global magnitude-frequency statistics of the failures and impacts of large water-retention dams and mine tailings impoundments. *Earth-Science Reviews*, 232(July), 104144. <https://doi.org/10.1016/j.earscirev.2022.104144>

Rickenmann, D. (1999). Empirical relationships for debris flow. *Natural Hazards*, 19(1), 47–77.

Rickenmann, D. (2001). Comparison of bed load transport in torrents and gravel bed streams. *Water Resources Research*, 37(12), 3295–3330.

Rico, M., Benito, G., & Díez-Herrero, A. (2008). Floods from tailings dam failures. *Journal of Hazardous Materials*, 154(1–3), 79–87. <https://doi.org/10.1016/j.jhazmat.2007.09.110>

Ritter, A. (1892). The propagation of water waves [in German]. *Vereine Deutscher Ingenieure Zeitschrift*, 36(2), 947–954.

Robertson, P. K., de Melo, L., Williams, D. J., & Wilson, G. W. (2019). *Report of the Expert Panel on the Technical Causes of the Failure of Feijão Dam I*.

Robson, P. (2017). *The River is Dead*. London Mining Network. London, United Kingdom

Rollason, E., Bracken, L. J., Hardy, R. J., & Large, A. R. G. (2018). The importance of volunteered geographic information for the validation of flood inundation models. *Journal of Hydrology*, 562, 267–280. <https://doi.org/10.1016/j.jhydrol.2018.05.002>

Rykiel, E. J. (1996). Testing ecological models: the meaning of validation. *Ecological Modelling*, 90, 229–244.

- Santamarina, B. J. C., Torres-Cruz, L. A., & Bachus, R. C. (2019). Why coal ash and tailings dam disasters occur. *Science*, 364(6440), 526.
- Sanz-Ramos, M., Bladé, E., Dolz, J., & Sánchez-Juny, M. (2022). Revisiting the Hydraulics of the Aznalcóllar Mine Disaster. *Mine Water and the Environment*, 41, 335–356. <https://doi.org/10.1007/s10230-022-00863-w>
- Schoeman, J. (2018). A Conceptual Elevation versus Volume Curve Determination Method For Tailings Dam Breach Studies. *Proceedings of the SANCOLD Annual Conference and AGM 2018, November 7-9, 2018, Cape Town, South Africa*.
- Schoklitsch, A. (1917). About dam break waves [in German]. *Itzungberichten Der Königliche Akademie Der Wissenschaften*, 126, 1489–1514.
- SAIH (2022). *Hydrology Data for the A39 El Guijo Gauge for April 24 to April 27, 1998 (Personal Communication)*. Automatic System of Hydrological Information
- Small, A., James, M., & Al-Mamun, M. (2017). Advancing the State of Practice for Tailings Dam Breach Assessment using Empirical Correlations. *Proceedings of the Canadian Dam Association 2017 Annual Conference, Kelowna, BC, Canada, 16-18 October 2017*.
- SNC-Lavalin Inc. (2015). *Post-Event Environmental Impact Assessment Appendix A: Hydrotechnical and Geomorphological Impact Assessment*. Report No. 621717 V-01
- Stava 1985 Foundation. (n.d.). *The Collapse of the Merriespruit Mining Dump - 1994*. Retrieved September 27, 2021, from <https://www.stava1985.it/il-disastro-di-merriespruit-in-sud-africa/>
- Stava 1985 Foundation. (n.d.). *The Collapse of the Aznalcóllar Mining Dump - 1998*. Retrieved May 16, 2022, from <https://www.stava1985.it/il-crollo-della-discarica-mineraria-di-aznacollar-spagna/>
- Stava 1985 Foundation. (n.d.). *The Collapse of the Taoshi Mining Dump - 2008*. Retrieved August 19, 2022, from <https://www.stava1985.it/il-disastro-di-taoshi/>
- Stewart, J. P., Bray, J. D., Seed, R. B., & Sitar, N. (1994). *Preliminary Report on the Principal Geotechnical Aspects of the January 17, 1994, Northridge Earthquake*.
- Suzuki, Y., Ishiguro, S., Usui, T., Kaizu, M., Goto, H., Sugito, N., Nakata, T., Hirouchi, D., Hori, K., Matsuda, N., Watanabe, M., & Une, H. (2011). *March 11, 2011, Tsunami Damage Map Associated with the Tohoku Earthquake*.
- Takahashi, T. (2014). Chapter 7: Debris flow disasters and their reproduction by computer simulations. In *Debris Flow: Mechanics, Prediction and Countermeasures* (2nd ed., p. 572). CRC Press.

- Takahashi, T. (1980). Debris flow on prismatic open channel. *Journal of the Hydraulics Division*, 106(3), 381–396.
- Taylor, A. (2011, September). A Flood of Red Sludge, One Year Later. *The Atlantic*.
<https://www.theatlantic.com/photo/2011/09/a-flood-of-red-sludge-one-year-later/100158/>
- Turi, D., Pusztai, J., & Nyari, I. (2013). Causes and Circumstances of Red Mud Reservoir Dam Failure In 2010 at MAL Zrt Factory Site in Ajka, Hungary. *Proceedings of the Seventh International Conference on Case Histories in Geotechnical Engineering*, 1–14.
- Turner, J., Ellithorpe, A., Ng, A., & Krupa, A. (2022). Impact of topography errors on Tailings Dam Breach Analysis. *Proceedings of the Tailings 2022 Online Conference, July 6-8, 2022*.
- USACE. (2022). *HEC-RAS (6.2)*. U.S. Army Corps of Engineers Institute for Water Resources
- USACE. (2021). *HEC-RAS (6.1)*. U.S. Army Corps of Engineers Institute for Water Resources
- USACE. (2007). *Risk Assessment for Dam Safety*. U.S. Army Corps of Engineers.
- U.S. Department of the Interior Bureau of Reclamation (USBR). (1988). *Downstream Hazard Classification Guidelines*.
- USBR. (2015). *Reclamation Consequence Estimating Methodology: Guidelines for Estimating Life Loss for Dam Safety Risk Analysis*. U.S. Department of the Interior, Bureau of Reclamation
- USGS. (2018). *SOCAL Wildfire QL2 DEM Elevation Data*. U.S. Geological Survey.
- UNESCO. (1981). *Avalanche Atlas*. United Nations Educational Scientific and Cultural Organization
- Vick, S. G. (1990). *Planning, Design, and Analysis of Tailings Dams* (2nd ed.). BiTech Publishers Limited. Vancouver, British Columbia, Canada
- Wagener, F. (1997). The Merriespruit slimes dam failure: Overview and lessons learnt. *Journal of South African Institute of Civil Engineering*, 39, 11–15.
- Wahl, T. L. (1998). Prediction of Embankment Dam Breach Parameters: Literature Review and Needs Assessment, Dam Safety Research Report. In *Water Resources Research Laboratory* (Issue July).
- Wahl, T. L. (2004). Uncertainty of Predictions of Embankment Dam Breach Parameters. *Journal of Hydraulic Engineering*, 130(5), 389–397.
[https://doi.org/10.1061/\(asce\)0733-9429\(2004\)130:5\(389\)](https://doi.org/10.1061/(asce)0733-9429(2004)130:5(389))

- Wahl, T. L. (2014). *Evaluation of Erodibility-Based Embankment Dam Breach Equations*.
- Walder, J. S., Iverson, R. M., Godt, J. W., Logan, M., & Solovitz, S. A. (2015). Overtopping of Non-cohesive Earthen Dams. *Water Resources Research*, 51, 6701–6724. <https://doi.org/10.1002/2014WR016620>. Received
- Walder, J. S., & O'Conner, J. E. (1997). Methods for predicting peak discharge of floods caused by failure of natural and constructed earth dams. *Water Resources Research*, 33(10), 2337–2348.
- Walsh, A., McDougall, S., Evans, S. G., & Take, W. A. (2021). Effect of Upstream Dam Geometry on Peak Discharge During Overtopping Breach in Non-cohesive Homogeneous Embankment Dams; Implications for Tailings Dams Water Resources Research. *Water Resources Research*, 1–22. <https://doi.org/10.1029/2020WR029358>
- Walsh, A. R. (2019). *Physical Modelling of Tailings Dam Breach*. Queen's University.
- WSC (n.d.). *Hydrologic Data for 08KH011 for 3-5 August 2014 (Personal Communication)*. Water Survey of Canada
- Wei, Z., Yin, G., Wang, J. G., Wan, L., & Li, G. (2013). Design, construction and management of tailings storage facilities for surface disposal in China: case studies of failures. *Waste Management & Research*, 31(2), 106–112. <https://doi.org/10.1177/0734242X12462281>
- Wentworth, C. K. (1922). A Scale of Grade and Class Terms for Clastic Sediments. *Journal of Geology*, 30(5), 377–392.
- Xinhua (2019) 200 people missing after tailings dam collapse in Brazil. <https://global.chinadaily.com.cn/a/201901/26/WS5c4b7997a3106c65c34e69bd.html>
- Zhao, H., & Kowalski, J. (2020). Topographic uncertainty quantification for flow-like landslide models via stochastic simulations. *Natural Hazards and Earth System Sciences*, 20, 1441–1461. <https://doi.org/https://doi.org/10.5194/nhess-20-1441-2020>
- Zheng, Z. (2018). *Research on rheological properties of tailings and dynamic properties of dam break in copper-iron tailings pond [in Mandarin]*. Shanghai Jiaotong University.
- Zheng, Z., Lei, L., Liu, N., He, J., & Xing, A. (2017). Dynamic analysis characteristics of dam-break of tailings pond at Tonglūshan copper-iron mine in Hubei Daye. *Metal Mines*, 12, 136–141. <https://doi.org/10.19614/j.cnki.jsks.2017.12.027>
- Zhuang, Y., Jin, K., Cheng, Q., Xing, A., & Luo, H. (2022). Experimental and numerical investigations of a catastrophic tailings dam break in Daye, Hubei, China. *Bulletin*

of Engineering Geology and the Environment, 81(9).
<https://doi.org/10.1007/s10064-021-02491-0>

Zubrycky, S. (2020). *Spatial Impact Trends on Debris Flow Fans in Southwestern British Columbia*. University of British Columbia.

Appendix A: Tailings Dam Breach and Runout Database

Table A.1 Investigated Tailings Storage Facilities and their Impoundment Characteristics

| ID | TSF (Colloquial Name) | Country | TSF Arrangement | Dam Raising Method ¹ | Primary Type of Tailings ¹ | Regulatory Dam Height ² (m) | Impounded Volume ¹ (m3) |
|-----|---|--------------|------------------------------------|---------------------------------------|--|--|--|
| 1 | Prestavèl (Stava) | Italy | Stepped Side-Hill | - | Fluorite | 55 | 300,000 |
| 1i | <i>Upper Basin</i> | | <i>Side-hill</i> | <i>Upstream</i> | | 33 | 192,000 |
| 1II | <i>Lower Basin</i> | | <i>Side-hill</i> | <i>Upstream</i> | | 22 | 120,000 |
| 2 | Gillibrand No. 6 (Tapo Canyon) | USA | Side-hill | Upstream | Sand, Gravel, and Concrete Wash | 24 | Unknown |
| 3 | Harmony 4A ³ (Merriespruit) | South Africa | Ring-Dyke ³ | Upstream | Gold | 31 | 7,000,000 |
| 4 | Aznalcóllar ⁴ (Los Frailes) | Spain | Composite Side-Hill | - | Zinc, Lead, Copper, and Silver | 28 | 15,000,000 ⁴ |
| 4i | <i>North Pyroclastic Pond</i> | | <i>Side-hill</i> | <i>Downstream</i> | | | 10,260,000 |
| 4ii | <i>South Pyritic Pond</i> | | <i>Side-hill</i> | <i>Downstream</i> | | | 4,740,000 |
| 5 | Tashan (Taoshi or Xiangfen) | China | Cross-Valley | Upstream | Iron | 51 | 290,000 |
| 6 | MAL Reservoir X ⁵ (Ajka or Kolontár) | Hungary | Ring-Dyke ⁵ | Downstream | Bauxite | 27 | 4,200,000 |
| 7 | Kayakari | Japan | Cross-Valley | Upstream | Gold and Silver | 36 | 400,000 |
| 8 | Mount Polley | Canada | Side-hill | Centreline / Upstream Hybrid | Copper and Gold | 57 | 73,500,000 |
| 9 | Fundão ⁶ (Mariana, Bento Rodrigues, or Samarco) | Brazil | Cross-Valley ⁶ | Upstream | Iron | 106 | 56,400,000 |
| 10 | Tonglūshan North Compartment ⁷ | China | Ring-Dyke ⁷ | Upstream | Copper | 25 | 8,700,000 |
| 11 | Cadia NTSF ⁸ | Australia | Side-Hill ⁸ | Upstream | Gold | 94 | Unknown ⁸ |
| 12 | Feijão Dam I (Brumadinho) | Brazil | Cross-Valley / Side-Hill Hybrid | Upstream | Iron | 87 | 12,726,000 |

Table A.1 Notes:

1. Re-validated from Ghahramani et al. (2020) and Rana et al. (2021b).
2. The Regulatory Dam Height is the maximum dam height for the TSF compartment at the time of the breach.
3. The Harmony TSF was a composite side-hill TSF with three compartments (4A, 4B, and 4C) at the time of the breach (Van Niekerk and Viljoen, 2005). The breach only occurred at the 4A compartment, therefore only Harmony 4A is considered in this thesis.
4. Sanz-Ramos et al. (2022) argued new evidence suggests a total impounded volume between 20,000,000 m³ to 28,000,000 m³.
5. The MAL Red Mud Reservoir was a composite ring-dyke with seven compartments (Reservoirs VI through X and Xa) at the time of the breach (Turi et al., 2013). The breach only occurred at Reservoir X; therefore, the breach is comparable to a tailings dam breach at a single compartment TSF.
6. The Fundão TSF was designed to have two compartments (sand and slimes), but due to the design changes, limited size of internal embankments, and poor operation practices there was substantial mixing of the sand and slimes tailings (Morgenstern et al., 2015). Therefore, the breach is comparable to a tailings dam breach at a single compartment TSF.
7. The Tonglüshan TSF was a composite ring-dyke with two compartments (North and South) at the time of the breach (Zheng, 2018). The breach only occurred at the North compartment; therefore, the breach is comparable to a tailings dam breach at a single compartment TSF.
8. The Cadia TSF was a stepped side-hill TSF with two compartments (NTSF and STSF) at the time of the flows (Jefferson et al., 2019). The breaches only occurred at the NTSF compartment; therefore, the breach is comparable to a tailings dam breach at a single compartment TSF. The regulatory dam height for the entire stepped facility is 164 (Franks et al., 2020). The volume of the STSF is also unknown.

Table A.2 Investigated Tailings Dam Breach and Runout Events with their High-Level Classifications and Characteristics

| ID | Breach Event | Date of Breach | CDA Class ¹ | Travel Path Confinement ^{1,2} | Zone 1 Runout Distance ¹ (m) | Zone 1 Inundation Area ¹ (m ²) |
|-----|--|----------------|------------------------|--|---|---|
| 1 | Prestavél ³ (Stava) | 19-Jul-85 | 1A | Channelized | 4,800 | 650,000 ² |
| 1i | <i>Upper Basin</i> | | 1A | | | |
| 1ii | <i>Lower Basin</i> | | 1A | | | |
| 2 | Gillibrand No. 6 (Tapo Canyon) | 17-Jan-94 | 1A or 2A | Channelized | 730 | 30,000 |
| 3 | Harmony 4A (Merriespruit) | 22-Feb-94 | 1A | Unconfined | 2,200 | 990,000 |
| 4 | Aznalcóllar ⁴ (Los Frailes) | 25-Apr-98 | 1A | Channelized / Unconfined Hybrid | 29,000 ³ | 16,000,000 ³ |
| 4i | <i>North Pyroclastic Pond</i> | | 1B | | | |
| 4ii | <i>South Pyritic Pond</i> | | 1A | | | |
| 5 | Tashan (Taoshi or Xiangfen) | 08-Sep-08 | 1A | Unconfined | 2,300 | 430,000 |
| 6 | MAL Reservoir X ⁵ (Ajka or Kolontár) | 04-Oct-10 | 1A | Channelized / Unconfined Hybrid | 17,800 ⁵ | 7,300,000 ⁵ |
| 7 | Kayakari ⁶ | 11-Mar-11 | 2A | Channelized | 1,800 ⁵ | 84,000 ⁵ |
| 8 | Mount Polley | 04-Aug-14 | 1B | Channelized with terminal obstruction | 9,000 | 2,000,000 |
| 9 | Fundão (Mariana, Bento Rodrigues, or Samarco) | 05-Nov-15 | 2A | Channelized | 99,000 | 2,100,000 |
| 10 | Tonglüshan North Compartment ⁷ | 12-Mar-17 | 1A or 2A or 2B or 2A | Unconfined with partial terminal obstruction | 500 ⁶ | 270,000 |
| 11a | Cadia NTSF Event I ⁸ | 09-Mar-18 | 2A or 2B | Unconfined | 380 ⁷ | 97,000 ⁸ |
| 11b | Cadia NTSF Event II ⁸ | 11-Mar-18 | 2A | Unconfined | 520 ⁷ | 88,000 ⁸ |
| 12 | Feijão Dam I ⁹ (Brumadinho) | 25-Jan-19 | 2A | Channelized | 9,000 | 3,040,000 ⁹ |

Table A.2 Notes:

1. Re-validated from Ghahramani et al. (2020) and Rana et al. (2021b).
2. Channelized / Unconfined Hybrid indicates the tailings flow were limited to a wide low slope valley. Therefore, there was only one main flow path, but the width and slope of the valley does not produce the high stresses and destructiveness described in Ghahramani et al. (2020) and Rana et al. (2021).
3. Ghahramani et al. (2022) updated this from 500,000 m² in Ghahramani et al. (2020). This thesis found evidence that suggests Ghahramani et al. (2022) may have overestimated the width of the Zone 1 runout by 15 m along 4,200 m, leading to an inundation area overestimate by approximately 63,000 m². Further investigation is required to validate these estimates, however.
4. Sanz-Ramos et al. (2022) presented new evidence that suggests the Zone 1 Runout Distance and Inundation Area are approximately 65,000 m and 46,000,000 m² respectively.
5. Ghahramani et al. (2022) originally reported an inundation area of 6,000,000 m² but was later updated to 7,300,000 for unpublished work. This thesis found evidence that suggests they may have underestimated the extent of Zone 1. The Zone 1 runout distance and inundation area may be large as 50,700,000 m and 11,000,000 m². Further investigation is required to validate these estimates.
6. Ghahramani et al. (2022) estimated a Zone 1 inundation area of 150,000 m². This thesis found evidence that suggests they may have overestimated the extent of Zone 1, due to overlap with the Tōhoku-Pacific Ocean tsunami impact area (as mapped by Suzuki, Sugito, et al., 2011). The Zone 1 was updated in this thesis in consideration of the overlap with the tsunami to the values presented in the table.
7. The Tonglūshan runout distance following the likely tailings flood wave front could be considered as high as 800 m.
8. The Cadia NTSF experienced two separate events (Jefferson et al., 2019), therefore they are separated for the work in thesis. A novel Zone 1 was mapped for each event as a refinement of the combined Zone 1 for both events from Ghahramani et al. (2020).
9. The Zone 1 inundation area was updated from 2,700,000 m² to 3,040,000 m² by Ghahramani et al. after the publication of Ghahramani et al. (2020) for later unpublished work. The updated inundation area is reported here.

Table A.3 Primary Data Sources and References listed by Event (Page 1 of 2)

| ID | Breach Event | Government or Technical Reports and Data | Academic Articles, Theses, and Textbooks | News and Civilian Sources |
|----|------------------------------------|--|---|--|
| 1 | Prestavèl (Stava) | None | Muramoto et al., 1986 Berti et al., 1988 Genevois & Tecca, 1993 Chandler & Tosatti, 1995 Van Niekerk & Viljoen, 2005 Luino and De Graff, 2012 Takahashi, 2014 Pirulli et al., 2017 | Stava 1985 Foundation, n.d. |
| 2 | Gillibrand No. 6 (Tapo Canyon) | Stewart et al., 1994 NOAA, n.d. (Climate Data) | Harder & Stewart, 1996 | None |
| 3 | Harmony 4A (Merriespruit) | None | Wagener, 1997 Duvenhage, 1998 Fourie et al., 2001 Blight & Fourie, 2005 Van Niekerk & Viljoen, 2005 | AP Archive, 2015 Stava 1985 Foundation, n.d. |
| 4 | Aznalcóllar (Los Frailes) | Eptisa, 1998 IGME, 2001 Ayala-Carcedo, 2004 SAIH, 2022 (Hydrology Data) | Gallart et al., 1999 McDermott & Sibley, 2000 Alonso & Gens, 2006a Alonso & Gens, 2006b Gens & Alonso, 2006 Sanz-Ramos et al., 2022 | Engels, n.d., (Tailings.info) Stava 1985 Foundation, n.d. |
| 5 | Tashan (Taoshi or Xiangfen) | None | Wei et al., 2013 | Stava 1985 Foundation, n.d. |
| 6 | MAL Reservoir X (Ajka or Kolontár) | National Assembly of Hungary Investigation Committee, 2011 | Turi et al., 2013 Mecsi, 2013 Bánvölgyi, 2018 | Taylor et al., 2011 (The Atlantic) Index, 2010 |

Table A.3 Primary Data Sources and References listed by Event (Page 2 of 2)

| ID | Breach Event | Government or Technical Reports and Data | Academic Articles, Theses, and Textbooks | News and Civilian Sources |
|-------------|--|---|--|-------------------------------|
| 7 | Kayakari | Suzuki et al., 2011 Matsuda et al., 2014 | Ishihara et al., 2015 | None |
| 8 | Mount Polley | Morgenstern et al., 2015 BCMCM, 2015 SNC-Lavalin, 2015 Golder, 2016 WSC, n.d. (Hydrology Data) Cariboo Regional District, 2015 (Video Footage) | Cuervo et al., 2017 | None |
| 9 | Fundão (Mariana, Bento Rodrigues, or Samarco) | CPRM, 2015 Morgenstern et al., 2016 Fundação Renova, 2016 Robson, 2017 | Arcuri et al., 2015 Machado, 2017 Palu & Julien (2019) Palu, 2019 | None |
| 10 | Tonglūshan North Compartment | None | Zheng et al., 2017 Zheng, 2018 Zhuang et al., 2021 | None |
| 11a and 11b | Cadia NTSF Event I and Event II | Jefferies et al., 2019 | None | None |
| 12 | Feijão Dam I (Brumadinho) | CPRM, 2019 Robertson et al., 2019 National Water and Sanitation Agency of Brasil, n.d. (Hydrology Data) | de Lima et al., 2020 | Petley, 2019 (Landslide Blog) |

Table A.3 Notes:

1. Observations, commentary, and data from Ghahramani et al. (2020) and Rana et al., (2021a & 2021b) were used for all events in this thesis.
2. See the Reference section within the body of this thesis for full references details.

Table A.4 Outflow Volumes

| ID | Tailings Solids (V _s in m ³) | Interstitial Water (V _i in m ³) | Supernatant Pond ¹ (V _P in m ³) | Total Outflow (V _{Out} in m ³) | Discharge Mechanism ² | Confidence in Tailings Volume ³ | Confidence in Void Ratio ³ | Confidence in Supernatant Pond Volume ³ |
|----------------|--|---|--|--|----------------------------------|--|---------------------------------------|--|
| 1 | 88,300 | 76,900 | 20,000 | 185,200 | Liquefied Flow | High | High | Moderate |
| 1i | 56,100 | 48,900 | 11,800 | 116,800 | Liquefied Flow | | | |
| 1ii | 32,200 | 28,000 | 8,200 | 68,400 | Liquefied Flow | | | |
| 2 | 27,500 | 27,500 | 0 | 55,000 | Liquefied Flow | Moderate | Moderate | Moderate |
| 3 | 288,000 | 242,000 | 85,000 | 615,000 | Mostly Liquefied Flow | Moderate | Moderate | Moderate |
| 4 ⁴ | 777,400 | 532,600 | 5,440,000 | 6,750,000 | Mostly Erosion | Very Low. See Note 4. | Low | Low |
| 4i | 676,500 | 473,500 | 3,720,000 | 4,870,000 | Erosion | | | |
| 4ii | 100,900 | 59,100 | 1,720,000 | 1,880,000 | Liquefied Flow | | | |
| 5 | Unknown | Unknown | Unknown | 190,000 | Liquefied Flow | Moderate | Very Low | Very Low |
| 6 | 180,000 | 180,000 | 840,000 | 1,200,000 | Mostly Erosion | Low | Low | High |
| 7 | 20,500 | 20,500 | 0 | 41,000 | Liquefied Flow | High | Moderate | High |
| 8 ⁵ | 7,900,000 ⁵ | 6,500,000 | 10,600,000 | 25,000,000 | Erosion | High | High | High |
| 9 | 19,280,000 | 12,920,000 | 0 | 32,200,000 | Liquefied Flow | High | High | High |
| 10 | 265,000 | 235,000 | 0 | 500,000 | Mostly Liquefied Flow | Moderate | Moderate | Moderate |
| 11a | 737,100 | 432,900 | 0 | 1,170,000 | Mostly Slumped | High | High | High |
| 11b | 100,800 | 59,200 | 0 | 160,000 | Mostly Liquefied Flow | High | High | High |
| 12 | 5,597,580 | 4,053,420 | 0 | 9,651,000 | Liquefied Flow | High | High | High |

Table A.4 Notes:

1. This refers to the supernatant pond volume that discharged during the breach, not the impounded supernatant pond volume at the time of the breach.
2. Assigned tailings transport mechanism (i.e., liquefied, eroded, or slumped) is based on qualitative or quantitative information from previous work. When “mostly” is used, it indicates that the tailings are estimated to have predominantly discharged through a single mechanism, but a limited volume of tailings may have discharged by another transport mechanism. See Appendix B for specific sources and reasoning to support each classification.
3. The assigned confidence for each volume is based on subjective assessment of the data and information used to estimate the volumes in previous work or the current thesis. The confidence in tailings volume refers to the confidence in the sum of the tailings solids and interstitial water. The confidence in the void ratio refers to the relative proportion of tailings solids and interstitial water. See Appendix B for specific sources and reasoning to support each classification.
4. Sanz-Ramos et al. (2022) presented new evidence that suggests the total outflow volume is approximately 11.5 M m³ to 15.4 M m³. The investigation for Aznalcóllar for this thesis was completed prior to Sanz-Ramos et al. and was not updated due to time restraints. the total outflow volume requires additional investigation and the volumes presented here are likely erroneous. They are included only for reference to values used in the HEC-RAS model
5. The tailings solids volume presented here for the Mount Polley event includes 600,000 m³ of dam construction materials

Table A.5 Breach Processes

| ID | Failure Conditions ¹ | Failure Mechanism ¹ | Dominant Breach Process ² | Initiation Time | Formation Time ³ (T _f) | Outflow Duration |
|-----|--|--|--------------------------------------|---------------------------------|---|------------------|
| 1 | Heavy antecedent rainfall. Inadequate drainage. Steep dam slope. | Slope instability / static liquefaction of the tailings | Cascade Process II | None | - | - |
| 1i | | | Process II | None | - | 30 s |
| 1ii | | | Process II | None | - | 30 s |
| 2 | Saturated and loose tailings | Earthquake induced liquefaction of the tailings. | Process II | None | - | Unknown |
| 3 | Saturated and loose tailings. Heavy antecedent rainfall | Slope instability triggered by overtopping and erosion | Process II | 1.5 hrs to 2 hrs | - | Unknown |
| 4 | Weak overconsolidated foundation layer | Foundation failure along low-strength glaciolacustrine layer, leading to overtopping and erosion | Process I | None | 2 hrs | 7 hrs |
| 5 | Steep dam slopes. Saturated tailings. Excessive supernatant pond | Slope instability / static liquefaction, possibly initiated by a rainfall event | Process II | Unknown (Likely little to none) | - | Unknown |
| 6 | Heavy antecedent rainfall. Weak foundation. Light bonded (brittle) dam materials. | Foundation and brittle dam failure leading to erosional failure | Process I / Process II Hybrid | 12 mins | 15 mins | 15 mins |
| 7 | Saturated tailings | Extraordinarily strong earthquake induced liquefaction | Process II | None | - | Unknown |
| 8 | Steep dam slopes, weak foundation layer, large volume of water in the supernatant pond | Foundation failure along low-strength glaciolacustrine layer, leading to overtopping and erosion | Process I | None | 3.5 hrs | 15 hrs |
| 9 | Loose, saturated tailings. Lateral extrusion of slimes | Slope instability / static liquefaction of the tailings | Process II | None | - | Unknown |
| 10 | Unknown | Underground mining activity leading to foundation subsidence and failure | Process II | Unknown (Likely little to none) | - | Unknown |
| 11a | Weak foundation layer | Foundation failure leading to static liquefaction of tailings | Process II | 8 hrs | - | Unknown |
| 11b | | | Process II | None | - | Unknown |
| 12 | Loose, saturated, and lightly bonded (brittle) tailings. Steep dam slope | Slope instability / static liquefaction of the tailings | Process II | None | - | 5 mins |

Table A.5 Notes:

1. The failure conditions and mechanisms listed here are simplified summaries for each event. Refer to the descriptions in Appendix B and the references therein for a full sequence of the failure conditions and mechanism.
2. The dominant breach process was determined based on the sequence of events during the breach within technical reports or academic literature.
3. The formation time for Process II breaches was considered to be instantaneous, or 0 seconds.

Table A.6 Breach Heights and Trapezoid Breach Geometries

| ID | Dam Height at Breach Location (H_{DB} in m) | Crest Height ¹ (H_c in m) | Breach Height ¹ (H_B in m) | Slab Breach Height ¹ (H_S in m) | Bottom breach width (B_B in m) | Top breach width (B_T in m) | Left breach side slope (Z_L at xH:1V) | Right breach side slope (Z_R at xH:1V) | Confidence in Breach Geometry ² | Confidence in Hydraulic Control ² |
|-----|--|---|--|---|-----------------------------------|--------------------------------|--|---|--|--|
| 1i | 33 | 29 | 22 | - | 50 | 148 | 2.4 | 2.0 | High | Moderate |
| 1ii | 22 | 19 | 13 | - | 10 | 220 | 8.5 | 7.5 | High | Moderate |
| 2 | 24 | 24 | 12 ³ | - | 42 | 145 | 2.4 | 6.5 | High | Low |
| 3 | 31 | 31 | 27 ⁴ | - | 55 | 150 | 1.75 | 1.75 | Moderate | High |
| 4 | 28 | 28 | 26 ⁵ | - | 56 | 84 | 0.50 | 0.50 | Low | High |
| 5 | 50.7 | 25 | 17 | - | 100 | 194 | 2.75 | 2.75 | Low | Low |
| 6 | 22 | 22 | 22 ⁶ | - | 60 | 60 | 0.00 | 0.00 | Moderate | High |
| 7 | 36 | 24 | - | 12 | 50 | 50 | 0.00 | 0.00 | Moderate | Low |
| 8 | 40 | 40 | 36 ⁷ | - | 42 | 260 | 1.75 | 3.90 | High | High |
| 9 | 106 | 94 | 94 | - | 180 | 650 | 2.50 | 2.50 | Low | Moderate |
| 10 | 25 | 25 | 12 ⁸ | - | 235 | 260 | 0.00 | 0.00 | Low | High |
| 11a | 68 | 68 | - | 20 ⁹ | 240 | 300 | 1.25 | 1.25 | High | Low |
| 11b | 68 | 68 | - | 24 | 30 | 30 | 0.00 | 0.00 | High | Low |
| 12 | 87 | 80 | 80 | - | 100 | 560 | 2.88 | 2.88 | Moderate | High |

Table A.6 Notes:

1. See Chapter 3 within the body of this thesis for a definition for the various heights and where they are applicable.
2. The assigned confidence is based on subjective assessment of the data and information used to estimate the breach geometry in previous work or the current thesis. The confidence in breach geometry refers to the precision or data used to estimate the breach heights and trapezoid breach geometry (e.g., survey information versus photographs). The confidence in hydraulic control refers to the complexity and subjectivity of the true hydraulic control. See Appendix B for specific sources and reasoning to support each classification.
3. The Gillibrand Pond No. 6 Event breach channel had a tailings deposition depth around 12 m, indicating the breach height may include an additional 12 m.
4. The Harmony 4A Event breach channel had a tailings deposition depth around 4 m, indicating the breach height may include an additional 4 m.
5. The Aznalcóllar breach height here excludes the approximately 2 m subsidence during the foundation failure.
6. The water surface elevation in MAL Reservoir X was 215.88 m at the time of failure, therefore the height of water above breach bottom is approximately 20.88 m.
7. The Mount Polley breach height here excludes the approximately 4 m subsidence during the foundation failure. The water surface elevation was 2.3 m below the crest at the time of failure, therefore the height of water above breach bottom is approximately 37 m.
8. The Tonglūshan breach channel had a tailings deposition depth around 4 m, indicating the breach height may include an additional 4 m.
9. Jefferies et al. (2019) estimated the true failure surface originated in the foundation for Cadia Event I. The breach height therefore could have included an additional 48 m, however the Event I slump self-dammed and limited the slab breach height to 20 m.

Table A.7 Runout Parameters

| ID | Fluid Yield Stress ¹ (τ_y in Pa) | Fluid Dynamic Viscosity ¹ (μ in Pa s) | Representative Particle Size (d_s in mm) | Tailings Particle Density ² (ρ_s in kg/m ³) | Landcover Types and Selected Manning's Coefficients ³ | Confidence in Calibrated Yield Stress and Viscosity ⁴ |
|-------------------|--|--|--|---|--|--|
| 1 ⁵ | 3.2 | 1.8 | 0.02 | 2,890 | Fields: 0.04 Treed Regions: 0.08 Semi-Urban: 0.08 | Moderate |
| 2i ⁶ | 4,000 | 2 | 0.06 | Unknown | Moderately Vegetated Riparian Zone: 0.06 | Very Low |
| 2ii ⁶ | 800 | 50 | | | | Very Low |
| 3 | 250 | 4 | 0.1 | Unknown | Suburban region: 0.08 Wetlands: 0.08 | High |
| 4 ⁷ | 2.5 | 0.4 | 0.1 ⁷ | 2,700 ⁷ | Lightly vegetated floodplains: 0.055 | Very Low |
| 4i | | | 0.1 | 2,700 | | |
| 4ii | | | 0.01 | 4,300 | | |
| 5 | 800 | 25 | Unknown | Unknown | Fields: 0.04 Light semi-urban: 0.04 and 0.08 | Low |
| 6 | 3.2 | 3.2 | 3.2 | 3 | Fields: 0.04 Treed Regions: 0.08 Semi-Urban: 0.08 | Very Low |
| 7 | 250 | 15 | 0.02 | Unknown | Fields: 0.03 Treed Regions: 0.08 | Moderate |
| 8 | 0.2 | 0.002 | 0.1 | 2,780 | Dense vegetated riparian area eroded to smooth bedrock: 0.05 | Very Low |
| 9 ⁸ | 50 ⁸ | 0.2 ⁸ | 0.05 | 3,180 | Fields, Suburban, Forest Area: 0.07 | Moderate |
| 10 ⁹ | 250 ⁹ | 2.5 ⁹ | 0.05 | 2,820 | Fields: 0.04 | Low |
| 11a ¹⁰ | - | - | 0.06 | 2,690 | - | - |
| 11b | 1,780 | 560 | | | Barren Tailings Surface 0.02 | Moderate |
| 12 | 400 | 25 | 0.2 | 4,500 | Mining and Barren Regions: 0.05 Fields and Pasture: 0.05 Rivers: 0.06 Brush and Vegetation: 0.08 Urban, Forested Regions: 0.12 | High |

Table A.7 Notes:

1. The Yield Stress and Viscosity were selected for each event with the Quadratic formula and a semi-systemic calibration process. Caution should be used when comparing these values to measured rheology parameters, other back-analyzed or calibrated rheology parameters, or rheology values appropriate for other non-Newtonian formulas.
2. The numerical modelling within this thesis does not use the tailings particle density as an input. See Chapter 4 within the body of the thesis for the numerical modelling methodology.
3. The landcover is based on available descriptions, photographs, and Google Earth Imagery of the Zone 1 pre- and post-failure. The Manning's coefficient was selected based on the landcover as part of this thesis. See Chapter 3 within the body of the thesis for the methodology for selecting this parameter.
4. The assigned confidence for the calibrated yield stress and viscosity is based on subjective assessment of the numerical modelled results compared to the observed runout characteristics. See Chapter 4 within the body of the thesis for the numerical modelling methodology and Appendix B for specific sources and reasoning to support each classification for each event.
5. The Upper and Lower Basins of the Prestavèl TSF were relatively homogenous (Luino & De Graff, 2012), therefore a uniform representative particle size and tailings particle density is presented here.
6. The Gillibrand Pond No. 6 was modelled with two separate simulations for each flow type within this thesis. See Appendix B for further details.
7. The representative particle size of the North Pyroclastic Pond was used in the numerical modelling for Aznalcóllar as the majority of the tailings were estimated to originate from the North Pyroclastic Pond.
8. Machado (2017) presents measured yield stress and viscosity values for a range of volumetric solids concentrations for the Fundão tailings. The numerical modelling within this thesis was based on these measured values rather than employing the semi-systemic calibration process. See Appendix B for further details.
9. Zheng (2018) presents measured yield stress and viscosity values for a range of volumetric solids concentration for the Tonglūshan tailings. The numerical modelling within this thesis employed the semi-systemic calibration process rather than using the measured rheology. See Appendix B for further details.
10. The Cadia NTSF Event I was not modelled within this thesis. See Appendix B for further details.

Table A.8 Local Runout Observations (Page 1 of 3)

| ID | Peak Depths | Final Depths | Arrival Times ¹ | Other |
|----|--|--|--|---|
| 1 | None | 0.4 m throughout Stava Valley (approximately, no specific location) | 12:22:55 PM - Breach occurs 12:23:45 PM - Tailings front at Village of Stava 12:25:45 PM - Tailings front at Section 10' 12:27:40 PM - Tailings front at Romano Bridge 12:28:00 PM - Tailings front at Avisio River 12:30:40 PM - Flow subsides | Superelevation of flow is 16 m by the Romano Bridge |
| 2 | 1 m tall tailings splashes on vegetation (no specific location) | None | None | None |
| 3 | 2.5 m at first row of houses | 0.5 to 1 m deep at the first row of houses 0.5 m deep through the village of Merriespruit (approximately, no specific location) | None | None |
| 4 | 4 m at El Guijo gauge | 0.4 m at El Guijo gauge | 01:00 AM - Breach occurs 02:30 AM - Tailings front arrives at El Guijo gauge 03:00 AM - Most of the tailings have discharged 03:30 AM - Peak depth at El Guijo gauge 07:00 AM - Tailings front at Guadiamar gauge 08:00 AM - Tailings discharge nearly done at Aznalcóllar TSF 06:00 PM Apr 26 - El Guijo gauge reaches final depth (may be erroneous due to damage) | None |
| 5 | None | None | None | None |
| 6 | 2 m at Village of Kolontár (approximately) 1 m at Village of Devecser (approximately) | None | 12:00 PM Oct 4 - Structural issues noted 12:12 PM Oct 4 - Breach formation time begins 12:25 PM Oct 4 - Tailings front at Kolontár 04:00 PM Oct 5 - Tailings front at Mersevát 11:00 PM Oct 5 - Tailings front at Szergény | None |

Table A.8 Local Runout Observations (Page 2 of 3)

| ID | Peak Depths | Final Depths | Arrival Times ¹ | Other |
|----|---|--|--|---|
| 7 | None | 1 m at east side of Farmer's house. 0.3 m at southwest side of Farmer's house | None | None |
| 8 | 1 m to 1.7 m above pre-failure water surface elevation at Polley Lake | 0.5 m in Middle Hazeltine Creek 0.2 m or less in Hazeltine Canyon Section 0.07 m above pre-failure water surface elevation in Quesnel Lake | 12:50 AM - Sump pond level spikes 01:00 AM - Breach occurs (estimated) 01:08 AM - Power line destroyed, cutting power to site 02:05 AM - Wavelets recorded arriving at WSC 08KH011 04:25 AM - Breach visually observed to be nearly fully formed 04:30 AM - Peak depth at Polley Lake may have been observed 05:00 AM - Depth at Polley Lake decreasing 09:00 AM - Tailings discharge observed to be like a turbid river at the TSF breach 04:00 PM - Tailings discharge cease at the TSF breach | 18.6 M m ³ of tailings, water and eroded material reached Quesnel Lake. 0.6 to 1.7 M m ³ material eroded from the Zone 1 inundation area 2.7 m and 10.3 m (average and max) erosion depth at Middle Hazeltine Creek 2.9 m and 7.2 m (average and max) erosion depth at Hazeltine Canyon Section 2.1 m and 10.3 m (average and max) erosion depth at Lower Hazeltine creek |
| 9 | None | 4 m at Paracatu de Baixo | 03:45 PM Nov 5 - Breach Occurs 04:00 PM Nov 5 - Tailings front at Bento Rodrigues 08:00 PM Nov 5 - to 10:00 PM - Tailings front at Paracatu de Baixo 03:30 AM Nov 6 - Tailings front at Barra Longa 07:00 AM Nov 6 - Tailings front at Candonga Reservoir | 2,000,000 m ³ of tailings deposited at Santarem Dam 2,400,000 m ³ of tailings deposited at Bento Rodrigues 6,100,000 m ³ of tailings deposited within Gualaxo do Norte and Carmo rivers and floodplains 2,800,000 m ³ of tailings deposited within the Doce River and floodplains upstream of the Candonga Dam 8,400,000 m ³ of tailings deposited with the Candonga Reservoir |

Table A.8 Local Runout Observations (Page 3 of 3)

| ID | Peak Depths | Final Depths | Arrival Times ¹ | Other |
|-----|-------------|---|--|---|
| 10 | None | Contour information from survey data for entire deposition zone | None | None |
| 11a | None | Profile data from survey data along entire deposition zone | None | None |
| 11b | None | Profile data from survey data along entire deposition zone | None | None |
| 12 | None | None | 12:28:21 PM - Breach Occurs 12:33 PM - Most of the tailings have discharged 13:00 PM - Tailings front at Paraopeba River | 28 m/s tailings frontal velocity near the dam toe 18 m/s tailings frontal velocity near the overburden dump 2.2 m/s to 5.0 m/s tailings velocity at Alberto Flores Road (no time associated) 3.7 M m3 to 4.7 M m3 deposited with the Ferro Carvão river valley |

Table A.8 Notes:

1. The date and times are in local time for the region, which includes daylight savings for most events

Table A.9 Terrain Data used for the HEC-RAS Modelling in this Thesis

| ID | Modelled Event | Terrain Data | Horizontal Resolution ¹ (m) | Source | Terrain Modifications | Confidence in Quality ² |
|-----|---|--------------------------------------|---|--|---|------------------------------------|
| 1 | Prestavèl (Stava) | WorldDEM DTM | 12 | Airbus Defense and Space (Commercial) | River Channel | Moderate |
| 2 | Gillibrand No. 6 ³ (Tapo Canyon) | SOCAL Wildfire QL2 DEM | 1 | United States Geological Survey (Public) | Breach Channel | Low ² |
| 3 | Harmony 4A (Merriespruit) | WorldDEM DTM | 12 | Airbus Defense and Space (Commercial) | Breach Channel | Moderate |
| 4 | Aznalcóllar ^{4,5} (Los Frailes) | DTM05 | 5 | National Geographic Institute of Spain (Public) ⁴ | Breach Channel, River Channel | Moderate ⁵ |
| 5 | Tashan (Taoshi or Xiangfen) | ALOS World 3D | 30 | Japan Aerospace Exploration Agency (Public) | Breach Channel | Low |
| 6 | MAL Reservoir X (Ajka or Kolontár) | EU-DEM | 25 | European Environment Agency (Public) | Breach Channel, River Channel, Vegetation Removal | Very Low |
| 7 | Kayakari | DEM5A | 30 | Geospatial Information Authority of Japan (Public) | None | Moderate |
| 8 | Mount Polley | WorldDEM DTM | 12 | Airbus Defense and Space (Commercial) | Breach Channel, River Channel | Low |
| 9 | Fundão (Mariana, Bento Rodrigues, or Samarco) | ALOS World 3D | 30 | Japan Aerospace Exploration Agency (Public) | Breach Channel, River Channel, Artefact Removal | Very Low |
| 10 | Tonglūshan North Compartment | WorldDEM DTM | 12 | Airbus Defense and Space (Commercial) | Breach Channel, Berm Addition | Moderate |
| 11b | Cadia NTSF Event II ⁶ | 0.1 m interval Contours ⁵ | 0.1 m | Newcrest Mining Limited (Private) ⁶ | Breach Channel | High |
| 12 | Feijão Dam I (Brumadinho) | WorldDEM DTM | 12 | Airbus Defense and Space (Commercial) | Breach Channel | Moderate |

Table A.9 Notes:

1. The resolution is sometimes reported in arcseconds. The nominal value in meters is reported here, the actual resolution may differ slightly depending on the location of the event.
2. The assigned confidence for each terrain is subjectively based on the resolution, any reported vertical accuracy measures, and the required terrain modifications to make the original terrain data fit for runout modelling purposes. See Chapter 4 for the process for terrain modification Appendix B for specific sources and reasoning to support each classification.
3. The SOCAL Wildfire QL2 DEM is assessed as high-quality terrain data. It is estimated that the downstream environment has materially changed during the time between the breach and the date of the survey. Consequently, it is not known how representative the terrain data may be for the Gillibrand No. 6 event.
4. The terrain data used for the Aznalcóllar event was an alternate version of the DTM05 distributed on the Open Data Portal. The alternate version was based on the original DTM05 data, but bridges and other features were removed to convert the DTM05 to bare earth terrain data. The alternate version of the DTM05 was also downsampled to 20 m.
5. The DTM05 is assessed as high-quality terrain data. Sanz-Ramos et al (2022) state that the downstream environment materially changed during the remediation after the breach and before the survey for the DTM05. Consequently, it is not known how representative the terrain data may be for the Aznalcóllar event.
6. For the Cadia Event, Newcrest Mining Limited provided contour data from the site-specific surveys for the breach, as shown in Jefferies et al. 2019. Terrain rasters were interpolated from the contour data for the modelling in this thesis.

Table A.10 Recommendations for Improvements for Each Event (Page 1 of 2)

| ID | Recommendations for Improvement | Ease of Implementation | Usefulness of Recommendation |
|----|--|--|--|
| 1 | <ol style="list-style-type: none"> 1. Update Zone 1 Inundation Area 2. Recreate pre- and post-failure surface in TSF; use block start model for cascade breach | <ol style="list-style-type: none"> 1. High: Existing documents can be used for update 2. Moderate to Low: Data exists to do this work, but process is non-trivial | <ol style="list-style-type: none"> 1. Very high: key model calibration and validation constraint 2. High: can improve modelled results near Stava and be insight for forward-analysis cascade breach scenarios |
| 2 | <ol style="list-style-type: none"> 1. Determine alignment and channel geometry of creek in Tripas Canyon and geometry of downstream culvert/bridge 2. Determine outflow volume of each flow type, viscous and fluid. 3. Model viscous and fluid runout simultaneously in a single simulation | <ol style="list-style-type: none"> 1. Low: Field visit required for accurate channel survey, and channel may have materially changed since the failure event 2. Nearly Impossible: This information is perishable, and likely no longer available. 3. Moderate: Other models have this capability, but calibration of two parameters for two flow types and potentially the relative portion of the volume is non-trivial | <ol style="list-style-type: none"> 1. Moderate: The channel likely is relevant for the Zone 1 to Zone 2 transition. 2. Paramount: Outflow volume is one of the most influential inputs 3. Moderate to Low: Usefulness is contingent on the certainty of the volume for each flow type (Recommendation 2) |
| 3 | <ol style="list-style-type: none"> 1. Determine and confirm arrival times, through review of civilian news or interviews with survivors of the event | <ol style="list-style-type: none"> 1. Low: Eyewitness recollection of details two decades after the event would be low, no further information was found in this thesis from other sources | <ol style="list-style-type: none"> 2. Moderate: The model calibration is relatively successful, but would be further supported by additional constraints |
| 4 | <ol style="list-style-type: none"> 1. Update the total outflow volume based on information from Sanz-Ramos et al. (2022) 2. Update the Zone 1 inundation area based on information from Sanz-Ramos et al. (2022) 3. Obtain or reconstruct terrain data that represents pre-failure conditions | <ol style="list-style-type: none"> 1. High: Existing documents can be used for update 2. High: Existing documents can be used for update 3. Low: This information is likely perishable and may no longer be available | <ol style="list-style-type: none"> 1. Paramount: Outflow volumes are highly influential on runout models 2. Paramount: Zone 1 inundation area directly affects the calibration process and therefore model validity 3. Moderate: Despite commentary in Sanz-Ramos et al. (2022), no major concerns were found with using modern terrain data. Information exists for the required terrain modifications |
| 5 | <ol style="list-style-type: none"> 1. Revisit the investigation into outflow volume and breach characteristics with Mandarin literature and resources 2. Obtain or reconstruct good quality terrain data that represents pre-failure conditions | <ol style="list-style-type: none"> 1. Moderate to Low: Unknown amount of information in Mandarin literature. No further information was found in this thesis from other English sources 2. Moderate to Low: Good quality terrain data may not exist for this region | <ol style="list-style-type: none"> 1. Very High: The investigation was highly uncertain and based on limited information 2. Very High: The modelled runout diverted into an adjacent channel and had poor areal fit |
| 6 | <ol style="list-style-type: none"> 1. Confirm the total outflow volume and the void ratio for the red mud tailings 2. Update the Zone 1 inundation area 3. Obtain better quality terrain data that presents bare-earth conditions | <ol style="list-style-type: none"> 1. Moderate: This information is likely perishable and may no longer be available. As the event is relatively recent, it is more likely that the information is available somewhere. 2. Moderate: Google Earth Imagery is available for this exercise, but the exact extent may be subjective 3. Moderate: It is likely good quality data exists for this area, but may come with a high financial cost for the large extent of the runout | <ol style="list-style-type: none"> 1. Paramount: Outflow volumes are highly influential on runout models 2. Paramount: Zone 1 inundation area directly affects the calibration process and therefore model validity 3. Paramount: The terrain data took substantial effort to modify and still drastically reduced model performance |

Table A.10 Recommendations for Improvements for Each Event (Page 2 of 2)

| ID | Recommendations for Improvement | Ease of Implementation | Usefulness of Recommendation |
|----|--|---|---|
| 7 | <ol style="list-style-type: none"> 1. Confirm the overlap between the tsunami and tailings runout and the extent of Zone 1 within the overlapping area 2. Obtain or reconstruct terrain data that represents pre-failure conditions by the farmer's house | <ol style="list-style-type: none"> 1. Low: Despite being a relatively recent event, the tsunami likely destroyed any concrete evidence of the Zone 1 extent within the overlapping area 2. Moderate, but Unknown: This information may exist somewhere, but it was not found in the course of this thesis | <ol style="list-style-type: none"> 1. Paramount: Zone 1 inundation area directly affects the calibration process and therefore model validity 2. Moderate: Other than the fields by the farmer's house, the terrain appeared representative of pre-failure conditions |
| 8 | <ol style="list-style-type: none"> 1. Use a model with variable solids concentration capabilities 2. Use a mobile-bed model to simulate the downstream erosion | <ol style="list-style-type: none"> 1. High: Models currently exist with this capability 2. Low: Models currently exist with this capability and observations on the downstream erosion exist, but modelling effort is a lot higher | <ol style="list-style-type: none"> 1. High: Variable solids concentration is likely be important to the runout modelling 2. High: An erodible bed model was found to be important for a good areal match in this thesis |
| 9 | <ol style="list-style-type: none"> 1. Use a model with variable solids concentration capabilities 2. Obtain better quality terrain data that presents bare-earth conditions 3. Model the entire Zone 1 extent | <ol style="list-style-type: none"> 1. High: Models currently exist with this capability 2. Low: Good quality terrain on the extent needed would come at a high financial cost 3. Moderate: This is contingent on the quality of the terrain data (Recommendation 2), but is relatively straightforward, if time consuming. | <ol style="list-style-type: none"> 1. High: Variable solids concentration is likely be important to the runout modelling, particularly for the full Zone 1 extent 2. Paramount: The terrain data took substantial effort to modify and still drastically reduced model performance 3. High: The high confidence arrival time is at the Candonga reservoir, at the Zone 1 termination |
| 10 | <ol style="list-style-type: none"> 1. Obtain the pre- and post-failure terrain data from Zheng (2018) and repeat the modelling in HEC-RAS to confirm the rheology discrepancy | <ol style="list-style-type: none"> 1. Low: It is assumed that this terrain data would not be put in the public domain | <ol style="list-style-type: none"> 1. Moderate: Continued knowledge of rheology measurement practices for tailings dam breach runout modelling are useful, but a single event may not be applicable to other events |
| 11 | <ol style="list-style-type: none"> 1. Model the initial slump (Event I) 2. Use a block start model for the slab failure for the liquefied flow (Event II) | <ol style="list-style-type: none"> 1. High: Models currently exist that can simulate slumping behaviour 2. Low: Additional survey information would be required from Newcrest Mining Ltd. | <ol style="list-style-type: none"> 1. High: The high amount of information associated with this event would mean any insights from this modelling are more certain and useful 2. Moderate: This would continue validating (or invalidating) the slab convention but is only a single event. More events are required to support any assessment of the slab convention |
| 12 | <ol style="list-style-type: none"> 1. Use a block start model to compare against the parametric breach, to suggest refinements for the parametric breach approach 2. Use a variable solids concentration model to simulate the interaction of the Paraopeba river and the tailings landslide dam | <ol style="list-style-type: none"> 1. Moderate: This can be done with a reconstructed post-failure surface (which is non-trivial to do) or with the post-failure survey data, which would need to be added to the public domain 2. High: Models currently exist with this capability | <ol style="list-style-type: none"> 1. Moderate: It is assessed that the parametric approach worked relatively well for this event, so a comparison for other events would be more insightful 2. High: The high amount of information associated with this event would mean any insights from this modelling are more certain and useful |

Appendix B: Tailings Dam Breach and Runout Investigations and Modelling Summaries

A summary of the failure event, key inputs, model set-up, model results, and discussion of certainty is included for each event. The mapped model results are for the maximum depth and maximum flow velocity within the model. The mapped model results also include the Zone 1 from Ghahramani et al (2020) and locations of interest mentioned for each event, which are typically locations of runout observations. The local runout observations are also directly compared in methods appropriate to the particular observation. The modelled deposition is not included in the mapped model results, but it and other results can be viewed within the individual HEC-RAS models.

Appendix B.1 Prestavèl (Stava), Italy, 1985

B1.1 Facility Background and Failure Narrative

The Prestavèl fluorite mine had a stepped side-hill arrangement TSF in Northern Italy, with two compartments, both constructed as upstream dams (Luino & De Graff, 2012). The Upper and Lower Basins collapsed on July 19, 1985, at 12:23 PM. The Upper Basin is estimated to have collapsed first, after static liquefaction of the sandy-silt tailings. The tailings flow cascaded onto the Lower Basin, then the combined outflow from both basins flowed along the Porcellini and Stava creeks. The nearby village of Stava was destroyed by the tailings runout and further damage was caused to the town of Tesero farther downstream. The tailings formed a landslide dam in the Avisio River where the majority of the tailings deposited (Muramoto et al., 1986; Takahashi, 2014). The tailings runout killed 268 people. The event is colloquially known as the Stava event, after the village.

Impounded Volumes

The combined volume impounded in the basins was 250,000 m³ to 300,000 m³ (Chandler & Tosatti, 1995; Luino & De Graff, 2012), which includes the supernatant pond, tailings solids, and interstitial water. Luino & De Graff roughly estimate there was 50% more impounded in the Upper Basin, which aligns with the general geometries and photographs of the basins. The higher volume estimate was used and proportioned between the Upper and Lower Basins according to the volume distribution estimate from Luino & De Graff. The combined supernatant pond volume at the time of failure was estimated as 15,000 to 25,000 m³ (Chandler & Tosatti, 1995; Colombo & Colleselli, 2003). The average supernatant volume of 20,000 m³ is assigned between the Upper and Lower Basins based on the ratio of their pond areas as measured in Muramoto et al. (1988), which are 11,800 m² and 8,200 m² for the Upper and Lower Basins respectively. This estimate corresponds to 168,200 m³ and 111,800 m³ of tailings impounded in the Upper and Lower Basins respectively.

Zone 1 Description

The Stava Valley contains fields, tree stands, and semi-urban areas, as seen in the photos of the runout in Takahashi (2014) and Luino & De Graff (2012) as well as current aerial imagery. The tailings were confined by the valley walls during the entire runout (Ghahramani et al., 2020)

The highest reported inundation area is 435,000 m² (Van Niekerk & Viljoen, 2005, Luino & De Graff, 2012, Pirulli et al., 2017), however this value appears to be limited to the inundation area within the Stava Creek area, excluding the Porcellini Creek and Avisio River areas. Ghahramani et al. (2022) presented an updated Zone 1 with an inundation area of 650,000 m² comprising all three watercourses. Luino & De Graff note the maximum width of the tailings flow at several specific locations along the Stava Creek, such as 50 m at the football field upstream of Tesero. The mapping by Ghahramani et al. is 15 m wider at the football field than in Luino & De Graff as well as generally throughout the runout zone, suggesting that the updated Zone 1 may be slightly overestimated in Ghahramani et al. A 15 m reduction in width of the Ghahramani et al. along the 4.2 km runout distance in the Porcellini and Stava creeks would align with mapping presented in figures in Luino & De Graff and Pirulli et al., which indicate inundation areas around 570,000 m² to 600,000 m². The overestimated Zone 1 inundation area from Ghahramani et al. without adjustment was used for calibration within this research to remain consistent with the other events in this thesis.

B1.2 Additional Runout Observations

The nearby seismograph at Cavalese provides a record for the timing of the flow, with Muramoto et al. (1988) and Takahashi (2014) offering the following interpretations:

- The breach is estimated to start at 12:22:55 PM,
- The tailings flow reaches the village of Stava, 600 m downstream of the TSF, between 12:23:35 PM and 12:23:55 PM,
- The tailings flow reaches an extreme bend, 3,300 m downstream of the TSF (labelled as Section 10' by Muramoto et al., 1988), between 12:25:35 PM and 12:25:55,
- The tailings flow reaches the Romano Bridge, 3,900 m downstream of the TSF (labelled as Section 13 by Muramoto et al., 1988), between 12:27:30 PM and 12:27:50 PM,
- The tailings flow reaches the Avisio River, 4,400 m downstream of the TSF, around 12:28:00 PM,
- The tailings flow subsides at around 12:30:40 PM when the seismograph record returns to normal.

Luino and de Graff (2012) offered a different interpretation of the seismograph and arrival timing than Takahashi (2014); however, Takahashi used the frequencies of the

seismograph data to support the interpretation, which was considered more sophisticated. Takahashi also describes a numerical reproduction of the flow velocities for the event; however, it involved several simplifications of flow dynamics and the geometry of the channel, rather than direct observations. Therefore, the velocity values presented therein are not considered for the calibration of the HEC-RAS model.

B1.3 Model Inputs

Outflow Volumes

Muramoto et al. (1988) surveyed the basins and present the total outflow volumes from each of the basins, with a cumulative outflow volume of 185,200 m³. The volumes are separated into slime tailings and sands tailings; however Takahashi (2014) clarifies that the total volume represents the tailings solids, interstitial water, and supernatant ponds. Luino & De Graff (2012) estimated an additional 40,000 to 50,000 m³ of debris was entrained, which is believed to primarily be vegetation and destroyed structures, as erosion of the substrate was limited along the flow path (Takahashi, 2014; Pirulli et al., 2017). Tree trunks, coarser particles, and other debris was deposited on either side of the flow path throughout the Stava valley (Luino & De Graff, 2012), indicating that the overall flow volume may have been relatively consistent (i.e., the volume of tailings and debris deposited was equal to the volume of debris entrained prior to flow cessation).

The supernatant pond from each basin with a total volume of 20,000 m³ was discharged during the cascading breach. The remaining volume of 165,200 m³ representing the tailings is separated into tailings solids and interstitial water to result in a total volumetric solids concentration of 47.6%, as noted by Takahashi (2014). Laboratory testing by Genevois & Tecca (1993) indicated an undisturbed void ratio ranging from 0.75 to 1.0 for the sand portion of the dams, and 0.9 to 1.0 for the slimes within the basins. The average back-calculated void ratio of 0.87 from Takahashi aligns with the laboratory data, as most of the tailings were slimes. The estimated volumes are presented in Table B.1.

Table B.1 Prestavèl Outflow Volumes

| Basin | Tailings Solids (m³) | Interstitial Water (m³) | Supernatant Pond (m³) | Total (m³) |
|--------------|--|---|---|------------------------------|
| Upper | 56,150 | 48,850 | 11,800 | 116,800 |
| Lower | 32,200 | 28,000 | 8,200 | 68,400 |
| Total | 88,350 | 76,850 | 20,000 | 185,200 |

Breach Processes and Geometries

Heavy precipitation and inadequate drainage within the TSFs lead to high water levels. The upstream constructed dams were built on swampy foundations and were quite steep. These conditions were detrimental to stability and eventually resulted in essentially a slope instability failure (Berti et al., 1988; Chandler & Tosatti, 1995; Colombo & Colleselli, 2003). These conditions are hallmarks of a sudden Process II, which is further evidenced by the flood wave arrival time in the village of Stava 600 m away within a minute.

The breach geometry was estimated using the survey presented by Muramoto et al. (1986) in scaled figures and is presented in Table B.2. The post-breach facility surface is complicated, introducing some uncertainty whether the dam crest alignment is truly the hydraulic control. For example, Takahashi (2014) estimates the hydraulic control of the Upper Basin as only 120 m wide and cutting across the corner of the facility

Table B.2 Prestavèl Breach Geometry

| Basin | Dam Height (m) | Crest Height (m) | Breach Height (m) | Bottom Breach Width (m) | Top Breach Width (m) | Left Breach Side Slope (xH:1V) | Right Breach Side Slope (xH:1V) |
|-------|----------------|------------------|-------------------|-------------------------|----------------------|--------------------------------|---------------------------------|
| Upper | 33 | 29 | 22 | 50 | 148 | 2.4 | 2.0 |
| Lower | 22 | 19 | 13 | 20 | 220 | 8.5 | 7.0 |

Terrain and Manning's Coefficient

The terrain data source was the Airbus WorldDEM DTM, with a spatial resolution of 12 m. The terrain data is reported as bare earth; however, the Stava Creek near the Romano Bridge included several ridges almost 20 m high across the riverbed. These ridges are attributed to interference from the bridges, buildings, and heavy vegetation in the gully downstream of the Romano Bridge. The ridges were manually removed, to keep the slope consistent to regions without suspected interference, and to match available photos of the Romano Bridge. The modification to the terrain near the bridges are shown in Figure B.1. The Prestavèl TSF was reclaimed in 1988, therefore the terrain data collected in 2015 does not include the remnants of the Prestavèl TSF. Consequently, no breach channel edits were required.

The fields were assigned a Manning's coefficient of 0.04 while the treed or semi-urban areas were given a Manning's coefficient of 0.08. Each Manning's coefficient region was manually delineated based on Google satellite imagery.

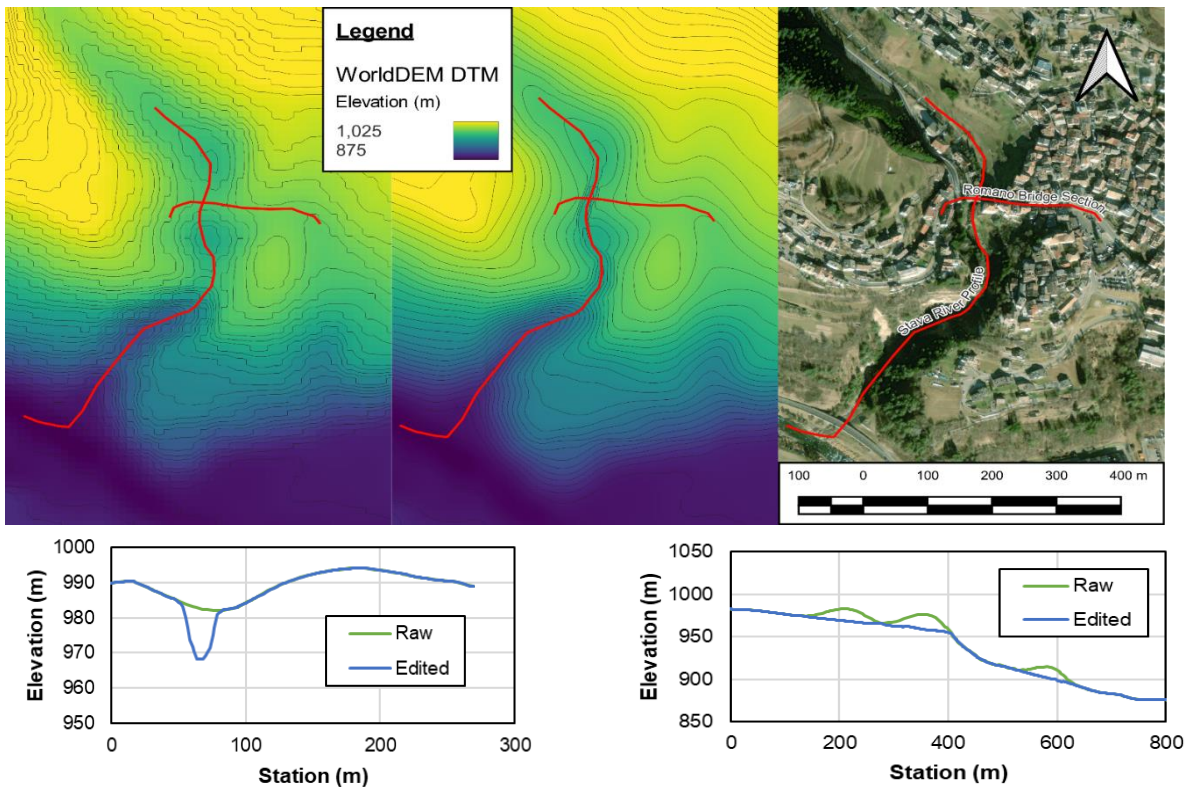


Figure B.1 Terrain Modifications and Imagery for Prestavèl near the Romano Bridge. A) Terrain Before Channel Modification, B) Terrain After Channel Modification, C) Satellite Imagery for Comparison, D) Cross-section Along the Romano Bridge, E) Profile Along the Stava Creek Underneath the Romano Bridge

B1.4 HEC-RAS Model Set-up

Both basins were assumed to breach instantly and simultaneously for simplicity within the HEC-RAS model, using a breach weir coefficient of 0.928. The stage-storage curves for the Upper and Lower Basins were idealized as individual level-pool semi-cones. The outflow volume calculated by the parametric breach method for the Upper Basin is directly added to the Lower basin elevation volume as an inflow. From there, the breach outflow is calculated according to the parametric breach at the Lower basin, and input into the 2D domain.

The computation resolution was 12 m due to the limitations of the DEM resolution. A Normal Depth Boundary Condition is used 500 m beyond the confluence of the Stava Creek with the Avisio River. The flow of the Avisio River and its mixing with the deposited tailings mass is not modelled.

The representative particle size was 20 microns for both basins, based on the range provided by Chandler & Tosatti (1995) for the tailings slimes considering it was the majority of the released tailings (Muramoto et al. 1986). The additional debris volume entrained in the runout was not included in the HEC-RAS model, as debris entrainment options within HEC-RAS would considerably increase the complexity of the model.

B1.5 HEC-RAS Model Results

The calibration plot is shown in Figure B.2, with each tick mark roughly representing a 1.78x increase in the rheology inputs. It is expected that as the rheology inputs are decreased, a point is reached where the increased flowability of the tailings overestimates the inundation area. The Ω_{Tm} metric should account for this through the increased false positive area, however the overestimation in the Zone 1 inundation area from Ghahramani et al. (2022) used in the calibration reduces or eliminates the false positive area. Consequently, there is no decrease in Ω_{Tm} metric for very flowable materials in the calibration process, despite intuition and experience suggesting a tailings flow with nearly 50% solids by volume should have measurable rheology. Based on the Ω_{Tm} metric alone, the best inputs are 1 Pa and 0.001 Pa·s for the yield stress and viscosity respectively, which is the bottom left in Figure B.2.

A conventional trial-and-error approach was used to determine the best inputs to match the observed arrival times, within the region of the lowest Ω_{Tm} values in Figure B.2. The final selected yield stress and viscosity were 3.2 Pa and 1.8 Pa·s, respectively, which were marginally worse than the optimal values according to the Ω_{Tm} metric, but slightly better for the arrival time. The comparison of observed to modelled arrival times is shown in Figure B.3. The HEC-RAS model matches the arrival time at the village of Stava and the Avisio River well, with slightly lesser match for Section 10' and the Romano Bridge. The modelled maximum depth and velocities of the Prestavèl runout are shown in Figure B.4. The modelled flow width by the football field mentioned in Luino and De Graff (2012) is 48 m, which is in alignment with the description of the observed flow width.

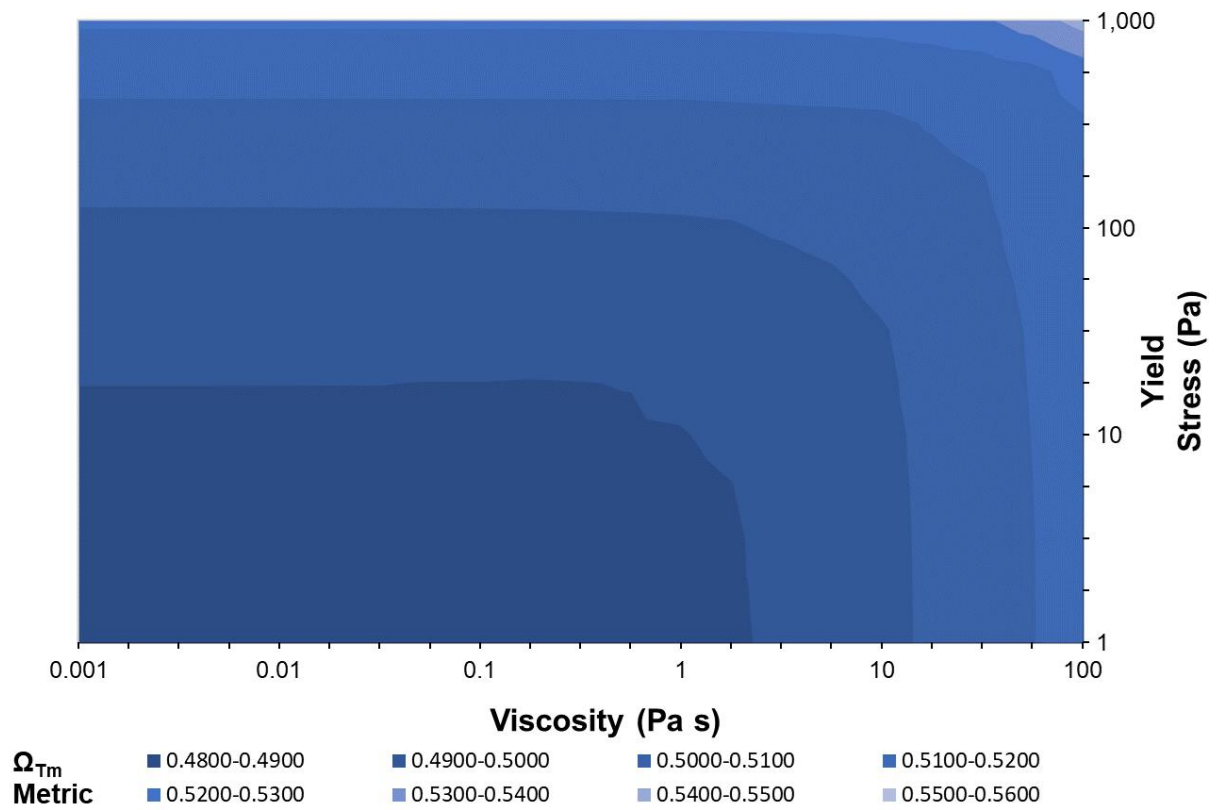


Figure B.2 Prestavèl Rheology Calibration Plot in Log-Log Scale

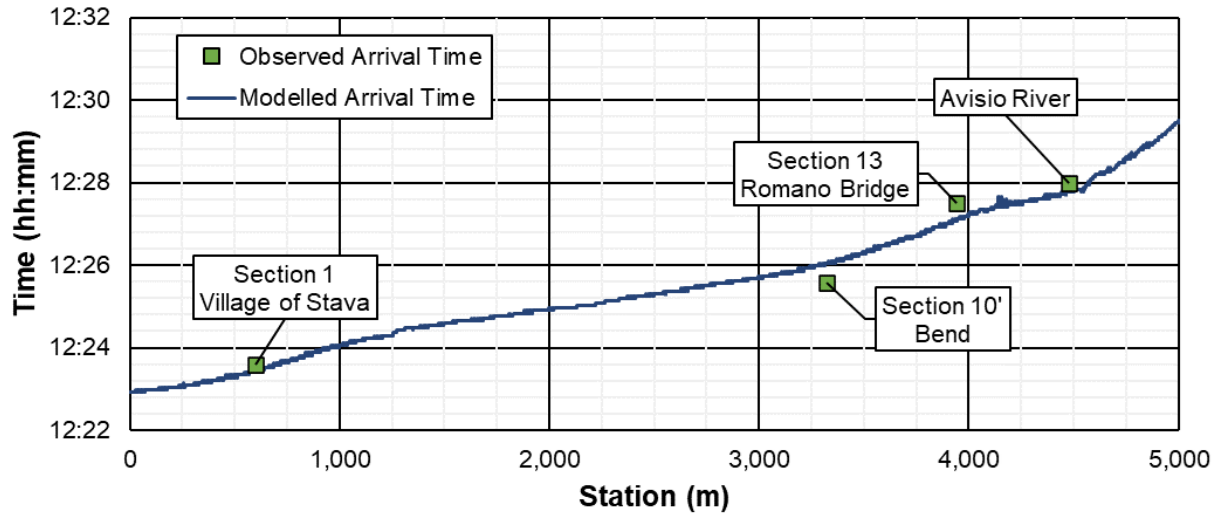


Figure B.3 Prestavèl Arrival Time Results

LEGEND

Observed Inundation area



Locations of Interest



Maximum Depth (m)

≤ 1.0

1.0 - 2.0

2.0 - 3.0

3.0 - 4.0

4.0 - 5.0

> 5.0

Maximum Velocity (m/s)

≤ 3.0

3.0 - 6.0

6.0 - 9.0

9.0 - 12.0

12.0 - 15.0

15.0 - 18.0

18.0 - 21.0

21.0 - 24.0

24.0 - 27.0

> 27.0

300 0 300 600 900 1,200 m

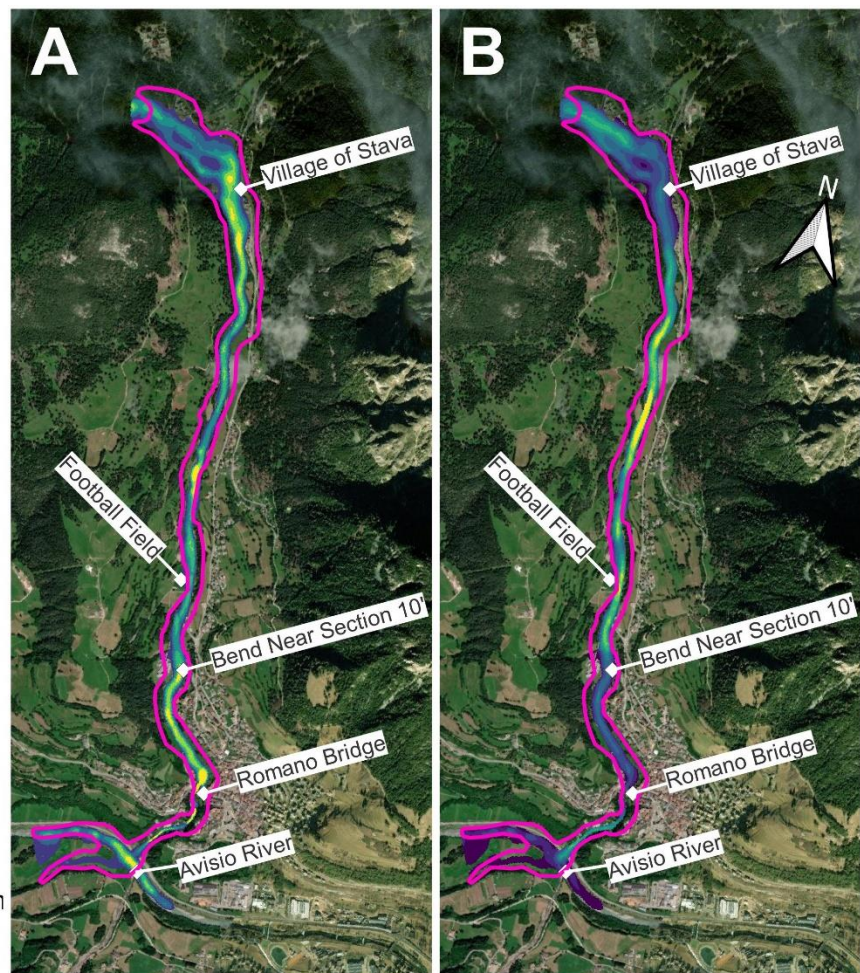


Figure B.4 Prestavèl HEC-RAS Model Results A) Maximum Depth and B) Maximum Velocity

B1.6 Recommendations for Future Research

The Zone 1 mapped by Ghahramani et al. (2022) may need updating, given the likely overestimation of the flow width. The Zone 1 mapping affects the entire modelling and calibration process, therefore is the highest priority for improvement. Other mapping exists (e.g., Luino & De Graff, 2012, Pirulli et al., 2017) which can be compared to the Ghahramani et al. (2022) mapping.

The approach taken within this thesis for the cascade breach may result in a slightly attenuated breach flow, as the velocity of the Upper Basin breach flow is effectively neutralized in the Lower Basin stage-storage curve. A block start breach model is likely a better approach for a cascading Process II breach and may result in different flow, therefore affecting the runout calibration. Such an approach will necessitate a reconstruction of the pre and post-failure surfaces, which would take additional effort.

The late arrival to Section 10' but early arrival at the Romano Bridge may indicate further refinement of Manning's coefficient (areal extent and values) near those locations is warranted to reduce the arrival time misfit. The misfit is relatively small and such a refinement is not particularly explanatory or useful for forward analysis, and therefore not a high priority for improvement.

Relatively good reporting on building damage and fatality rates are available for the Prestavèl event. After the numerical model is improved according to the recommendations above, a study on vulnerability estimates of the Prestavèl event would be of interest for industry, but this is not within the scope of this thesis.

Appendix B.2 Gillibrand Pond No. 6 (Tapo Canyon), United States, 1994

B2.1 Facility Background and Failure Narrative

The Gillibrand Pond No. 6 was a triangular shaped side-hill facility in California, USA. Pond No. 6 was used to settle fines from sand and gravel aggregate and concrete waste wash. The fines material was initially deposited in an old aggregate quarry pit, but additional raises above the natural pit rim were in the upstream method (Harder & Stewart, 1996). At 4:30 AM on January 17, 1994, a 6.7 magnitude earthquake occurred 21 km away from the Gillibrand operations. The south-west side of the dam collapsed during the earthquake, resulting in a viscous flow slide and fluid tailings runout (Harder & Stewart, 1996). The flow side portion of the outflow arrested proximal to Pond No. 6, but the fluid tailings were observed around more than a kilometer away in the downstream Tripas Canyon through stains and splash marks on vegetation and trees. The event is also known as the Tapo Canyon event after the nearby regional park.

Impounded Volumes

The total impounded volume is unknown (Rana et al., 2021b). Harder & Stewart (1996) noted that the western half of the facility sometimes had ponded water of unknown origin. They presumed the origin of the water to be from upstream conveyance ditches and ponds, however a nearby NOAA weather station (Camarillo Airport) recorded less than 1 mm of rain in the preceding month, implying the surface of Pond No. 6 may have been dry prior to the failure. Alternatively, the source of the surface water could be from the concrete truck rinsing and washing.

Zone 1 Description

The land cover proximal to Pond No. 6 is generally industrial, packed earth, or sparsely grassed (P.W Gillibrand Co., n.d.). Based on the aerial imagery from the US Geological Survey (USGS, 1994), the vegetation was moderate within the creek channel in the downstream canyons prior to the failure, but outside of the riparian area is paved or sparsely grassed. The tailings were confined by the valley during the entire runout (Ghahramani et al., 2020).

The Zone 1 mapping from Ghahramani et al. (2020) indicates an area of 32,000 m². This area includes the viscous flow slide region and the fluid tailings runout above the banks, which Ghahramani et al. (2020) interpreted to terminate 730 m downstream of the breach based on USGS imagery. Another 60 m downstream of the

Zone 1 extent there is a culvert or bridge visible in the USGS imagery and Google Earth Imagery.

B2.2 Additional Runout Observations

The splash marks on the trees within the riparian area are described by Harder & Stewart (1996) as 1 m. No information where along the 1,000 m or so of affected river mentioned by Harder & Stewart these splashes were observed, limiting the use of this depth observation. Harder & Stewart noted the blocks of the dam and the viscous portion of the outflow stopped 180 downstream of the dam.

B2.3 Model Inputs

Outflow Volumes

Ghahramani et al. (2020) estimated a total outflow volume of 55,000 m³ based on the post-failure contours in Harder & Stewart (1996). They also assigned a CDA class of 2A, for the Pond No. 6, indicating no or negligible supernatant pond was present or released. Harder & Stewart (1996) were not explicit if such the pond they described existed at the time of failure. Overall, it cannot be confirmed if Pond No. 6 should be 1A or 2A under the CDA classification.

Harder & Stewart (1996) noted the tailings were saturated due to a combination of groundwater and additional wash water. No void ratio estimates exist; therefore, it was assumed to be 1. Table B.3 presents the final volume estimate used in this thesis. For the subsequent numerical modelling, it was assumed that there was no supernatant pond. The uncertainty in the void ratio and presence of a supernatant pond means the volumetric solids concentration of 50% is poorly evidenced. There is not enough information to support an estimate of the volume for each two flow characteristics (viscous and fluid) that were described by Harder & Stewart.

Table B.3 Gillibrand Pond No. 6 Outflow Volumes

| Compartment | Tailings Solids (m ³) | Interstitial Water (m ³) | Supernatant Pond (m ³) | Total (m ³) |
|-------------|--------------------------------------|---|--|----------------------------|
| Pond No. 6 | 27,500 | 27,500 | Unknown, estimated to be 0 m ³ | 55,000 |

Breach Process and Geometry

Sediment boils were observed at Pond No. 6, evidencing earthquake-induced liquefaction occurred (Harder & Stewart, 1996). An upstream dam containing saturated and liquefied tailings that failed during an earthquake is evidently a Process II breach.

The breach geometry was likewise taken from the post-failure survey and is presented in Table B.4. The outflow and breach through the southwest side of the dam is orientated at roughly 45° to the crest alignment, rather than perpendicular. This is inferred to be caused by the slope direction in the area proximal to the breach and a section of the dam that rotationally translated to the right side of the breach that redirected the flow. These nuances make defining the hydraulic control difficult.

Table B.4 Gillibrand Pond No. 6 Breach Geometry

| Dam Height (m) | Crest Height (m) | Breach Height (m) | Bottom Breach Width (m) | Top Breach Width (m) | Left Breach Side Slope (xH:1V) | Right Breach Side Slope (xH:1V) |
|---------------------------|-----------------------------|------------------------------|------------------------------------|---------------------------------|---|--|
| 24 | 24 | 12 ¹ | 42 | 145 | 2.4 | 6.5 |

¹ The breach channel had a tailings deposition depth around 12 m, indicating the breach height may include an additional 12 m.

Terrain and Manning's Coefficient

The terrain data source is the USGS SOCAL Wildfire QL2 DEM, with a horizontal resolution of 1 m. This data was generated from aerial LiDAR flown in 2018 after the wildfires in Southern California. Vegetation and buildings were removed, and the vertical Root Mean Square Error at a 95% confidence level is reported as 0.112 m. The breach channel was cut into the TSF, and the translated dam section was added to the terrain. These modifications are shown in Figure B.5.

The creek in Tripas Canyon is small, however it was comparatively large enough to contain the fluid runout within a kilometre (Ghahramani et al. 2020), suggesting that the creek channel should be added to the terrain data. The vegetation in the riparian area obscures any indication of the creek channel alignment or size, therefore no channel modifications were performed. The Tripas Canyon riparian appears to have a different alignment than shown in the UGSS aerial imagery (1994) and the Zone 1 inundation area mapping by Ghahramani et al. (2020). It is likely that the terrain has materially changed since the breach, further reducing the validity of any channel modifications. The moderate vegetation in the riparian area and grassed areas was represented with a composite Manning's coefficient of 0.06.

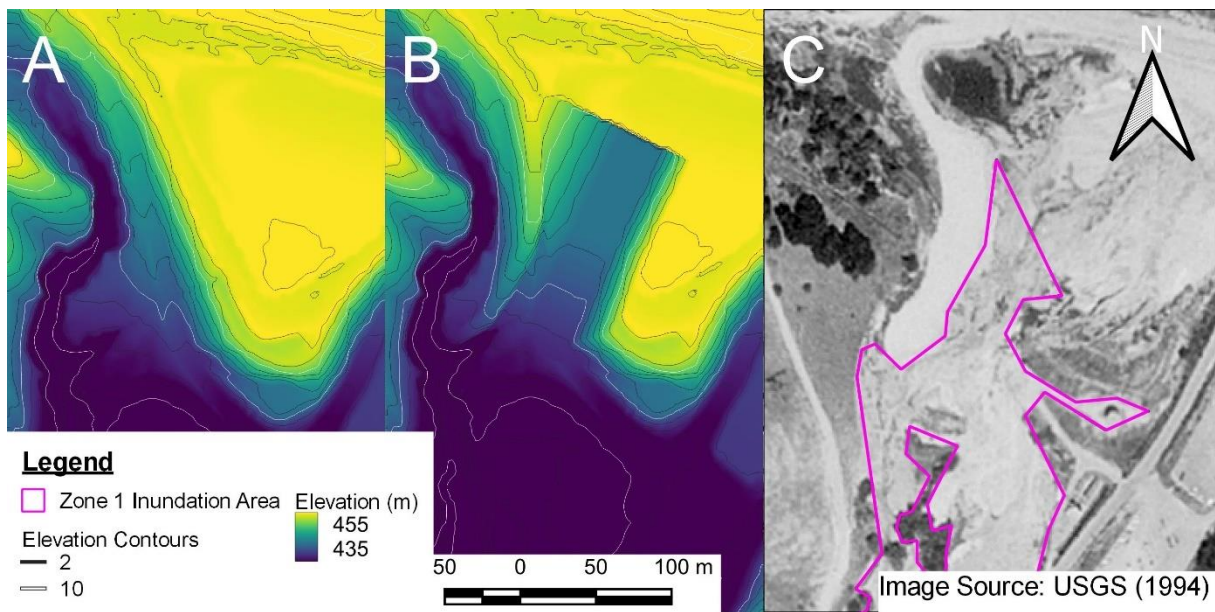


Figure B.5 Terrain Edits and Imagery for Gillibrand Pond No. 6 A) Terrain Before Breach Channel Modification, B) Terrain After Breach Channel Modification, and C) USGS Aerial Imagery for Comparison

B2.4 HEC-RAS Model Set-up

Initial models used the total outflow volume and attempted to represent both the viscous and fluid portions of the runout. These models performed very poorly and a single yield stress and viscosity value were deemed insufficient to approximate the characteristics of either flow condition. Two separate models were developed instead, a viscous runout scenario and a fluid runout scenario. The total outflow volume of 55,000 m³ was equally split for each model, as there is not enough data to support more sophistication than this arbitrary estimate. The Zone 1 inundation area from Ghahramani et al. (2020) was clipped within a radius of 180 m of the Pond No. 6 to use for the calibration process for the viscous runout scenario.

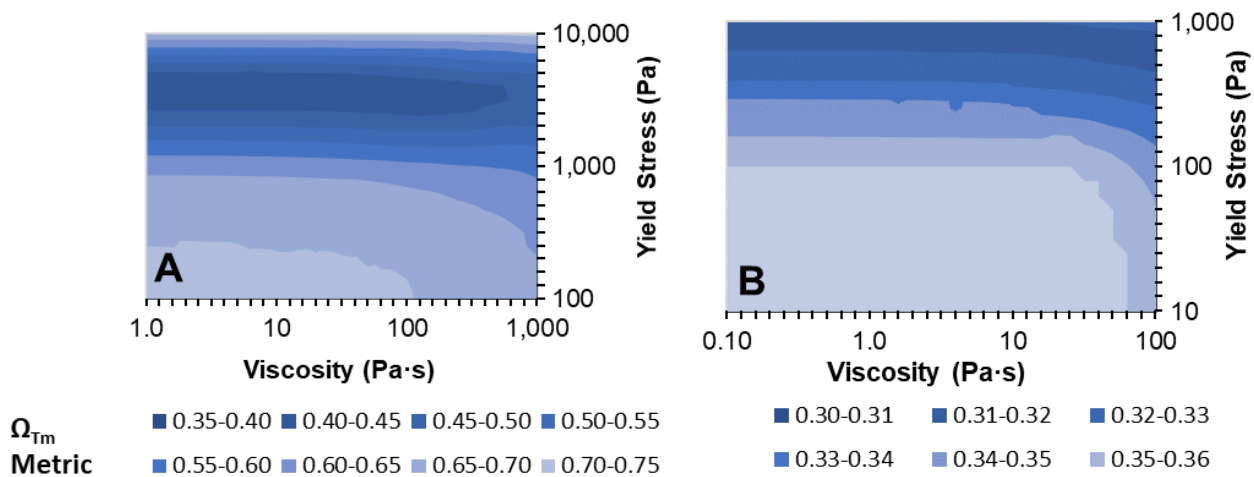
The remaining model set-up was identical between the two model scenarios. The post-failure survey in Harder & Stewart (1996) indicates the total outflow is roughly cone shaped, therefore the stage-storage curve was an idealized level-pool semi-cone for each model. The breach weir coefficient was 0.928. The computational grid resolution was 5 m and an outflow boundary condition was used at the downstream end of the Zone 1 inundation area. The representative particle size used was 100 microns, but Harder & Stewart do not specify the exact median particle size between the clay to silty sands soils observed in the facility.

B2.5 HEC-RAS Model Results

The calibration plots are shown in Figure B.6, with each tick mark roughly representing a 1.25x increase in the rheology inputs. The best inputs are shown in Table B.5 for each model scenario, based purely to the Ω_{Tm} metric. The maximum depth for the fluid scenario in the Tripas Canyon ranges between 1.7 to 2.5 in the downstream half of the Zone 1 inundation area, much higher than the 1 m “splashes” mentioned by Harder & Stewart (1996). No further calibration was performed, as the additional sophistication is not warranted by the insufficient local runout observations and uncertainty in the volume for each flow type. The modelled maximum depths and velocities of the Gillibrand Pond No. 6 runout are shown in Figure B.7 and Figure B.8 for the viscous and fluid scenarios respectively. Figure B.10

Table B.5 Gillibrand Pond No. 6 Rheological Parameters

| Model Scenario | Assumed Outflow Volume (m ³) | Yield Stress (Pa) | Viscosity (Pa·s) |
|----------------|--|-------------------|------------------|
| Viscous | 27,500 | 4,000 | 2 |
| Fluid | 27,500 | 800 | 50 |



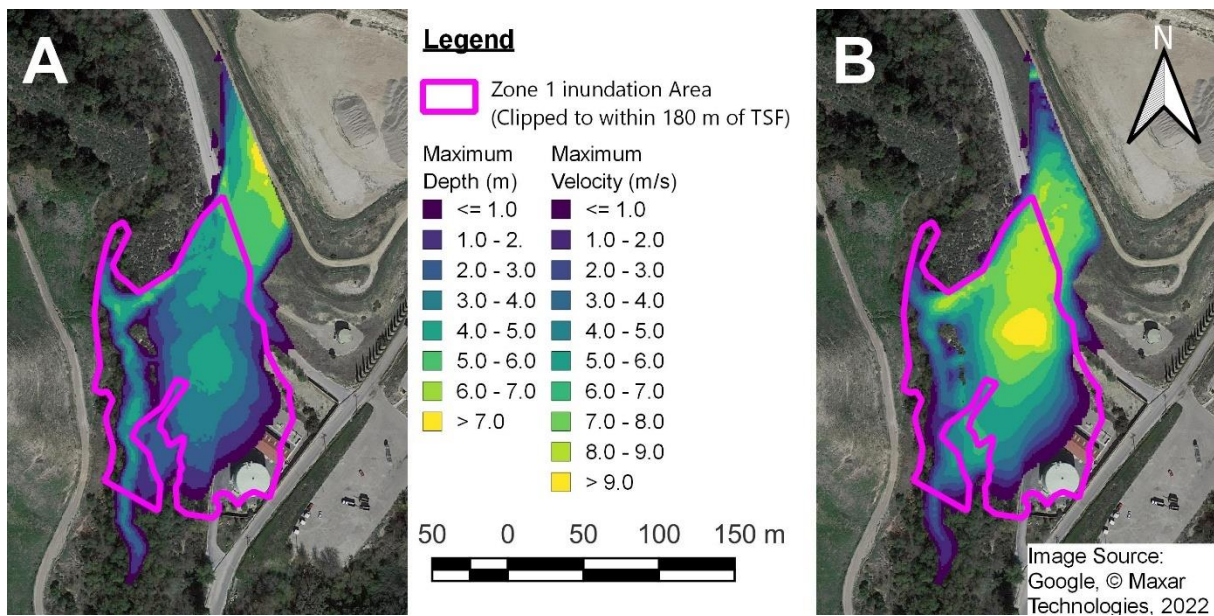


Figure B.7 Gillibrand Pond No. 6 HEC-RAS Model Results (Viscous Scenario) A) Maximum Depth and B) Maximum Velocity

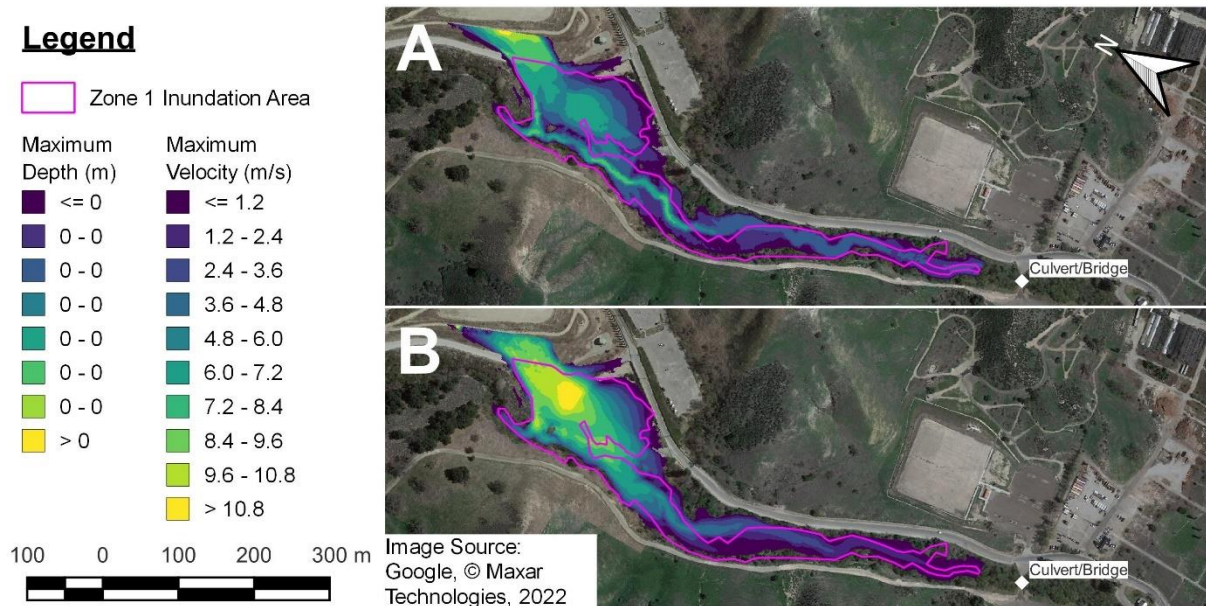


Figure B.8 Gillibrand Pond No. 6 HEC-RAS Model Results (Fluid Scenario) A) Maximum Depth and B) Maximum Velocity

B2.6 Recommendations for Future Research

The terrain data from the USGS appears to be high accuracy and resolution but is no longer representative of the conditions during the failure. Furthermore, the geometry and size of the creek channel in Tripas Canyon may be an important element for the back-analysis, but this was not explored here.

The volume of the two fluid types is unknown. The slight underestimation of the inundation area for the viscous flow type (shown in Figure B.7) and the overestimation of the depth in the Tripas Canyon (shown in Figure B.8) suggests more of the volume was of the viscous type, but this is speculative at best. The two flow types at the Gillibrand Pond No. 6 event would have interacted with each other, which is not included in the two separate HEC-RAS models. A model capable of two or more phases is necessary to model this interaction. The calibrated viscosity of the viscous model is lower than the calibrated viscosity in the fluid model, which is intuitively incorrect. It is not feasible to refine the calibration until the other model inputs or modelling approaches identified as needing improvement are addressed.

Appendix B.3 Harmony 4A (Merriespruit), South Africa, 1994

B3.1 Failure Event Narrative

The Harmony Gold mine near the town of Virginia, South Africa, deposited tailings into a composite ring-dyke TSF with upstream dams (Wagener, 1997). After an extreme rainfall event on the afternoon of February 22, 1994, the north dam of compartment 4A experienced overtopping for several hours (Wagener). Eventually a minor slump triggered static liquefaction of the dam and tailings. The failure was described by eyewitnesses as “a loud bang”, and “a series of loud noises like explosions”, interpreted to be the collapse of blocks of tailings (Wagener; Blight & Fourie, 2005). The flow swept through the suburb of Merriespruit, killing 17 people and damaging the Sand River environment (Wagener). Although the Harmony TSF is a composite TSF, the breach was limited to the 4A compartment and is therefore comparable to a single compartment failure event. The event is colloquially referred to the Merriespruit event after the impacted suburb.

Impounded Volumes

The total impounded volume was reported as 7 M m³ by Rico et al., (2008), but has not been confirmed (Rana et al., 2021). In fact, the surface area of 1,3000,000 m² and minimum dam height of 16 m of the 4A compartment alone suggest the total impounded volume estimate may be on the low side. Wagener (1997) and Van Niekerk & Viljoen (2005) estimate the available supernatant pond storage was between 70,000 m³ to 100,000 m³, which must have been full at the time of failure given the observed overtopping.

Zone 1 Description

The suburb of Merriespruit was the predominant region within Zone 1, and the land cover is correspondingly light density single-family dwellings. Beyond the suburb, the tailings runout reached a bird sanctuary, which is primarily vegetated wetland (Duvenhage, 1998, Van Niekerk & Viljoen, 2005). The tailings were unconfined during the runout (Ghahramani et al., 2020)

Ghahramani et al. (2020) estimated the Zone 1 inundation area to be 900,000 m³, which was repeated in Ghahramani et al. (2022). The uncertainty was noted to be relatively high owing to low resolution of Landsat imagery and the use of oblique photographs to support the mapping. The actual georeferenced shapefile contradicts this

reporting, indicating an area of 994,000 m² for the Zone 1 inundation area. The georeferenced shapefile was assumed to be correct and used in this thesis.

B3.2 Additional Runout Observations

The high watermark of the tailings flow at the first row of houses in Merriespruit (350 m downstream from the dam crest) was shown by Wagener (1997) as 2.5 m. Video footage after the event shows civilian wading through knee high mud in the village of Merriespruit, indicating final depths around 0.5 m (AP Archive, 2015). This runout observation is also corroborated by the photograph in Wagener at the first row of houses.

Van Niekerk & Viljoen (2005) state the arrival time to the bird sanctuary as 5 minutes, but do not provide any evidence or reasoning for this determination. The timing of the breach is not precisely known, with best estimates placing 100 minutes to 120 minutes after the end of the rainfall at 7 PM (Fourie et al., 2001). Without a confirmed time of failure, it does not appear credible that any arrival time could be reliably estimated. Consequently, the arrival time from Van Niekerk & Viljoen is not included in the database or numerical modelling.

B3.3 Model Inputs

Outflow Volumes

Wagener (1997) reported an outflow volume of 530,000 m³ for the tailings volume, excluding the supernatant pond volume released. The average of the reported supernatant pond volumes (inclusive of the rainfall volume) was used for the supernatant pond. The overtopped volume and flow that preceded the breach for roughly 2 hrs was estimated as 30,000 m³ to 50,000 m³ by Ghahramani et al. (2022) but was excluded from the volume estimates and subsequent numerical modelling in this thesis.

Fourie et al. (2001) investigated the in-situ tailings in a meta-stable state but did not discharge from the TSF and found void ratios from 0.4 to 1.6. Furthermore, they found that void ratios higher than 0.84 were in a liquefiable state in in-situ condition. Liquefiable tailings were stratified with non-liquefiable tailings, suggesting non-liquefiable tailings were transported out of the facility on a layer of liquefiable tailings (Blight & Fourie, 2005). This indicates the average void ratio of the outflow could be lower than 0.84. Regardless, the tailings were separated into solids and interstitial water according to a void ratio of 0.84. All volumes are presented in Table B.6, and the final calculated volumetric solids concentration is 46.8%.

Ghahramani et al. (2022) assessed the volumetric solids concentration of the total outflow volume as 50%, which corresponds to a void ratio of 0.72. They based the solids concentration on common soil properties of gold tailings in addition to observable mudflow characteristics (solids concentration of 45% to 55%) within photographs and eyewitness reports (personal communication, 2021). Both estimates have void ratios within the range reported by Fourie et al. (2001) and overall reflect the uncertainty in determining such the solids concentration for past events.

Table B.6 Harmony 4A Outflow Volumes

| Compartment | Tailings Solids (m ³) | Interstitial Water (m ³) | Supernatant Pond (m ³) | Total (m ³) |
|-------------|--------------------------------------|---|---------------------------------------|----------------------------|
| 4A | 288,000 | 242,000 | 85,000 | 615,000 |

Breach Process and Geometry

Prolonged overtopping as occurred at Harmony 4A implies a Process I breach. Eyewitness accounts and the expert investigations support a Process II breach however (Wagener, 1997, Fourie et al., 2001, Blight & Fourie, 2005). The limited erosional features in the remaining tailings deposit, marginal stability of the upstream dam, and the reported series of bangs suggest Process II was the dominant process.

The dam height of the Harmony 4A dam at the breach location is 31 m tall (Wagener, 1997, Blight & Fourie, 2005). The exact depth of liquefaction is not known (Blight & Fourie) however photographs and profiles of the post-failure surface indicate approximately 4 m deep of tailings self-damming the breach channel (Wagner, Blight & Fourie, Stava 1985 Foundation Archives). Based on photographs, the breach width of 150 m reported by Van Niekerk & Viljoen (2005) is interpreted as the top breach width (roughly 5 dam heights) with a corresponding bottom breach width of 55 m (roughly 2 dam heights). This interpretation of the breach geometry aligns with Petkovšek et al. (2020). Table B.7 summarizes the breach geometry.

Table B.7 Harmony 4A Breach Geometry

| Dam Height (m) | Crest Height (m) | Breach Height (m) | Bottom Breach Width (m) | Top Breach Width (m) | Left Breach Side Slope (xH:1V) | Right Breach Side Slope (xH:1V) |
|-------------------|---------------------|----------------------|----------------------------|-------------------------|-----------------------------------|------------------------------------|
| 31 | 31 | 27 ¹ | 55 | 150 | 1.75 | 1.75 |

¹ The breach channel had a tailings deposition depth around 4 m, indicating the breach height may include an additional 4 m.

Terrain and Manning's Coefficient

The terrain data source was the Airbus WorldDEM DTM, with a spatial resolution of 12 m. The structures and wetland vegetation appear to be removed as expected for a bare earth terrain dataset. A buttress was constructed against the north dam after the failure and is visible within the terrain dataset and satellite imagery. This buttress was removed along with the addition of the breach channel. Other than the buttress, the terrain dataset was considered sufficient for modelling in HEC-RAS.

The Manning's coefficient was selected as 0.08 and uniformly applied to the whole model domain for both the suburban and wetland areas to reflect the moderate obstruction and flow resistance from those land covers.

B3.4 HEC-RAS Model Set-Up

The HEC-RAS model set-up was relatively standard for the Harmony 4A event. The breach weir coefficient was 0.928 to represent the Process II breach. To include some portion of Process I as described in Section B3.3, the stage-storage curve was assigned a linear relation. The tailings flow width narrows to 330 m, so the computational resolution was selected as 36 m. No outflow boundary was used as the majority of the tailings deposited within Merriespruit and the bird sanctuary wetlands and not transported by the Sand River. The representative particle size was 100 microns, based on the measured range of d_{50} values from Fourie et al. (2001).

B3.5 HEC-RAS Model Results

The calibration plot is shown in Figure B.9, with each tick mark roughly representing a 1.58x increase in the rheology inputs. Based on the Ω_{Tm} metric, the best inputs are 160 Pa and 160 Pa·s for the yield stress and viscosity respectively. The peak depth at the first row of houses was modelled as 3.1 m, or 0.6 m above the observed depth. Conventional trial-and-error within the lowest Ω_{Tm} region was completed to reduce this depth error. A yield stress and viscosity of 250 Pa and 4 Pa·s respectively results in a peak depth of 2.7 m at the first row of houses with only a marginal decrease in the Ω_{Tm} metric performance. The modelled final depths throughout Merriespruit ranged between 0.4 m to 1 m, but generally were around 0.5 m, in alignment with the AP Archive (2015) footage. The modelled maximum depths and velocities of the Harmony 4A runout are shown in Figure B.10.

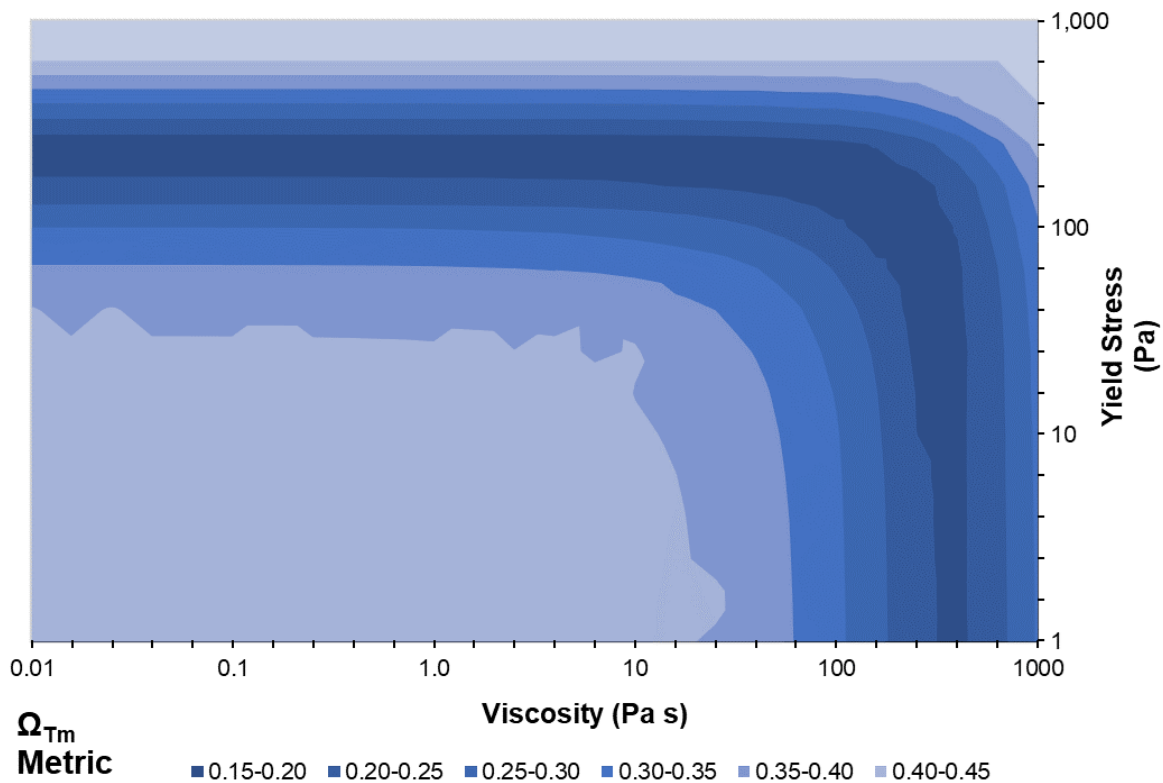


Figure B.9 Harmony 4A Gold Rheology Calibration Plot in Log-Log Scale

B3.6 Recommendations for Future Research

Arrival times are important parameters for confirming that a numerical model reflects the real life phenomena. The arrival time at the bird sanctuary reported by Van Niekerk & Viljoen (2005) was assessed as not considered credible without further evidence. Further investigation into local news reporting or eyewitness accounts is warranted to either support or firmly refute the arrival time estimate and promote more confidence in any back analysis of the Harmony 4A event.

The area match of the present modelling is quite good (as measured by the low Ω_{Tm}) and relatively good depth match at the first row of houses. The use of a linear stage-storage curve is difficult to confirm as appropriate without some form of observed timing for the Harmony 4A event. A level-pool curve would result in increased depth and velocities proximal to the breach, suggesting a linear curve may be a reasonable approximation of the breach process for this event.

Relatively good reporting on building damage and fatality rates may be available for the Harmony 4A event. A study on vulnerability estimates including the Harmony 4A event would be of interest for industry but is not within the scope of this thesis.

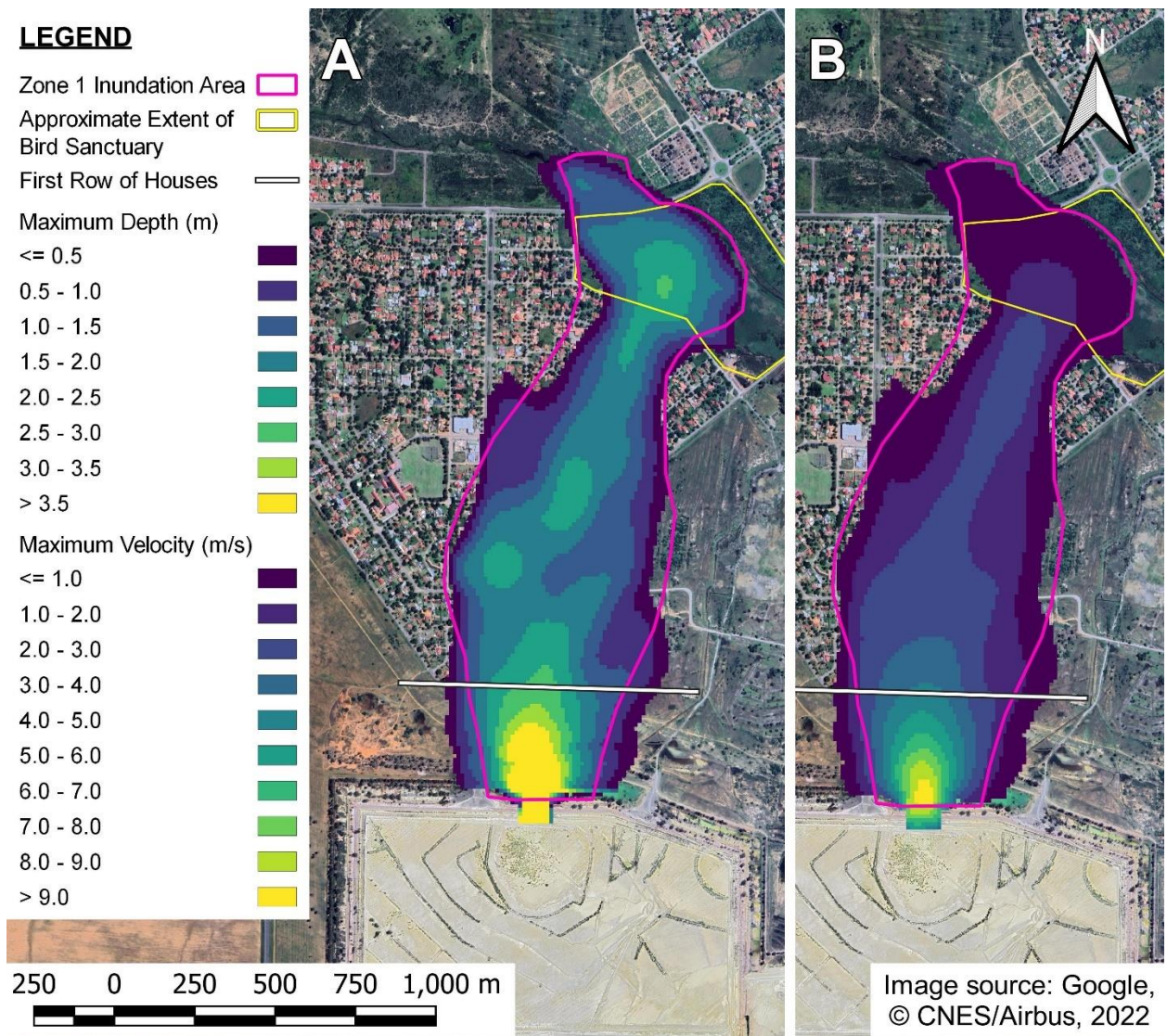


Figure B.10 Harmony 4A HEC-RAS Model Results A) Maximum Depth and B) Maximum Velocity

Appendix B.4 Aznalcóllar (Los Frailes), Spain, 1998

B4.1 Facility Background and Failure Narrative

The Aznalcóllar tailings facility was a side-hill composite facility for zinc, lead, and copper tailings from the nearby Los Frailes open pit. One compartment was for the pyroclastic tailings in the north and another for pyrite tailings in the south. Early in the morning of April 25, 1998, the foundation of the tailings dam failed, displacing a 700 m long section of downstream constructed dam around 50 m horizontally (McDermott & Sibley, 2000; Alonso & Gens, 2006a), including nearby the central embankment. The translation decreased the elevation of the dam crest by up to 2.4 m and disconnected the central embankment from the perimeter embankment (Alonso & Gens, 2006a). The supernatant pond volumes from either or both cells subsequently began to overtop and erode the weakened dam to the foundation at a single location within the 700 m displaced section. The tailings flow affected the floodplains of the Agrio and Guadiamar rivers, nearby agricultural land, and passed several towns within the zone 1 inundation area (McDermott & Sibley, 2000; Gallart et al, 1999; Eptisa, 1998; Ghahramani et al, 2020). The cause of the displacement was found to be the undrained brittle behaviour of the clay foundation (McDermott & Sibley, 2000). The event is colloquially called Los Frailes, after the name of the open pit at the mine site.

After the investigations and modelling were finished within this thesis but prior to thesis completion, Sanz-Ramos et al. (2022) published a review of existing and newly uncovered information for the Aznalcóllar event. The general approach and goals they took were similar to this thesis, however Sanz-Ramos et al. focused on Aznalcóllar alone and had greater data access than herein. The modelling was not updated for practical time considerations, however the findings from Sanz-Ramos et al. are mentioned as relevant.

Impounded Volumes

The reported total impounded volume varies within the literature. McDermott & Sibley (2000) state the total volume of impounded tailings was 15.0 M m³ and were assessed to be most accurate by Rana et al. (2021) based on the McDermott & Sibley's involvement with the mine owner and the legal proceedings (personal communication, 2022). Considering the dam height and natural ground slope are relatively consistent, within this research the tailings volume was proportioned based on surface area of the

compartments (1.5 km^2 and 0.5 km^2 for the North and South cells respectively, McDermott & Sibley). Supernatant ponds are visible in both compartment in the satellite imagery prior to the failure (Rana et al., 2021). The total supernatant pond volume of 5.44 M m^3 (McDermott & Sibley) was similarly distributed between the two cells.

Sanz-Ramos et al. (2022) created pre-construction and post-failure topographies and estimated the total impounded volume to be between 20 M m^3 and 28 M m^3 . The topographic evidence appears compelling, and does match other estimates (e.g., CMA, 1998, Arenas et al., 2001, Borja et al., 2001). No distribution between the two cells or tailings volumes versus supernatant pond are provided in Sanz-Ramos et al. They also measured the surface areas as 1.15 km^2 and 0.4 km^2 for the North and South cells respectively.

Zone 1 Description

The region is arid, and the floodplain is lightly covered with Mediterranean brush (Gallart et al., 1999). There is some variation in the density of vegetation, however it appears to be primarily bare earth with limited brush outside of the main channel. The vegetation increases in density proximal to the river channel. The tailings flow was confined by the Guadiamar River valley during the runout (Rana et al., 2021), however they did reach some 1.6 km upstream of the breach location as well. Gallart et al. (1999) observed very little erosion occurred during the breach, however they noted that geomorphological impacts over time would be likely due to the tailings deposits.

Ghahramani et al. (2020) and Rana et al. (2021) mapped the Zone 1 inundation area to be 16.0 km^2 and terminated 29 km downstream of the TSF, based on the LandSat 4-5 satellite imagery. Inspection of the same satellite imagery reveals deposition and impacts are visible further downstream. McDermott & Sibley (2000) and Gallart et al. (1999) also noted deposition occurred at the Don Simón ford, some 41 km downstream of the Aznalcóllar TSF. According to the Zone 1 inundation area definition from Ghahramani et al. (2020), the inundation mapping should include the full 41 km runout. For consistency with the rest of the model database, the mapping by Ghahramani et al. (2020) without adjustment was used during the calibration.

Sanz-Ramos et al. (2022) present clear aerial imagery that confirms the tailings and mud was above bankfull flow at the Don Simón ford. They further state that the distance of mud deposits above the riverbanks was between 43.0 km to 50.4 km measured from the breach location. The total area affected by the muds is estimated by

Sanz-Ramos et al. is 27.0 km², more than 50% greater than Ghahramani et al. (2020). Sanz-Ramos et al. commented that while little physical changes occurred during the breach, major geomorphological changes occurred with the subsequent restoration activities. These changes in terrain may introduce errors or condition the hydraulic behaviour in numerical modelling of the event (Sanz-Ramos et al.).

B4.2 Additional Runout Observations

Recorded data and eyewitness accounts (Eptisa, 1998), provide sufficient evidence to form a timeline for the breach process:

- A power line near the toe of the embankment failed before 1 AM, which is attributed to the initial horizontal displacement of the foundation (Eptisa, 1998).
- An electrician investigating the downed power line noticed there was no longer any supernatant pond in the north pyroclastic cell around 3 AM, indicating that most of the breach outflow had occurred by then.
- Photographs of the breach were taken some time in the morning around 8:00 AM, when water and tailings were still slowly discharging from the breach but essentially the breach outflow was complete (Alonso & Gens, 2006a)

There are two analog staff gauges on the Guadiamar River operated by the Hydrographic Confederation of the Guadalquivir, with data reporting done by the Automatic Hydrological Information System of the Guadalquivir (SAIH). The tailings flood wave damaged the gauges, however the paper record from the first gauge, A39 El Guijo, was recovered and the Geological Survey of Spain (IGME) reported the stage data, as reproduced in Figure B.11 (IGME, 2001). The El Guijo gauge is roughly 7.2 km downstream of the breach location along the Guadiamar River centerline.

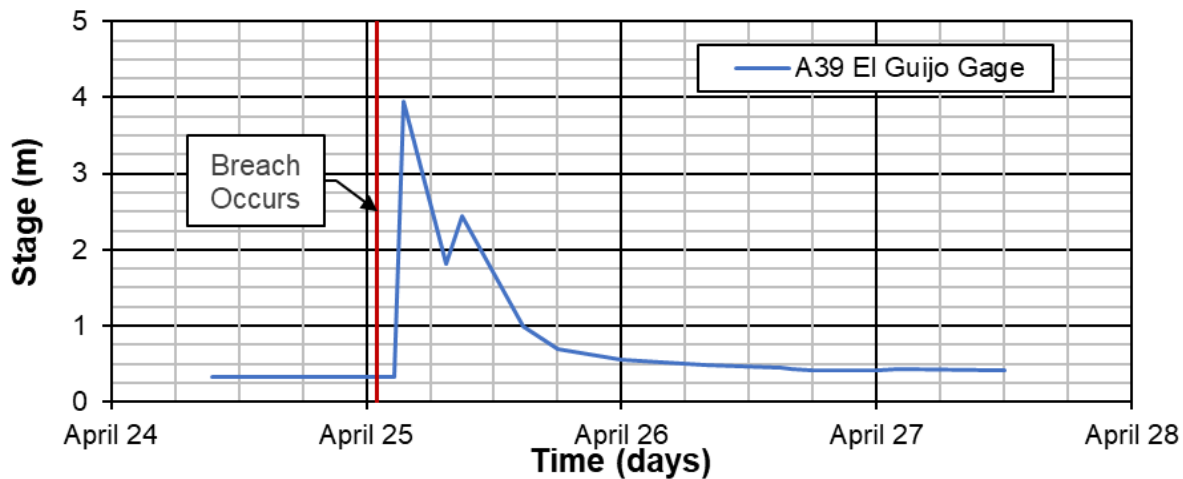


Figure B.11 Recorded Stage at the A39 El Guijo Gauge Operated by the Hydrographic Confederation of the Guadalquivir (IGME, 2001).

The double peak at the El Guijo gauge was interpreted as the sequential arrival of a primary water flood wave followed by a mud flood or mudflow consisting of a greater portion of the tailings (IGME, 2001; Ayala-Carcedo, 2004; Rico et al., 2008). SAIH indicated any data above a stage of 2 m may be incorrectly measured by the gauge due to the limits of the original gauge and the damage during the tailings runout (personal communication, 2022). High watermarks of 4 m on a bridge near Sanlúcar la Mayor, roughly 5.2 km downstream from the El Guijo gauge, roughly corroborating the peak depth recorded by the gauge (Eptisa, 1998).

The second gauge, A22 Guadimar, is roughly 25 km downstream of the breach location along the Guadimar River centerline. It reportedly recorded a frontal arrival time at 7:00 AM (Gallart et al., 1999), however, the SAIH did not confirm the recovery of the paper record from this gauge (personal communication, 2022).

Sanz-Ramos et al. (2022) assessed the hydraulics of the flow at the El Guijo gauge by extrapolating the reported rating curve. Such an extrapolation is inappropriate as it would not include the abrupt change in flow section shape at the channel banks (Lang et al., 2010). Therefore, the conclusions in Sanz-Ramos et al. (2022) based on the flow at El Guijo are not considered appropriate for model calibration.

B4.3 Model Inputs

Outflow Volumes

The total released volume was reported anywhere from 0.5 M m³ to 10.3 M m³ (Sanz-Ramos et al., 2022), and are inconsistently defined as tailings, process water and tailings,

or other. The volumes of 1.3 M m^3 of tailings and 5.5 M m^3 of tailings water from McDermott & Sibley (2000) were assessed to be most accurate by Rana et al. (2021). The “tailings water” was assumed to be primarily from the supernatant ponds and proportioned by the surface area between each cell.

Some of the pyritic tailings liquefied during the foundation failure, but the vertical walls of tailings as tall as 20 m indicate limited erosion of the pyritic tailings during the breach (Alonso & Gens, 2006a). The coarser pyroclastic tailings showed erosional patterns and appear to be primarily transported by the supernatant pond during the breach, evidenced by photos in Alonso & Gens (2006a). Using simplified geometry and the post-failure survey from Alonso & Gens (2006a) and Gens & Alonso (2006), the liquefied pyritic tailings would be on the order of $150,000 \text{ m}^3$. The remaining $1,150,000 \text{ m}^3$ of tailings is estimated to come from erosion in the north pyroclastic cell during the breach. This volume is less than what would be estimated by using the rule of thumb from Small et al. (2017), but not unreasonably so. The breach translation primarily occurred at the south pyrite cell, so the central embankment may have exerted some limiting hydraulic control on the northern pond outflow, reducing the outflow velocity and erosion. The tailings volumes were further separated into tailings solids and interstitial water using the average reported void ratio for each tailings material (0.7 and 0.65 for the northern and southern ponds respectively) from Alonso & Gens (2006a). All volumes are presented in Table B.8, and the calculated outflow volumetric solids concentration is 12%.

Sanz-Ramos et al. (2022) primarily rely on the volume calculated using the flow data from the extrapolated rating curve at the El Guijo gauge to estimate the total outflow volume, which indicates a volume of 11.5 Mm^3 . Notwithstanding the gauge is 7.2 km downstream of the breach, the extrapolation has already been discussed as inappropriate. The post-failure topographic data for the in Sanz-Ramos et al. (2022) indicates a maximum outflow volume of 15.4 M m^3 . This volume is larger than McDermott & Sibley (2000) by over a factor of two, which would dramatically affect the runout modelling.

Table B.8 Aznalcóllar Outflow Volumes used in HEC-RAS Model¹

| Compartment | Tailings Solids (m ³) | Interstitial Water (m ³) | Supernatant Pond (m ³) | Total (m ³) |
|------------------------|--------------------------------------|---|---------------------------------------|----------------------------|
| North Pyroclastic Cell | 676,500 | 473,500 | 3,720,000 | 4,870,000 |
| South Pyritic Cell | 100,900 | 59,100 | 1,720,000 | 1,880,000 |
| Total | 777,400 | 532,600 | 5,440,000 | 6,750,000 |

¹ The volumes here were estimated using McDermott & Sibley (2000) and prior to the publications Sanz-Ramos et al. (2022), who present evidence that the total outflow volume is possibly as high as 15.4 M m³. The distribution between compartments and material types should be reassessed with the new volume estimate from Sanz-Ramos et al. (2022).

Breach Process and Geometry

Failure of clay foundations is generally described as non-erosional, however for Aznalcóllar the breach process is primarily erosional. The long duration of outflow supports an erosional and Process I breach. Alonso & Gens (2006a) reported the subsidence at the dam crest after the translation ranged between 1.4 m to 2.4 m, discounting a complete Process II breach progressing to the natural ground. As the tailings liquefaction was limited to the South Pyritic Cell, it could be considered a 1A breach while the North Pyroclastic Cell would be considered a 1B breach under the CDA classification. The breach formation time was estimated as 2 hours based on the timeline presented in Section B4.2.

The height of the Aznalcóllar dam is reported as a relatively level 27 m to 28 m along the east side of the facility (McDermott & Sibley, 2000; Gens & Alonso, 2006) and breached to the natural ground. Since the terrain is relatively flat in the region, the crest height can be considered the same as the dam height. The breach geometry (i.e., top breach width, bottom breach width, and breach side slopes) was coarsely estimated as from photographs available from the Stava 1985 Foundation (n.d.). The breach geometry is summarized in Table B.9.

Sanz-Ramos et al. (2022) estimated the dam height and breach height including the subsidence during the foundation failure as almost 25 m, based on the post-failure topography. This post-failure topography includes repairs completed the day after the breach, so it is not clear if this lower value is appropriate for modelling.

Table B.9 Aznalcóllar Breach Geometry

| Dam Height (m) | Crest Height (m) | Breach Height ¹ (m) | Bottom Breach Width (m) | Top Breach Width (m) | Left Breach Side Slope (xH:1V) | Right Breach Side Slope (xH:1V) |
|----------------|------------------|--------------------------------|-------------------------|----------------------|--------------------------------|---------------------------------|
| 28 | 28 | 26 | 56 | 84 | 0.50 | 0.50 |

¹The breach height here excludes the approximately 2 m subsidence during the foundation failure. The water surface elevation at the time of failure and therefore the height of water above breach bottom is not known.

Terrain and Manning's Coefficient

The National Geographic Institute provides an open-access digital terrain model, DTM05, for the entirety of Spain. It has a 5 m horizontal resolution and reported altimetric accuracy (RMSE) of 0.2 m. A coarser 20 m resolution version of the DTM05 is distributed by the Open Data Portal, which was used in the modelling work. The coarser terrain data maintains a good definition of the floodplain but has bridge decks within the model domain already removed. The DTM was collected in November 2019, therefore it may not be representative of pre-failure topography, which Sanz-Ramos et al. noted were changed during the rehabilitation after the failure (2022).

The Aznalcóllar TSF is clearly defined in the terrain, and the breach channel was cut into it. The river bathymetry in either terrain would not be captured by the LiDAR flights and shows probable vegetative obstructions resulting in ridges throughout the river profile. Based on the satellite imagery, terrain data, and typical widths and depths of the Agrio and Guadamar rivers in the Zone 1 extent reported by Gallart et al. (1999), a standard 50 m wide and approximately 3 m deep channel with 3H:1V side slopes was cut into the terrain data to maintain hydraulic connectivity. An example of the river channel edit is shown in Figure B.12.

A single Manning's coefficient of 0.055 was selected to represent the surface roughness of the entire model domain, corresponding to the predominantly bare earth outside of the river channel (e.g., as shown in Figure B.12C).

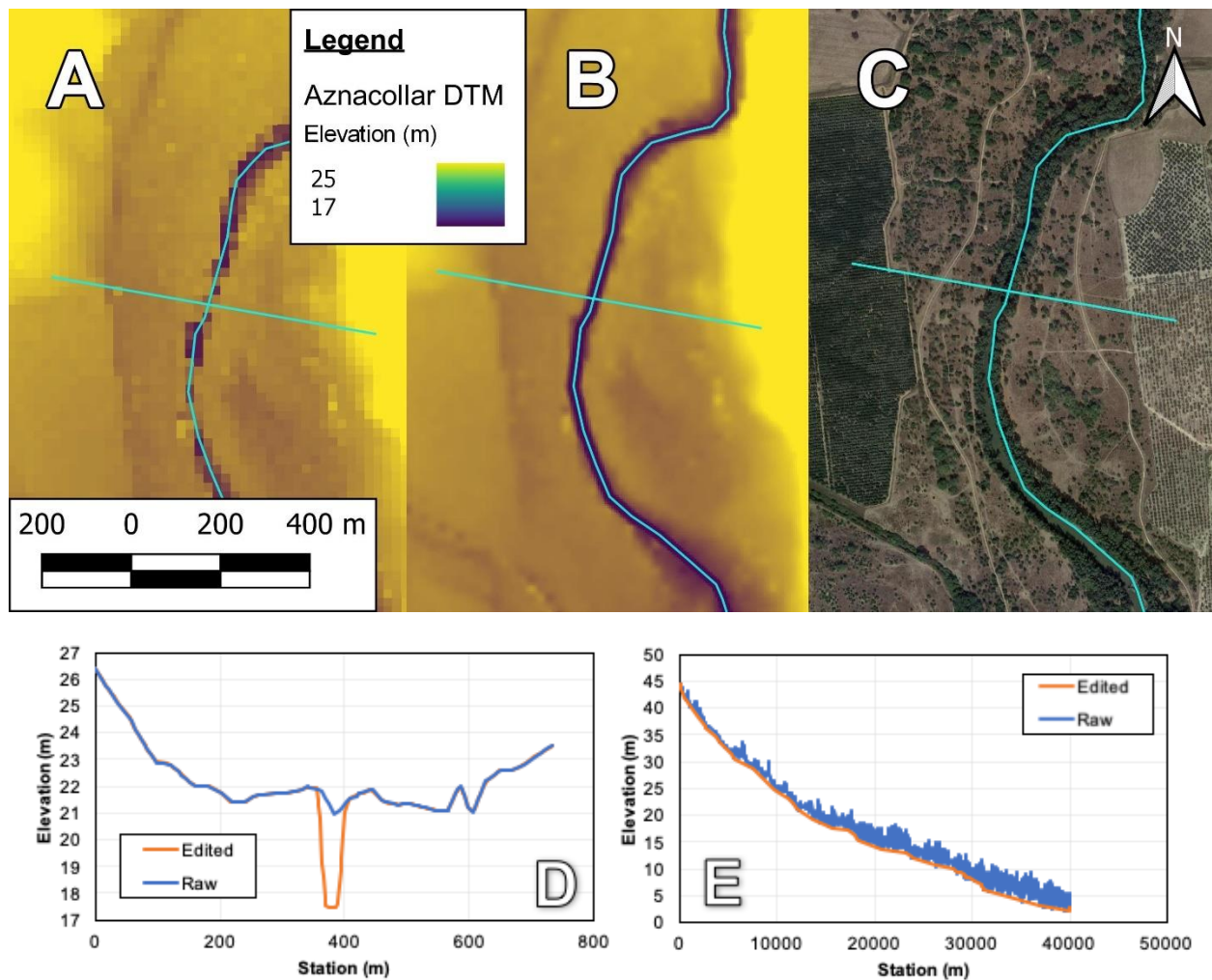


Figure B.12 Terrain Modifications and Imagery for Aznalcóllar. A) Terrain Before Channel Modifications, B) Terrain After Channel Modifications, C) Satellite Imagery for Comparison, D) Cross-section Along the Turquoise Line, E) Profile Along the Entire Channel Within the Model Domain

B4.4 HEC-RAS Model Set-up

The breach was modelled as an overtopping breach, with the dam crest decreased 2 m below the initial dam crest level to represent the initial subsidence prior to the erosion. A linear stage-storage curve was used, given the relatively long breach formation time and insufficient available evidence to support a more sophisticated curve shape. The volumetric solids concentration likely varied over the duration of the outflow; however, a single outflow concentration was used given the single fluid limitation within HEC-RAS.

The model domain extends an additional 3.5 km downstream from the Zone 1 extent as mapped by Ghahramani et al. (2020) to allow sufficient space for the tailings flow to transition to bankfull flow, after which a Normal Depth BC is used. The tailings flow width narrows to 260 m in some locations, so the computation resolution was selected as 40 m. Breaklines were used for the river centerline and at any linear infrastructure such as roads in the model domain that were narrower than 40 m in any direction. The representative particle size was 100 microns, based on the measured d_{50} values from Alonso & Gens (2006a) for the pyroclastic tailings, as they represent the majority of the estimated tailings solids discharged from the facility.

B4.5 HEC-RAS Model Results

The calibration plot is shown in Figure B.13, with each tick mark roughly representing a 1.58x increase in the rheology inputs. Based on the Ω_{Tm} metric, the best inputs are 2.5 Pa and 0.4 Pa·s for the yield stress and viscosity respectively. Furthermore, the timing at various locations with the stated rheology inputs aligns with the observations well. At 3:12 AM, 95% of the total volume release volume has discharged from the facility, which aligns with the observations of the electrician. The front arrival time, peak arrival time, and peak depth align with the recorded data at the El Guijo gauge, as shown in Figure B.14. The modelled frontal arrival time at the Guadiamar gauge is 7:00 AM, matching the comment from Gallart et al. (1999). The modelled tailings outflow was mostly confined to the river channel at the Zone 1 termination as mapped by Ghahramani et al. (2020).

It should be cautioned that the apparent low model misfit is based on outflow volumes and a Zone 1 inundation area that may be both far below the actual volume and area (as noted by Sanz-Ramos et al., 2022). Consequently, the modelled results herein should not be relied upon for forward-analysis until an update to the modelled is completed.

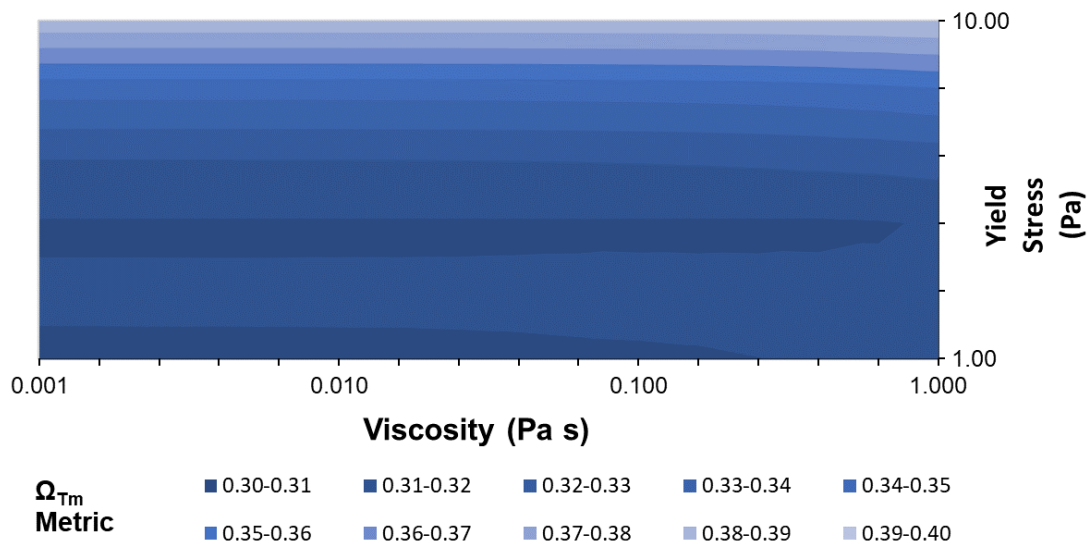


Figure B.13 Aznalcóllar Rheology Calibration Plot in Log-Log Scale

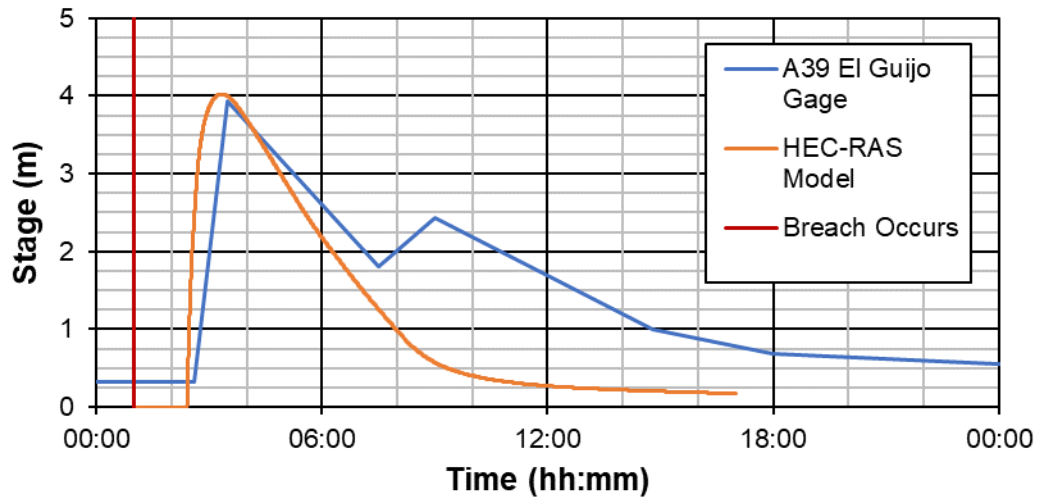


Figure B.14 Recorded Stage at the A39 El Guijo Gauge (IGME, 2001) and HEC-RAS Model Results.

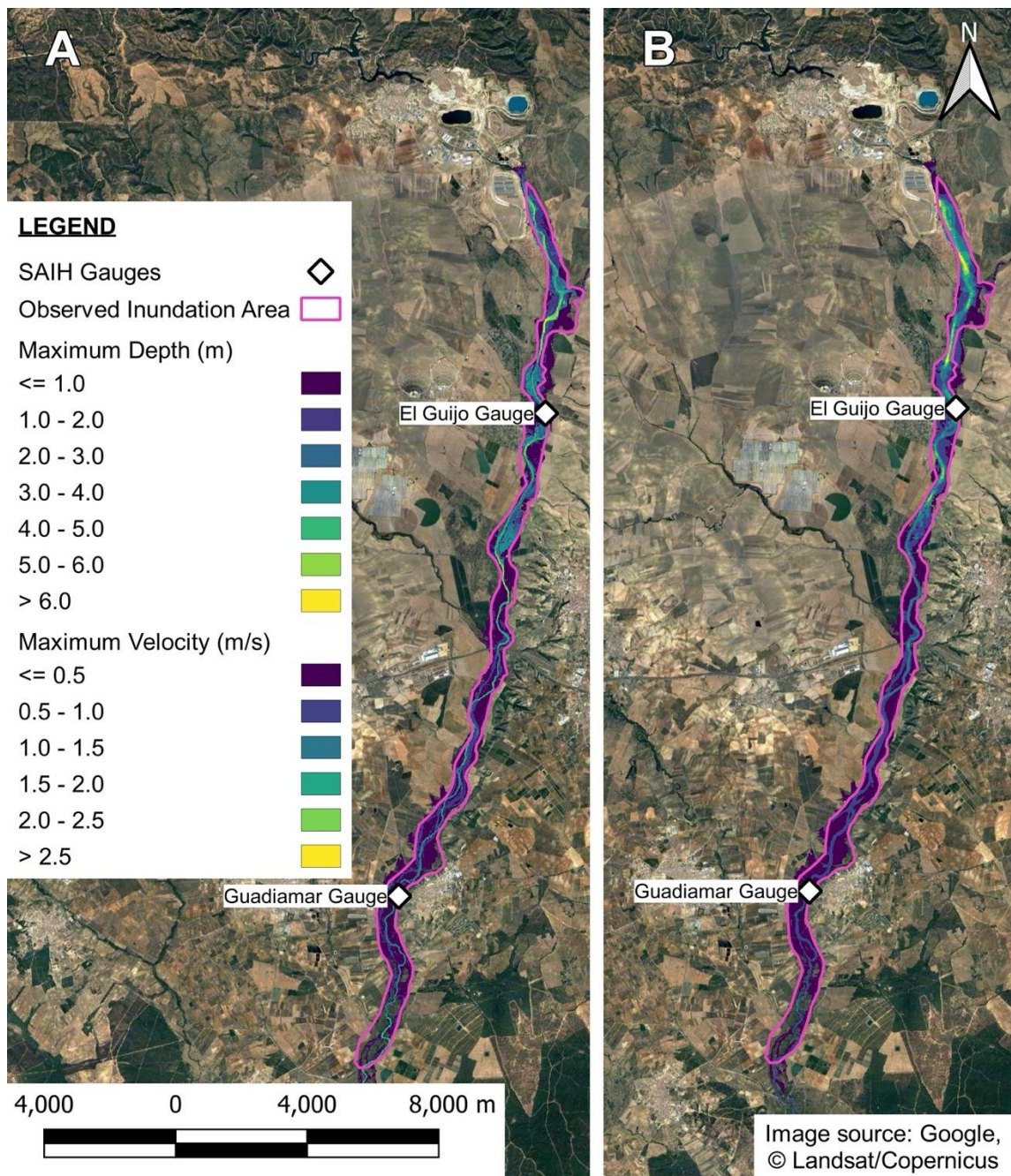


Figure B.15 Aznalcóllar HEC-RAS Model Results A) Maximum Depth and B) Maximum Velocity

B4.6 Recommendations for Future Research

The outflow volume used within the model is likely less than the actual outflow. Considering the outflow volume has a high influence on model results (Ghahramani et al., 2022), the HEC-RAS model cannot be remotely considered representative of the actual failure event until the outflow volume has been updated. The mapping by Ghahramani et al. (2020) needs updating based on the findings in Sanz-Ramos et al.

(2022). A change in the Zone 1 further impacts the modelling and calibration herein. The roughness of the floodplain was uniform within the entire model domain, and some additional evaluation of variable roughness in the floodplain and river channel may increase confidence in the model but would be a lesser priority than refining the Zone 1 inundation area, outflow volume, and the accompanying model updates.

Appendix B.5 Tashan (Taoshi or Xiangfen), China, 2008

B5.1 Facility Background and Failure Narrative

The Tashan iron mine and associated TSF was initially built in 1977 in the county of Xiangfen, China. The mine and TSF were closed in the 1980s but was later re-opened in 2005. The deposition in the TSF re-started in 2007, but the expansion designs did not follow regulatory requirements and standard practices, specifically relating to steep dam slopes and high levels of saturation within the tailings and upstream constructed dam (Wei et al., 2013). The 2007 expansion increased the dam height by 14 m by late 2008.

The TSF failed at 7:58 AM local time on September 8, 2008. The tailings runout buried the village of Taoshi, within 500 m of the TSF. The casualties reached over 300 people and caused about \$13 USD of direct losses (Wei et al., 2013). The event is also known as the Taoshi or Xiangfen event, after these local civic names. This thesis found no additional local runout observations for this event to support the model calibration and validation.

Impounded Volumes

The impounded tailings volume was reported as 290,000 m³ by Wei et al. (2013). Wei et al. also included commentary on the supernatant pond and its role on the failure, however it is not clear what the volume of the supernatant pond is or if the 290,000 m³ value is meant to be inclusive of the supernatant pond.

Zone 1 Description

The Tashan TSF was confined within a narrow valley, but the topography transitions to steep unconfined slopes within 300 m. The shapefile from Ghahramani et al. (2020) indicates the Zone 1 inundation is 430,000 m².

The Zone 1 is observed to be stepped farmlands on the steep slopes, based on Google Imagery after 2010. Wei et al. (2013) described substantial impacts to the village and market, indicating the current imagery may not be representative of the village of Taoshi at the time of the failure. Pre-Failure LandSat 5 imagery was used to delineate the extent of the village. Within the upstream half of the Zone 1 extent, the landcover is occupied by the village of Taoshi and stepped farmlands, in roughly equal proportions. The remaining half of the Zone 1 is predominantly the stepped farmlands. Based on the description in Wei et al. and the post-failure LandSat 5 imagery, the village was reduced to rubble, explaining the change in landcover after the failure. The village extent is shown

in Figure B.17, however the exact extent is limited by the low resolution of the LandSat 5 imagery.

B5.2 Model Inputs

Outflow Volumes

The outflow volume was reported by Wei et al. (2013) as 190,000 m³, however no discussion of the contents was included in Wei et al. At best it could be inferred to mostly tailings (i.e., tailings solids and interstitial water), based on a single figure in Wei et al. In any case, the total outflow volume of 190,000 m³ was assumed to be at a solids concentration of 50%. This implies that the supernatant pond volume was negligible, and the tailings void ratio was 1, or there was a material volume in the supernatant pond and the void ratio in the tailings was less than 1. Both assumptions have some face validity but cannot be confirmed at this time.

Breach Process and Geometry

Wei et al. (2013) described the breach in terms of a slope failure due to steep slopes and high levels of saturation at the 2007 expansion. This was interpreted as a Process II failure. The total dam height of the initial TSF and the expansion was 50.7 m, however the crest height was roughly half of that. The sliding surface initiated in the 2007 expansion and extended a few meters below the 2007 expansion as well. The heights were inferred from a single figure in Wei et al., which may not even be to scale, therefore the estimates here carry large uncertainty. Furthermore, it is not known if the breach progressed further below the slide surface shown in Wei et al.

The trapezoid breach geometry was estimated using the heights and elevations from Wei et al. (2013), the estimated location of the dam crest, and the terrain data (discussed in the following subsection). Essentially, the trapezoid was taken as the shape of the valley between 7 m to 24 m above the valley invert at the location of the dam crest. The breach geometry is shown in Table B.10.

Table B.10 Tashan Breach Geometry

| Dam Height (m) | Crest Height (m) | Breach Height (m) | Bottom Breach Width (m) | Top Breach Width (m) | Left Breach Side Slope (xH:1V) | Right Breach Side Slope (xH:1V) |
|-----------------------|-------------------------|--------------------------|--------------------------------|-----------------------------|---------------------------------------|--|
| 50.7 | 24 | 17 | 100 | 190 | 2.75 | 2.75 |

Terrain and Manning's Coefficient

The ALOS World 3D-30 m (AW3D30) was used, which is a DSM. It is unclear if the AW3D30 DSM includes the structures from Taoshi village, as the satellite that surveyed the data, Daichi, flew from 2005 to 2011 (JAXA, n.d.). If the satellite survey was before the destruction of the village, the DSM would not represent bare-earth conditions. If the survey was after the failure, the DSM could represent the bare-earth conditions.

It was initially believed that the structures were included, based on a visual assessment of the terrain data. The contours of the slope were redrawn to remove any knobs and irregularities considered to be structures. These terrain modifications were the most speculative, subjective, and poorly evidenced of all the modifications in this thesis. Furthermore, the terrain modifications resulted in a poorer model performance than models without the modifications. The terrain modifications were ultimately not used in the final calibration process for those reasons.

The Manning's coefficient for the farmland was 0.04. The upper portion of Taoshi was utterly destroyed (Wei et al., 2013; Stava 1985 Foundation), so the Manning's coefficient was kept at a low value of 0.04 to represent the negligible resistance of the village that was swept away. The lower portion of Taoshi did not fare as poorly as the upper portion, therefore the Manning's coefficient used was 0.08.

B5.3 HEC-RAS Model Set-Up

The stage-storage curve for the outflow volume was an idealized semi-cone and the breach weir coefficient was 0.928 for the Process II breach. The computational grid resolution was 10 m, as the steeper slopes required a finer computational resolution than the terrain resolution. No outflow boundary condition was used, as the runout came to a rest on the slopes (Ghahramani et al., 2020).

B5.4 HEC-RAS Model Results

The calibration plot is shown in Figure B.16, with each tick mark roughly representing a 1.25x increase in the rheology inputs. A previous calibration with a wide range of yield stress and viscosities but a coarser interval was completed, which informed the narrower range shown here. Based on the Ω_{Tm} metric, the best inputs are 800 Pa and 25 Pa·s for the yield stress and viscosity respectively. The areal performance is quite low, represented by the comparatively high value of Ω_{Tm} . The modelled maximum depths and velocities of the Tashan runout are shown in Figure B.17.

Roughly one third (by total outflow volume) of the modelled tailings runout is diverted into an adjacent channel outside of the Zone 1 extent. Once diverted into the channel, the runout continues for a long way, increasing the False Positive Area and increasing Ω_{Tm} . The terrain modifications attempted for the village resulted in greater volumes diverting to the adjacent channel and a higher Ω_{Tm} . Gibson et al. (2022) noted similar difficulties for modelling the 2018 Santa Barbara debris flow event. They described the shape of the Santa Barbara fan as “convex”, which diverted the flow from the observed flow paths and decreased model performance. A convex shape is also observed in the terrain for the Tashan event. Gibson et al. also had much higher quality terrain data compared to the modelling for the Tashan event.

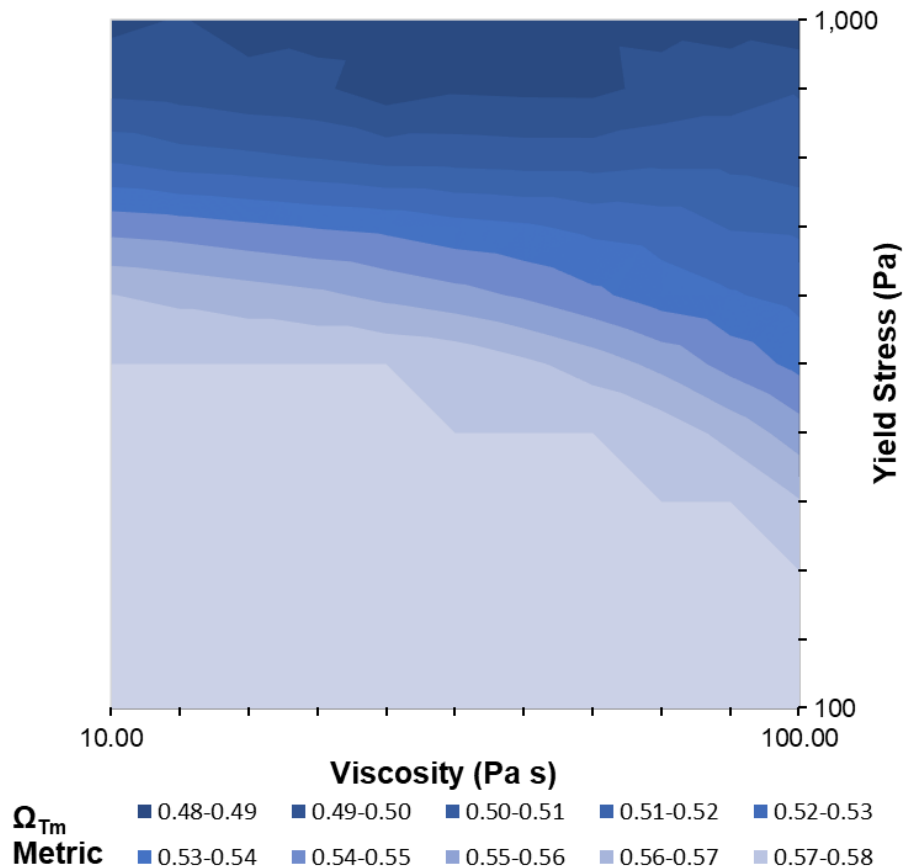


Figure B.16 Tashan Rheology Calibration Plot in Log-Log Scale

Legend

| | |
|----------------------------|------------------------|
| ◇ Taoshi Village | |
| Pre-Failure Village Extent | |
| Zone 1 Inundation Area | |
| Maximum Depth (m) | Maximum Velocity (m/s) |
| ≤ 1.0 | ≤ 2.0 |
| 1.0 - 2.0 | 2.0 - 4.0 |
| 2.0 - 3.0 | 4.0 - 6.0 |
| 3.0 - 4.0 | 6.0 - 8.0 |
| 4.0 - 5.0 | 8.0 - 10.0 |
| 5.0 - 6.0 | 10.0 - 12.0 |
| 6.0 - 7.0 | 12.0 - 14.0 |
| 7.0 - 8.0 | 14.0 - 16.0 |
| 8.0 - 9.0 | 16.0 - 18.0 |
| > 9.0 | > 18.0 |

Image Source:
Google, © Maxar Technologies

500 0 500 1,000 m

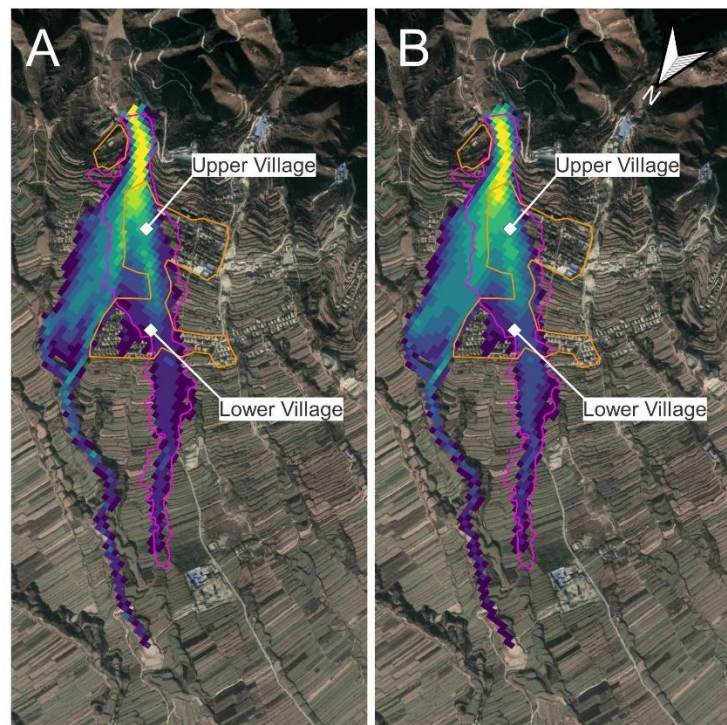


Figure B.17 Tashan HEC-RAS Model Results A) Maximum Depth and B) Maximum Velocity

B5.5 Recommendations for Future Research

The information available for the investigation was very limited. The volumes for the tailings solids, interstitial water, and supernatant pond are not known, therefore the volumetric solids concentration was assumed for this scenario. This limitation prevents a meaningful comparison of mobility or calibrated yield stress and viscosity values against other modelled events. The breach geometry was inferred and has high uncertainty. There were no local runout observations that could be used to improve the model calibration and validation process. It is likely that resources in Mandarin or otherwise inaccessible to western researchers can provide more insight than available in English on this event. The HEC-RAS model had a better areal fit to the observed Zone 1 inundation area without terrain modifications. This does not exclude the possibility that the AW3D30 data was not surveyed prior to the failure (i.e., it included structures and does not represent bare-earth conditions). A high quality DTM may be required to improve the runout modelling.

Appendix B.6 MAL Reservoir X (Ajka or Kolontár), Hungary, 2010

B6.1 Facility Background and Failure Narrative

The Hungarian Aluminium Production and Trading Company (MAL) stored the waste product from the aluminium refinery in several TSFs near the city of Ajka (Turi et al., 2013). Aluminium tailings are colloquially referred to as red mud, based on their colour and consistency. Reservoirs VI through X and Xa shared some embankments in a composite TSF arrangement. At approximately 12:10 PM on October 4, 2010, the dam breached at the northwest corner of Reservoir X. Eyewitnesses describe flow initiated through cracks in the dam, before the V shape rupture increased in size as the supernatant pond discharged (Turi et al.). The village of Kolontár and the town of Deveser were affected the most by the tailings flow. Ten civilians died and hundreds more were injured or rendered homeless (Mecsi, Turi et al., Bánvölgyi, 2018). The tailings continued along the Torna Creek and Marcal River and reached the Danube River (Mecsi). The cause of the failure was attributed to the marginal stability of dam, the brittle behaviour of the dam material, the volume and acidity of the impounded water, and the compressibility of the foundation. The event is colloquially known as Ajka or Kolontár after the nearby communities.

Impounded Volumes

Turi et al (2013) reported the designed ultimate capacity for Reservoir X was between 4.2 M m^3 to 4.5 M m^3 at the crest elevation of 216 m. The elevation of the impound material (including the supernatant pond) at the time of failure was 215.88 m, indicating the total impounded volume was near the ultimate designed capacity (Turi et al., 2013). At the end of 2009, 3.4 M m^3 of tailings material had been deposited and around 0.85 M m^3 of supernatant pond water was impounded, which aligns with the ultimate designed capacity.

Turi et al. present bathymetric measurements that indicate a supernatant pond volume of $850,000 \text{ M m}^3$ and a maximum depth of nearly 8 m. Bánvölgyi (2018) also estimated the pond volume as $835,000 \text{ M m}^3$, corroborating the value from Turi et al. It is not clear if the deposited material described by Turi et al. excludes the supernatant pond volume. The sum of the reported deposited volume and supernatant pond, and the supernatant pond elevation aligns with the ultimate designed capacity at 216 m, lending some credibility to this assumption, however.

Zone 1 Description

The surrounding area is predominantly agricultural (Turi et al., 2013, Bánvölgyi, 2018). The populated areas (e.g., Kolontár and Devecser) appear to be primarily single-story structures of low to moderate density based on Google Earth imagery and photographs after the event in Turi et al. Pockets of treed areas were noted around the Torna creek, particular by Devecser, but are thicker vegetation appeared to be relatively sparse otherwise. The travel path is mainly unconfined (Rana et al., 2021b), but the tailings flow strictly followed the Torna Creek, indicating some channelization.

Ghahramani et al. (2020) estimated the Zone 1 runout distance and inundation area as 17.8 km and 6.0 km² respectively, based on Google Earth Imagery. This limits the Zone 1 to the Torna Creek up to the village of Apácatorna. The same imagery source was inspected, and the tailings do appear confined to the Torna Creek at that location. Farther downstream on the Torna Creek and Marcal Rivers, intermittent tailings stains on farmland were observed continuing along the Marcal River to a total distance of 50.7 km downstream of Reservoir X. Bánvölgyi reported a total 10.7 km² of agricultural land was affected (i.e., excluding the populated area). This suggests the Zone 1 extent may be underestimated by Ghahramani et al. by a factor of almost two. The shapefile from Ghahramani et al. indicates a total area of 7.3 km², rather than 6.0 km² as reported. For consistency with the rest of the model database, the 7.3 km² Zone 1 shapefile by Ghahramani et al. (2020) without adjustment was used during the calibration.

B6.2 Additional Runout Observations

The eyewitness accounts in Turi et al. (2013) suggest structural concerns for the dam were first noted around noon of October 4, 2010. The supernatant pond was noted to be flowing out of a crack near the top of the dam crest. Between 12:12 PM and 12:14 PM, the breach progressed into a V-shape, with several blocks of the dam failing sometime afterwards. By 12:30 PM, most of the pond had discharged.

The village of Kolontár is about 1.5 km downstream of Reservoir X following the breach flow path. Turi et al. report eyewitness account of the tailings arrived in Kolontár prior to 12:25 PM, however there is limited corroborating evidence. The post-failure photographs of Kolontár show numerous mud stains about as high as an adult, indicating a peak flow depth around 2 m high (Turi et al., Taylor, 2011). The investigation report by the National Assembly of Hungary (2011) stated a hydrometric station at Torna Creek at

the village of Kolontár measured a peak depth of 3.4 m at 12:30 PM, however further details regarding this hydrometric station were not found to confirm the statement.

The town of Devecser is about 5.7 km downstream of Reservoir X following the breach flow path. Despite the greater population, no available reporting is available to estimate the arrival time like in Kolontár. The photographs generally shown mud stains slightly above waist height, indicating a peak flow depth around 1 m (Taylor, 2011).

Additional arrival times were found in civilian reporting (Index, 2010) downstream of the Ghahramani et al. (2020) Zone 1 runout distance but within the extent additional stains observed. The reported timing is as follows:

- At the village of Mersevát some 45.1 km away from Reservoir X the tailings were noted to arrive around 4:00 PM on October 5, or 27.8 hours after the breach.
- At the village of Szergény some 51.4 km away from Reservoir X the tailings were noted to arrive around 11:00 PM on October 5, or 34.8 hours after the breach.

B6.3 Model Inputs

Outflow Volumes

The total outflow volume has been reported between 0.6 M m³ (WISE, 2022) to 1.64 M m³ (National Assembly, 2011), indicating substantial uncertainty in the estimates. The credible supernatant pond volume around 0.84 M m³ suggests that the outflow volume must be greater than that, as some of the outflow was tailings liquefied (Mecsi, 2013). Bánvölgyi (2018) noted a hydraulic model from an expert panel suggested about 1.2 M m³ discharged when the dam ruptured, but no evidence or discussion of this hydraulic model is included. There were also subsequent concerns regarding a secondary breach or additional outflow, with reported estimates of some 500,000 m³ tailings could be discharged (Index, 2010). An emergency berm was constructed within a week of the failure (Index), but no concrete evidence was found regarding a secondary or continued discharge. A survey was commissioned by the National Assembly that estimated the total discharged volume was 1.64 Mm³ in February 2011, some four months after the failure.

While poorly evidenced in Bánvölgyi, the 1.2 M m³ estimate was considered for the total outflow volume for the modelling. As the entire supernatant pond can be reasonably assumed to discharge, that would indicate the remaining outflow volume of 360,000 m³ were tailings. Idealized geometric estimates for the Reservoir X cone of depression give a tailings volume of 200,000 m³ to 400,000 m³. Following the rule of

thumb from Small et al. (2017) the supernatant pond volume of 840,000 m³ could erode around 420,000 m³ of tailings (i.e., interstitial water and tailings solids). These two findings corroborate the approximately 360,000 m³ of tailings associated with the outflow volume of 1.2 M m³. The difference in volume of 440,000 m³ to reach the 1.64 M m³ as surveyed for the National Assembly is assumed to have occurred over time during the 4 months between the failure and the survey.

Bánvölgyi (2018) reported the deposited tailings within Reservoir X had a solids concentration of 50%, however it is not clear whether this ratio is by volume or mass. Mecsi (2013) reports typical void ratios as between 2 to 4 and specific gravities of 2.9 to 3.3 for settled aluminium tailings, however it appears no testing was done on the consolidated tailings within Reservoir X. The values from Mecsi indicate a gravimetric solids concentration of 50% or a volumetric solids concentration of 25% for the deposited tailings at MAL Reservoir X. The tailings within Reservoir X that did not discharge during the breach reached an average residual slope of between 8% to 15%, based on the dam height, the extent of cone of depression, and the bathymetry in Turi et al., (2013). It belies belief that a material that is only 25% solid by volume could maintain such slopes. Consequently, the void ratio was assumed to be 1 for the purpose of separating the tailings into tailings solids and interstitial water. The estimated volumes are presented in Table B.11 **Error! Reference source not found.**, and the total outflow volumetric solids concentration is calculated as 15%.

Table B.11 MAL Reservoir X Outflow Volumes

| Compartment | Tailings Solids (m ³) | Interstitial Water (m ³) | Supernatant Pond (m ³) | Total (m ³) |
|-------------|--------------------------------------|---|---------------------------------------|----------------------------|
| Reservoir X | 180,000 | 180,000 | 840,000 | 1,200,000 |

Breach Process and Geometry

The downstream dam was built using hydraulically placed slag and ash from the nearby power plant. The embankment had low tensile strength due to the hydraulic chemical bond from the ash and was characterized by variable strengths and seepage rates (Mecsi, 2013) The chemical bond also exhibited brittle behaviour (Turi et al., 2013).

Rana et al. (2021a) labelled the MAL Reservoir X breach with a CDA classification of 1A, based on the presence of the supernatant pond and the liquefiable tailings. The breach process at Reservoir X is less straightforward, with the descriptions in Turi et al.,

2013 suggesting both processes. The supernatant pond flow through the initial cracks and V-shape breach progression are akin to an internal erosion type breach, or a Process I breach. The brittle behaviour of the slag and fly ash construction material and collapse of the dam sections are more typical of a Process II breach. The duration of total outflow (i.e., more than 20 mins) is comparatively long for a Process II breach but short for a Process I breach. Consequently, the breach process was assessed as equally Process I and Process II. The breach formation time was estimated as 0.25 hours based on the timeline presented in Section B6.2.

The dam, crest, and breach heights are reported by Mecsi (2013) as 22 m, based on the crest elevation of 217 m and toe elevation around 195 m at the northwest corner of Reservoir X. The ultimate breach width reported in Turi et al. (2013) was 60 m, which aligns with the narrowest section of the breach visible on Google Earth Imagery. Photographs of the breach and commentary in Mecsi and Turi et al. indicate vertical or near vertical breach side slopes. The breach geometry for the MAL Reservoir X is shown in Table B.12.

Table B.12 MAL Reservoir X Breach Geometry

| Dam Height (m) | Crest Height (m) | Breach Height ¹ (m) | Bottom Breach Width (m) | Top Breach Width (m) | Left Breach Side Slope (xH:1V) | Right Breach Side Slope (xH:1V) |
|----------------|------------------|--------------------------------|-------------------------|----------------------|--------------------------------|---------------------------------|
| 22 | 22 | 22 | 60 | 60 | 0 (vertical) | 0 (vertical) |

¹The water surface elevation was 215.88 m at the time of failure, therefore the height of water above breach bottom is approximately 20.88 m

Terrain and Manning's Coefficient

Multiple terrain data sources were considered, SRTM V3, ALOS World 3D-30m, and the EU-DEM V1.1. All three data sources appear quite similar and equally riddled with random noise, vegetation bias, or other errors commonly observed in free data by Meadows and Wilson (2021). The errors visually look like many small mounds and depressions throughout the terrain. The EU-DEM V1.1 was selected for the HEC-RAS modelling. It was claimed to be suitable for flood modelling after corrections, bias adjustments, and artefact removals were performed (Indra Sistemas, 2015). The horizontal resolution is 25 m, with a reported vertical accuracy of 2.77 m (RMSE) for Hungary.

The EU-DEM data required substantial edits prior to modelling. The crest of Reservoir X varied between elevation 200 m to 209 m and did not match the alignment shown in Google Earth Imagery and literature on the failure (i.e., Turi et al., 2013, Mecsi, 2013, and Bánvölgyi, 2018). The entire TSF was removed from the terrain and the crest elevation at 216 m was re-added to approximate the TSF at the time of failure. The breach channel was added at the northwest corner of Reservoir X. Torna Creek is a constructed channel (Mecsi), therefore the Torna Creek channel was burned into the terrain. The burned channel geometry was a consistent 8 m wide and approximately 1 m deep with 3H:1V side slopes, based on Google Earth aerial imagery and Google Maps Streetview near the Torna Creek. Lastly, the elevation in the EU-DEM at the forest near Devecser appears to be representative of the top of the trees rather than bare earth. The vegetation was removed to create a smoother surface sloping towards the Torna Creek. The edited surface was informed by Google Earth Imagery and the surface adjacent to Devecser and the forest in the EU-DEM terrain. The edits at the forest and Torna Creek are shown in Figure B.18. The depressions and mounds are visible to the west of Devecser and continue throughout the EU-DEM.

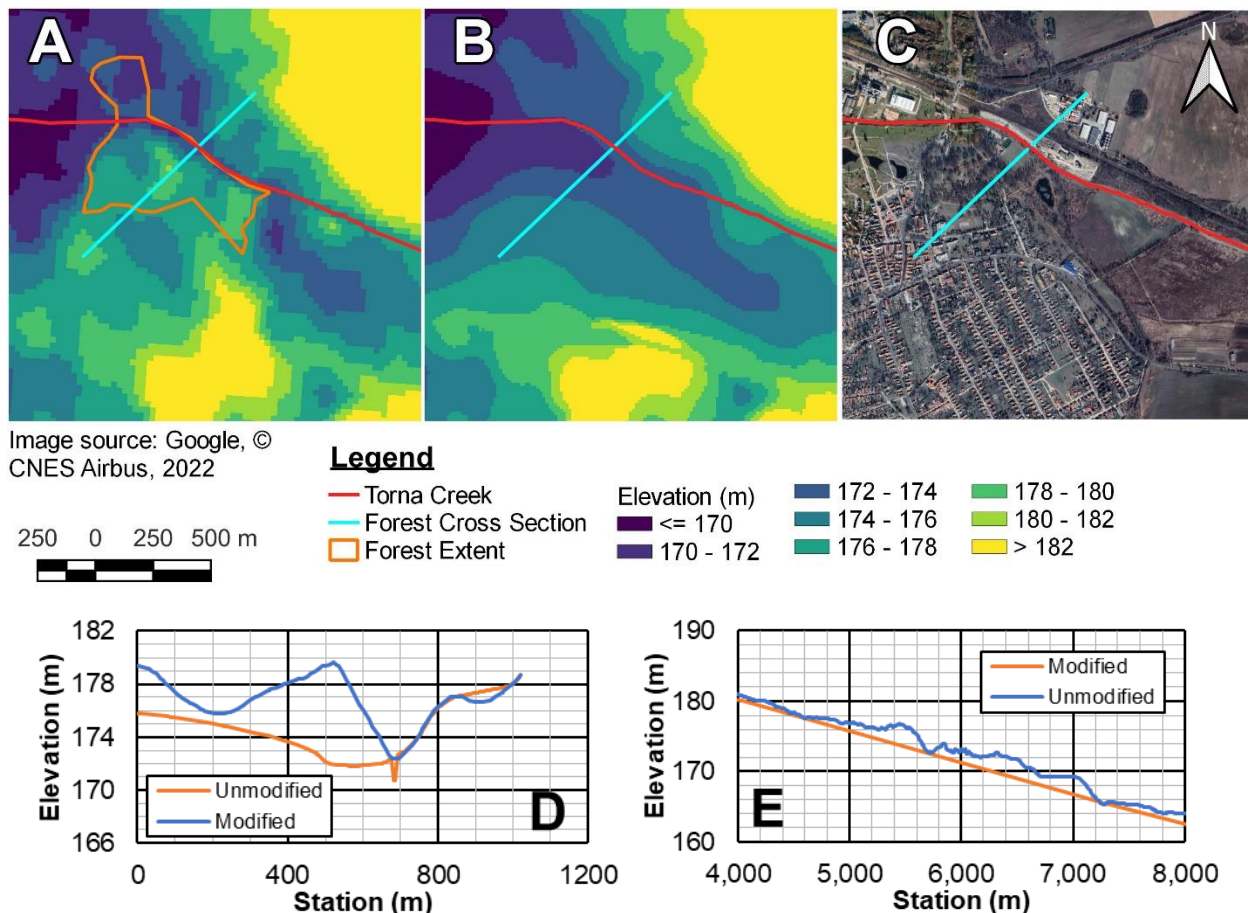


Figure B.18 Terrain Edits and Imagery for MAL Reservoir X at Devecser. A) Terrain Before Edits, B) Terrain After Edits, C) Satellite Imagery for Comparison, D) Cross-section Through the Devecser Forest, E) Profile along a Section of the Torna Creek by the Devecser Forest

The Manning's coefficient was varied within the HEC-RAS model. The fields and agricultural area were represented with a value of 0.04. The town of Devecser and the adjacent forest were assigned a higher value of 0.08 to represent the greater flow resistance associated with the moderate density developed urban area and treed areas. As the village of Kolontár appears to be fields interspersed with the single family dwellings, an intermediate value between field and suburban of 0.06 was used.

B6.4 HEC-RAS Model Set-Up

The breach was modelled as an internal erosion failure mode within HEC-RAS. The piping coefficient was 0.5, based on commentary in Brunner (2020). The piping elevation was set 4 m below the water surface elevation of 215.88 m to reflect the description from Turi et al. (2013) regarding the breach formation starting near the dam crest at 12:10 PM.

The average between an idealized level-pool semi-cone stage-storage curve and a linear stage-storage curve was used to represent both aspects of the breach process. The weir coefficient was 1.18, or halfway between 0.928 and 1.44, for the same reason.

The model domain extends an additional 5.2 km downstream from the Zone 1 runout distance as mapped by Ghahramani et al. (2020) to allow sufficient space for the tailings flow to transition to bankfull flow, after which an outflow boundary condition is used. The tailings flow width narrows to 120 m in some locations; however, the computation resolution was limited to 25 m by the EU-DEM resolution. Breaklines were used for the Torna Creek centerline. There was no available information to inform the representative particle size, therefore it was assumed to be 4 microns to suit the silty clay descriptions in Bánvölgyi (2018) and Mecsi et al. (2013).

B6.5 HEC-RAS Model Results

The calibration plot is shown in Figure B.19, with each tick mark roughly representing a 1.78x increase in the rheology inputs. Based on the Ω_{Tm} metric, the best inputs are 3.2 Pa and 3.2 Pa·s for the yield stress and viscosity respectively. Using these calibrated values, the modelled runout generally matches the observations at Kolontár and Devecser, as shown in Table B.13. It is cautioned that the observations are based only on photographs without a formal scale, and therefore have a larger degree of uncertainty. The modelled maximum depth and velocities of the MAL Reservoir X runout are shown in Figure B.20.

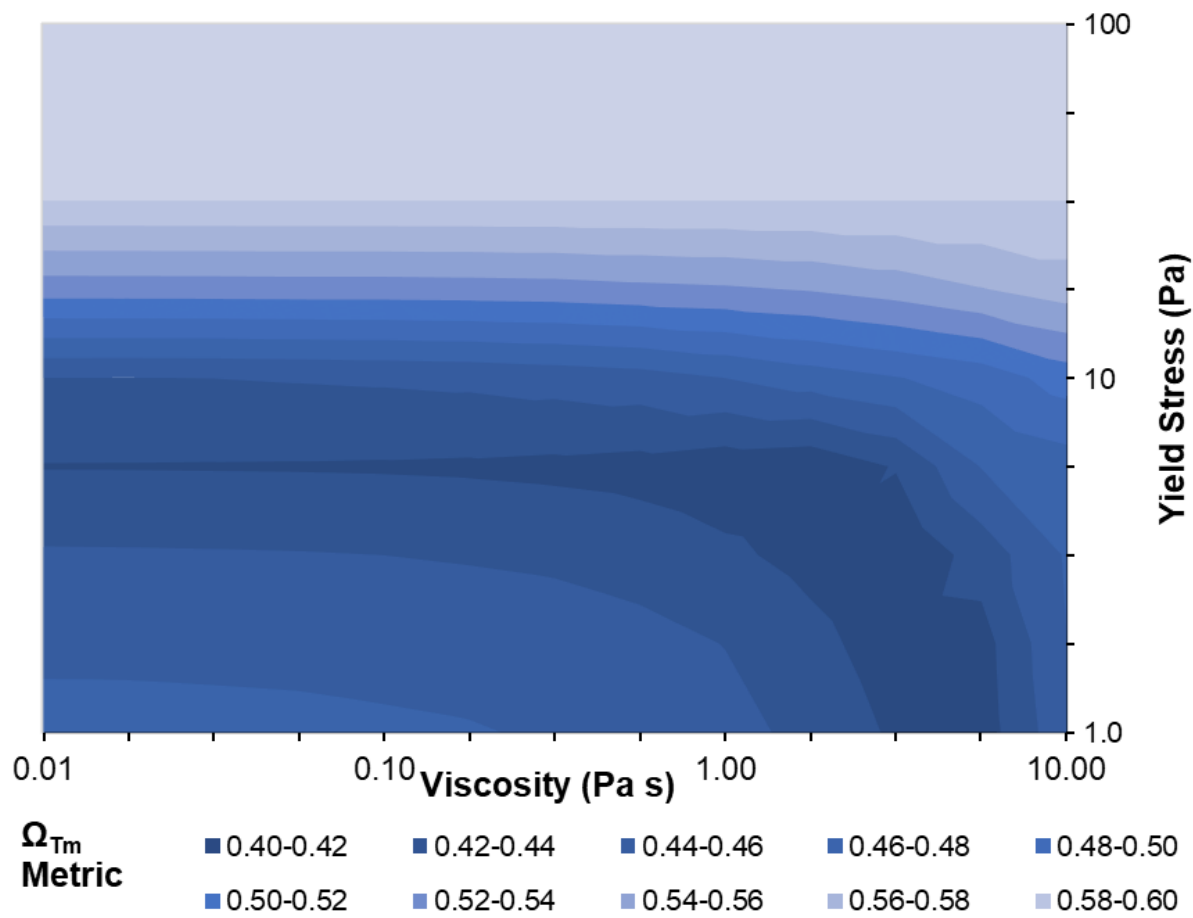



Figure B.19 MAL Reservoir X Rheology Calibration Plot in Log-Log Scale

Table B.13 MAL Reservoir X Observations and Modelled Results Comparison



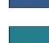


| Observation | Observed Value | Modelled Value |
|---|-------------------|----------------|
| Frontal Arrival Time at the Village of Kolontár | Before 12:25 PM | 12:25 PM |
| Maximum Depth at the Village of Kolontár | Approximately 2 m | 1.5 m to 2.1 m |
| Peak Depth Arrival time at Torna Creek in the Village of Kolontár | 12:30 PM | 12:32 PM |
| Maximum Depth at Torna Creek in the Village of Kolontár | 3.4 m | 5.1 m |
| Maximum Depth at Devecser | Approximately 1 m | 0.6 m to 1.0 m |

Despite these local observations suggesting the model is performing moderately well, the Ω_{Tm} is relatively high, indicating a poor model performance in terms of areal fit. This is particularly evident in Figure B.20, where large areas of overestimated or underestimated are visible. The maximum depth is also very splotchy, due to the mounds and depressions in the terrain data. Furthermore, as the Zone 1 inundation area by Ghahramani et al. (2020) is likely underestimated, the true Ω_{Tm} is consequently also underestimated.

LEGEND

 Observed
Inundation Area

Maximum
Depth (m)

 ≤ 0.5
 0.5 - 1.0
 1.0 - 1.5
 1.5 - 2.0
 2.0 - 2.5
 2.5 - 3.0
 3.0 - 3.5
 > 3.5

Maximum
Velocity (m/s)







 ≤ 1.0
 1.0 - 2.0
 2.0 - 3.0
 3.0 - 4.0
 4.0 - 5.0
 > 5.0

Image source: Google, ©
CNES/Airbus, 2022

1,000 0 1,000 2,000 m

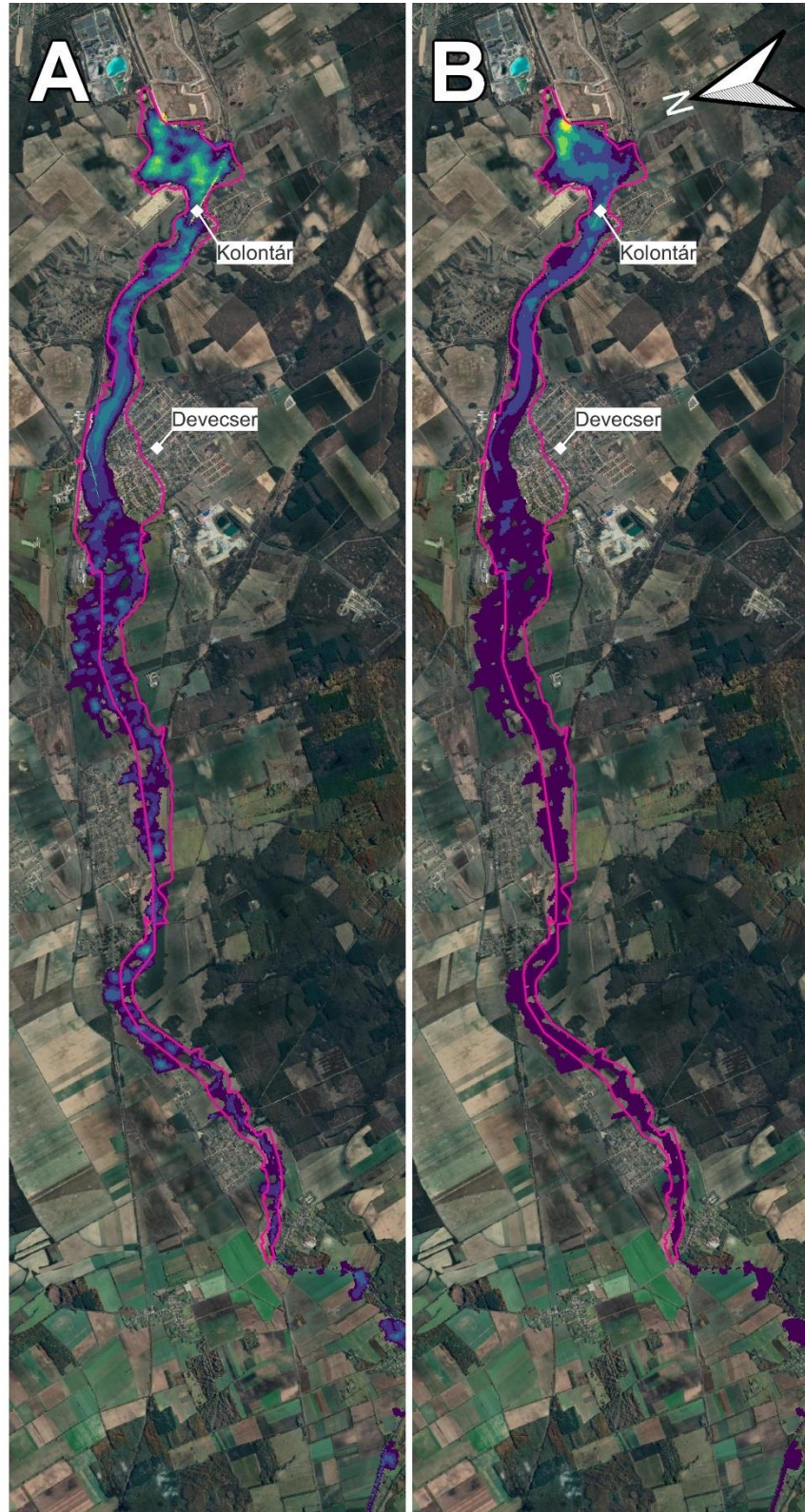


Figure B.20 MAL Reservoir X HEC-RAS Model Results A) Maximum Depth and B) Maximum Velocity

B6.6 Recommendations for Future Research

There are three primary recommendations for future modelling of the MAL Reservoir X event, all of which are quite fundamental to a valid tailings dam breach model. The available data suggest the Zone 1 extent estimated by Ghahramani et al. (2020) is underestimated. As the current modelling was calibrated using the underestimated Zone 1 inundation area, the HEC-RAS model should be updated along with an update to the Zone 1 extent.

The reported outflow volume estimates vary by a large degree. The supernatant pond volume appears reliable but the volume of liquefied tailings that discharged needs to be estimated with greater certainty. The proportion of tailings solids to interstitial water within the impounded tailings also needs a proper assessment to improve the volumetric solids concentration estimate made here.

The publicly available terrain data for the region around the MAL Reservoir X is severely lacking. Despite being advertised as a DEM suitable for flood modelling, substantial effort was needed to improve the EU-DEM for this thesis, and concerns regarding the overall quality remain. Without the removal of the forest near Devecser, the vegetation bias diverts the majority of the tailings outflow around the residential area and outside the Zone 1 inundation area, regardless of rheology calibration or other inputs. The mounds and depressions also appeared to affect the flow path, particularly downstream of Devecser. Further numerical modelling without an improvement to the terrain data would be of limited insight.

Appendix B.7 Kayakari, Japan, 2011

B7.1 Facility Background and Failure Narrative

The Kayakari TSF at the Ohya gold mine in Japan was an upstream cross-valley facility (Ishihara et al., 2015). At 2:46 PM on March 11, 2011, the Tōhoku earthquake (M=9.0) occurred 150 km southeast of the Ohya mine. A limited volume of the tailings deposit liquefied and discharged over the starter dam of the Kayakari TSF. Ishihara et al. estimated the liquefaction likely occurred at the same time as the main earthquake shock. The tailings ran down the valley towards the ocean, impacting farmlands and entering the Oboki River about 1 km downstream of the Kayakari TSF. Approximately 30 minutes to 60 minutes after the main earthquake shock and the tailings runout, the Tōhoku-Pacific Ocean tsunami struck the east coast of Japan, (Suzuki et al., 2011) which included the same area as the tailings runout. Ishihara et al. attribute no fatalities to the tailings runout.

Impounded Volumes

Ishihara et al. (2015) also noted some form of diversion and drainage channels were installed to prevent surface water collecting on the facility, however they could not find any design or record drawings. A single aerial image from Google Earth Imagery 2 years prior to the failure show no ponded water on the facility. Based on these observations, it was estimated that there was no supernatant pond at the time of the failure.

The volume was estimated with idealized geometry, which ranged between 360,000 m³ to 470,000 m³ depending on the dimensions or idealized shape. The estimated range aligns with the value of 400,000 m³ reported in Ishihara et al. (2015), therefore 400,000 m³ is considered a reliable if approximate estimate of the impounded tailings volume.

Zone 1 Description

The majority of the valley downstream of the Kayakari TSF contains fields or farmlands, as shown on Google Earth Imagery and the photographs in Ishihara et al. (2015). Forest and moderate vegetation are also apparent on the hillslopes either side of the valley floor and immediately downstream of the TSF. There are a few structures within the Zone 1, including a farmer's house discussed by Ishihara et al. The tailings were confined within the valley and did not impact the vegetated sides of the valley (Ghahramani et al., 2020).

Ghahramani et al. (2020) reported the Zone 1 runout distance and inundation area as 2,000 m and 150,000 m² respectively. The tsunami run-up and damage were mapped

by Suzuki et al. (2011) and Matsuda et al. (2014) respectively and were digitized herein for comparison to the Zone 1 extent. The tsunami mapping and Zone 1 inundation area are shown in Figure B.21.

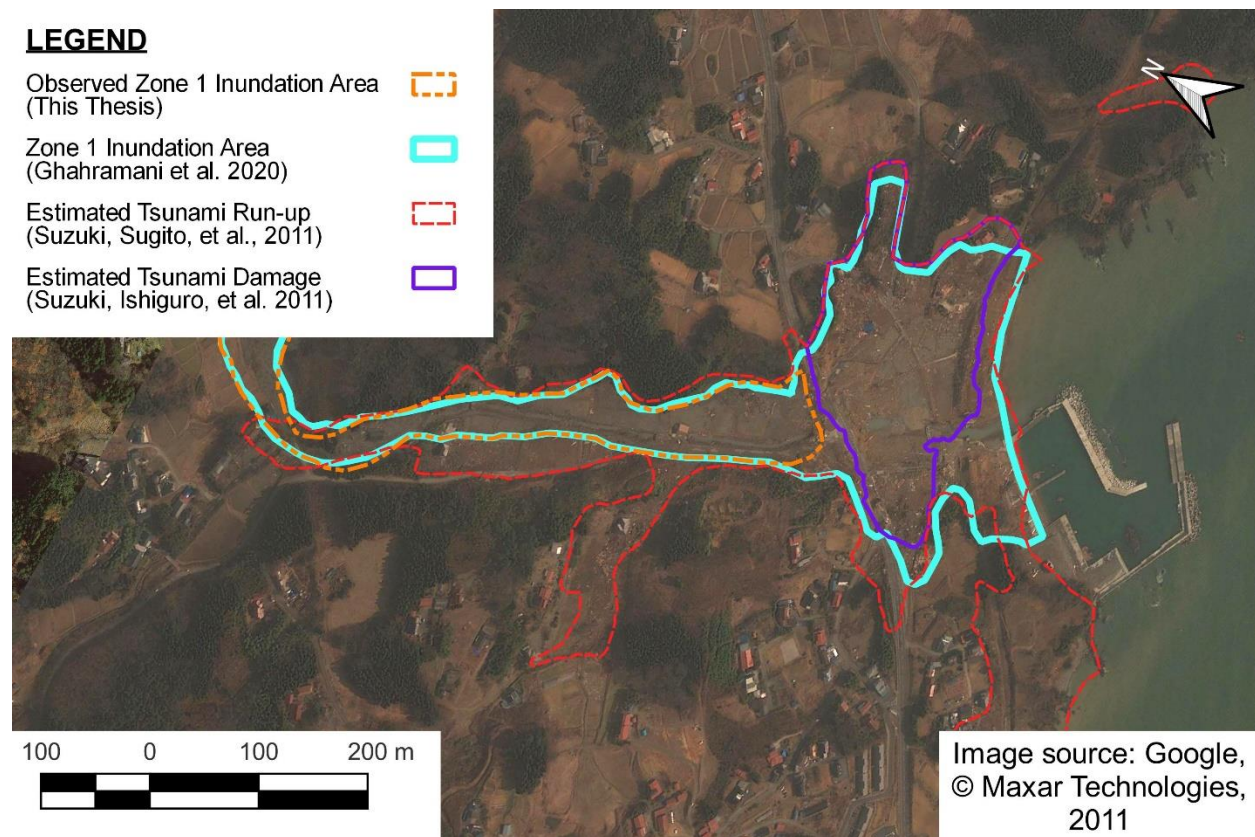


Figure B.21 Overlap between Kayakari Zone 1 Inundation Extent (Ghahramani et al., 2020) and Tōhoku-Pacific Ocean Tsunami Impact (Matsuda et al., 2014; Suzuki et al., 2011)

The run-up was mapped to 18.7 m above sea level up the Oboki river, which includes an overlap with the Zone 1 extent of a distance of roughly 800 m and an area of 86,000 m². The run-up and damage mapping were completed by visually interpreting aerial photographs and Google Earth imagery and the mapping was performed as quickly as possible to inform relief activities and reconstruction works (Suzuki et al., 2011; Matsuda et al. 2014). As the tsunami arrived after the tailings runout, the tsunami impact would be superimposed on the tailings runout impact. Elsewhere in the region (i.e., without this uncertainty between the tailings runout and tsunami run-up) the tsunami run-up was mapped up to 20 m as well, therefore it appears unlikely that the run-up was overestimated in the Oboki River due to confusion with the tailings impact. It is still difficult to definitively attribute the damage to the tailings runout versus the tsunami without a field

investigation, however. Matsuda et al. mapped the tsunami impact as primarily occurring near the mouth of the Oboki River by the ocean. A 3 m tall berm for the highway upstream of the river mouth was noted. The texture and colour of the impacted area is markedly darker upstream of the berm and herein interpreted as the tailings being primarily arrested by the berm. Consequently, some 70,000 m² downstream of the highway berm was removed from the Zone 1 inundation area as mapped by Ghahramani et al. (2020) prior to modelling. This updated Zone 1 inundation area is also shown in Figure B.21.

B7.2 Additional Runout Observations

Ishihara et al. (2015) presented photographs of the final tailings depth around the damaged farmer's house, which was the only source for a local observation for this event. The photograph is of the south side of the house (i.e., the downstream-facing side, as the tailings were flowing south towards the ocean). The tailings depth on the east side of the house, closer to the centre of the flow path is in line with or slightly above windowsills, and estimated as around 1 m. The west side of the house is not visible from the angle of the photographs, but the southwest corner has tailings around the bottom of the doorframe and is estimated at around 0.3 m deep.

B7.3 Model Inputs

Outflow Volumes

The outflow volume is estimated by Ishihara et al. (2015) as 41,000 m³. Based on the average thickness of the outflow (about 5 m), and the area extent of the outflow volume (roughly 9,000 m²) this estimate appears quite reasonable. Ishihara et al. use a void ratio of 1.4, and a saturated water table 2-3 m below the surface in their seismic analysis. Assuming fully saturated conditions and a void ratio of 1.4 gives an interstitial water volume of 24,000 m³, however this volume was reduced to 20,500 m³ to reflect water table slightly below the surface. This gives a volumetric solids concentration of 50%. The photographs in Ishihara et al. appear akin to a thick mudflow, in line with the estimated volumetric solids concentration. All volumes are presented in Table B.14.

Table B.14 Kayakari Outflow Volumes

| Compartment | Tailings Solids (m ³) | Interstitial Water (m ³) | Supernatant Pond (m ³) | Total (m ³) |
|-------------|--------------------------------------|---|---------------------------------------|----------------------------|
| Kayakari | 20,500 | 20,500 | 0 | 41,000 |

Breach Process and Geometry

The commentary and slope stability modelling in Ishihara et al. (2015) regarding the earthquake induced liquefaction and the absence of a supernatant pond confidently places the Kayakari tailings dam breach event as a CDA class of 2A with a Process II breach.

Ishihara et al. (2015) show a scaled profile of the breach, which was used to determine the heights for the breach geometry. The breach height was measured as 4 m at the crest, while the slab thickness was noted by Ishihara et al. as 5 m, indicating the slab convention is more relevant. The remaining breach geometry was determined using the terrain data, DEM5A, used in the runout modelling (see the following subsection for details). The breach bottom width was also measured as 50 m at the starter dam crest. The side slopes of the valley are approximately 2.25H:1V at the starter dam. Since the depth of flow would be expected to be at most 5 m proximal to the breach, the breach side slopes were changed to 0H:1V to better reflect the average width at the hydraulic control. The breach geometry is presented in Table B.15

Table B.15 Kayakari Breach Geometry

| Dam Height (m) | Crest Height (m) | Slab Breach Height (m) | Bottom Breach Width (m) | Top Breach Width (m) | Left Breach Side Slope (xH:1V) | Right Breach Side Slope (xH:1V) |
|-------------------|---------------------|---------------------------|----------------------------|-------------------------|-----------------------------------|------------------------------------|
| 36 | 25 | 12 | 50 | 50 | 0 (vertical) | 0 (vertical) |

Terrain and Manning's Coefficient

The publicly available DEM5A terrain data from the Geospatial Information Authority of Japan (GSI) was used for the runout modelling. The terrain data was generated by an aerial LiDAR survey flown in 2016. The horizontal resolution is 5.3 m, and the vertical accuracy is reported as less than 0.3 m (Standard Deviation). Visually, the DEM5A data appears to be a bare-earth dataset, but no information was found to confirm this or otherwise. A number of buildings survived the tailings runout and tsunami run-up, as evident on Google Earth Imagery. Furthermore, some small berms and ditches were

observed in the fields by the farmer's house in imagery prior to the failure. None of these features are visible in the DEM5A and current imagery.

The buildings were added to the terrain as their size and shape could be reasonably estimated using current imagery. The berms and ditches were not added as their location could not be reconciled with the current shape of the DEM5A, nor their dimensions estimated or approximated with the available imagery. The fields were assigned a Manning's Coefficient of 0.03, while the treed regions were assigned a coefficient of 0.08.

B7.4 HEC-RAS Model Set-Up

The stage-storage curve for the breach was linear, to best represent the rather uniform thickness of the slab. The breach weir coefficient was 0.928 for the Process II breach. The outflow narrows to as small as 30 m, however the computational resolution was limited to 6 m, based on the terrain resolution. Breaklines were ultimately used along the Kayakari Stream and the Oboki River, however model troubleshooting without these Breaklines resulted in the same runout characteristics. No outflow boundary was used, however the mouth of the Oboki River was included in the model domain. This was done to prevent the model boundary artificially constraining the runout to upstream of the highway berm. If the rheology inputs were too low and the flow velocities too high, the tailings would overtop the highway berm, and indicate poor model performance in the calibration process with the low rheology inputs. A breakline was also used along the highway berm. The representative particle size was assumed to be 20 microns, based on the silt description in Ishihara et al. (2015).

B7.5 HEC-RAS Model Results

The calibration plot is shown in Figure B.22, with each tick mark roughly representing a 1.58 increase in the rheology inputs. Based on the Ω_{Tm} metric, the best inputs are 250 Pa and 16 Pa·s for the yield stress and viscosity respectively. The modelled final depths at the east side and the southwest corner of the farmer's house were less than 0.05 m and approximately 0.20 m respectively. Conventional trial-and-error calibration did not substantially increase the final depths at farmer's house towards the observed values of 1 m and 0.3 m respectively. The modelled maximum depth and velocities of the Kayakari runout are shown in Figure B.23.

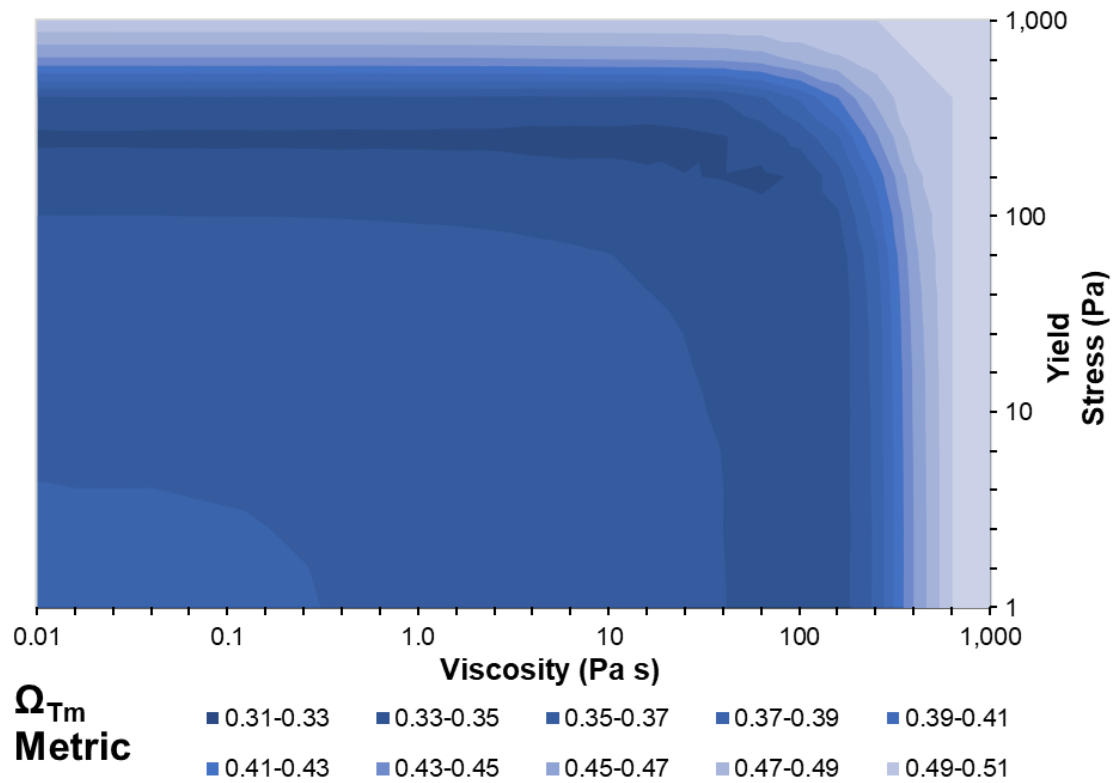


Figure B.22 Kayakari Rheology Calibration Plot in Log-Log Scale

B7.6 Recommendations for Future Research

The terrain data in the region near the farmer's house needs to be confirmed and pre-failure conditions may need to be digitally reconstructed if the topography materially changed after the failure. This thesis used an adjustment of the Zone 1 inundation area. The extent of the overlap of the tsunami and the tailings runout also needs to be further confirmed.

Appendix B.8 Mount Polley, Canada, 2014

B8.1 Facility Background and Failure Narrative

The Mount Polley TSF in BC, Canada, is a side-hill modified centreline arrangement TSF for copper and gold tailings. Modified centreline is a hybrid of upstream and centreline construction. In the early morning on August 4, 2014, the foundation under the North embankment deformed and the dam crest experienced sudden subsidence (Morgenstern et al., 2015, BCMEM, 2015). The large supernatant pond volume at the time of the failure overtopped the deformed dam and eroded the remaining dam material over the following hours. A portion of the tailings runout reached the nearby Polley Lake while the remainder continued through the Hazeltine Creek and discharged into the Quesnel Lake (Golder, 2016, Cuervo et al., 2017).

Impounded Volumes

The impounded volumes are reported in Morgenstern et al. (2015) for the supernatant pond, tailings solids, and interstitial water, based on information from the provided by the mine owner, Mount Polley Mining Corporation. The volumes are 10.6 M m³, 36.1 M m³, and 27.2 M m³ respectively, for a total impounded volume of 73.9 M m³.

Zone 1 Description

Cuervo et al. (2017) described the pre-failure conditions of the area impacted by the tailings flow. The Hazeltine Creek was a well-defined single channel which flowed from Polley Lake to Quesnel Lake. Between the lakes, the channel passes through wetlands below Polley Lake, a canyon section, and a delta at the mouth of Quesnel Lake. The vegetation along the creek is dense and woody debris litter the channel. The substrate for most of the downstream area was glacial till, however the canyon section consisted of bedrock below the soil. The tailings were confined by the valley during the entire runout (Ghahramani et al., 2020)

Ghahramani et al. (2020) mapped the Zone 1 inundation as 2.0 km² with a runout distance of 9 km. The mapping also closely matches the results presented in Cuervo et al. (2017), which was also based on field investigations.

B8.2 Additional Runout Observations

Interviews with mine personnel conducted by BCMEM (2015) and Morgenstern et al. (2015) and instrumentation records provide a timeline for many features of the breach. A mine operator drove past the breach location at 10:40 PM on August 3 with no note of

breach initiation. The initial foundation failure is not particularly clear, and interpretations vary, but the foundation failure occurred sometime between 11:30 PM August 3 and 12:30 AM August 4 (Morgenstern et al., BCMEM). The overtopping and subsequent erosion is agreed to have begun sometime shortly after 12:50 AM, when the perimeter sump pond level spiked. At 1:08 AM, the electricity cut out on site, attributed to the destruction of power line 300 m downstream of the breach location. An eyewitness estimated the breach was 100 m wide and 30 m deep in the early light of 4:25 AM, roughly indicating the breach was close to full development at that time. A helicopter video taken at 8:46 AM by the Cariboo Regional District shows the breach in its approximate ultimate shape. The breach outflow was continuous in the video, and comparable to turbulent river flow at 9:00 AM (Morgenstern et al.). The breach outflow abated at 4:00 PM that day, 15 hours after the breach began (BCMEM).

Polley Lake increased in elevation somewhere between 1 m to 1.7 m (BCMEM, 2015, Golder, 2016). Combined with the lake surface area of 4.0 km², an estimated inflow volume of around 4.0 M m³ to 6.8 M m³ reached Polley Lake. Some of the volume subsequently discharged from Polley lake before 6:00 AM, possibly around 0.8 M m³, based on the mine personnel eyewitnesses (BCMEM). Eyewitnesses note the peak elevation was around 4:30 AM but was already decreasing by 5:00 AM.

SNC-Lavalin (2015) and Cuervo et al. (2017) compiled estimates of erosion along the Hazeltine Creek during the runout from field investigations and remote sensing data. The net erosion along the Hazeltine creek was 0.6 to 1.7 M m³ with two thirds of the volume occurring in the first 3 km of the runout. This region is termed the Plug area; however, tailings deposition eventually dammed the outflow from Polley Lake. This deposition likely occurred during the tail of the breach outflow, where velocities were lower and solids concentrations were higher. The net erosion volumes exclude vegetation, which may be a large portion considering the vegetation density within the Hazeltine Creek area. While the net erosion volume is small compared to the outflow volume from the Mount Polley TSF, the erosion was concentrated in a small area within Hazeltine Creek, with average and maximum erosion depths of around 2.5 m and 10 m respectively. It is estimated that 18.6 M m³ of water, tailings solids, eroded soil, and debris reached the Hazeltine Mouth (SNC-Lavalin).

The Water Survey of Canada (WSC) operates a staff gauge, Quesnel Lake Near Likely (08KH011), near the Quesnel Lake outlet in the west arm, roughly 8.8 km north of

the mouth of Hazeltine Creek. The gauge records at a 5-minute interval in Coordinated Universal Time (UTC). An 80 mm increase in the Quesnel Lake level was recorded beginning between 2:01 AM and 2:06 AM on August 4, 2015 (local time). Based on the maximum depth of the west arm of 113 m (Golder, 2016), the shallow water wave celerity is estimated at 20 m/s to 30 m/s. The estimated celerity aligns with Pugh and Harris (1982) for a landslide volume and reservoir depth of similar scale. Consequently, the tailings are estimated to reach the mouth of Hazeltine Creek around 1:50 AM to 2:00 AM, a mere 50 minutes to 60 minutes after the Process I breach began.

B8.3 Model Inputs

Outflow Volumes

The outflows volumes are reported in Morgenstern et al. (2015) based on information from the provided by the mine owner, Mount Polley Mining Corporation, and presented in Table B.16. The calculated void ratio of 0.75 for the outflowing tailings matches the reported range of 0.6 to 0.8 prior to the failure (Morgenstern et al., 2015). The construction materials are assumed to be dry rockfill, and only includes solid particles with no interstitial water, following the assumptions for the slope stability in Morgenstern et al. (2015). The average volumetric solids concentration of 32% may not appropriately reflect the low solids concentration in the initial outflow when it consisted mostly of the supernatant pond nor the higher solids concentration in the latter stages of the outflow of tailings alone.

Table B.16 Mount Polley Outflow Volumes

| Tailings Solids (m³) | Construction Materials (m³) | Interstitial Water (m³) | Supernatant Pond (m³) | Total (m³) |
|--|---|---|---|----------------------------------|
| 7,300,000 | 600,000 | 6,500,000 | 10,600,000 | 25,000,000 |

Breach Process and Geometry

The failure trigger is clearly the foundation failure, however Morgenstern et al. (2015) attribute erosion as the dominant breach and tailings transport mechanism. The long duration of the outflow also supports a Process I breach. The initial crest deformation involved a 3.3 m to 5 m subsidence, discounting a full Process II as the dominant breach mechanism. The breach formation time was estimated as 3.5 hours based on the eyewitness accounts described in Section B8.2.

The breach geometry was based on the drawings and description of the breach process in Morgenstern et al. (2015). The breach channel is highly variable through the dam; however, a clear control section is visible near the dam core at the dam crest centerline. Table B.17 summarizes the breach geometry.

Table B.17 Mount Polley Breach Geometry

| Dam Height (m) | Crest Height (m) | Breach Height ¹ (m) | Bottom Breach Width (m) | Top Breach Width (m) | Left Breach Side Slope (xH:1V) | Right Breach Side Slope (xH:1V) |
|----------------|------------------|--------------------------------|-------------------------|----------------------|--------------------------------|---------------------------------|
| 57 | 40 | 36 | 42 | 260 | 1.75 | 3.75 |

¹The breach height here excludes the approximately 4 m subsidence during the foundation failure. The water surface elevation was 2.3 m below the crest at the time of failure, therefore the height of water above breach bottom is approximately 37 m

Terrain and Manning's Coefficient

The terrain data source was the Airbus WorldDEM DTM, with a spatial resolution of 12 m. The terrain data is reported as bare earth. Multiple ridges reaching up to 10 m in height and 200 m in length were observed in the canyon section of Hazeltine Creek. These ridges were considered erroneous based on the lack of ridges observed in the profile in Cuervo et al. (2017). A continuous river profile was burned into the terrain, which was informed by the pre-failure images and profile data presented in SNC-Lavalin (2015) and Cuervo et al. (2017). It was challenging to create a smooth channel geometry that was suitable for the highly variable channel geometry from the wetlands to canyon to lake delta. Consequently, there is a slightly discontinuity between the edited terrain and original DEM data. Figure B.24 shows the channel at the canyon section before and after the terrain edits.

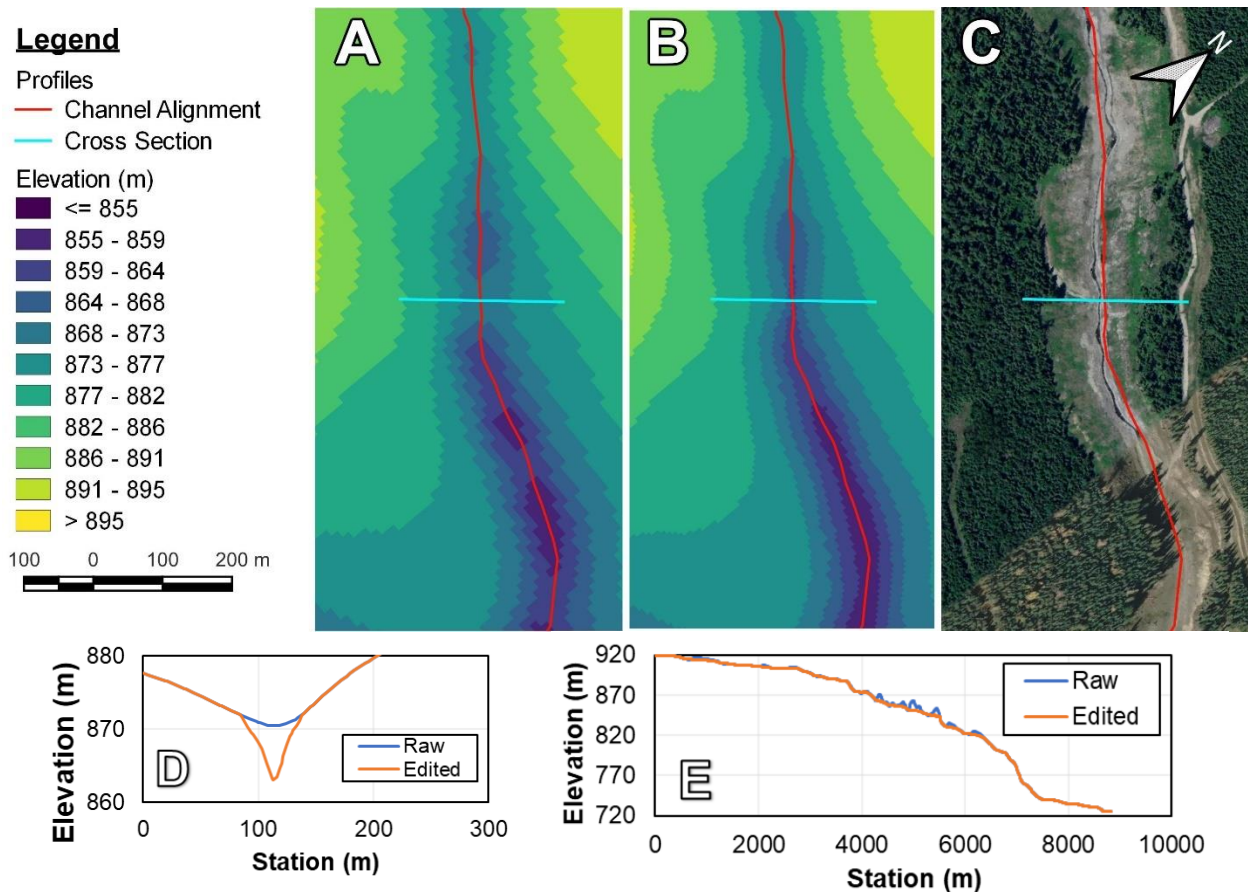


Figure B.24 Terrain Edits and Imagery for Mount Polley. A) Terrain Before Channel Burning, B) Terrain After Channel Burning, C) Satellite Imagery for Comparison, D) Cross-section Along the Blue Line, E) Profile Along the Entire Channel Within the Model Domain

The dense vegetation visible in aerial or satellite imagery and photos presented in Cuervo et al. (2017) prior to the failure suggest high resistance to flow and therefore a high Manning's coefficient of 0.10 to 0.16 is appropriate. Initial modelling in HEC-RAS used Manning's coefficient in this range, however Newtonian models (i.e., ones that did not include any rheological properties) could not reach the mouth of Hazeltine Creek at Quesnel Lake in order to meet the timing observation from the WSC gauge. Post-failure images from Cuervo et al. (2017) show the eroded channel as smooth with limited to no debris. This would be more comparable to a constructed earth channel with regards to the Manning's coefficient, which are on the order of 0.02 to 0.05. Consequently, the HEC-RAS model was assigned a Manning's coefficient value of 0.05 to balance the range of flow resistance that would be applicable during the event and to align with the estimated arrival time at Quesnel lake, based on observations from WSC gauge.

B8.4 HEC-RAS Model Set-Up

The breach was modelled as an overtopping breach, with the dam crest decreased 4 m below the initial dam crest level to represent the initial subsidence prior to the erosion. A linear stage-storage curve was used, given the relatively long breach formation time and insufficient available evidence to support a more sophisticated curve shape.

Polley Lake was represented with a Storage Area with a 2D Connection element between it and the 2D Flow Area for Hazeltine Creek. This allows an inflow and outflow for Polley Lake based on the modelled runout without any hindsight inappropriately forcing specific inflow or outflow volumes. The stage-storage curve was created starting on the surface area of the normal lake level (at 917 m based on the WorldDEM data) and linearly increases with elevation.

The computation resolution was selected as 30 m for the wetland area downstream of Polley Lake and the mouth of Hazeltine Creek. The tailings flow width narrows to 90 m in the canyon section, so a refinement region was used in that area to better capture the velocity variation across the canyon. The resolution of the refinement region was 12 m, limited by the resolution of the terrain. A Normal Depth BC was used at Quesnel Lake for the model outflow. No grain size distribution was found for the Mount Polley tailings; therefore, the representative particle size was assumed to be 100 microns to match the sandy silt description (BCMEM, 2015)

B8.5 HEC-RAS Model Results

The calibration plot is shown in Figure B.25, with each tick mark roughly representing a 3.16x increase in the rheology inputs. This relatively coarse interval is based on the long duration of two hours to complete a single model run. Based on the Ω_{Tm} metric, the best inputs are 0.2 Pa and 0.002 Pa·s for the yield stress and viscosity respectively.

The areal fit is moderately good until the canyon section, where the flow overtops the channel and spills into the adjacent forest area during the peak flow at the canyon. The modelled results with these inputs have moderate to poor fit for the rest of the observations as shown in Table B.18. No major improvement in the model fit was found using alternative rheology inputs and conventional trial-and-error calibration. Increasing the yield stress and viscosity improved the model results for some constraints (e.g., decreasing the volume that reached Quesnel Lake), while worsened results for other constraints (e.g., the flow didn't reach Quesnel Lake in time). The arrival time at Quesnel Lake was considered the most important constraint, other than the areal fit, and used to

inform the final rheology inputs, which remained as 0.2 Pa and 0.002 Pa·s. The modelled maximum depth and velocities of the Mount Polley runout is shown in Figure B.26.

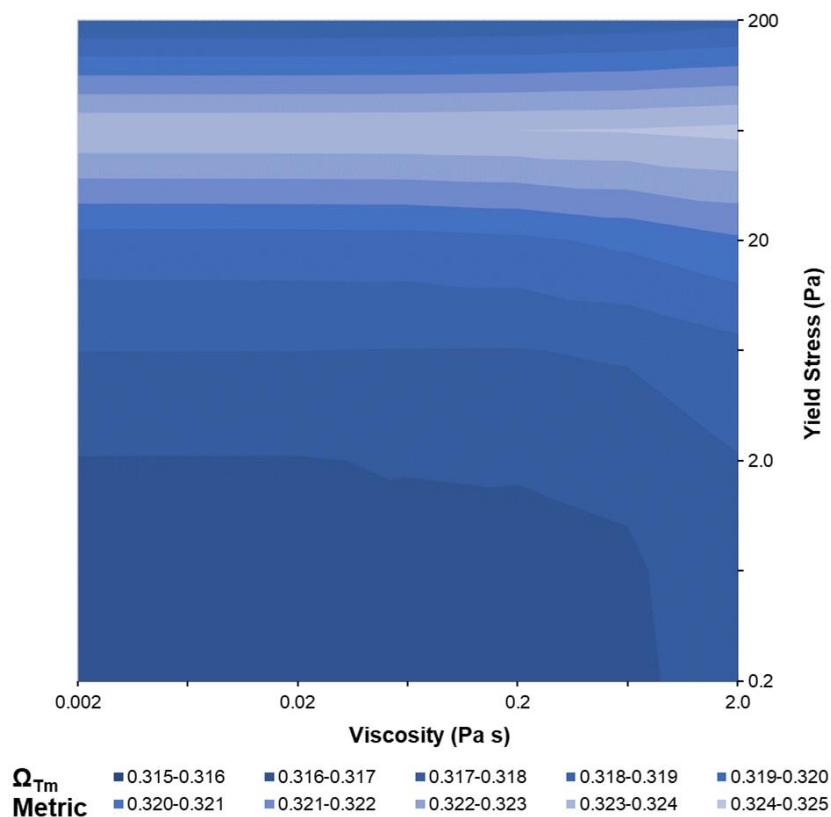


Figure B.25 Mount Polley Rheology Calibration Plot in Log-Log Scale

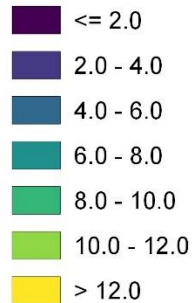
Table B.18 Mount Polley Observations and Modelled Results Comparison

| Observation | Observed Value | Modelled Value | Comment |
|--|---------------------------------|-----------------------|--|
| Polley Lake Elevation at 4:30 AM | 1 m to 1.7 m above normal value | 0.8 m | Modelled Polley Lake elevation peaks at 4:05 AM at 0.81 m |
| Time for Polley Lake to decrease 0.2 m | Approximately 0.5 hours | 9 hours | |
| Arrival Time at Quesnel Lake | Approximately 1:55 AM | 2:00 AM | |
| Volume Reaching Quesnel Lake | 18.6 M m ³ | 22.3 M m ³ | Modelled value does not account for net eroded volume from Hazeltine Creek |

LEGEND

 Zone 1 Inundation Area

Maximum Depth (m)



Maximum Velocity (m/s)

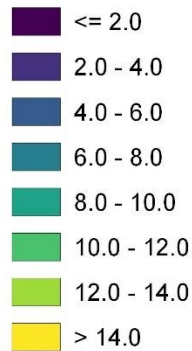


Image source: Google,
© Maxar Technologies,
2022

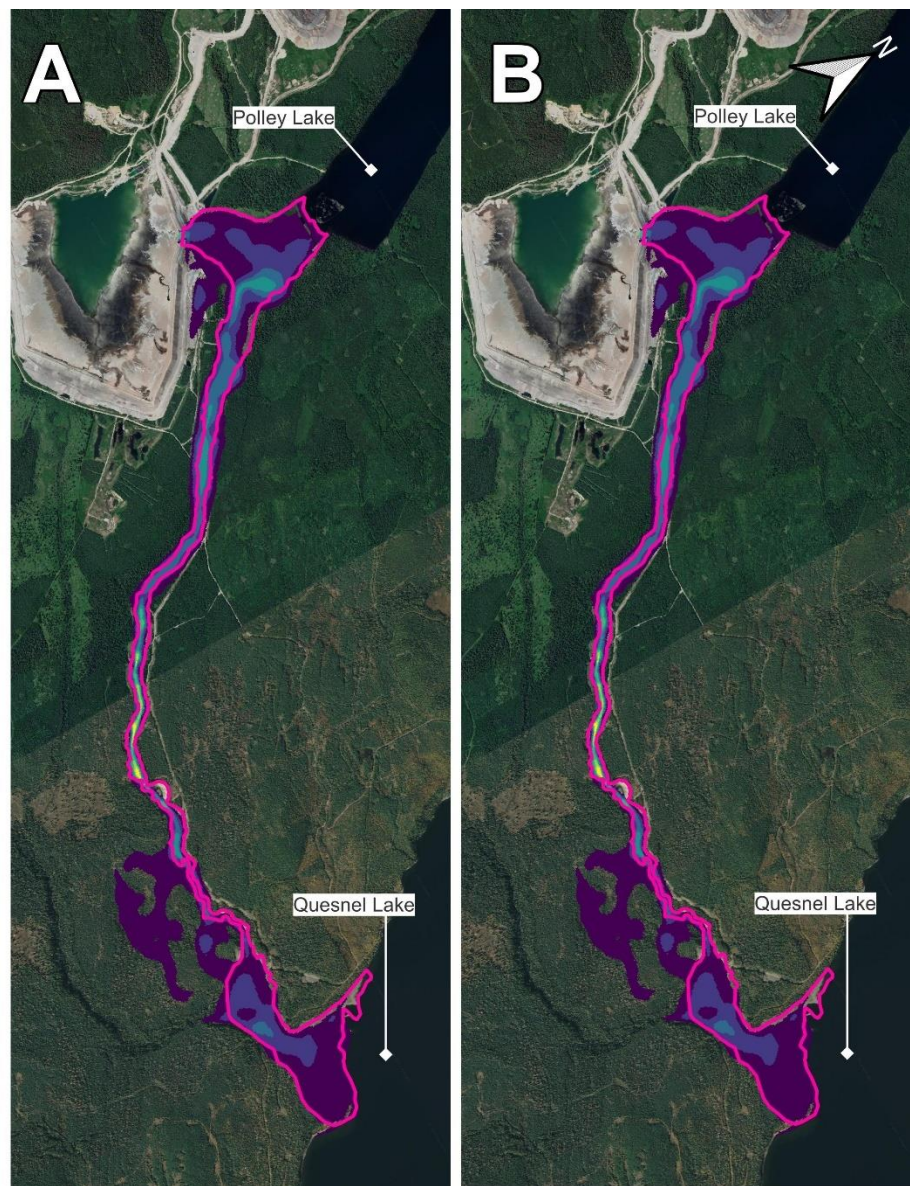


Figure B.26 Mount Polley HEC-RAS Model Results A) Maximum Depth and B) Maximum Velocity

B8.6 Recommendations for Future Research

There are two major improvements recommended for a numerical model of the Mount Polley failure. The average volumetric solids concentration was 32%, however it likely varied from below 20% during the initial overtopping to almost 50% during the tail of the breach. A single fluid approach may not be able to adequately model the behaviour for each condition. SNC-Lavalin (2017) and Cuervo et al. (2017) show that erosion in the Hazeltine Creek was substantial. The HEC-RAS modelling within this thesis is fixed-bed and does not include any erosion during the runout. A numerical model capable of both

improvements would require substantially more effort and data but appears necessary to improve the model fit to the observed events.

In addition to the major improvements above, there are several minor recommendations. The ridge modifications in the terrain edits were non-trivial and may warrant additional effort to reduce the minor discontinuity. The modelled results close to and at Polley Lake were found to be sensitive to the definition of the 2D Connection between the lake and the rest of the model. Simple refinements were used to reach numerical stability at Polley Lake, however further refinements may be warranted. Lastly, the downstream environment was heavily vegetated prior to the breach, but a lower than typical Manning's coefficient was required to meet the observed arrival time. This implies that the Mount Polley breach flow had the erosive power to rapidly remove the vegetation and therefore decrease the flow resistance. An exploration of this interaction would be insight for forward-analysis.

Appendix B.9 Fundão Event I (Mariana, Bento Rodrigues, or Samarco), Brasil, 2015

B9.1 Facility Background and Failure Narrative

The Fundão TSF was one of several TSFs at the Samarco Mariana Mining Complex in Minas Gerais, Brasil, for iron tailings. It was an upstream cross-valley TSF, and originally had been designed as a composite facility with an intermediate dam (“Dike II”). The weaker slimes tailings were to be separated from the main dam (“Dike I”) and the sands tailings with Dike II. Several design changes and operation difficulties resulted in slimes located underneath the left abutment at Dike I and saturated conditions in the sands (Morgenstern et al., 2016). At approximately 3:45 PM on November 5, 2015, the left abutment of Dike I collapsed, and the majority of the tailings volume liquefied in the ensuing flowslide. The failure cause was identified as the lateral extrusion of the slimes under the left abutment combined with small seismic shocks that triggered the sands to liquefy (Morgenstern et al.). This event is sometimes referred to as the Mariana, Bento Rodrigues, or Samarco event after the names of the village, city, or the mining complex.

The tailings runout overtopped the nearby Santarém Dam and flowed down the Santarém Stream before destroyed much of the village of Bento Rodrigues. Nineteen people at the mine site and Bento Rodrigues were killed. The tailings continued down the Santarém Stream and flowed 5.7 km up the Mirandinha Stream, a southern tributary to the Santarém Stream (Machado, 2017, Palu and Julien, 2019). The tailings flowed down into the Gualaxo do Norte and Carmo rivers, affecting the riverside villages of Bicas, Paracatu de Baixo, Gesteira, and Barra Longo. The tailings reached the Candonga Reservoir and hydroelectric facility, over 100 km downstream of the Fundão TSF. Fine tailings material were continued to be suspended in the reservoir. These fine tailings discharged into the river downstream of Candonga Reservoir and reached the Atlantic Ocean over 500 km downstream of the Candonga Dam (Robson, 2017, Palu & Julien, 2019).

More flowslides occurred after the main failure during rainfall (Fundação Renova, 2016), where additional tailings discharged from the Fundão TSF. The first flowslide on November 5, 2015 is the primary focus within this thesis, however the additional flowslides are mentioned as relevant. The first flowslide is labelled as Event I.

Impounded Volumes

The mining company, Samarco, undertook surveys after the failure to estimate the impounded volumes. Pre-dam digitized topography and post-failure LiDAR was used to estimate the total volume of the tailings as 56.4 M m^3 (Fundação Renova, 2016).

A supernatant pond was a constant presence at the Fundão TSF. Morgenstern et al. (2016) investigated the elevation and areal extent of the pond leading to the failure, however the supernatant volume pond was not reported. Rana et al. (2021) estimated the supernatant pond volume as negligible, while Machado (2017) estimated it to be 1 M m^3 . The tailings surface area of the entire facility was only 1 km^2 , based on imagery available in Google Earth for July 2015. An average supernatant pond depth of approximately 1 m would be required over the entire tailings surface for a supernatant pond volume of 1 M m^3 to be possible. The supernatant pond certainly exceeded the minimum beach width at times (Morgenstern et al., 2016) however it was 250 m away from the crest at the time of failure. Therefore Rana et al. (2021) was assessed as more credible, and a negligible supernatant pond was used within this thesis.

Zone 1 Description

MapBiomas publishes a land cover dataset for Brasil in 30 m resolution. The land cover for Collection 6 in 2014 was used to assess the land cover in addition to Google Earth imagery. The data indicate the land cover within Zone 1 comprises a mix of pastoral, agriculture, forested, waterbodies, and non-vegetated areas. The majority of the land cover is classified as forested by MapBiomas, including the waterbodies and adjacent floodplains. Most of the floodplain adjacent to the rivers appeared to be closer to short brush, grassy, or non-vegetated based on Google Earth imagery prior to the failure event. The tailings were confined by the valley during the entire runout (Ghahramani et al., 2020).

Ghahramani et al. (2020) estimated the Zone 1 inundation area to be 21 km^2 with a runout distance of 99 km, which is the area and distance between the Fundão TSF and the Candonga Reservoir. The large extent of the Zone 1 proved challenging for the numerical modelling, therefore only a portion of Zone 1 was included in the HEC-RAS model. This portion is roughly the first 42 km downstream of the Fundão TSF and is discussed further in Section B9.4.

B9.2 Additional Runout Observations

Machado (2017) interviewed Bento Rodrigues residents to determine an arrival time to the village. There is some uncertainty in the exact timing and location from each witness, however Machado (2017) generally concluded that the front of the tailings reached the village around 4:00 PM. The tailings were observed at Candonga Reservoir (approximately 100 km downstream of the Fundão TSF) at approximately 7:00 AM on November 6, 2022, or roughly 15 hours after the breach (CPRM, 2015). The peak outflow from the Candonga Dam was measured to be 1,900 m³/s at 10:00 AM on November 6, 2022 (Palu, 2019).

Arrival times between Bento Rodrigues and the Candonga Reservoir are associated with considerable uncertainty. Paracatu de Baixo is approximately 42 km downstream of the Fundão TSF. Robson (2017) reported police notified residents they had 15 minutes to evacuate the village at 8:00 PM on November 5, 2015. Arcuri et al. (2015) reported that the tailings mud passed Paracatu de Baixo at 10:00 PM on November 5, 2015, however it could also be interpreted as the peak depth occurred at that time. Photographs of Paracatu de Baixo in Robson indicate final depths at the roofs of single level dwellings, or very approximately as 4 m. Damage and staining on higher dwellings indicate the peak depth might have been higher than 4 m, but this observation is similarly uncertain.

Further downstream at Barra Longa (approximately 78 km downstream of the Fundão TSF), Robson (2017) reported the arrival time as 3:30 AM on November 6, 2015. Similar to Paracatu de Baixo, police were able to evacuate the population prior to the tailings arrival. Limited information is available to fully confirm either observation. They both roughly align with the arrival time to the Candonga Reservoir, suggesting a relatively consistent celerity of 1.8 m/s within the Gualaxo do Norte and Carmo rivers (downstream of Bento Rodrigues). Palu (2019) estimated the flood wave celerity downstream of the Candonga Dam to be 1.2 m/s which partially corroborates the magnitude of the estimated celerity upstream of the Candonga Reservoir.

The volume of tailings deposited upstream and within of the Candonga Reservoir is reported between 23.8 M m³ to 28.8 M m³ (e.g., Fundação Renova, 2016, Palu and Julien, 2019). The reported deposited volume is further separated in Table B.19.

Table B.19 Fundão Event I and Event II Deposited Volumes (Fundação Renova, 2016)

| Location | Distance from Fundão TSF (km) | Deposited Tailings Volume (m ³) | Tailings Volume Passing (m ³) |
|---|-------------------------------|---|---|
| Fundão TSF | 0 | - | 32,200,000 |
| Santarem Dam | 3.5 | 2,000,000 | 30,200,000 |
| Bento Rodrigues | 6.5 | 2,400,000 | 27,800,000 |
| Gualaxo do Norte and Carmo rivers and floodplains | 7.5 to 83 | 6,100,000 | 21,700,000 |
| Doce River upstream of the Candonga Reservoir | 83 to 99 | 2,800,000 | 18,900,000 |
| Candonga Reservoir | 99 to 116 | 10,500,000 | 8,400,00 |

It is noted the estimates above do not differentiate between Event I and the subsequent flowslides. Furthermore, the estimates were made in July 2016, when subsequent rainfall and erosion may have mobilized volumes downstream from where they might have been immediately after the event. Consequently, such estimates should be treated as approximate.

B9.3 Model Inputs

Outflow Volumes

The total outflow volume is reported as 32.2 M m³ for Event I (Morgenstern et al., 2016, Fundação Renova, 2016). The volumes were determined using pre-failure topography from the US Air Force and post-failure aerial photogrammetry contracted by Samarco (Fundação Renova, 2016), and is therefore considered reliable.

Morgenstern et al. (2016) calculated the rough portion of the impounded tailings as 77% sands and 23% slimes. They also report the in-situ void ratios for the sand and slimes as ranging between 0.4 to 0.75 and 0.75 to 1.25 respectively. The median void ratio from each tailings type and the relative proportion of each tailings type from Morgenstern et al. were used to calculate an average void ratio of 0.67 for the outflow volume. This resulted in an initial volumetric solids concentration of 60%. The estimated volumes are presented in Table B.20.

Table B.20 Fundão Event I Outflow Volumes

| Event | Tailings Solids (m ³) | Interstitial Water (m ³) | Supernatant Pond (m ³) | Total (m ³) |
|---------|--------------------------------------|---|---------------------------------------|----------------------------|
| Event I | 19,280,000 | 12,920,000 | 0 | 32,200,000 |

The bankfull discharge downstream of the Candonga Dam is 535 m³/s (Palu, 2019), therefore it was concluded that the flow within Santarem Creek and Gualaxo do Norte River is initially negligible compared to the breach flow. The cumulative water volume over the 100 km to the Candonga Reservoir combined with the decreasing tailings volume due to deposition would contribute to a decreasing volumetric solids concentration. An idealized geometric estimation for the cumulative volume of the river based on the length, observed channel widths from Google Earth, and an assumed average depth gave anywhere 2 M m³ to 6 M m³, or a volumetric solids concentration of 45% to 55% by the time the tailings reached the Candonga Reservoir. Palu (2019) estimated the volumetric solids concentration above the Candonga Reservoir to be 34%. This value is erroneously based on a total outflow of 56 M m³ which erroneously includes a supernatant pond volume of 24 M m³ and assumes negligible interstitial water. Therefore Palu (2019) was assessed as unreliable for numerical modelling of the Zone 1 inundation area.

Breach Process and Geometry

The eyewitness accounts at the Fundão TSF during the failure, the laboratory testing on the tailings, and numerical modelling described Morgenstern et al. (2017) point to the tailings liquefaction. A CDA classification of 2A and Process II breach is clearly applicable for the Fundão Event I breach.

There is limited information available on the post-failure surveys other than the reported outflow volumes. Machado (2017) assumed the breach progressed to the pre-existing terrain in the valley and based the breach geometry on the Shuttle Radar Topography Mission DSM from 2000 (SRTM V1). A similar approach was adopted within this thesis, except with SRTM V3 was used and the breach geometry was partially and qualitatively informed by pre-construction imagery from Morgenstern et al. (2016) and Google Earth. SRTM V3 is based on the same satellite survey as SRTM V1, however additional void filling and post-processing was completed. These adjustments were not believed to affect the region near the Fundão Dam. For this one event, the breach

geometry was not taken directly along the dam crest, and instead a simplified straight line between the left and right abutment. This was done as the hydraulic control would not be aligned with the left abutment setback. Furthermore, the inclusion of the setback into the breach geometry introduced numerical instabilities and volume conservation issues in HEC-RAS. The breach geometry from Machado (2017) and the current estimate are presented in Table B.21. The breach geometry within this thesis is a little larger in area, but generally the two estimates agree and are within the uncertainty of the method.

Table B.21 Fundão Event I Breach Geometry

| Source | Dam Height (m) | Crest Height (m) | Breach Height (m) | Bottom Breach Width (m) | Top Breach Width (m) | Left Breach Side Slope (xH:1V) | Right Breach Side Slope (xH:1V) |
|----------------|----------------|------------------|-------------------|-------------------------|----------------------|--------------------------------|---------------------------------|
| Machado (2017) | - | 90 | 90 | 18 | 702 | 3.84 | 4.0 |
| This Thesis | 106 | 94 | 94 | 180 | 650 | 2.5 | 2.5 |

Terrain and Manning's Coefficient

Two terrain data sources were considered, the ALOS World 3D-30m (AW3D30) and SRTM V3. Both are publicly available DSMs with 1 arc-second (approximately 30 m) horizontal resolution. As DSMs, they include vegetation and do not represent bare earth. The AW3D terrain was visually assessed to be better throughout the Zone 1 and has been quantitatively found to have lower error (Meadows and Wilson, 2021). Consequently, the AW3D terrain was used for the runout modelling while the SRTM V3 was used to inform the pre-existing natural ground for the breach geometry, as described above.

The AW3D30 data still required substantial edits prior to modelling. Ridges around 10 m tall existed throughout the Santarém Creek and Gualaxo do Norte River with a maximum ridge height of almost 40 m tall. A standard channel with 6 m bottom width and 1H:1V sides slopes was used to maintain hydraulic conductivity but it is acknowledged that it would not realistically represent the actual terrain. The river widths were highly variable, and a typical depth was not available, rendering any channel geometry somewhat arbitrary. An example of a series of ridges is shown in Figure B.27, which is representative of the entire channel length within the Zone 1 extent in the AW3D30 data. Another example of a modification for the Fundão model is shown in Section 4.1 of the main thesis.

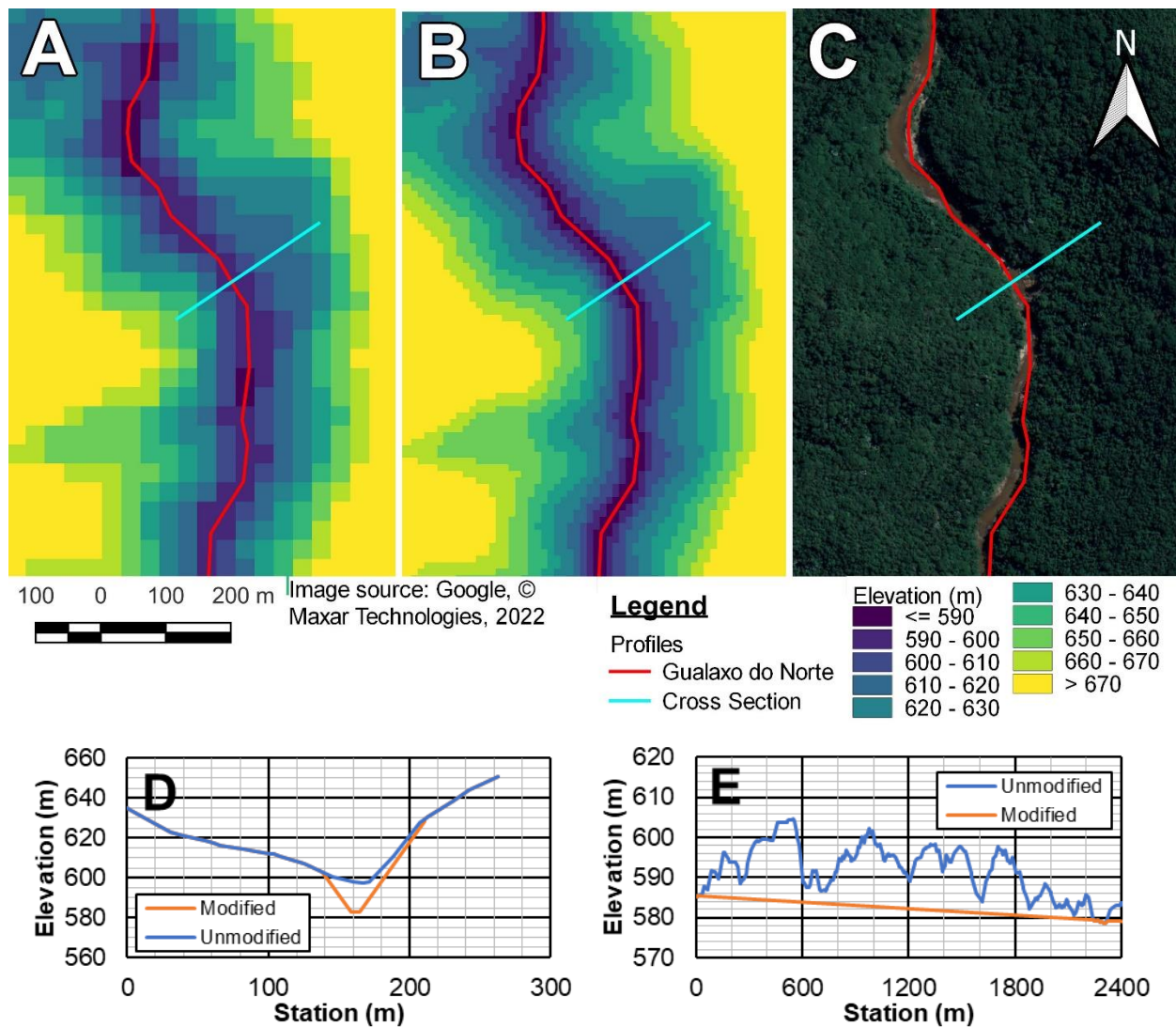


Figure B.27 Typical Terrain Edits and Imagery for Fundão Event I. A) Terrain Before Channel Burning, B) Terrain After Channel Burning, C) Satellite Imagery for Comparison, D) Cross-section Along the Blue Line, E) Profile Along a section of the Gualaxo do Norte River

Approximately 82 km downstream of the Fundão TSF or 4 km downstream of Barra Longa, multiple ridges or artefacts almost 140 m tall and over a kilometre in length affect the terrain in the Doce River. These are assumed to be interference from clouds, however the AW3D cloud mask does not note any cloud interference. Regardless, this interference was considered too difficult to edit given its large extent and magnitude or error.

The MapBiomass land cover data was not used in the HEC-RAS model, based upon the substantial misclassification observed near the rivers. A uniform Manning's coefficient of 0.07 was selected to represent the mix of non-vegetated and short brush the dominated the Zone 1 area.

B9.4 HEC-RAS Model Set-Up

A subset of the Zone 1, the first 42 km or up to Paracatu de Baixo, was selected for modelling in HEC-RAS. This limitation was based on the additional required work to edit the ridges in the terrain beyond Paracatu de Baixo, the cloud interference downstream of Barra Longa, and the long computation time needed for 42 km. The observed inundation area within the first 42 km is 11.3 km². An idealized level-pool semi-cone was used for the stage-storage curve the failure, with a breach weir coefficient of 0.928. The flow width of the terrain narrows to 40 m in some locations; however the computation resolution was limited 30 m due to the resolution of the terrain data. A Normal Depth BC is used at the termination of the HEC-RAS model downstream of Paracatu de Baixo.

Machado (2017) and Dias (2017) collected tailings deposited within the Zone 1 area and performed geotechnical and rheological characterization tests. The representative particle size was 0.05 mm to match the measured range of the tailings from these tests. Instead of the typical rheology calibration approach used for other events, the rheology was directly taken from the Machado (2017) and Dias (2017) test results. This approach was used as the rheology data is available and it is less computational demanding than the brute-force rheology calibration needed for other events. The yield stress and viscosity for several volumetric solids concentrations from the rheology tests are shown in Table B.22. The trends were extrapolated for the 60% solids concentration, as the highest volumetric solids concentration measured in Machado (2017) was 55%. The volumetric solids range was based on the estimated maximum and minimum volumetric solids concentration discussed in Section B9.3.

**Table B.22 Rheology for the Fundão Tailings Extrapolated from Measured Trends
(Adopted from Machado, 2017)**

| Volumetric Solids Concentration (%) | Yield Stress (Pa) | Viscosity (Pa·s) |
|-------------------------------------|-------------------|------------------|
| 45% | 3 | 0.05 |
| 52% | 50 | 0.2 |
| 60% | 170 | 1.2 |

B9.5 HEC-RAS Model Results

The areal fit for all volumetric solid concentration simulations is relatively good and consistent despite the uncertainties associated with the breach geometry and poor-quality

terrain. The Ω_{Tm} metrics are 0.284, 0.289, and 0.296 for 45%, 52% and 60% respectively. Other observations and modelled results within the first 42 km are compared in Table B.23. In general, the higher volumetric solid concentration model results have a closer fit closer to the Fundão TSF while the lower volumetric solids concentration model results are better farther away as expected. The maximum depths and velocities shown in Figure B.28 are from the model with a volumetric solid concentration of 45%.

Table B.23 Fundão Event I Observations and Modelled Results Comparison

| Observation | Distance from Fundão TSF (km) | Observed Value | Volumetric Solids Concentration | | |
|-----------------------------------|-------------------------------|-----------------------------|---------------------------------|------------|------------|
| | | | 45% | 52% | 60% |
| Volume Passing Santarém Dam | 3.5 | 30,200,000 m ³ | 31,400,000 | 31,000,000 | 30,100,000 |
| Arrival Time at Bento Rodrigues | 6.2 | Around 4:00 PM | 3:53 PM | 3:53 PM | 3:53 PM |
| Volume Passing Bento Rodrigues | 7.5 | 27,800,000 m ³ | 30,600,000 | 30,000,000 | 28,300,000 |
| Arrival Time at Paracatu de Baixo | 42 | Between 8:00 PM to 10:00 PM | 9:49 PM | 10:14 PM | 11:30 PM |
| Depths at Paracatu de Baixo | 42 | Around or above 4 m | 6 m | 15 m | 20 m |

LEGEND

Observed Inundation Area 

Maximum Depth (m)

<= 5.0

5.0 - 10.0

10.0 - 15.0

15.0 - 20.0

20.0 - 25.0

25.0 - 30.0

30.0 - 35.0

35.0 - 40.0

40.0 - 45.0

45.0 - 50.0

50.0 - 55.0

55.0 - 60.0

60.0 - 65.0

65.0 - 70.0

> 70.0

Maximum Velocity (m/s)

<= 4.0

4.0 - 8.0

8.0 - 12.0

12.0 - 16.0

16.0 - 20.0

20.0 - 24.0

24.0 - 28.0

> 28.0

2 0 2 4 km

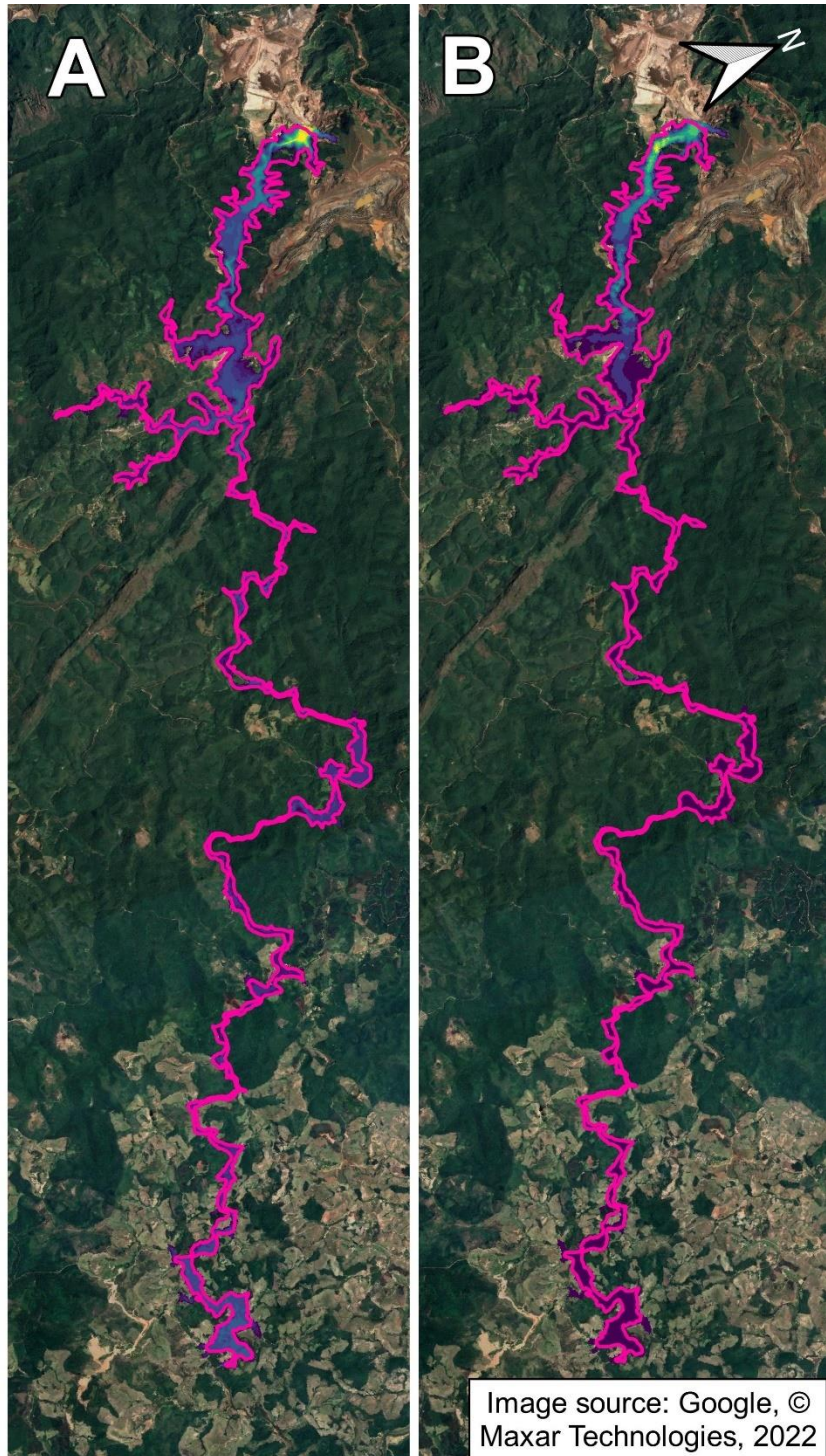


Figure B.28 Fundão Event I HEC-RAS Model Results up to 42 km for $C_v = 45\%$ A) Maximum Depth and B) Maximum Velocity

B9.6 Recommendations for Future Research

There are three primary recommendations for future modelling of the Fundão Event I. The complete Zone 1 runout should be modelled, as only a portion of the Zone 1 runout was

modelled herein. The confidence in the model can be improved by through assessing the complete Zone 1 inundation and the arrival time to the Candonga reservoir is more certain than at Paracatu de Baixo. This can be achieved with more time or a with a stronger computer. The publicly available terrain data used was a DSM with an overwhelming number of issues that required editing. Better terrain data likely would need to be purchased or otherwise obtained prior to the complete Zone 1 runout model. Lastly, a model with the capability for variable volumetric solids concentration is needed to address the decreasing solids concentration over time that occurred in the Gualaxo do Norte and Doce rivers.

Appendix B.10 Tonglüshan North Compartment, China, 2017

B10.1 Facility Background and Failure Narrative

The Tonglüshan TSF is located near Daye, in the Hubei province of China (Zhuang et al. 2021). It is an upstream constructed ring-dyke for copper and iron tailings, with an internal embankment to separate the TSF into northern and southern compartments (Zheng, 2018). At 2:20 AM on March 12, 2017, the dam at northwest corner of the TSF broke and swung 45° outwards like a door (Zheng et al., 2017). The resulting tailings flow swept through the downstream farmlands, killing 2 people and injuring 6 more (Zheng et al., 2017). A preliminary investigation attributed the failure to foundation failure due to subsidence from mining activities (Zhuang et al., 2021). Although the Tonglüshan TSF is a composite TSF, the breach was limited to the northern compartment and is therefore comparable to a single compartment failure event.

Impounded Volumes

Zheng (2018) presents the stage-storage curve for the total impounded volume, including the impounded volume up to the final crest elevation at 42 m. As the dam crest was at 39 m at the time of failure (Zheng, 2018), the impounded volume would be around 14.4 Mm³. Based on Google Earth Imagery, the northern compartment corresponds to roughly 60% of the surface area, therefore it could contain approximately 8.7 M m³.

Rana et al. (2021b) assessed the supernatant pond volume as negligible, while Zheng et al. (2017) describes water storage 1.0 m to 2.8 m deep in the northeastern part of the TSF. There was no specific supernatant pond volume found reported beyond the depths in Zheng et al. Inspection of the TSF on Google Earth showed varying supernatant pond locations and sizes. In the months preceding the failure the supernatant pond appears relatively small and about 400 m away from the eventual breach location. Based on the above, it cannot be concluded if the supernatant pond was negligible or not without further information. This thesis followed Rana et al. (2021b) and assumed the supernatant pond volume was negligible.

Zone 1 Description

Farmlands to the north of the Tonglüshan TSF primarily form the Zone 1 inundation (Zheng, 2018, Rana et al., 2021b). A village or residential area is located west of the farmlands on slightly elevated terrain. A river borders the farmland to the east and separate it from the rest of the city of Daye. Another TSF is located to the north of the

farmlands, which partially confined the tailings flow (Rana et al., 2021b). The outskirts of the village structures were reached, but the tailings flow did not proceed through the populated area. Other than the TSF to the north, the tailings flow was unconfined (Rana et al., 2021).

The Zone 1 mapping from Ghahramani et al. (2020) has an area of 267,000 m² and runout distance 500 m. Following the likely tailings flood wave front path, the runout distance could be considered up to 800 m. The mapped shapefile also aligns with the work by Zheng et al. (2017) and Zhuang et al. (2021).

B10.2 Additional Runout Observations

Zheng (2018) presented contours of the observed final depth of the tailings, which were also shown in Zhuang et al. (2021). Neither study included a direct comparison between the results of their DAN3D models to the observed depths or included a profile line. The observed deposition contours were digitized to support the calibration process. The observed deposition contours are shown in Figure B.29A.

B10.3 Model Inputs

Outflow Volumes

Zheng et al. (2017) conducted a drone survey of the TSF and runout after the failure and estimated the total outflow volume as 500,000 m³. Zheng (2018) also notes a volume 78,700 m³ associated with the dam movement. This volume was not included in the outflow volume as it did not flow with the tailings after the rotation. As noted previously, the supernatant pond volume was assumed to be negligible in the outflow volume.

Geotechnical tests were also performed by Zheng (2018) which indicate an average void ratio of 0.795 and saturation above 95%. This corresponds to an average volumetric solids concentration of 55% if there was no supernatant pond and the saturation is simplified to 100%. The range of calculated volumetric solids concentration ranged from 53% to 63%, based on individual samples. Zhuang et al. (2021) provided separate geotechnical data, including from tailings within the failure source area. Their analysis concluded that the volumetric solids concentration ranged from 47% to 53%, and the tailings in the source area was 53% at the time of failure. Both estimates are comparable however the estimate from Zhuang et al. (2021) was used within this thesis, as it was based on data from within the failure source area. All volumes are presented in Table B.24.

Table B.24 Tonglüshan Outflow Volumes

| Compartment | Tailings Solids (m ³) | Interstitial Water (m ³) | Supernatant Pond (m ³) | Total (m ³) |
|-------------|--------------------------------------|---|---|----------------------------|
| North | 265,000 | 235,000 | Unknown, estimated to be 0 m ³ | 500,000 |

Breach Process and Geometry

Zheng et al. (2017), Zheng (2018), and Zhuang et al. (2021) are not explicit or descriptive of the breach or the rotation of the dam. Zheng (2018) noted the tailings liquefied during rheology testing, but it is unclear if the tailings liquefied during the breach (Rana et al., 2021b). Combined with the uncertainty of the supernatant pond volume, a CDA classification cannot be assigned with confidence. The numerical models that Zheng (2018) and Zhuang et al. (2021) used (DAN3D and FLOW-3D, and DAN3D respectively) had block-start initial conditions with low rheological inputs. This approach is appropriate for a CDA class 2A and Process II breach, therefore the same was adopted within this thesis.

Zheng (2018) clearly describes the dam height at the time of failure as 27 m. The top breach width was estimated as 260 m based on figure of the drone survey in Zhuang et al., (2021). The left breach side slope is described as vertical by Zheng (2018). The remaining breach geometry is uncertain or inconsistently reported. The breach depth is shown in Zheng (2018) as 12 m with photographs, but also reported as 16 m elsewhere in Zheng (2018) and Zhuang et al. (2021). Zheng (2018) reports deposition within the breach channel as 4 to 5 m deep, therefore the breach height was assigned as 12 m according to the conventions within this thesis. The right breach side slope was assigned approximately 2H:1V to align with the rotated dam section. This slope was based on the general dimensions of the rotated dam from Zheng (2018) as well as visually estimates. Table B.25 **Error! Reference source not found..** shows the final breach geometry

Table B.25 Tonglüshan Breach Geometry

| Dam Height (m) | Crest Height (m) | Breach Height (m) | Bottom Breach Width (m) | Top Breach Width (m) | Left Breach Side Slope (xH:1V) | Right Breach Side Slope (xH:1V) |
|-------------------|---------------------|----------------------|----------------------------|-------------------------|-----------------------------------|------------------------------------|
| 25 | 25 | 12 ¹ | 235 | 260 | 0 (vertical) | 2 |

¹The breach channel had a tailings deposition depth around 4 m, indicating the breach height may include an additional 4 m.

Terrain and Manning's Coefficient

The drone survey and elevation data from Zheng et al. (2017) was not available for use in this thesis. Instead, the Airbus WorldDEM DTM, with a spatial resolution of 12 m, was purchased. The data appears to be from prior to 2011, based on the crest elevation of the dam in the terrain data compared to the construction timeline in Zheng (2018). Roadways or berms less than 10 m wide within the farmlands are visible in Google Earth Imagery and the numerical modelling in Zheng (2018), however they are not visible in the WorldDEM DTM data. No other issues or obstructions were noted in the terrain data.

The crest elevation of the Tonglüshan TSF was increased in the terrain data to match the dam crest elevation of 37 m at the time of failure (Zheng, 2018) along with the addition of the breach geometry as usual. The rotated section of the dam was also manually added at its final location. The geometry of the rotated dam was informed by Zheng et al. (2017), who noted the total length and width of the rotated dam section as approximately 320 m and 145 m. A standard berm design of 4 m wide with 3H:1V side slopes at constant elevation of 16 m was added to the terrain where visible in Google Earth Imagery prior to the failure. This results in 16 berms that range from 0.8 m to 1.5 m above the natural ground elevation in the WorldDEM DTM. Figure B.29 shows the terrain before and after the terrain edits. It is possible that the berms closer to the dam were destroyed by the tailings runout, however the pre-breach topography used in Zheng (2018) appears to include all berms as fixed-bed features in their model.

The farmlands were assigned a Manning's coefficient of 0.04. The village to the west of the farmlands is not within the Zone 1 inundation mapping by Ghahramani et al. (2020) or the mapping by Zheng et al. (2017) however it was assigned a Manning's coefficient of 0.08 for the event the tailings flow reached those areas within the rheology calibration process in HEC-RAS.

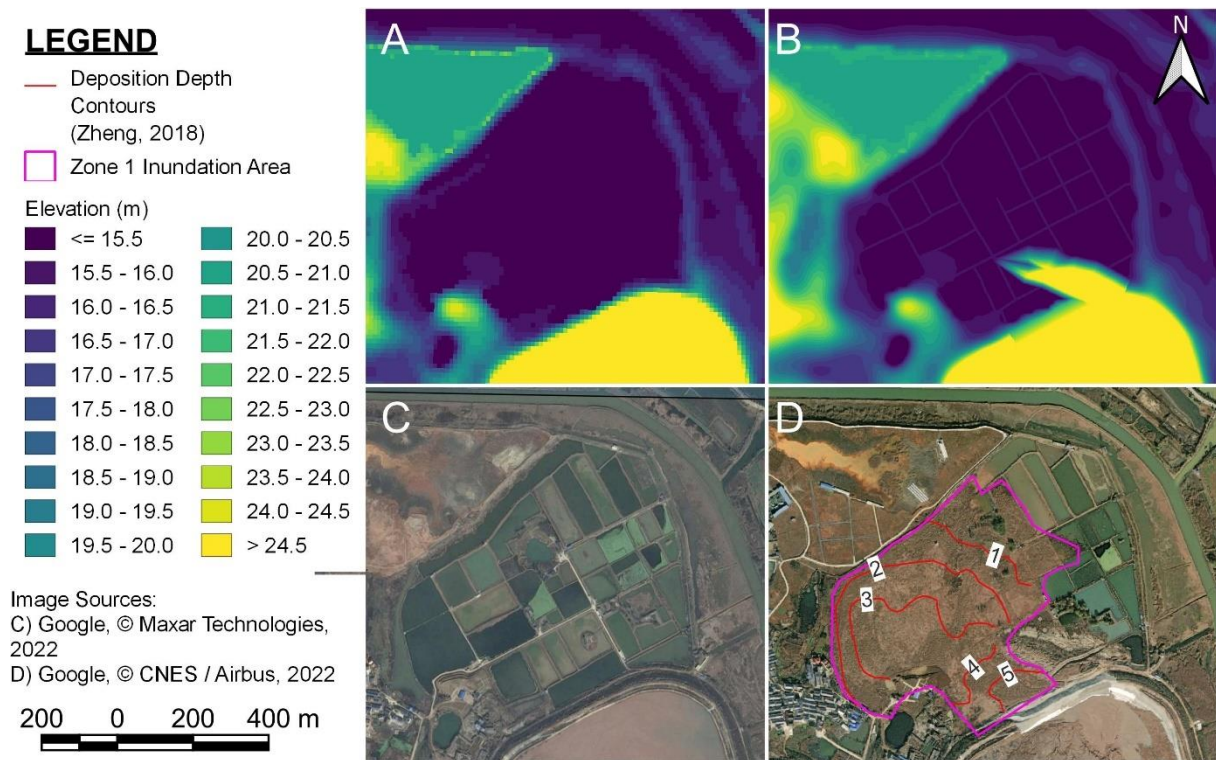


Figure B.29 Terrain Edits and Imagery for Tonglūshan. A) Terrain Before Editing, B) Terrain After Editing, C) Pre-Failure Satellite Imagery for Comparison, D) Post-Failure Satellite Imagery for Comparison

B10.4 HEC-RAS Model Set-Up

The HEC-RAS model set-up was quite simple. The stage-storage curve for the breach was an idealized level-pool semi-cone and the breach weir coefficient was 0.928, both corresponding to the methodology for a Process II breach in this thesis. The small extent of the outflow allowed a relatively fine computational resolution of 12 m Breaklines were used along the berms added to the terrain and the rotated dam. No outflow boundary was used as all the tailings were contained within the farmlands.

Zheng (2018) conducted geotechnical and rheological testing on the tailings that remained within the Tonglūshan TSF. The representative particle size within HEC-RAS was 50 microns, based on the measured range of d_{50} values from the geotechnical tests. The results from the rheology testing are presented in Table B.26. Zheng et al. (2021) found the rheology inputs for a volumetric solids concentration of 50% provided the best results in DAN3D with Bingham rheology, even though the tailings in the failure source area were measured at 53%. Despite the availability of measured rheology, the full

calibration algorithm was run given the short model run time to observe how the calibration process compared to measured rheological values.

Table B.26 Measured Rheology for the Tonglūshan Tailings (Adopted from Zheng, 2018)

| Volumetric Solids Concentration (%) | Yield Stress (Pa) | Viscosity (Pa·s) |
|-------------------------------------|-------------------|------------------|
| 45% | 5.1 | 0.26 |
| 48% | 5.2 | 0.31 |
| 50% | 11.4 | 0.35 |
| 53% | 17.5 | 0.66 |
| 56% | 20.5 | 0.52 |
| 59% | 33.5 | 0.99 |

B10.5 HEC-RAS Model Results

The calibration plot is shown in Figure B.30, with each tick mark roughly representing a 1.26x increase in the rheology inputs. Based on the Ω_{Tm} metric, the best inputs are 250 Pa and 2.5 Pa·s for the yield stress and viscosity respectively. The final depths (i.e., the depths when flow has ceased in the HEC-RAS model) are compared to the observed deposition depths from Zhuang et al. (2021) in Figure B.31 along the profile line shown in Figure B.29A. The final depths are underestimated in the first half of the profile, but the match is closer in the second half. The dips in the depth correspond to the location of the added berms. The modelled depths are also comparable to the results from Zhuang et al. (2021), despite the difference in rheology inputs. Conventional trial-and-error rheology calibration was not able to improve the final deposition without unduly affecting the areal match.

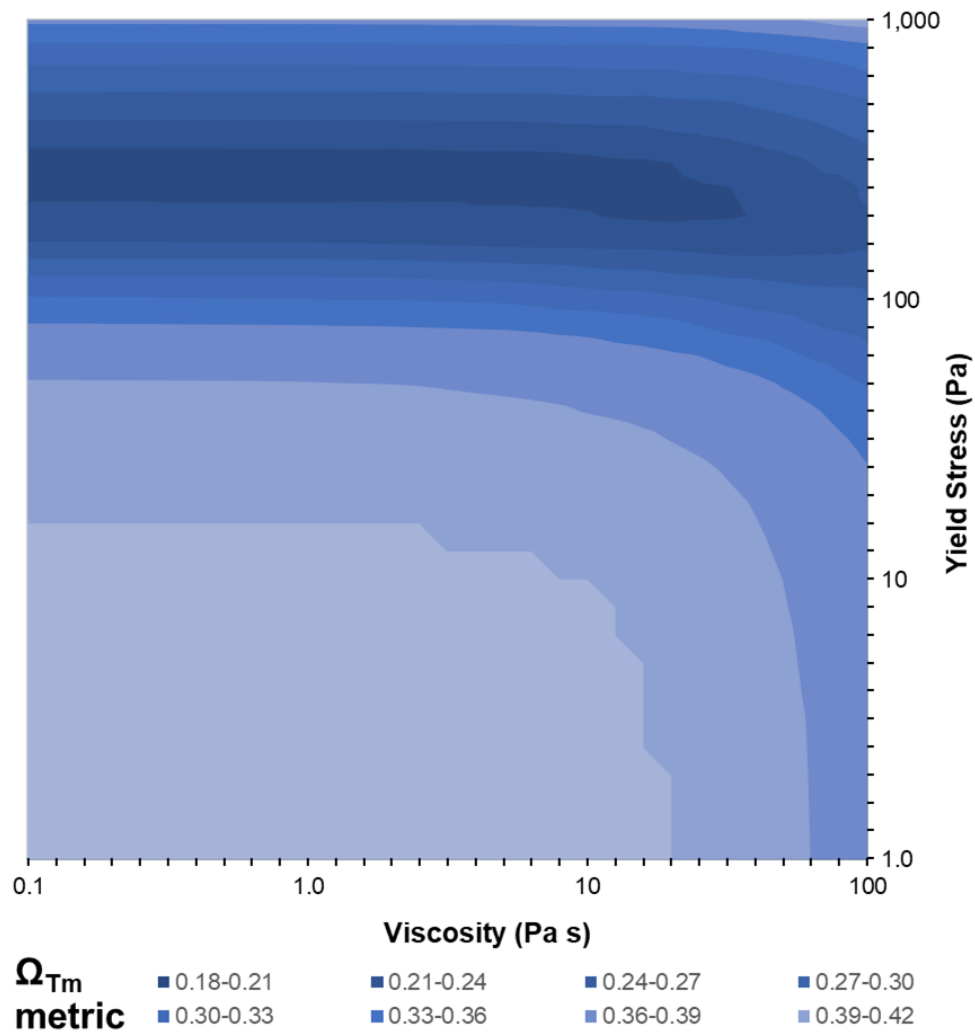


Figure B.30 Tonglüshan Rheology Calibration Plot in Log-Log Scale

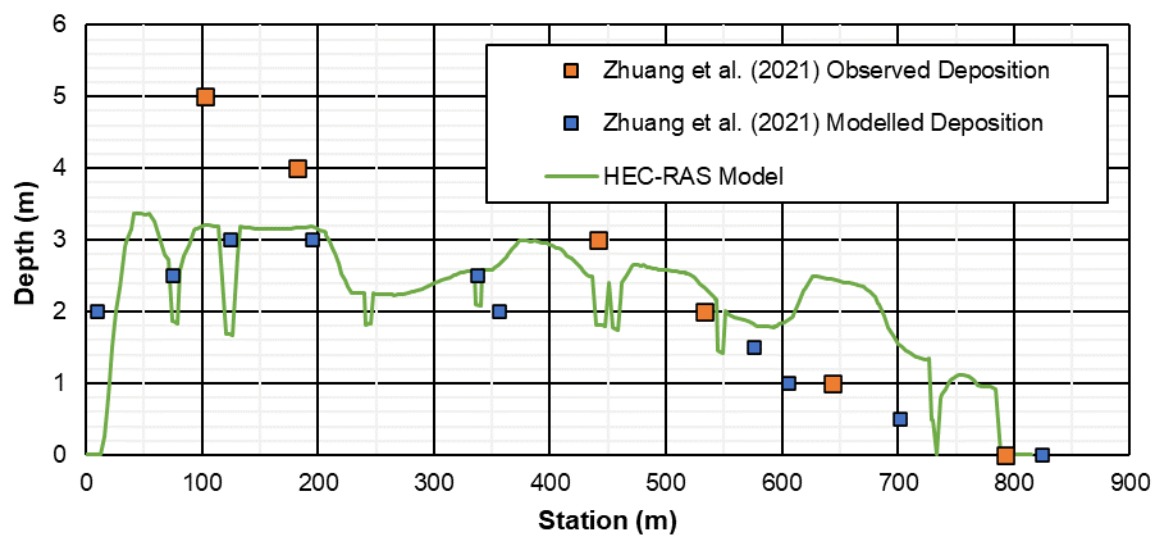


Figure B.31 Tonglüshan Runout Profile with Modelled Results

LEGEND

Zone 1 Inundation Area



Profile Line Along Flow Direction



Maximum Depth (m)

≤ 1.0



1.0 - 2.0



2.0 - 3.0



3.0 - 4.0



4.0 - 5.0



5.0 - 6.0



6.0 - 7.0



7.0 - 8.0



8.0 - 9.0



9.0 - 10.0



> 10.0



Maximum Velocity (m/s)

≤ 1.0



1.0 - 2.0



2.0 - 3.0



3.0 - 4.0



4.0 - 5.0



5.0 - 6.0



6.0 - 7.0



7.0 - 8.0



8.0 - 9.0



9.0 - 10.0



10.0 - 11.0



11.0 - 12.0



12.0 - 13.0



> 13.0



100 0 100 200 300 m

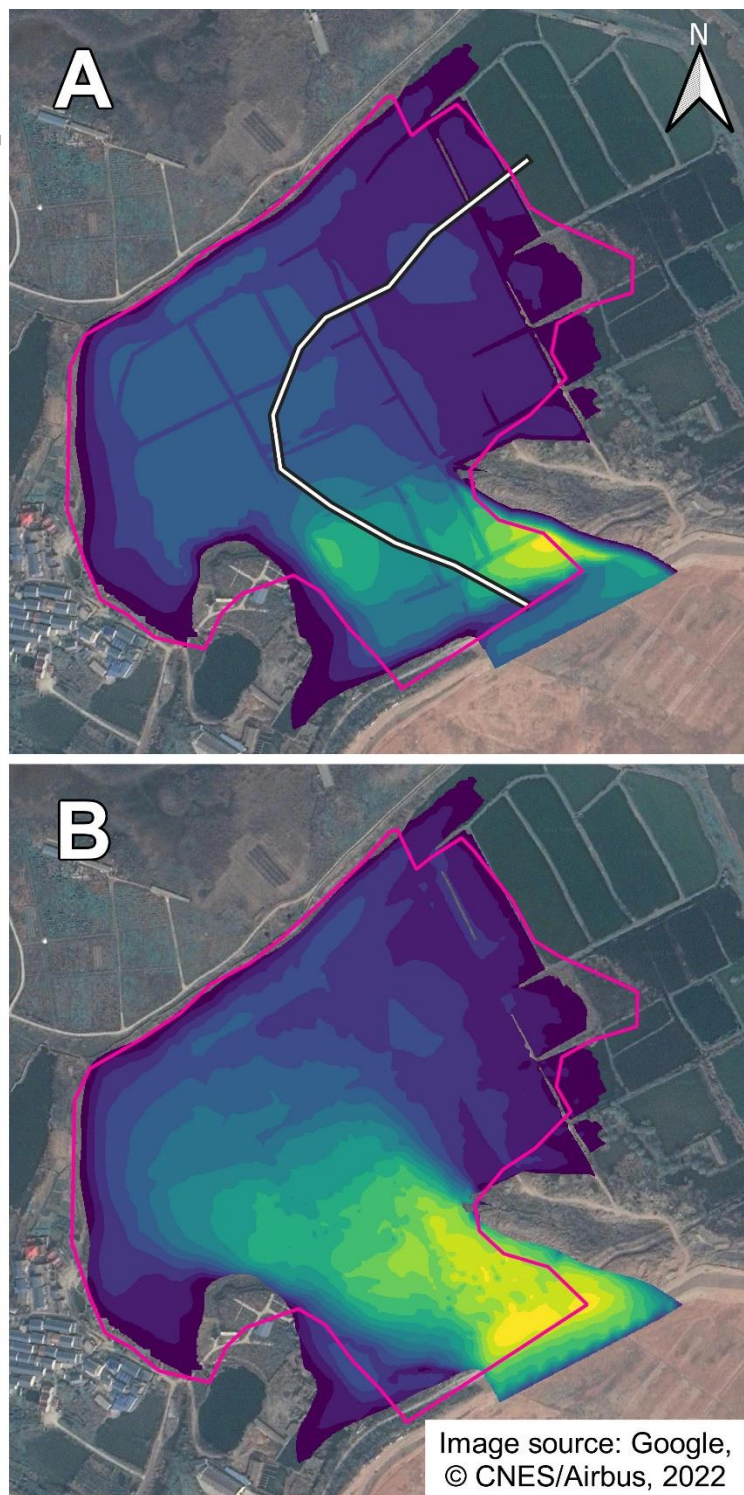


Figure B.32 Tonglùshan HEC-RAS Model Results A) Maximum Depth and B) Maximum Velocity

B10.6 Recommendations for Future Research

The rheology testing from Zheng (2018), the numerical modelling in Zhuang et al. (2021), and the calibration process in this thesis raises questions regarding rheology and numerical models, similar to comments from Ghahramani et al. (2022). Zhuang et al. (2021) were able to use rheology values close to what was measured within the facility post-failure and achieve a close match between the observed and modelled inundation area. Their DAN3D model appears extremely sensitive to the input values; using the measured tailings rheology at 53% (i.e., the volumetric solids concentration observed in the failure source area) performed poorly. The calibrated rheology values in HEC-RAS were around an order of magnitude above the measured values but the model results were not as sensitive to the rheology inputs. Several possible explanations for this are postulated below, however the work required to support or disprove any of them is not within the scope of this thesis.

It is possible that differences in model set-up and approach between here and Zhuang et al. (2021) contribute to the inconsistent rheology. Zhuang et al. attributed the underestimated depth proximal to the breach to be from the small volume of tailings (estimated to be more than 80,000 m³) remaining in the TSF in the model. The modelling herein had similar underestimated depths as Zhuang et al, but the parametric approach forced all 500,000 m³ to discharge through the breach. This volume discrepancy may explain the difference in calibrated rheology. Alternatively, Ghahramani et al. (2021) found that rheology values are non-transferable between different numerical models, which may apply here. Ghahramani et al. found Bingham rheology values DAN3D required higher values than the numerical models with the Quadratic rheology values, contrary to the results here.

The numerical modelling in Zheng et al. (2017) and Zhuang et al. (2021) used detailed terrain data from a site-specific survey, which includes features such as the berms and the rotated dam. These features had to be manually added to the terrain data used herein, which included several assumptions regarding their geometry. Furthermore, the WorldDEM DTM data itself is of lower horizontal resolution and likely vertical accuracy than the drone survey in Zheng et al. Any bias in the WorldDEM DTM or incorrect assumptions in the terrain edits may influence the rheology calibration more so than any rheology value or model choice.

The rheology testing in Zheng (2018) was completed at shear rates between 25 hz and 200 hz. O'Brien (1986) and O'Brien & Julien (1988) concluded that rheology testing for mudflows and debris flows should be conducted at shear rates around or less than 10 hz, and the Bingham model is no longer applicable beyond 20 hz. Boger (2009) noted differences in measured rheology values around a factor of 4 depending on the shear rate used. Therefore, it is possible that the rheology testing in Zheng is not representative of the actual Tonglüshan tailings rheology due to overly high shear rates during the rheology lab testing.

Appendix B.11 Cadia NTSF, Australia, 2018

B11.1 Facility Background and Failure Narrative

The Cadia gold mine has a stepped side-hill arrangement TSF in southwestern Australia. The lower compartment (the Southern TSF, or STSF) and the upper compartment (the Northern TSF, or NTSF) both have upstream dams, although the first raise of the NTSF is relatively large and represents over 50% of the dam height of the NTSF. Cracks on the NTSF were noticed sometime between 8:00 AM to 9:00 PM on March 9, 2018, prompting inspections, a hold on operations, and eventual evacuation of mine personnel and residents throughout the day. Sometime in the early evening, a wide slump occurred at the corner of the NTSF after the foundation failed. The outflow volume was fully contained within the STSF compartment. At 7:21 PM March 11, 2018, additional tailings liquefied and resulted in a second flow event. These liquefied tailings runout overflowed the initial slump and extended the runout distance, but also remained within the STSF (Jefferies et al., 2019).

The Cadia TSF is in a stepped arrangement, but the breach was limited to the NTSF compartment and therefore is comparable to a single compartment breach. Each flow event was investigated separately in this thesis and are referred as Event I and Event II respectively. Event I corresponds to the sudden movement that Jefferies et al. (2019) termed Phase II. Only Event II was modelled with HEC-RAS within this thesis, as HEC-RAS is not a recommended numerical model for slumping scenarios (CDA, 2021).

Impounded Volumes

No reported impounded volume exists for the NTSF, STSF, or the Cadia TSF as a whole. A simple geometric estimate using the TSF surface area, and an approximate average depth likely would be quite inexact given the variable ground elevation throughout the TSF footprint evident in photographs of Stage 1 from Jefferies et al (2019). A small supernatant pond existed at the NTSF at the time of failure but is also of unknown volume. The NTSF supernatant pond was around 1.8 km away from the breach at the time of the breach

Zone 1 Description

The surface of the STSF was the only area impacted by both flow events. The land cover is primary tailings, dirt road, and stripped soil. Aerial LiDAR was flown for the breach location on March 9, 2018, when the cracking was identified, on March 10, 2018, after

Event I, and on March 14, 2018 after Event II. The survey data from March 9 and March 10 were obtained from Newcrest and used within the investigation and numerical modelling. See Section B11.3 for more detail on the Cadia survey information. The tailings were unconfined during the runout (Ghahramani et al., 2020)

The Zone 1 inundation area mapped by Ghahramani et al. (2020) includes both Event I and Event II for a total area of 116,000 m². Additional mapping was conducted for this thesis to produce an area for each event. The mapping was conducted using the Cadia DEMs for Event I and Google Earth Imagery for Event II. The Zone 1 inundation areas were mapped as 97,000 m² and 87,900 m² and the runout distances were mapped as 385 m and 480 m for Event I and Event II respectively. The total area excluding overlap between each flow event is 127,600 m², which is aligned with the estimate from Ghahramani et al. (2020).

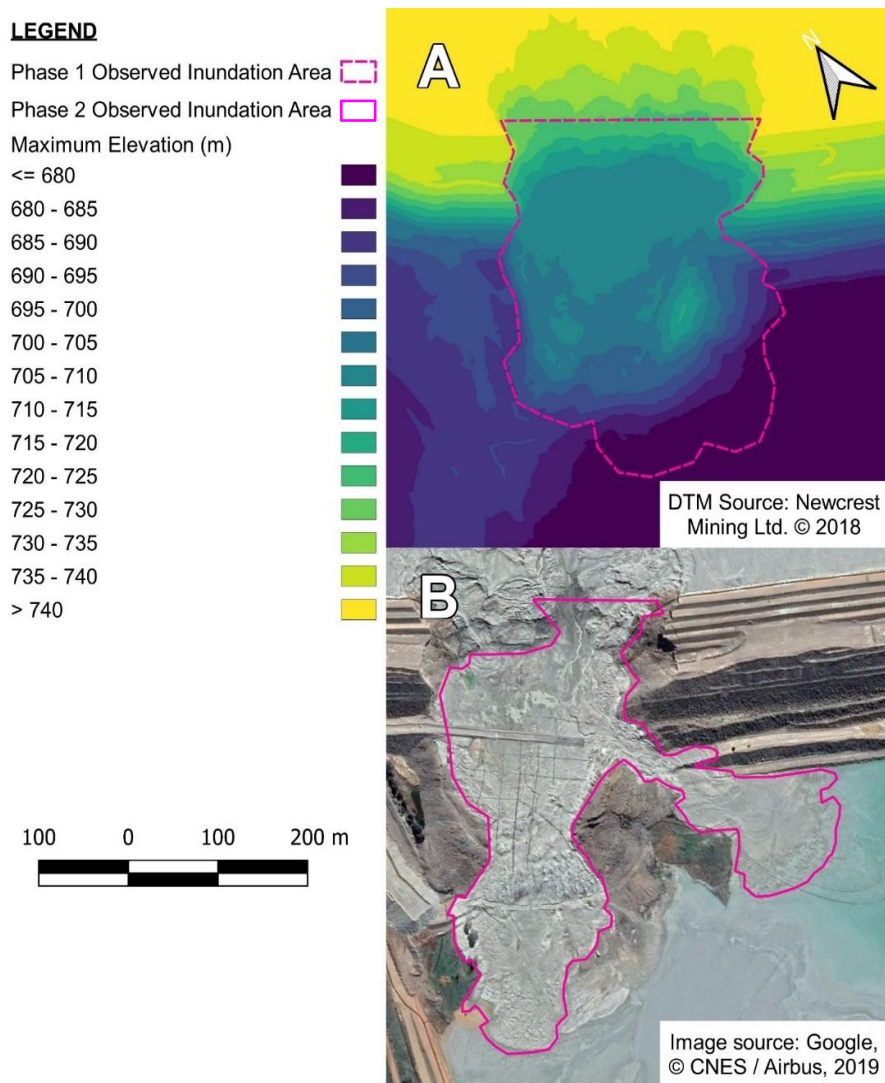


Figure B.33 shows the separated Zone 1 inundation areas.

LEGEND

Phase 1 Observed Inundation Area

Phase 2 Observed Inundation Area

Maximum Elevation (m)

<= 680

680 - 685

685 - 690

690 - 695

695 - 700

700 - 705

705 - 710

710 - 715

715 - 720

720 - 725

725 - 730

730 - 735

735 - 740

> 740

100 0 100 200 m

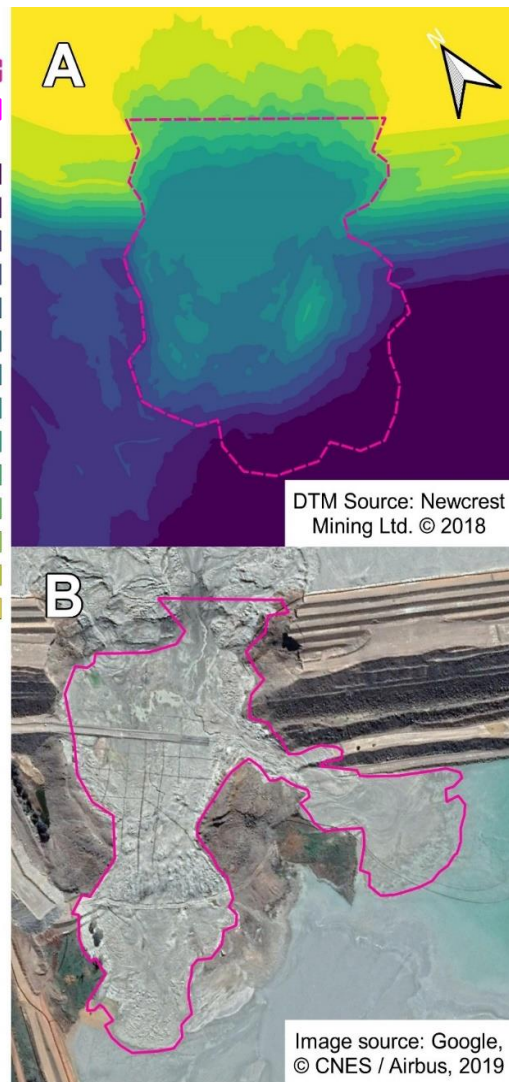
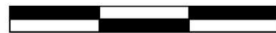


Figure B.33 Cadia NTSF Zone 1 Inundation Area A) Event I and B) Event II

B11.2 Additional Runout Observations

A combination of digitized profiles from Jefferies et al. (2019) and the Cadia DEMs were used to create Figure B.34, which shows the pre-failure surface, the initial slump from Event I and the surface after Event II. The top of the Event I slump is at 707 m. and about 60 m downstream of the stage 10 crest alignment (around station 400 m). The slab for Event II has a slightly concave down shape, implying more of the outflow volume in Event II originated higher up on the residual slope from Event I. The backscarp of the Event II slab is at elevation 741 m. about 200 m upstream from the stage 10 crest. Event II raised the elevation of the slump by around 3 m (Jefferies et al., 2019).

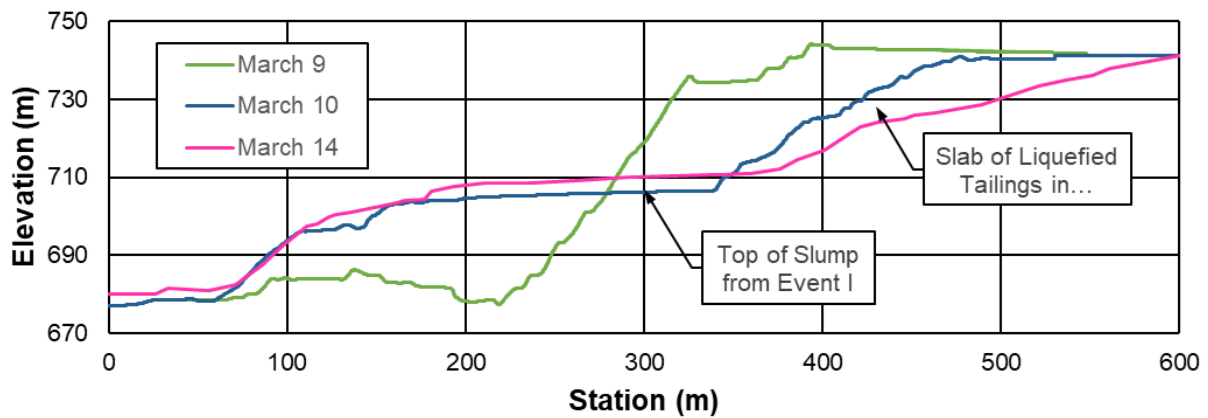


Figure B.34 Cadia NTSF Runout Profile (adapted from Jefferies et al. 2019)

B11.3 Model Inputs

Outflow Volumes

Jefferies et al. (2019) determined the outflow volume using the aerial LiDAR and reported as the cumulative outflow volume on March 10 and March 14. The supernatant pond was noted as too small and too far away to affect the integrity of the NTSF (Jefferies et al., 2019), and did not discharge during either flow event.

The void ratio in the in-situ tailings ranged from 0.56 to 0.67 according to the tailings characteristics investigation in 2017 conducted by the design engineer ATC Williams. The tailings were described as saturated and the phreatic level was just 4 m below the surface (Jefferies et al., 2019). The average void ratio of 0.6 was used and it was assumed that the entire volume was saturated. This results in a volumetric solids concentration of 63%, however it could be slightly lower or higher depending on the in-situ void ratio and saturation at the time of the failure. The volumes used in the numerical modelling are presented in Table B.27.

Table B.27 Cadia NTSF Outflow Volumes

| Event | Tailings Solids (m ³) | Interstitial Water (m ³) | Supernatant Pond (m ³) | Total (m ³) |
|----------|-----------------------------------|--------------------------------------|------------------------------------|-------------------------|
| Event I | 737,100 | 432,900 | 0 | 1,170,000 |
| Event II | 100,800 | 59,200 | 0 | 160,000 |
| Total | 837,900 | 492,100 | 0 | 1,330,000 |

Breach Processes and Geometries

The tailings had propensity for liquefaction, which likely occurred in the tailings deposit during Event I after the foundation failed (Jefferies et al., 2019). The CDA classification system specifically relates to the flow characteristics and not the failure mode. Jefferies

et al. use the terms flowslide and slump interchangeably for Event I. Cruden and Varnes (1996) define flowslides as liquefied flow that move considerable distances. Event I had limited sand boils, suggesting liquefied flow, but it did not move a considerable distance. CDA (2021) classifies slumps as 2B, but notes the boundary is framework and not a clear distinction for all cases. Event I therefore could be either 2A or 2B, depending on the interpretation of the flow characteristics, which did not have any eyewitnesses. Event II is less subjective, demonstrating more sand boils and deposition patterns consistent with liquefied flow (Jefferies et al., 2019), and therefore is a 2A event. Regardless, both flows are Process II breaches.

The breach geometry is presented in Table B.28 and was estimated based on the DEMs and survey within Jefferies et al. (2019). The breach heights were 16 m and 5 m for Event I and Event II respectively, while the max slab thicknesses were 20 m and 14 m, indicating both events can be classified as slabs. The breach trapezoid was measured at the alignment of the Stage 10 crest, or roughly station 400 on Figure B.34. The breach trapezoid for Event II was interpreted to be limited to a narrower section on left side of the Event I breach, informed by the annotated drawings in Jefferies et al. (2019).

Table B.28 Cadia NTSF Breach Geometry

| Event | Dam Height (m) | Crest Height (m) | Slab Breach Height (m) | Bottom Breach Width (m) | Top Breach Width (m) | Left Breach Side Slope (xH:1V) | Right Breach Side Slope (xH:1V) |
|----------|-------------------|---------------------|---------------------------|----------------------------|-------------------------|-----------------------------------|------------------------------------|
| Event I | 94 | 68 | 20 ¹ | 60 | 128 | 1.25 | 1.75 |
| Event II | | | 24 | 30 | 30 | 0 (vertical) | 0 (vertical) |

¹Jefferies et al. (2019) estimated the true failure surface originated in the foundation. The breach height therefore could have included an additional 48 m, however the Event I slump self-dammed and limited the slab breach height to 20 m.

Terrain and Manning's Coefficient

The contours (0.1 m vertical interval) from March 9 and March 10 were provided by Newcrest Mining Ltd., which were used to develop DEMs for the investigation and numerical modelling. The HEC-RAS model used the March 10 DEM for Event II. The created DEMs have horizontal resolutions of approximately 0.1 m. No quantitative measure of the vertical error exist however visually the DEM closely match the figures from Jefferies et al., (2019). Noise was observed in the terrain data near the STSF supernatant pond to the left of the Event I slump, which resulted in vertical discontinuities

1 m tall. The supernatant pond was manually smoothed in addition to the Event II breach channel burning. Lastly, the original contour data is limited to the slump area, therefore, to prevent constraining the runout during rheology calibration a roughly 100 m extension to the DEM was added downstream of the slump. The Manning's coefficient was uniformly assigned as 0.02 to represent the barren surface of the tailings, sand, or soil.

B11.4 HEC-RAS Model Set-Up

For the numerical modelling of Event II, an idealized level-pool semi-cone was used for the stage-storage curve to represent most of the outflowing tailings originating at a higher elevation, as noted in Section B11.2. The breach weir coefficient was 0.928.

The slump has slopes around 20% and the left finger has widths as low as 30 m. The computation cell resolution was selected as 5 m to help address both concerns. No outflow boundary was used. The representative particle size was 60 microns, based on the measured range of d_{50} values from Jefferies et al. (2019).

B11.5 HEC-RAS Model Results

The calibration plot is shown in Figure B.35, with each tick mark roughly representing a 1.77x increase in the rheology inputs. Based on the Ω_{Tm} metric, the best inputs are 1,000 Pa and 560 Pa·s for the yield stress and viscosity respectively. The modelled final depth on the slump was less than the 3 m noted by Jefferies et al. (2019). Conventional trial-and-error was used to improve the modelled results. Rheology inputs of 1,780 Pa and 560 Pa·s still resulted in depths lower than was observed, but in general the shape and depth match between the modelled and observed runout is satisfactory, as shown in Figure B.36. The modelled maximum depth and velocities of the Cadia Event II runout is shown in Figure B.37.

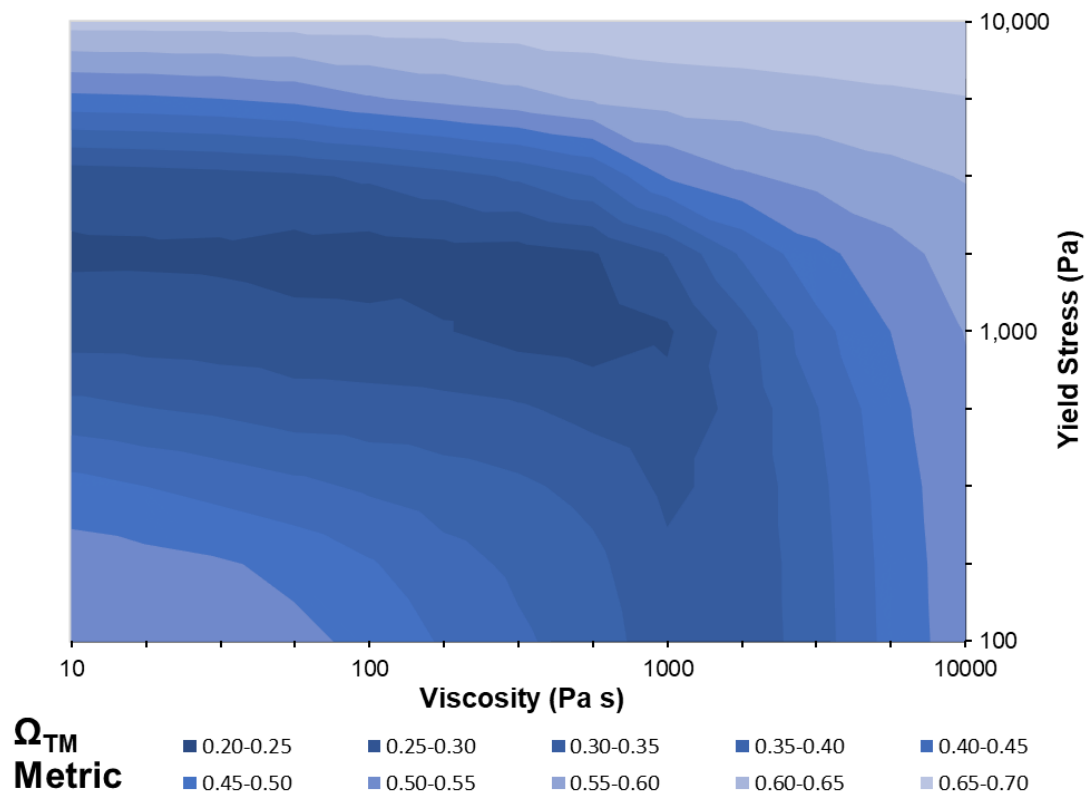


Figure B.35 Cadia NTSF Event II Rheology Calibration Plot in Log-Log Scale

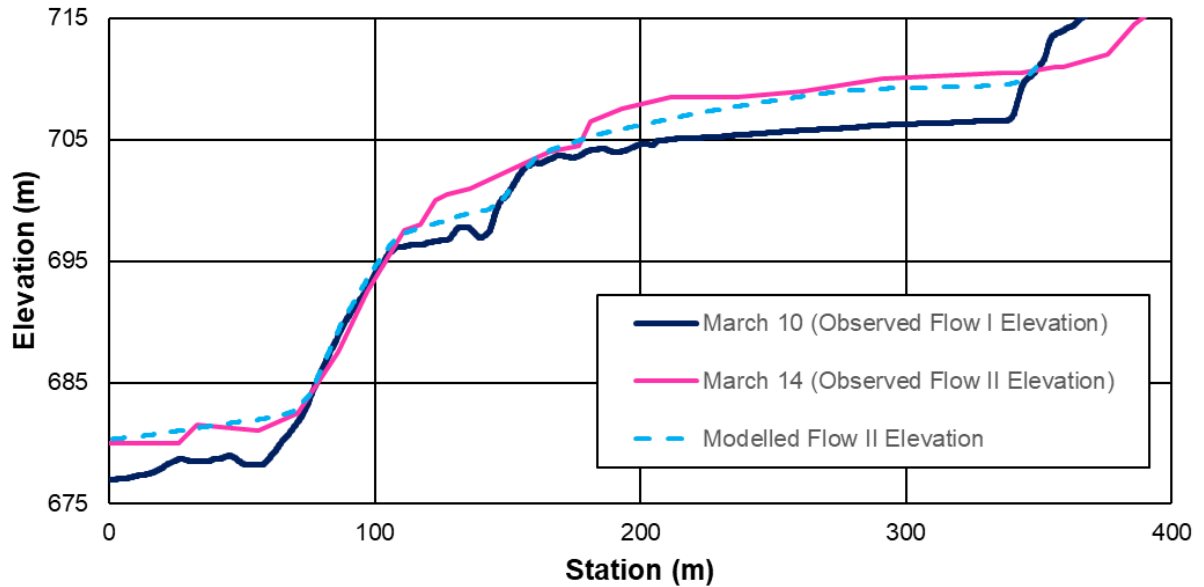


Figure B.36 Cadia NTSF Event II Runout Profile with Modelled Results

LEGEND

Observed Inundation Area

EPR Profile

Maximum Depth (m)

≤ 2.0

2.0 - 4.0

4.0 - 6.0

6.0 - 8.0

8.0 - 10.0

10.0 - 12.0

> 12.0

Maximum Velocity (m/s)

≤ 1.5

1.5 - 3.0

3.0 - 4.5

4.5 - 6.0

6.0 - 7.5

7.5 - 9.0

9.0 - 10.5

10.5 - 12.0

12.0 - 13.5

> 13.5

100 0 100 200 m

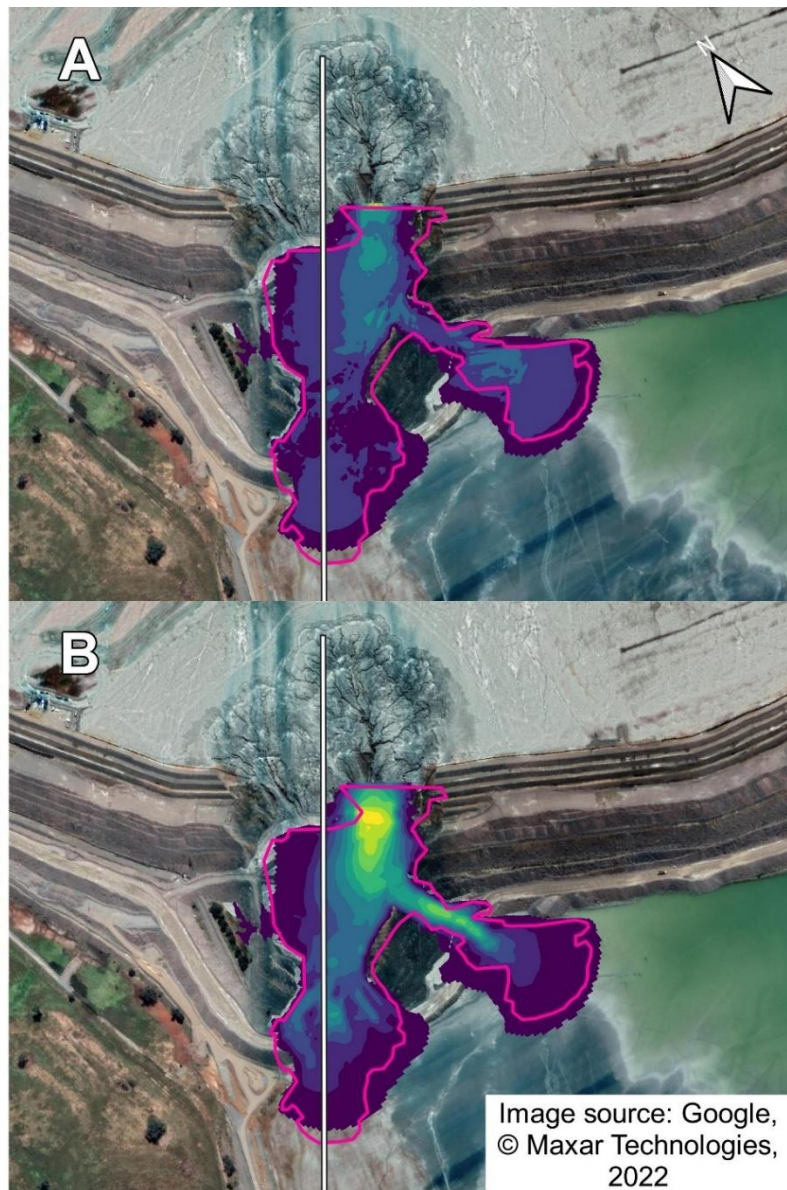
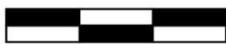


Figure B.37 Cadia NTSF Event II HEC-RAS Model Results A) Maximum Depth and B) Maximum Velocity

B11.6 Recommendations for Future Research

The Cadia Event I event was either a flowslide or a slump. HEC-RAS currently is not an appropriate tool for both flow types and as such Event I was not modelled within this thesis. Given the relatively low reporting on 2B cases, the comparatively rich information available for Cadia Event I is an opportunity to fill some of the knowledge gap in modelling such flow types.

Portions of the DEM from the March 10 survey include slopes around 20%. The assumption for all depth-averaged model like HEC-RAS is that the vertical length scale is smaller than the horizontal length scale. This assumption is commonly stated to be

invalid around 10%, however calibrated results using HEC-RAS have been obtained on steeper slopes (Newmiller, 2017). An assessment of potential numerical error of the runout on the 20% slopes for Cadia Event II may be warranted.

The parametric breach approach was challenging to adapt to for the Cadia Event II event. The toe of the residual slope was not aligned with the dam crest and is instead some 50 m downstream of the crest. Cadia Event II is not unique in this regard however for this event the offset between the toe and crest represents more than 10% of the total runout distance. Therefore, the HEC-RAS model and results may be sensitive to the placement of the boundary condition, either at the dam crest or toe of the residual slope. This sensitivity was not explored within this thesis. A block start model with the spatial distribution informed by the difference in the surveys between March 10 and March 14 may perform better than the parametric breach approach.

Despite these concerns above, the Cadia Event II has more information available for calibration and current modelled results match the observed runout well. This is shown through the relatively low Ω_{Tm} metric and close depth match along the profile from Jefferies et al. (2019). Other events within this thesis may have greater opportunities for improvement.

Appendix B.12 Feijão Dam I (Brumadinho), Brasil, 2019

B12.1 Facility Background and Failure Narrative

The Córrego do Feijão Iron Ore Mine in Minas Gerais, Brasil had an upstream, side-hill arrangement TSF (“Dam I”). Dam I was in a closure stage after the final tailings were deposited in 2016. At 12:28 PM on January 25, 2019, monitoring cameras captured the Dam I suddenly and catastrophically collapsing. The tailings outflow swept through mine facilities and continued through the Ferro Carvão River valley. The runout physically impacted rural residences and Vila Cachoeirinha, a small town on the bank of the Ferro Carvão. The tailings reached the confluence with the Paraopeba River some 10 km downstream (CPRM, 2019; Robertson et al., 2019; Lumbroso et al., 2019, de Lima et al., 2020) and formed a landslide dam at the confluence of the Ferro Carvão River with the Paraopeba River. Over 270 people were killed by the tailings runout. Continued sediment plume and environmental impacts occurred over 100 km of the Paraopeba River for months after the breach (CPRM, 2019, de Lima et al., 2020, Ghahramani et al., 2020).

Impounded Volumes

Pre-dam digitized topography and post-failure LiDAR was used to estimate the total volume of the tailings as 12.726 M m³ by Robertson et al. (2019). The facility had a supernatant pond during tailings deposition, but surface water management practices had been implemented since 2018 in an attempt to remove the pond. These attempts were not fully successful, given the observations of wet areas interpreted as a supernatant pond in the months leading to the failure event (Robertson et al., 2019).

Zone 1 Description

The mine facilities downstream of the dam include an overburden dump, stockpile area, canteen, and administrative offices (Robertson et al., 2019). Beyond the mine site, the Ferro Carvão River valley includes a mix of low to mid-density residential, rural farmland or pastures, and forested or vegetated cover (MapBiomas, 2018). The confluence of the Ferro Carvão River with the Paraopeba River is around 9.3 km downstream of Dam I, following the valley thalweg. The tailings were confined by the valley during the entire runout (Ghahramani et al., 2020).

Ghahramani et al. (2020) estimated the Zone 1 inundation area to be 2.7 km² and a runout distance of 9.0 km (following the breach flow centreline rather than the channel thalweg). The mapping was subsequently refined, and the current mapping indicates an

area of 3.1 km² for the Zone 1 inundation area. The refined mapping was used in this thesis.

B12.2 Additional Runout Observations

Feijão is unique for a tailings dam failure in that there are many high-quality videos of the event that provide insight into the failure and runout (Robertson et al., 2019, de Lima et al., 2020). The video camera monitoring the dam (CAM1) give clear evidence for several flow characteristics at the breach, as interpreted by the following groups:

- At 12:28:21 on January 25, 2019, the crest began deforming, signaling the start of the breach process (Robertson et al., 2019),
- The breach took less than 10 seconds to fully develop (Robertson et al., 2019, de Lima et al., 2020),
- The duration of the breach took around 6.5 minutes, with most of the outflow occurring within 5 minutes (Robertson et al., 2019),
- The frontal velocity of the tailings flows proximal to the breach (within 330 m of Dam I) is estimated between 28 m/s to 33 m/s (Petley, 2019, de Lima et al., 2020).

Another security camera at the overburden dump, roughly 800 m downstream of the toe of Dam I allows an estimate of the frontal velocity as well. Petley (2019) and de Lima et al., (2020) used this video to calculate a velocity of 18.4 m/s. de Lima et al. (2020) also use a civilian video taken at Alberto Flores Road (around 8.5 km downstream from the dam) and estimate a velocity between 2.2 m/s to 5 m/s. No information on the timing of the video is available, therefore it is not clear if the velocity corresponds to the front of the tailings wave or the tail and limits the use of this observation to model calibration.

The National Water and Sanitation Agency of Brasil (ANA) operates river monitoring stations, including on the Paraopeba. The Alberto Flores station (#40740000) is located on the Paraopeba River some 1.1 km upstream of the confluence of the Ferro Carvão River and digitally records stage data every 15 minutes in Coordinated Universal Time (UTC). On January 25, 2019, the station recorded an increase in water level due to backwatering from the landslide dam beginning between 13:00 PM and 13:15 PM (local time). This is strong evidence that the arrival time to the Paraopeba River is on the order of 30 minutes (CPRM, 2019). The water level increased to 7 m over the following 9 hours. The slope of the Paraopeba appears to be 0.4%, suggesting the landslide dam could have been around 11 m tall at the confluence, but it is difficult to confidently make this

conclusion without detailed bathymetry of the Paraopeba River. As the tailings did not directly reach the Alberto Flores station (CPRM, 2019), the 9 hours to the peak water level is reflective of the time the Paraopeba River took to infill behind the landslide dam and not the duration of tailings flow. CPRM (2019) estimates that 5.0 to 6.0 M m³ of the tailings reached the Paraopeba River, based on pre-failure topography and post-failure LiDAR of the Ferro Carvão River.

Within civilian news, the tailings arrival time to Paraopeba River is generally between 14:40 PM to 15:50 PM (e.g., Globo, 2019; Ramalhoso & Rebello, 2019; Xinhua, 2019). However, no locations are provided and nor is there any evidence to confirm the arrival time beyond repeated reporting, which may or may not be individual eyewitness accounts. Inferred locations for the observations are around the centre of Brumadinho, based on the interviews with the host of Rádio Regional FM de Brumadinho, which is stationed some 5 km downstream of the Paraopeba confluence (UOL News, 2019). Based on the questionable reliability and unconfirmed location, this observation is considered neither reliable for numerical model calibration nor relevant to Zone 1.

B12.3 Model Inputs

Outflow Volumes

Robertson et al. (2019) determined the outflow volume using pre-failure topography and post-failure LiDAR. Despite the wet areas observed, the supernatant pond volume was estimated to be negligible by Robertson et al. (2019) and Rana et al. (2020) at the time of the failure. The void ratio in the in-situ tailings was approximately 1.0 according to a 2005 field investigation, which combined with the estimated phreatic surface results in interstitial water volume of approximately 5.0 M m³ prior to the failure, or a volumetric solids concentration of 58% within the facility prior to failure (Robertson et al., 2019). This same portion of tailings solids and interstitial water was used for the outflow volume. The volumes used in the numerical modelling are presented in Table B.29.

Table B.29 Feijão Dam I Outflow Volumes

| Compartment | Tailings Solids (m ³) | Interstitial Water (m ³) | Supernatant Pond (m ³) | Total (m ³) |
|-------------|--------------------------------------|---|---------------------------------------|----------------------------|
| Dam I | 5,598,000 | 4,053,000 | 0 | 9,651,000 |

Breach Process and Geometry

The tailings are described as liquefiable and brittle (Robertson et al., 2019). There was no supernatant pond volume or negligible supernatant pond volume. The video from CAM1 distinctly shows highly flowable tailings during the breach. A CDA classification of 2A and Process II breach is clearly applicable for the Feijão event.

The breach geometry is presented in Table B.30 and was estimated based on the post-failure LiDAR shown in Robertson et al. (2019). The heights and top width are readily apparent from the plan view and profiles. No contours or other information is included with the pre- and post- failure topographies however, making the definition of the bottom breach width and breach side slopes challenging. Furthermore, the breach shape appears to be U-shaped, rendering trapezoid approximations subjective. For example, the geometry could arguably be defined equally well with a breach bottom width and breach side slopes of 160 m and 2.5H:1V or 40 m and 3.25H:1V.

Table B.30 Feijão Dam I Breach Geometry

| Dam Height (m) | Crest Height (m) | Breach Height (m) | Bottom Breach Width (m) | Top Breach Width (m) | Left Breach Side Slope (xH:1V) | Right Breach Side Slope (xH:1V) |
|-------------------|---------------------|----------------------|----------------------------|-------------------------|-----------------------------------|------------------------------------|
| 86 | 80 | 80 | 100 | 560 | 2.88 | 2.88 |

Terrain and Manning's Coefficient

The terrain data source was the Airbus WorldDEM DTM, with a spatial resolution of 12 m. The terrain data is reported as bare earth, however many small ridges on the order of a few metres tall were noticed in the Ferro Carvão thalweg. Some of the ridges corresponded to observed features such as irrigation dams and roads while others may be from vegetation interference. The height of the ridges is relatively small compared to the modelled flow depths (10 m to 30 m deep). Consequently, the ridges were considered to introduce only a small error or be a real feature and they were not removed from the terrain. The breach channel was cut into the terrain as normal.

The land cover within the Ferro Carvão River valley is relatively varied, ranging from barren mine areas to rural residential to heavy forest and vegetation (MapBiomass,

2018, Lumbroso et al., 2020). The MapBiomass Land Use Collection 5 is a raster with 30 m resolution that defines the areal extent and land cover type across Brasil. The land cover product for 2018 was used within the HEC-RAS model and the selected Manning's coefficients for each land cover type is presented in Table B.31. It was noticed that several areas appeared to be misclassified within the MapBiomass data; for example, the residential area of Vila Cachoeirinha is labelled as agriculture and pasture. The land misclassification is further discussed in Section B12.4.

Table B.31 Feijão Dam I Land Cover and Selected Manning's Coefficients

| MapBiomass (2018) Land Cover Types | Manning's Coefficient |
|--|-----------------------|
| Mining, Natural (Rocky), Agriculture, Pasture, Other | 0.05 |
| River | 0.06 |
| Mixed Agriculture and Brush | 0.08 |
| Urban, Forest, Savanna | 0.12 |

B12.4 HEC-RAS Model Set-Up

The HEC-RAS model for the breach and upstream portion of the Zone 1 area was relatively standard. An idealized level-pool semi-cone was used for the stage-storage curve for the Process II breach. The breach weir coefficient was 0.928. The average width of the Zone 1 inundation area is 300 m, however in some location it narrows to around 60 m. The selected computation resolution was 20 m to suit the narrower sections and is alignment with the model set-up from Gibson et al (2022) for their Feijão tailings dam breach model in HEC-RAS. Additional manual delineation was sparsely used within HEC-RAS where required to correct the assigned Manning's coefficient at specific locations in Zone 1 where the MapBiomass Collection 5 data appeared to be misclassified.

Two Normal Depths BCs are used in the Paraopeba River, one upstream and another downstream of the Ferro Carvão confluence. This approach is based on hindsight that the Zone 1 terminates at the confluence. HEC-RAS is currently limited to a single fluid, therefore modelling and interaction and mixing with the Paraopeba River following the landslide dam is not possible. This approach is similar to Gibson et al. (2022), with their HEC-RAS model terminating at the confluence as well. The representative particle size was 200 microns, based on the d_{50} from Robertson et al. (2019).

B12.5 HEC-RAS Model Results

The calibration plot is shown in Figure B.38, with each tick mark roughly representing a 1.58 increase in the rheology inputs. Based on the Ω_{Tm} metric, the best inputs are 400 Pa and 100 Pa·s for the yield stress and viscosity respectively. However, the modelled results do not align with the observations in other ways, primarily the arrival time to the Paraopeba River. Conventional trial-and-error calibration resulted in rheology inputs of 400 Pa and 25 Pa·s that met reached the Paraopeba within the observed timing from the Alberto Flores gauge. The modelled results with these inputs reasonably fit the rest of the observations as shown in Table B.32. The modelled maximum depth and velocities of the Feijão runout is shown in Figure B.39.

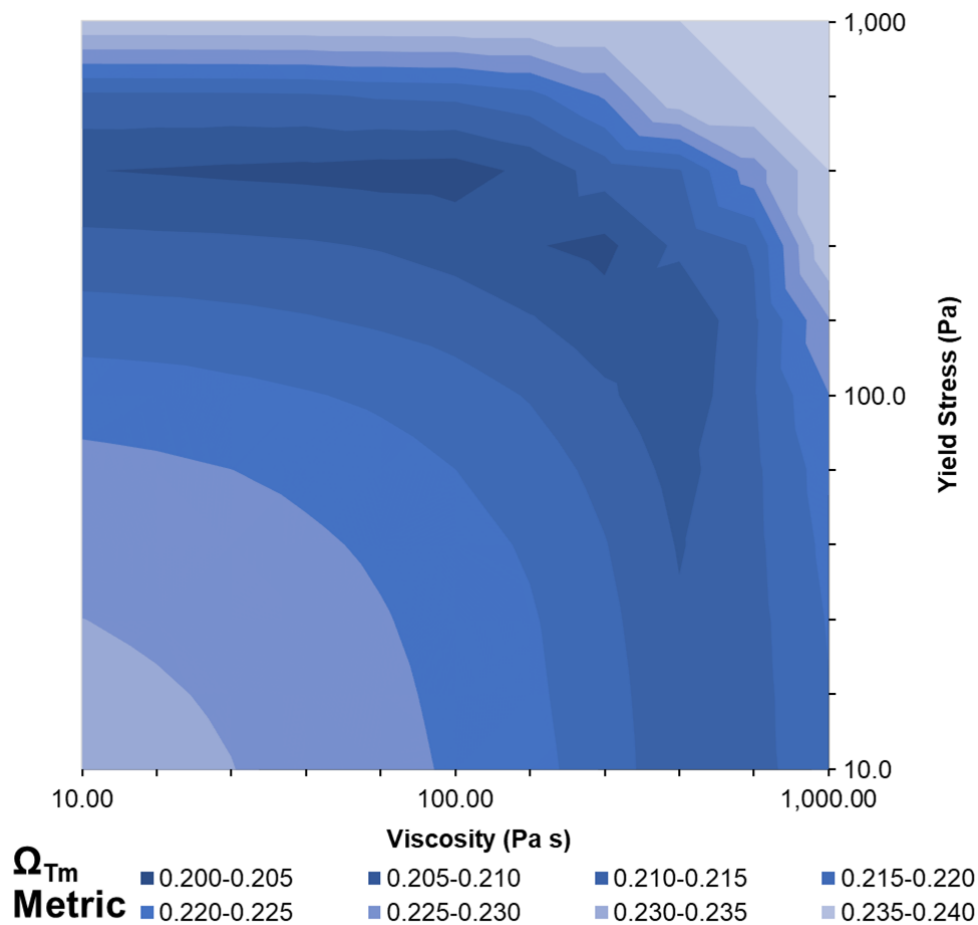


Figure B.38 Feijão Dam I Rheology Calibration Plot in Log-Log Scale

Table B.32 Feijão Dam I Observations and Modelled Results Comparison

| Observation | Observed Value | Modelled Value | Comment |
|---|--|---------------------------|--|
| Duration of Breach (Robertson et al., 2019) | < 5 minutes | 3:20 mm:ss 5:26 mm:ss | 95% of total volume has discharged 99% of total volume has discharged |
| Frontal Velocity at Dam I (P1) (Lima et al., 2020) | 28 m/s to 33 m/s | 26.3 m/s | Modelled peak velocity of 28.5 m/s occurs in model results within 50 m of P1 |
| Frontal Velocity at Overburden Area (P2) (Lima et al., 2020) | 18.4 m/s | 17.1 m/s | Modelled velocities range between 15.3 m/s to 18.0 m/s within 50 m upstream and downstream of P2 |
| Velocity at Alberto Flores Road (P3) (Lima et al., 2020) | 2.2 m/s to 5 m/s | Peak velocity: 2.6 m/s | Velocity at centre of the road is greater than 2.2 m/s for 21 minutes |
| Arrival Time at the Confluence (CPRM, 2019) | 13:00 PM to 13:15 PM | 13:08 PM | |
| Height of Landslide Dam (CPRM, 2019) | 11 m | 10.8 m | The observed height of the landslide dam is not fully confirmed |
| Volume Reaching the Paraopeba (CPRM, 2019) | 5.0 M m ³ to 6.0 M m ³ | 6.0 M m ³ | The observed volume reaching the Paraopeba is not fully confirmed |

LEGEND

Velocity Points



Alberto Flores Gauge



Observed Inundation Area



Maximum Depth (m)

≤ 5.0



5.0 - 10.0



10.0 - 15.0



15.0 - 20.0



20.0 - 25.0



25.0 - 30.0



30.0 - 35.0



35.0 - 40.0



40.0 - 45.0



45.0 - 50.0



50.0 - 55.0



> 55.0



Maximum Velocity (m/s)

≤ 3.0



3.0 - 6.0



6.0 - 9.0



9.0 - 12.0



12.0 - 15.0



15.0 - 18.0



18.0 - 21.0



21.0 - 24.0



24.0 - 27.0



> 27.0



750 0 750 1,500 m

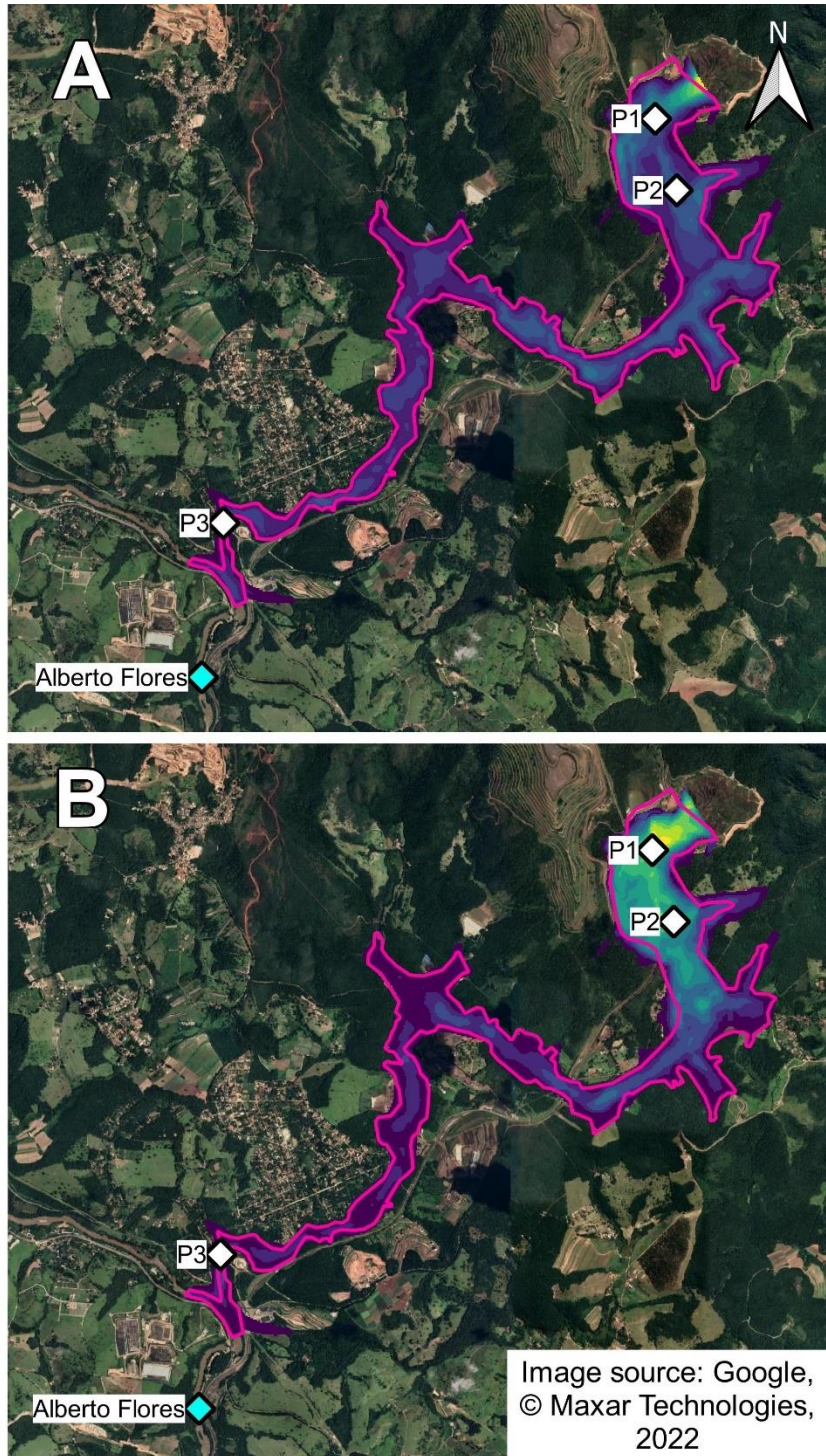


Figure B.39 Feijão Dam I HEC-RAS Model Results A) Maximum Depth and B) Maximum Velocity

B12.6 Recommendations for Future Research

The U-shaped breach geometry for Feijão Dam I is not confidently defined. The post-failure LiDAR exists and can be used to better inform the breach geometry if it were publicly accessible.

The tailings flow in the Ferro Carvão River valley appears to be modelled very well, meeting multiple observations throughout Zone 1 (i.e., the velocities at several points, areal extent, arrival time at the Paraopeba River, and total volume reaching at the Paraopeba River). The tailings flow and landslide dam at the confluence of the Ferro Carvão with the Paraopeba River also appears to be reasonably modelled evidence by the modelled height of the landslide dam. However, the landslide dam may be affected by the addition of channel bathymetry in the Paraopeba and the mixing of the tailings flow with the Paraopeba River. An erodible bed model with multiple fluid types can be used to investigate this interaction at the transition between primary and secondary impact zones.

Relatively good reporting on building damage and fatality rates may be available for the Feijão event. A study on fatality rates from this event the would be of interest for industry but is not within the scope of this thesis.